University of Southampton

Faculty of Engineering and Physical Science

Electronics and Computer Science

Miniaturised platforms for rapid diagnosis of antibiotic resistance

by

Yuetao Li

Thesis for the degree of Doctor of Philosophy

August 2020

UNIVERSITY OF SOUTHAMPTON

ABSTRACT

FACULTY OF ENGINEERING AND PHYSICAL SCIENCE

Electronics and Computer Science

Thesis for the degree of Doctor of Philosophy

MINITURISED PLATFORMS FOR RAPID DIAGNOSIS OF ANTIBIOTIC RESISTANCE

by

Yuetao Li

Pathogenic bacteria are biological cells that can cause infectious diseases. Antimicrobial resistance (AMR) is a phenomenon whereby pathogenic bacteria can survive even after exposure to previous effective antibiotics. If necessary action is not taken, AMR is predicted to be the leading cause of mortality. Antibiotic efficiency against bacteria is determined by antimicrobial susceptibility testing (AST). Conventional AST methods are time-consuming because they determine growth after many doubling times and each doubling time is at least 20 minutes. The lack of time efficient diagnostic tools accelerates AMR because antibiotics are usually prescribed without the susceptibility test results. This research describes the development of three miniaturised AST systems that are fast-test, low-cost and high-sensitivity.

The first detection system is a dielectrophoresis (DEP) enhanced optical system that can detect the presence of β-lactamases from a minimum of 10^3 colony-forming unit (CFU)/mL bacterial sample in 1 hour. The bacteria in a test sample were first enriched by filtering followed by DEP concentration. Then, the presence of β-lactamases was determined through a colour change using the dye nitrocefin, a β-lactam analogue, in an optical chip. The sensitivity of the DEP-enhanced optical system is four orders of magnitude better than conventional plate-based assays and the clinical selectivity is 100%.

The second detection system is a miniature pH system that can detect the presence of β-lactamases from a low concentration sample of 10^5 CFU/mL bacterial sample in 1 hour. An iridium oxide pH sensor is used to detect the pH reduction due to β-lactam antibiotic hydrolysis. This pH system is robust, simple and suitable for application in point-of-care situations. The sensitivity of the pH system is two orders of magnitude better than conventional plate-based assays and the clinical selectivity is 75%.

The third detection system measures the impedance of a suspension of bacteria exposed to antibiotics to infer growth rate and susceptibility, which can indicate the minimum inhibitory concentration (MIC) of β-lactam antibiotics, ciprofloxacin, gentamicin, ceftazidime, colistin and doxycycline for various species of bacteria. The MIC detected by the impedance system can be done in 1 hour and shows >90% concordance with conventional broth dilution method that takes over 20 hours.

In summary, this thesis describes three miniaturized, AST systems aimed at rapid diagnosis of the presence of β-lactamases or broadband antibiotic susceptibility within 1 hour with low cost and high sensitivity.

Table of Contents

Table of Contents ..... **i**
Table of Tables ..... **vii**
Table of Figures ..... **ix**
Research Thesis: Declaration of Authorship ..... **xxi**
Acknowledgements ..... **xxiii**
Definitions and Abbreviation ..... **XXV**
Chapter 1: Introduction **1**
1.1 Motivation 1
1.2 State-of-art diagnosis 1
1.3 Research directions 2
1.4 Main achievements 3
1.4.1 DEP-enhanced optical system for measuring β-lactam cleavage (DEP-enhanced optical system) 4
1.4.2 pH detection system for measuring β-lactam cleavage (pH system) 6
1.4.3 Impedance system for assessing the susceptibility of bacteria to different classes of antibiotics (Impedance system) 6
1.5 Novelty 6
1.5.1 DEP-enhanced optical system 6
1.5.2 pH detection system 7
1.5.3 Impedance system 7
1.6 Thesis structure 7
1.7 Declaration 8
Chapter 2: Understanding of AMR **10**
2.1 Bacteria 10
2.2 Antibiotics 11
2.3 AMR 14
2.3.1 Mechanisms of AMR 14
2.3.2 Horizontal gene transfer 15
2.4 Conventional AST methods and their limitations. 16

2.5 EUCAST breakpoints table 19
2.6 β-Lactam resistance 21
2.6.1 β-Lactam antibiotics 21
2.6.2 The causes of β-lactam antibiotics resistance 22
2.6.3 β-Lactamases 23
2.6.4 Nitrocefin 24
2.6.5 pH reduction 25

Chapter 3: Reviews of rapid AST methods 27

3.1 Impedance methods 27
3.1.1 Medium conductivity detection 27
3.1.2 Growth medium permittivity detection 32
3.1.3 Charge transfer resistance detection 33
3.1.4 Double layer capacitance detection 36
3.1.5 Ion release detection 37
3.2 Optical methods 39
3.2.1 Morphological observation 39
3.2.2 Length monitor 40
3.2.3 Fluorescence observation 41
3.2.4 Droplet fluorescence observation 42
3.3 pH methods 43
3.3.1 Metabolism detection 43
3.3.2 β-Lactam ring hydrolysis 45
3.4 Other rapid AMR diagnosis methods 46
3.4.1 Genotypic diagnosis 46
3.4.2 DEP method 47
3.4.3 Electrochemical methods 48
3.5 Commercial Devices 48
3.6 Discussion and conclusion 51

Chapter 4: Reviews of microfluidic platforms 55

4.1 Dielectric dispersion 55

4.1.1 Interfacial polarization (β-dispersion) 55
4.1.2 Relaxation of attracted counter-ions (α-dispersion) 56
4.2 Bio-particle manipulation by DEP 57
4.3 Sensitive absorbance chips 62
4.4 pH detection 63
4.4.1 Conventional pH detection 63
4.4.2 ISFET pH detection 64
4.4.3 Metal-Metal Oxide pH detection 65
4.5 Discussion and conclusion 65

Chapter 5: Theory 67

5.1 Interfacial polarisation and its applications 67
5.1.1 Complex permittivity 67
5.1.2 Dielectric relaxation 68
5.1.3 Interfacial polarisation 69
5.1.4 The effective dipole moment of a sphere or an ellipsoid particle 70
5.1.5 DEP force 72
5.1.6 MMT of a particle suspension 72
5.2 Impedance detection 73
5.2.1 Electrode double layer and parasitic capacitance 73
5.2.2 Electrode polarisation: Pt black 75
5.2.3 Electrode polarisation: four-terminal system 77
5.2.4 Transconductance amplifier 79
5.3 Ideal electrodes 79
5.3.1 Nernst equation 79
5.3.2 Ideal non-polarisable electrode: Ag/AgCl electrode 80
5.3.3 Ideal polarisable electrode: Pt electrode 80
5.4 pH detection 82
5.4.1 Definition of pH value 82
5.4.2 pH buffer 82
5.4.3 IrOx pH sensor 83

5.5 Beer-Lambert law 84
5.6 Summary 84

Chapter 6: Electrical properties of *E. coli* suspension: simulations 85

6.1 Three-shell ellipsoid *E. coli* model 85
6.2 Simulations of the impedance of an *E. coli* suspension 86
6.2.1 Permittivity and conductivity of an *E. coli* suspension 86
6.2.2 Normalized impedance change ratio (NICR) 93
6.2.3 Quotation of normalized impedance change ratio (QNICR) 97
6.2.4 Two-terminal impedance spectrum 102
6.3 DEP force on an *E. coli* bacterium 103
6.4 Discussion and conclusion 105

Chapter 7: Methodology 107

7.1 Bacteria culture and treatment 107
7.1.1 Bacteria culture 107
7.1.2 Sample treatment 108
7.2 DEP-enhanced optical system 109
7.2.1 Filter 109
7.2.2 DEP chip 110
7.2.3 Optical chip 111
7.2.4 Method (optical chip) 113
7.2.5 Method (DEP-enhanced optical system) 113
7.3 pH system 114
7.3.1 pH sensor 114
7.3.2 pH indicator 116
7.3.3 Calibration 116
7.3.4 Method 117
7.4 Impedance system 117
7.4.1 Impedance detection 119
7.4.2 Customized incubator 121
7.4.3 Calibration 121

7.4.4 Method 121

Chapter 8: Results and discussions 123

8.1 DEP-enhanced optical system 123

8.1.1 Optical chip calibration 123
8.1.2 Kinetic parameters 123
8.1.3 Supernatant and bacterial lysates 126
8.1.4 Sensitivity of β-lactamase diagnosis 127
8.1.5 Clinical test results 129
8.1.6 Bacteria enrichment 129
8.1.7 Integrated system 130

8.2 pH sensing system 131

8.2.1 pH sensor calibration and stability test 131
8.2.2 pH indicator calibration and stability test 133
8.2.3 Kinetic parameter 134
8.2.4 Supernatant and bacterial lysates 136
8.2.5 Sensitivity of β-lactamases diagnosis: *E. coli* TEM 137
8.2.6 Sensitivity of β-lactamases diagnosis: *E. coli* 11560 138
8.2.7 Clinical blind test 140

8.3 Impedance system 141

8.3.1 Bacterial concentration at OD=0.01 141
8.3.2 OD-based growth curve 141
8.3.3 Two- and four-terminal impedance system calibration and verification 145
8.3.4 MIC detect by the impedance method 149
8.3.5 Blind test for *K. pneumoniae* 156

8.4 Discussion and conclusion 158

8.4.1 DEP-enhanced optical chip 158
8.4.2 pH system 159
8.4.3 Impedance system 160

Chapter 9: Conclusion, improvement and future work 163

9.1 Optical system 163

9.2 pH system 167
9.3 Impedance system 167

Appendix: Matlab code for *E. coli* simulation 171
References 177

Table of Tables

Table 1-1: Summary of the DEP-enhanced optical system, pH system and impedance system for rapid AMR diagnosis. 4
Table 2-1: Summary of common species of pathogenic bacteria described in this thesis. Their transmission, general antibiotics for treatment and gram staining are listed [39]. 11
Table 2-2: Summary of the antibiotics described in this thesis. The primary effects, mechanisms of action, members of the antibiotics and target bacteria spectra are listed [39]. 13
Table 2-3: Steps for broth dilution method used in this project. The MIC is used to describe the antibiotic susceptibility [62]. 16
Table 2-4: Steps for the disk diffusion method. The zone diameter around the antibiotic disk is used to indicate the antibiotic susceptibility. 17
Table 2-5: MIC breakpoints (μg/mL) of resistance used in this thesis. If the MIC of testing bacteria is larger than the breakpoint, the strain is defined as resistance. Otherwise, it is defined as susceptible. 21
Table 2-6: Resistance profile of different β-lactamases to β-lactam antibiotics. β-Lactamase–producing bacteria are resistant to penicillins. ESBL-producing bacteria are resistant to penicillins and cephalosporins. Carbapenemase-producing bacteria are resistant to almost all β-lactam antibiotics. 24
Table 3-1: The steps of AMR diagnosis by novel clinical diagnostic devices [141]. 49
Table 3-2: The minimum bacterial concentration required, detection time, and advantages and disadvantages of the novel AMR diagnosis methods. 52
Table 6-1: The default electrical parameters used in this simulation. Five materials with different electronic properties were used in this simulation: medium, outer membrane, periplasmic, inner membrane and cytoplasm. The parameters are from Bai *et al.* (2006) [114]. 86
Table 7-1: The bacteria species, strains, genotype/mutation, name used in this thesis and the source of the bacterial sample. 107
Table 8-1: Kinetic parameters of TEM-1 on nitrocefin substrate detected by the plate reader, the optical chip and in the literature. Standard deviations from three repeats are shown. 125
Table 8-2: The K_M and k_{cat} of TEM-1 on carbenicillin substrate calculated from the Lineweaver-Burk plots detected by the pH indicator and pH sensor. 135
Table 8-3: The species, strains, β-lactamase genes and the pH reduction slope of the pH sensor. A pH reduction slope higher than 0.0044 pH/min (LoD of the pH sensor) was marked as red, which was seen as "resistant"; otherwise, it was diagnosed as 'susceptible'. The blind test was repeated three times. Five of eight blind test strains could produce β-lactamases and the pH sensor could diagnose three correctly. 140
Table 8-4: The bacterial concentrations of typical bacterial strains at OD = 0.01. The bacterial concentrations were counted using the plate count method. Deviations were from three repeats. 141

Table 8-5: MICs detected by OD-based broth dilution method (unit: µg/mL). CIP represents ciprofloxacin, GEN represents gentamicin, DOX represents doxycycline, CEF represents ceftazidime, COL represents colistin, IMI represents imipenem. 141
Table 8-6: The $QNICR_{1h}$ (%) of six antibiotics for ten bacterial isolates in different antibiotic concentrations (N=3). SP represents species, KP represents *K. pneumonia*, EC represents *E. coli*, SA represents *S. aureus*, AB represents *A. baumannii*, PA represents *P. aeruginosa,* CIP represents ciprofloxacin, GEN represents gentamicin, DOX represents doxycycline, CEF represents ceftazidime, COL represents colistin, IMI represents imipenem. The $QNICR_{1h}$ at MIC (OD-based) is marked in red. The strains which MIC >64 µg/mL in OD-based method is labelled by "Y" in the table. 150
Table 8-7: The OD-based MIC, $QNICR_{1h}$ (%) at MIC (OD-based), 1/2-fold MIC (OD-based) of certain tests. SP represents species, KP represents *K. pneumonia*, EC represents *E. coli*, SA represents *S. aureus*, AB represents *A. baumannii*, PA represents *P. aeruginosa,* CIP represents ciprofloxacin, GEN represents gentamicin, DOX represents doxycycline, CEF represents ceftazidime, COL represents colistin, IMI represents imipenem. 152
Table 8-8: The MIC (impedance-based) when the $QNICR_{1h}$-Threshold is set as 16% and the fold between the MIC (OD-based). SP represents species, KP represents *K. pneumonia*, EC represents *E. coli*, SA represents *S. aureus*, AB represents *A. baumannii*, PA represents *P. aeruginosa,* CIP represents ciprofloxacin, GEN represents gentamicin, DOX represents doxycycline, CEF represents ceftazidime, COL represents colistin, IMI represents imipenem. 57 out of 60 MICs detected by the impedance method was within 2-fold difference with that of the OD-based broth dilution method. 155
Table 8-9: MICs for bacterial isolates detected by the OD-based broth dilution method (N = 3, µg/mL). 156
Table 8-10: OD-based antibiotic susceptibility of testing strains depended on thresholds shown in table. The resistant (R) strains detected by the OD method were defined as having higher MIC than the threshold concentrations. In contrast, the not resistant strains (S) were defined as having lower MIC than the threshold concentrations. 156
Table 8-11: $QNICR_{1h}$ for bacterial isolates detected by the impedance method (N = 3, %). 157
Table 8-12: Antibiotic susceptibility based on the impedance method. The resistant (R) strains detected by the impedance method were defined as having higher $QNICR_{1h}$ than 16 %. In contrast, the not resistant strains (S) were defined as $QNICR_{1h}$ lower 16 %. The differences between Table 8-12 and Table 8-10 are marked in red. 157

Table of Figures

Figure 1-1: A schematic diagram of the achievements in this project. Three miniaturized platforms that aim to rapidly detect antimicrobial susceptibility are developed. The optical system and the pH device are able diagnose β-lactam resistance from low concentration samples. Impedance system demonstrates the ability to perform rapid AMR diagnosis of broadband antibiotics and showed a high accuracy in blind tests. To improve the sensitivity of optical detection, filter enrichment and DEP enrichment steps were added. 3
Figure 1-2: The schematic diagram of the DEP-enhanced optical system. The 10 mL bacteria sample is concentrated into 1 mL by filter, and then enriched into 100 µL of solution by the DEP chamber. Bacterial concentration is enriched by 2 orders of magnitude and the optical chip is used to detect the β-lactam susceptibility of the enriched bacteria afterwards. The integrated system has the ability to detect the β-lactam susceptibility at 10^3 CFU/mL. 5
Figure 2-1: Photos and schematic diagrams of GP and GN bacterial envelop. The GP bacteria generally have three envelope layers (plasma membrane, periplasmic space, outer membrane). The GP bacteria generally have two envelope layers (peptidoglycan and membrane) [39]. 10
Figure 2-2: A schematic diagram of changes in the concentration of bacteria in response to the addition and subsequent removal of bactericidal and bacteriostatic antibiotics [39]. Bactericidal antibiotics kill bacteria so that the bacterial concentrations decrease after the antibiotic has been added and cannot recover after the antibiotics are removed. In contrast, bacteriostatic antibiotics inhibit bacterial growth and bacteria can still grow after the antibiotics are removed. 12
Figure 2-3: A schematic diagram describing AMR spread based on plasmid transfer. (a) A few antibiotic-resistant bacteria are present among numerous antibiotic-susceptible bacteria. (b) Most antibiotic-susceptible bacteria are killed by antibiotics but the resistant bacteria survive. (c) The resistant bacteria grow well in an antibiotic environment. (d) The resistant bacteria transfer drug-resistance plasmids to the antibiotic-susceptible bacteria and spread the antibiotic resistance ability. 15
Figure 2-4: A schematic timeline of AMR diagnosis in conventional clinical laboratories. The shaded regions represent non-working time. Lengthy plating and AST steps cause AST results have to be delivered in 2 days [61]. 16
Figure 2-5: A schematic diagram of the breakpoints of a hypothetical drug. If the MIC is higher, or the inhibition zone diameter is smaller than breakpoint A, the bacteria are defined as resistant to that antibiotic. If the MIC is lower, or the inhibition zone diameter is greater than breakpoint B, the bacteria are defined as susceptible to that antibiotic. [39] 18
Figure 2-10: Guidance on reading the EUCAST breakpoint table. This thesis focuses on the MIC breakpoints of resistance detected by the broth dilution method [69]. 20
Figure 2-11: Core structures of penicillins, cephalosporins monobactams and carbapenems [71]. The β-lactam ring are marked as red. 22
Figure 2-12: A schematics of typical β-lactamases, ESBLs and carbapenemases. TEM and SHV are β-lactamases; CTX-M is an ESBL; KPC, NDM, IMP, OXA, VIM and IMI are carbapenemases. 23

Figure 2-9: (a) Chemical structure of nitrocefin (top) and hydrolysed nitrocefin (bottom) [85]. The β-lactam ring and the broken β-lactam ring are marked in red. (b) Absorbance spectrum of 100 μg/mL nitrocefin solution before and after hydrolysis, recorded through 1-cm path length. The greatest difference in absorbance between nitrocefin and hydrolysed nitrocefin is at 482 nm. 24
Figure 2-14: A schematic diagram of the β-lactam ring hydrolysis on a penicillin. The penicillin is hydrolysed to a penicilloic acid, which may release a proton in solution [86]. 25
Figure 3-1: (a) The experiment device by Ur and Brown (1975) and *E. coli* concentration detected visually against time compared with impedance reduction against time. A high-concordance relationship between impedance change and cell concentration was identified. 29
Figure 3-2: (a) A schematic diagram of the testing device and (b) the typical results of impedance reduction by Colvin *et al.* (1977). A 16-chamber impedance detection system was used to detect the medium resistance of bacterial suspensions. The impedance reduction was used to indicate the bacterial metabolism. The MIC detected by this method at 5 hours was within 2-fold difference with the MIC detected by the broth dilution method in 20 hours. 30
Figure 3-3: The initial bacterial concentrations against detection time of *E. coli* (black triangles) and *S. aureus* (circles). When initial concentrations reached 10^6 CFU/mL, the detection time was within 1 hour. Different bacterial species had different metabolism mechanisms and the detection time were variable in the same initial bacterial concentrations. 30
Figure 3-4: (a) A simplified model of an electrochemical well and (b) the corresponding circuit for describing the impedance change caused by bacterial metabolism. Cpol and Gpol are the polarization capacitance and conductance of each electrode, respectively. Gsol is the conductance of the solution, which is related to the metabolism in the bacterial suspension. The circuit was developed by Eden and Eden (1984)......31
Figure 3-5: The normalized impedance against time for (a) *E. coli* and (b) MRSA. The impedance reduced by >50% within 1 hour at 10^8 CFU/mL initial bacterial concentration. Mixing antibiotics with test bacteria could significantly slow the medium conductivity change [31]......32
Figure 3-6: (A) The schematic diagram of interdigitated ITO impedance immunosensor and (B) Nyquist plots of (a) the bare interdigitated ITO electrode, (b) after antibody immobilization and (c) after *E. coli* binding. The antibody–*E. coli* binding altered the charge transfer resistance. 34
Figure 3-7: (a) The schematic diagram of the system before bacteria binding. (b) The AMP structure. (c) The schematic diagram of the system after bacteria binding. (d) A photo of the interdigitated Au electrodes developed by Mannoor *et al.* (2010). This immunosensor can distinguish pathogenic bacterial species and detect bacterial concentrations at 10^3 CFU/mL. 35
Figure 3-8: Diagrams of (a) the Randles model, (b) the corresponding Nyquist plot, (c) the cross-view of the device and (d) a 3D schematic diagram of the device by Jiang *et al.* (2014). Their results demonstrate that a filter can be used to trap bacteria and improve the sensitivity of impedance detection......36

Figure 3-9: Impedance spectrum of *E. coli* growth in LB broth in 12 hours from Settu *et al.* (2015). Impedance magnitude was increased at low frequencies, which indicated reduced double layer capacitance during *E. coli* growth. After long-term incubation, a large amount of *E. coli* covered some part of the electrode surface and reduced the double layer capacitance......37
Figure 3-10: Impedance spectra (1 Hz to 100 kHz) of *E. coli* suspensions in (a) DI water and (b) PBS from Yang (2008). Ion release in the DI water caused significant medium resistance reduction. The impedance spectrum in PBS did not change when bacterial concentration increased......38
Figure 3-11: Image processing steps from Choi *et al.* (2013). An RGB photo was transformed to grey format and the background was eliminated. The photo quality was optimized and the photo was converted to binary format to enhance the image contrast. 39
Figure 3-12: A schematic diagram of rod-shaped bacteria loaded in a cell trap (Baltekin *et al.*, 2017). Test bacteria were mixed with antibiotics in the chamber and a charge-coupled device (CCD) camera monitored the bacterial length of each trap, which was used to show the antibiotic susceptibility......40
Figure 3-13: Kalashnikov *et al.* (2012) detected antibiotic susceptibility using fluorescence. In one chamber, test bacteria were mixed with a fluorescent dye and an antibiotic. In another chamber, test bacteria were mixed with a fluorescent dye without antibiotics (control). The fluorescence signals of the two chambers were observed simultaneously. The antibiotic susceptibility was calculated based on the ratio of the death rates of the antibiotic-present and antibiotic-absent chambers......41
Figure 3-14: Boedicker *et al.* (2008) designed a droplet microfluidic system to rapidly diagnose AMR. Single bacterium is mixed with antibiotics in a capsule and then incubated for 2.8 hours. The resistant bacteria emit a strong fluorescent signal after 2.8-hour incubation......42
Figure 3-15: *E. coli* MG1655 mixed with different concentrations (μg/mL, indicated on the chip) of kanamycin at (A) the start and (B) after 18 hours (Cira *et al.*, 2012). After 18-hour incubation, bacteria in chambers with kanamycin concentration > 4 μg/mL showed inhibited growth. In contrast, bacterial growth was observed in the presence of 2 μg/mL kanamycin and no kanamycin. Thus, the chip indicates that the MIC of kanamycin for *E. coli* MG1655 is 4 μg/mL......44
Figure 3-16: A schematic diagram of the pH monitoring system and typical results from the device (Tang *et al.*, 2013). A pH-sensitive chitosan gel was used to monitor bacterial metabolism. The effective thickness (EOT) of the channel was monitored by an optical microscope and the pH value was calculated in real-time. 44
Figure 3-17: Representative results of the Carba NP test [130]. Red indicates that the solution pH is unchanged. In contrast, yellow indicates reduced solution pH. If the imipenem-present and imipenem-absent chambers are both red, the testing strain might not have been inoculated or the testing strain might be a carbapenemase non-producer. If the imipenem-present chamber changes colour but the imipenem-absent chamber remains red, then the testing strain is a carbapenemase producer......45
Figure 3-18: A schematic graph of a quadruple-electrode array for rapid diagnosis of antibiotic susceptibility from Chung *et al.* (2011) [138]. Resistant bacteria were

concentrated at the centre of the electrode array while susceptible bacteria were concentrated at the gaps between the electrodes. 48
Figure 3-19: A photo of an Etest plate. MIC values are determined by the minimum antibiotic concentration where the bacterial growth is not separated from the antibiotic disk. 50
Figure 4-1: Photos of bio-particles DEP separation by (a) a polynomial electrode system and (b) a castellated electrode system (Markx *et al.*, 1994). In a polynomial electrode system, *E. coli* (experiencing nDEP) are concentrated in the middle and *M. lysodeikticus* (experiencing pDEP) are concentrated at the edge of the electrodes. In a castellated electrodes system, *M. lysodeikticus* (experiencing pDEP) are concentrated at the edge of the electrodes and yeast (experiencing nDEP) are concentrated at the gap between each castellated electrode. 58
Figure 4-2: (a) The schematic diagram of the DEPIM device by Suehiro *et al.* (1999) and (b) the results of conductance against time for different concentrations of *E. coli*. Parallel *E. coli* pearl chains connected in the channel, which led to increased channel conductance and capacitance. 60
Figure 4-3: (a) The electric field strength of the nDEP assistance electrodes and (b) a schematic diagraph of the DEP-enhanced EPA-DEPIM system for *E. coli* concentration detection (Hamada *et al.*, 2011). In the experiment, the bacteria were pre-enriched at the bottom of the channel before EPA-DEPIM detection. 61
Figure 4-4: A schematic diagram of the device (top), a photo of the DEP enrichment electrodes (middle) and a photo of the impedance detection electrodes (bottom) (Kim *et al.*, 2015). Asymmetric interdigitated electrodes were used to enrich bacteria, and the concentrated bacteria were flowed to impedance-sensing electrodes for impedance detection. 61
Figure 4-5: The cross-view of the optical detection cell by Sieben *et al.* (2010). A light-emitting diode (LED, green) and a photodiode (black) are glued on either side of a 25-mm path length channel. The LoD could reach 4.1 mAU. 62
Figure 4-6: A photo of the device by Sansalvador *et al.* (2016). An LED and a photodiode are glued to either side of a 1-cm path length channel. The absorbance of the medium is determined by the voltage output of the photodiode. 63
Figure 4-7: A schematic diagram of a glass pH probe, where a bulb made from specific glass forms the sensing part of the probe [198]. The reference electrode is embedded in the probe body and the OCP between the internal and reference electrodes is proportional to the pH of the test solution. 64
Figure 4-8: The cross-section of a typical ISFET sensor [floating gate (Si_3N_4), source, drain] [203]. The pH value of the aqueous solution affects the formation of metal-OH groups on the gate and changes the gate potential, which alternates the current through the transistor accordingly. 65
Figure 5-1: The schematic diagram of two parallel electrodes, each covers area A, separate with distance d with (a) pure conductor, (b) ideal dielectric material and (c) dielectric material contains unbounded charges in the middle. 68
Figure 5-2: A schematic diagram of two parallel electrodes, each covers area A, separate with distance d. Two different dielectric materials with different width (d_1 and d_2), different permittivity (ε_1 and ε_2) and different conductivity (σ_1 and σ_2) are in the middle of the parallel electrodes. 69

Figure 5-3: A schematic diagram of MMT of a particles suspension. (a) In the middle of two parallel electrode, a uniform electric field is applied between a particles suspension. (b) The dielectric property of the particles suspension can be seen as a new material with different dielectric property. $\varepsilon m*$ is the complex permittivity of the medium, $\varepsilon b*$ is the complex permittivity of the particle and $\varepsilon mix*$ is the complex permittivity of the new material. 72
Figure 5-4: A schematic diagram of an electrical double layer [221]. A Stern layer consists of two layers formed by unsolvated ions, solvated ions and water. The inner layer is formed by specifically adsorbed ions (both co and counter ions). The locus of electrical centres of these ions is call inner Holmholtz plane (IHP). The outside layer is formed by solvated ions. The locus of these nearest solvated ions centres is called outer Holmholtz plane (OHP). Outside the Stern layer, a diffusion layer is formed by solvated ions that not specific adsorbed but affected by the electric attraction [220]. 73
Figure 5-5: A schematic diagram of a microfluidic channel with two planer, parallel electrodes placed at the bottom. The two electrodes (named electrode E2 and E3, respectively) are connected to an impedance analyser and build a two-terminal impedance detection system. The simplified electric circuit of the two-terminal impedance detection system is shown. R_{23} and C_{23} are solution resistance and parasitic capacitance. C_{DL2} and C_{DL3} are double layer capacitance on electrode E2 and electrode E3. 75
Figure 5-6: The impedance magnitude and the phase of LB broth measured by 10 pairs interdigitated Pt (black dots) and Pt black (red dots) electrodes (400 µm length, 20 µm width and 20 µm gaps) from 10 Hz to 10 kHz. The width and depth of the channel were 400 µm and 125 µm, respectively. The applied voltage of two-terminal detection (PalmSence 3 impedance analyser, Netherland) was 0.1 peak-to-peak voltage (Vpp). 76
Figure 5-7: A schematic diagram of a microfluidic channel with four planar, parallel electrodes placed at the bottom of the channel. The inner two electrodes (named electrode E2 and E3, respectively) are connected to a voltage detection component and outer two electrodes (named electrode E1 and E4, respectively) are connected to a constant current injection, which build a four-terminal impedance detection system. The simplified electric circuit of the four-terminal impedance detection system is shown. The voltage detection component between E2 and E3 has very high impedance, so no current is able to flow through the double layer capacitance on E2 and E3 ($CDL2$ and $CDL3$). Therefore, no voltage drops on $CDL2$ and $CDL3$. The differential voltage between E2 and E3 is given by the bulk resistance ($R23$). 77
Figure 5-8: The impedance magnitude and the phase from 10 Hz to 1 MHz of MH1 detected by the four-terminal (red dots) method and the two-terminal (black dots) method. The width and depth of the channel were 400 µm and 125 µm, respectively. The inner two electrodes (E2 and E3) covered 0.08 mm^2 each and had 1 mm separation. The outer two electrodes (E1 and E4) covered 0.08 mm^2 each with 200 µm gap to E2 or E3, respectively. The applied voltage of the two-terminal detection (Novocontrol Gmtd, Germany) was 0.1 Vpp. E2 and E3 were connected to the impedance analyser while E1 and E4 were floating. The injection current of the four-terminal detection (Novocontrol Gmtd, Germany) was 10 µA. E2 and E3 were connected to the voltage detection component and E1 and E4 were connected to the current injection component. 78

Figure 5-9: The circuit diagram of a TCA used in the four-terminal impedance detection system. The current between E1 and E4 is set by the voltage source V_i and resistor R_i. It is independent of any resistance between E1 and E4 within limites. 79
Figure 5-10: The current-potential curve of an ideal non-polarisable electrode. Dashed line shows the behaviour of actual electrodes that over the limited ranges of current [220]. 80
Figure 5-11: The current-potential curve for an ideal polarisable electrode. Dashed line shows the behaviour of actual electrodes that over the limited ranges of applied potential [220]. 81
Figure 6-1: A schematic diagram of the cell envelop structure of a GN bacterium and the corresponding names used in the simulations. For GN bacteria, the cell envelop can be classified as three different shell layers with different dielectric properties: the outer membrane (omem), periplasmic area (periplasmic) and inner membrane (mem) [238]. 85
Figure 6-2: The schematic graph of a 3-shell ellipsoid *E. coli* model. The bacterium is 2.048-µm long and 0.548-µm wide. The outer membrane and (inner) membrane are 7 nm thick and the periplasmic layer is 10 nm thick. 86
Figure 6-3: The conductivity and permittivity of an *E. coli* suspension where the length of *E. coli* is changed. The bacterium length is changed from 1.048 µm to 2.048 µm (from a = 0.5 µm to a = 1 µm), so the volume fraction (P) is changed from 0.05 to 0.1. Other parameters remain the same. The permittivity is increased significantly and the conductivity is reduced significantly at <1 MHz. 87
Figure 6-4: The permittivity and conductivity of an *E. coli* suspension where the medium conductivity (kmed) is altered. The medium conductivity is changed from 0.3 S/m to 0.4 S/m and the other parameters remain the same. The conductivity is significantly changed in all frequency ranges but there is hardly any change to the permittivity. 88
Figure 6-5: The permittivity and conductivity of an *E. coli* suspension where the volume fraction (P) is altered. The volume fraction is increased from 0.06 to 0.1. Other parameters remain the same. The permittivity is increased significantly and the conductivity is reduced significantly at <1 MHz. 89
Figure 6-6: The permittivity and conductivity of an *E. coli* suspension where the conductivity of the *E. coli* outer membrane (komem) is changed. The outer membrane conductivity is increased from 0 to 0.001 S/m. Other parameters remain the same. The permittivity is reduced significantly at <1 MHz and the conductivity is increased significantly at <10 MHz. 90
Figure 6-7: The permittivity and conductivity of an *E. coli* suspension where the conductivity of the *E. coli* membrane (kmem) is changed. The membrane conductivity is changed from 0 S/m to 0.001 S/m. Other parameters remain the same. The permittivity is increased slightly between 100 kHz and 1 MHz and the conductivity is increased slightly at >100 kHz. 91
Figure 6-8: The permittivity and conductivity of an *E. coli* suspension where the conductivity of the *E. coli* cytoplasm (kcyto) is changed. The cytoplasm conductivity is changed from 0.26 S/m to 0.18 S/m. Other parameters remain the same. The permittivity is reduced slightly between 1 MHz and 100 MHz and the conductivity is reduced slightly at >10 MHz. 92

Figure 6-9: The permittivity and conductivity of an *E. coli* suspension where the permittivity of the *E. coli* outer membrane (Eomem) is reduced. The outer membrane permittivity is reduced from 10 to 6. Other parameters remain the same. The permittivity is reduced significantly at <100 kHz and the conductivity is reduced slightly at >1 MHz. 93
Figure 6-10: The NICR (%) of an *E. coli* suspension where medium conductivity (k) is changed from 0.35 S/m to 0.42 S/m and the bacterial concentration increases from 10^7 CFU/mL to 8×10^7 CFU/mL. This simulation shows the NICR results from bacterial concentration change and bacterial metabolism together. During bacterial growth, the cell number doubles every 20 minutes in 1 hour. Therefore, the *E. coli* concentration is 2×10^7 CFU/mL, 4×10^7 CFU/mL and 8×10^7 CFU/mL at 20 minutes, 40 minutes and 1 hour, respectively. The corresponding medium conductivity is 0.3675 S/m, 0.385 S/m and 0.42 S/m, respectively......95
Figure 6-11: The NICR (%) of an *E. coli* suspension where medium conductivity (k) changes from 0.35 S/m to 0.42 S/m but the bacterial concentration remains stable at 10^7 CFU/mL. The impedance change is very similar to that caused by both bacterial metabolism and bacterial concentration change together. 96
Figure 6-12: The NICR (%) of an *E. coli* suspension where the bacterial concentration increases from 10^7 CFU/mL to 8×10^7 CFU/mL, but the medium conductivity remains stable at 0.35 S/m. This simulation shows the impedance change caused by bacterial concentration change without bacterial metabolism......97
Figure 6-13: The QNICR (%) of two *E. coli* suspensions where the length (l) of a single *E. coli* in the antibiotic chamber changes from 1.048 µm (simplified as l=1 um) to 2.048 µm (simplified as l=2 um) but bacterial concentration and medium conductivity remain stable. The QNICR is reduced to -0.0025% at <100 kHz if the *E. coli* length is 2.048 µm. 99
Figure 6-14: The QNICR (%) of two *E. coli* suspension where the *E. coli* outer membrane conductivity (kom) in the antibiotic chamber changes from 0 S/m to 0.35 S/m but bacterial concentration and medium conductivity remain stable. The QNICR increases to around 0.0012% at <1 MHz (10^6 Hz) if the outer membrane conductivity is 0.01 S/m, to 0.0014% at <1 MHz if the outer membrane conductivity is 0.1 S/m, and to 0.0015% at <1 MHz if the outer membrane conductivity is 0.35 S/m, which is the same as that of the medium. 100
Figure 6-15: the QNICR (%) of two *E. coli* suspensions where the *E. coli* cytoplasm conductivity in the antibiotic chamber changes from 0.1 S/m to 0.5 S/m (normal *E. coli* cytoplasm conductivity is 0.22 S/m) but bacterial concentration and medium conductivity remain stable. The QNICR changes to about -0.0002% at 100 MHz (10^8 Hz) if the cytoplasm conductivity is 0.1 S/m, to about 0.0002% at 100 MHz if the cytoplasm conductivity is 0.3 S/m, to about 0.0004% at 100 MHz if the cytoplasm conductivity is 0.4 S/m, and to about 0.0007% at 100 MHz if the cytoplasm conductivity is 0.5 S/m......101
Figure 6-16: The QNICR (%) of two *E. coli* suspensions where antibiotics have partially inhibited the metabolism (km). The QNICR is increased to about 30% at <10 MHz (10^7 Hz) if the medium conductivity is 0.3675 S/m, to about 55% at <10 MHz if the medium conductivity is 0.385 S/m, to 100% at <10 MHz if the medium conductivity is 0.42 S/m, i.e. the same as that of the antibiotic-absent chamber......102

Figure 6-17: The simulated impedance spectrum from 10 Hz to 10 MHz when the solution conductivity (Km) changes from 0.3 S/m to 0.7 S/m because of bacterial metabolism. The simulation result shows that at <5 kHz, double layer capacitance dominates the impedance. At >500 kHz, parasitic capacitance dominates the impedance. An impedance magnitude of 10 kHz to 100 kHz can be used to monitor the medium conductivity. 103
Figure 6-18: The electric field strength of a hypothetical channel via COMSOL software. The channel depth is set as 30 µm. At the bottom of the channel, 20-µm wide with 20-µm gap interdigitated electrodes are placed. A 50 V_{pp} AC signal is applied to the interdigitated electrodes. High electric field zones are at the edges of the electrodes. Low electric field zones are at the top of the channel. 104
Figure 6-19: (a) In a pDEP setting, bacteria will be enriched at the edge of each electrode. (b) In an nDEP setting, bacteria will be enriched at the top of the channel......104
Figure 6-20: The effective $RefCM$ according to the medium conductivity (km) of an *E. coli* bacterium. The red line indicates $RefCM = 0$. Only when medium conductivity is <10 mS/m (orange curve) can $RefCM$ peak at around 0.7 at 1 MHz, which can provide a practical pDEP force in bacteria capture. 105
Figure 7-1: A schematic diagram of the enzyme extraction workflow. (1) *E. coli* (1 mL) was injected into a tube. (2) The tube was centrifuged at 14000 *g* for 5 minutes. (3) The supernatant was removed. (4) B-PER (20 µL) was added to the tube. (5) The tube was shaken at 850 rpm for 20 minutes to extract the proteins. (6) The lysates were removed for further experiments. 109
Figure 7-2: A brief description of the interdigitated electrode fabrication. (1) Ti (100 nm) and Pt (300 nm) are sputtered on a 4-inch glass wafer. Then, S1813 photoresist is spun on top. (2) The S1813 photoresist is exposed to UV through a mask. (3) The unexposed S1813 is washed out. The wafer is etched by oxygen plasma. (4) Electrodes are patterned. The photoresist is washed. 110
Figure 7-3: (a) A schematic diagram of the bacterial enrichment chamber. The PDMS channel was 50-µm deep. Pt electrodes (100 pairs, 20 µm × 4.0 mm with 20-µm gap) were patterned on a 0.7-mm thick glass substrate. (b) Electric field strength of the DEP chip simulated by COMSOL Multiphysics 5.3a. The high electric field zone is the edge of electrodes. 111
Figure 7-4: (a) A schematic diagram of the PMMA optical chip and (b) the cross-view of the optical chip. The LED generated light at 470 ± 10 nm wavelength. The detection channels were 300-µm wide, 300-µm deep and 25-mm long. The decoupling channels were 300-µm wide, 300-µm deep and 20-mm long. Each chip had eight absorbance detection channels......112
Figure 7-5: A schematic diagram of the integrated DEP-enhanced optical system workflow. Bacterial sample (10 mL) was manually pushed through a sterile filter using a syringe. The filter was back-flushed with 1 mL DI water to produce a concentrated bacterial suspension. The bacterial suspension was pumped into the DEP chip and the bacteria were captured on the electrodes by pDEP force. The concentrated bacteria were then retrieved and lysed for protein extraction in 100 µL solution containing nitrocefin. The lysed bacterial solution and the colorimetric substrate were immediately introduced into the optical module to monitor the absorbance change. 114
Figure 7-7: (a) A photo of the IrOx pH sensor and (b) the layout of electrodes in a pH detection chamber. Each pH-sensing chamber contains an IrOx electrode, an Ag/AgCl

film reference electrode and 2 Pt electrodes (not used). The IrOx film electrodes and the Ag/AgCl reference electrodes are 1 × 1 mm and are spaced 0.8 mm apart. The Pt electrodes are 0.4 mm × 2.8 mm and are spaced 2 mm apart......115
Figure 7-8: The IrOx and Ag/AgCl electrode fabrication process. (a) A 0.7-mm glass substrate wafer is coated with a 100-nm thick Cr layer, followed by a 300-nm thick Pt layer by sputtering. The S1813 positive photoresist is spun on the Pt surface. The wafer is exposed to UV light through an electrode pattern mask. Plasma is used to etch the exposed wafer. Patterned Pt electrodes are formed. (b) TMMF photoresist (S2000, Tokyo Ohka Kogyo Co., Ltd, Japan) is bound to the wafer by a press and the wafer is exposed to UV through an IrOx electrode pattern mask. Thus, a window is patterned on a designed IrOx electrode. (c) Anhydrous iridium chloride ($IrCl_4$, 1 g), 42 mL ethanol (C_2H_5OH) and 10 mL acetic acid (CH_3COOH) are mixed as a coating solution. The coating solution is stirred with a magnetic rod for 1 h, and then the window is dipped in it four times to coat on a thin $IrCl_4$ layer. The wafer is annealed at 300°C for 5 hours in air. (d) The TMMF scarified layer is removed with tweezers and the wafer is washed with ethanol. (e) Metal cables are soldered to the connection points and protected by epoxy gel (RS Corporation, UK). The wafer is immersed in silver electroplating solution (Spa Company, UK) and 0.5 mA DC current is applied to the reference electrodes for 15 minutes to coat them with an Ag layer. (f) The wafer is immersed in 15% NaClO solution (Sigma-Aldrich) for 4 minutes to coat a brown AgCl layer over the Ag layer. The Ag/AgCl electrode is rinsed with DI water and annealed in a 60°C oven for 12 hours for saturation and stabilization. (g) The schematic diagram of the IrOx pH sensor. 115
Figure 7-8: A schematic diagram of the two-terminal system. A customized incubator contains a 6-chip connection board, which consists of six impedance detection chips. Each chip has four electrodes in parallel. The middle electrodes (E2 and E3) are connected to a 12-channel multiplexer, which is controlled by a DAQ card. The multiplexer is connected to an impedance analyser. A computer controls the impedance analyser and DAQ card......118
Figure 7-9: A schematic diagram of the four-terminal system. The customized incubator, 6-chip connection board and impedance detection chips are the same as that in the two-terminal system. The four electrodes (E1, E2, E3, E4) are connected to a four-terminal detection kit. The four-terminal detection board consists of six four-terminal detection kits. The detection board is connected to a DAQ card, which is linked with a computer. 118
Figure 7-10: Cross view of an impedance detection chip. The inner two electrodes (E2 and E3) were 200-µm wide and spaced 1 mm apart. The outer two electrodes (E1 and E4) were 200-µm wide and spaced 200 µm apart from E2 and E3, respectively. The PMMA channel was 125-µm deep, 2-mm long and 400-µm wide. 119
Figure 7-12: A photo of a customized detection board. The detection board contains six impedance detection chips and three customized PCB holders. Each PCB holder was used to transmit signals for two impedance detection chips......119
Figure 7-12: (a) Simplified circuit of a four-terminal impedance detection kit. A sine signal (10 Hz, 0.1 V_{pp}) was generated by a LabVIEW-coded DAQ card. An operational amplifier (AD623, OpAmp) and resistor (5.6 kOhm) formed a TCA, which provided 18 µA constant AC between the outer electrodes (E1 and E4). The differential voltage between the inner electrodes (E2 and E3) was detected by a differential amplifier (AD822,

DiffAmp). The power supply of the AD623 and AD822 amplifiers was +5 V and -5 V. The output voltage of the differential amplifier was collected by a DAQ card. (b) A photo of the customized four-terminal impedance detection board with six four-terminal impedance detection kits in parallel. Each AD623 amplifier was used to generate a constant current for two chips. 120
Figure 8-1: Absorbance against Atto 488 concentration. The optical chip showed 24.44 ± 0.17 times higher sensitivity than the UV-Vis spectrometer. The experiment was repeated three times; error bars represent the standard deviations of three measurements. 123
Figure 8-2: The Lineweaver-Burk plots detected by (a) the bench-top plate reader at 470 nm and (b) the optical chip at 470 nm. Error bars represent the standard deviations of three repeats. 125
Figure 8-3: Absorbance change against time for *E. coli* TEM in (a) supernatant and (b) lysates form. The absorbance of the two forms was similar. Error bars represent the standard deviations from three repeats. The 10^7 CFU/mL data do not start from 0 due to a delay between solution mixing and injection into the optical chip. Blank represents the absorbance of the nitrocefin solution. 127
Figure 8-4: Absorbance change against time of *E. coli* CTX-M detected by (a) plate reader and (b) optical chip. The minimum bacterial concentration detected by the plate reader and the optical chip was 10^7 CFU/mL and 10^5 CFU/mL, respectively. The error bars represent the standard deviation of three repeats. Lower bacterial concentration range was used for the optical chip because the longer pathlength meant the optical chip was more sensitive. 128
Figure 8-5: The enrichment factors and capture efficiencies in different flow rates. The error bars represent standard deviations from three repeats. For 2000 µL/min flow rate, most of the bacteria were not captured and ended up in the waste. As the flow rate decreased, the capture efficiency increased. At a 20 µL/min flow rate, the DEP chip could capture 95.5% of input *E. coli* and bacterial concentration in the collected solution was eight times higher than that in the input solution. 130
Figure 8-6: The absorbance change against time after start of optical detection of *E. coli* TEM and wild-type *E. coli* TOP10 (*E. coli*). The LoD is defined as three times the standard deviation of the blank. Error bars represent the standard deviations from three repeats. The 10^5 CFU/mL and 10^4 CFU/mL data do not start from 0 due to a delay between solution mixing and injection into the optical chip. 131
Figure 8-7: The OCP of the IrOx electrode vs Ag/AgCl electrode at different pH. Error bars represent the standard deviations from three repeats. The standard deviation was 5.4 mV. 132
Figure 8-8: The OCP of the IrOx electrode vs Ag/AgCl electrode against time. A solution containing 1 mM HEPES and 30 mM NaCl was used to test the stability of the IrOx pH sensor. Within 50 minutes, the OCP drifted 0.007 mV, which is far blew resolution of the system (0.1 mV). Error bars represent the standard deviations from three repeats. 132
Figure 8-9: (a) The absorbance differences between 560 nm and 450 nm (ΔAbs) against pH. Error bars represent the standard deviations from three repeats. (b) A photo of the pH buffers mixed with the pH indicator. (c) The ΔAbs against time of a solution containing 1 mM HEPES and 30 mM NaCl. Error bars represent the standard deviations from three repeats. 134

Figure 8-10: Lineweaver-Burk plot of TEM-1 on carbenicillin substrate detected by (a) pH indicator and (b) pH sensor. Error bars represent the standard deviations from three repeats. 135
Figure 8-11: The pH of four solutions against time (15 hours). The pH of the solution containing *E. coli* CTX-M lysate supernatant and carbenicillin was reduced but that of the other solutions remained stable. The error bars represent the standard deviations from three repeats. 136
Figure 8-12: (a) Typical pH of a solution containing supernatant *E. coli* TEM and carbenicillin against time. (b) The average pH reduction slope from three repeats. Error bars represent the standard deviation from three repeats. The blank was carbenicillin solution without bacterial supernatant. 138
Figure 8-13: (a) Typical pH of solutions containing supernatant from different concentrations of *E. coli* NCTC 11560 and carbenicillin against time. (b) The average pH reduction slope from three repeats. The error bars represent the standard deviation from three repeats. The blank was carbenicillin solution without bacterial supernatant. 139
Figure 8-14: The typical standard growth curve of ceftazidime for *K. pneumoniae* 13368. Figure key shows the antibiotic concentrations in µg/mL. The MIC was tested as 16 µg/mL in both 20 hours and 4 hours. The experiment was repeated three times and obtained similar results. 143
Figure 8-15: The typical delayed growth curve of doxycycline for *S. aureus* EMRSA-15. Figure key shows the antibiotic concentration in µg/mL, where the MIC was 0.5 µg/mL in 20 hours. However, the bacteria began to grow at 0.125 µg/mL and 0.25 µg/mL after 5 and 7 hours, respectively. The MIC at 4 hours was 4-fold lower than that at 20 hours. 144
Figure 8-16: A typical fake growth curve of *E. coli* 12923 with doxycycline. Figure key shows the antibiotic concentration in µg/mL. The MIC was 1 µg/mL at 20 hours. The OD increased initially at 1 µg/mL doxycycline, but decreased after 3 hours. Therefore, the MIC at 3 hours is 2-fold higher than that at 20 hours. 145
Figure 8-17: Conductivity error for the two-terminal system at 10 kHz. The bias errors were within 0.005 S/m in the range of 0.35–0.75 S/m, and the average conductivity deviation was 0.78% of the original solution. Thus, the LoD (3 × conductivity bias error) of the two-terminal detection system was 2.33% of the detected conductivity. The error bars represent the standard deviation from three repeats. 146
Figure 8-18: Conductivity error for the four-terminal detection system at 10 Hz. The conductivity bias errors were within 0.002 S/m in the range of 0.35–0.75 S/m, and the average conductivity deviation was 0.31% of original solution. Thus, the LoD of this four-terminal detection system was 0.93% of the detected conductivity. The error bars represent the standard deviation from three repeats. 146
Figure 8-19: Typical impedance spectrum of *E. coli* 12923 grown in MH1 broth for 1 hour. The impedance spectrum was detected by the two-terminal impedance system. Figure key shows the minutes after addition of the sample. The initial OD of the bacterial suspension was set at 0.01. The temperature for detection was set at 37°C. The data for time 0 (minutes after sample adding) was deleted because the temperature at time 0 was not stabilized at 37°C. The experiment was repeated three times. 147
Figure 8-20: The zoom-in of the impedance spectrum for 10–100 kHz shown in Figure 8-19. Figure key shows the minutes after the addition of the sample. Within 1 hour, the

impedance magnitude at 10 kHz was reduced from 23.6 kOhm to 19.9 kOhm, which indicated that $NICR_{1h}$=15.67%......148
Figure 8-21: The typical impedance spectrum of MH1 broth in 1 hour. The impedance spectrum was detected by the two-terminal impedance system. Figure key shows the minutes after sample injection. The temperature was set at 37°C, and the interval for impedance testing was set as 6 minutes. The data for time 0 were deleted because the temperature at time 0 was not stabilized at 37°C. The experiment was repeated three times. 148
Figure 8-22: The zoomed-in impedance spectrum of that shown in Figure 8-19. Figure key shows the minutes after sample injection. The impedance at 10 kHz drifted from 22.6 kOhm to 22.9 kOhm in 1 hour, which indicated that $NICR_{1h}$= -1.32%. 149
Figure 8-23: The $QNICR_{1h}$ (%) at MIC (OD-based) and 1/2-fold MIC (OD-based) of 22 tests. KP 368 represents *K. pneumonia* 13368, KP M6 represents *K. pneumonia* M6, EC L01 represents *E. coli* LEC-001, EC 923 represents *E. coli* 12923, SA E15 represents *S. aureus* EMRSA-15, SA 144 represents *S. aureus* 9144. AB AYE represents *A. baumannii* AYE, AB 978 represents *A. baumannii* 17978. PA P1 represents *P. aeruginosa* PAO1, CIP represents ciprofloxacin, GEN represents gentamicin, DOX represents doxycycline, CEF represents ceftazidime, COL represents colistin, IMI represents imipenem. 154
Figure 9-1: The absorbance spectrum of grey PMMA, transparent PDMS and PDMS mixed with Sudan II. At 470 nm, PDMS with 450 μg/mL Sudan II dye had a similar absorption coefficient with the grey PMMA. 164
Figure 9-2: (a) The manufacturing process for the moulding optical chip. Tinted PDMS gel was injected into 3D printing moulds, and then baked at 60°C for 3 hours. Fluidic input and output were punched in 1-mm diameter. Two layers of patterned PDMS were bonded by oxygen plasma bonding for 30 seconds. The moulding optical chip was placed in a customized PCB with a 470-nm LEDs and light-voltage converter glued to either side. (b) A photo of the customized PCB and one channel of the moulding optical chip. Each PCB contained four channels......165
Figure 9-3: The absorbance against Atto 488 detected by the moulding optical chip. Error bars represent the standard deviations from three measurements......166
Figure 9-4: The schematic diagram of a spiral retention device reported by Kwon *et al.* (2017). This device separated cells based on the inertial focusing effect. 167
Figure 9-5: A schematic diagram of two PDMS impedance detection chips, which are bonded together to perform differential measurements (with and without antibiotics). 168
Figure 9-6: Droplet formation process in a moulding impedance chip. Aqueous solution was added first, and a droplet was generated by air pressure. FC-40 oil was used to fill the gap to inhibit aqueous evaporation......169
Figure 9-7: Typical photos of aqueous-oil interface on either side of the channel. The channel contained a clear aqueous–oil interface......169

Research Thesis: Declaration of Authorship

Print name:	Yuetao Li

Title of thesis:	Miniaturised platforms for rapid diagnosis of antibiotic resistance

I declare that this thesis and the work presented in it are my own and has been generated by me as the result of my own original research.

I confirm that:

1. This work was done wholly or mainly while in candidature for a research degree at this University;
2. Where any part of this thesis has previously been submitted for a degree or any other qualification at this University or any other institution, this has been clearly stated;
3. Where I have consulted the published work of others, this is always clearly attributed;
4. Where I have quoted from the work of others, the source is always given. With the exception of such quotations, this thesis is entirely my own work;
5. I have acknowledged all main sources of help;
6. Where the thesis is based on work done by myself jointly with others, I have made clear exactly what was done by others and what I have contributed myself;
7. Parts of this work have been published as:
    - W. Jamieson, C. Allen, Y. Li, C. Turner, S. Kalsi, H. Morgan and M. Sutton, 'Development of a rapid phenotypic test on a microfluidic device for carbapenemase detection using the chromogenic compound nitrocefin', *Diagnostic microbiology & infectious disease*, 2019, in press.
    - Y. Li, S. Kalsi and H. Morgan, 'Rapid Detection of β-lactam Resistant Bacteria via An Integrated Microfluidic System,' Oral Presentation, *BioMedEng18*, 6-7 September 2018, London, UK.
    - Y. Li, S. Kalsi and H. Morgan, 'Rapid Detection of β-lactam Resistant Bacteria via An Integrated Microfluidic System,' Oral Presentation, *ICMFLOC 2018, The second International Conference of Microfluidics, Nanofludics, and Lab-on-a Chip*, 8-10 June 2018, Beijing, China.

- Y. Li, S. Kalsi and H. Morgan, 'Rapid Detection of β-lactam Resistant Bacteria via An Integrated Microfluidic System,' Poster Presentation, *21st NanoBioTech-Montreux*, 13-15 November 2017, Montreux, Switzerland.

Signature:		Date:	

Acknowledgements

First, I am hugely appreciative of my first supervisor, Professor Hywel Morgan. He shares his vast knowledge in biomedical engineering with me and helps me in all the time of the research and writing-up of this thesis. His guidance facilitated my journey throughout the 4-year PhD study. His enthusiasm in science motivates me throughout my further academic career.

Second, I would like to thank my second supervisor, Dr Mark Sutton. His massive knowledge in microbiology helps me complete all my microbiological research. I really appreciate him for continuous encouragement in the whole time of my PhD.

I appreciate Dr Sumit Kalsi for his enormous help and guidance in my 4-year research. I would like to particularly thank him for his time and support when I start my PhD.

My great thank goes to all the people within Centre for Hybrid Biodevices. University of Southampton. Special mentions to Roel, Josh, Victor, Nikita, Joao, Jon, Fabrizio, Kri, Fernando, Ric, Junyu, Dan, Anna, Carlos, Richardo, Kai, Joseph, Shilong and Chunxiao for their help in both science and daily life. Their presence makes this journey treasured and enjoyable.

I also want to thank all group members from Technology Development Group in Public Health England, especially Carrie, Matt, Lucy, Charlie, Mel, Karen, Bonnie, Louise and Sirine. They provide me endless helps in microbiological experiments and leave valuable memories to me.

With the oversight of my main supervisor, editorial advice has been sought. No changes of intellectual content were made as a result of this advice.

I would like to thank all my friends here in UK, Wei, Yue, Jingfan, Tianyu, Yuening, Fei and Yichi, who have inspired, accompanied and assisted me during the 4-year PhD study. I would also like to express my gratitude to all my friends back in China, especially to Jianqing, Zihua, Qiao and Jinjie, for their constant support and encouragement.

I am very grateful for the company of my girlfriend, Yiling. I would like to thank her for being understanding and kind. I also want to mention our two kittens, Arthur and Archie, who inspired me when I wrote up this thesis.

Finally, I would like to express my deepest and sincerest thanks to my parents. I would never be who I am without their endless love and care. They are the most important people in my whole life.

Definitions and Abbreviation

ABS	Acrylonitrile Butadiene Styrene
AC	Alternative Current
AE	Antibiotic Effect
AM-EWOD	Active Matrix Electrowetting-On-Dielectric
AMP	Antimicrobial Peptides
AMR	Antimicrobial Resistance
AST	Antimicrobial Susceptibility Testing
ATCC	American Type Culture Collection
B-PER	Bacteria Protein Extraction Reagent
CCD	Charge-Coupled Device
CFU	Colony-Forming Units
COC	Cyclic Olefin Copolymer
DAQ	Data Acquisition
DEP	Dielectrophoresis
DEPIM	DEP Impedance Measurement
DI	Deionized
EOT	Effective Thickness
EP	Electropermeabilization
EPA-DEPIM	EP-Assisted DEPIM
ESBL	Extended-Spectrum β-Lactamase
EUCAST	European Committee On Antimicrobial Susceptibility Testing
FDA	Food And Drug Administration
FISH	Fluorescent *in situ* Hybridization
GN	Gram-negative
GP	Gram-positive
GFP	Green Fluorescent Protein
iDEP	Insulator-Based DEP
IHP	Inner Holmholtz Plane
ISFET	Ion-Sensitive Field Effect Transistor
ITO	Indium–Tin Oxide
LAMP	Loop-Mediated Isothermal Amplification
LB	Luria-Bertani
LDR	Ligase Detection Reaction
LED	Light-Emitting Diode
LoC	Lab-on-a-Chip
LoD	Limit of Detection
MALDI-TOF	Matrix Assisted Laser Desorption Ionization Time of Flight
MH1	Mueller-Hinton 1
MIC	Minimum Inhibitory Concentration
MMT	Maxwell Mixture Theory
MRSA	Methicillin-Resistant *Staphylococcus aureus*

MS	Mass Spectroscopy
MSSA	Methicillin-Susceptible *Staphylococcus aureus*
NCTC	National Collection of Type Cultures
nDEP	Negative DEP
OCP	Open Circuit Potential
OD	Optical Density
OHP	Outer Holmholtz Plane
PBP	Penicillin-Binding Protein
PBS	Phosphate-Buffered Saline
PCB	Print Circuit Board
PCR	Polymerase Chain Reaction
pDEP	Positive DEP
PDMS	Polydimethylsiloxane
PHE	Public Health England
PID	Proportional-Integral-Derivative
PMMA	Polymethyl Methacrylate
PoC	Point of Care
NICR	Normalized Impedance Change Ratio
QNICR	Quotation of Normalized Impedance Change Ratio
RF	Radio Frequency
RPA	Recombinase Polymerase Amplification
SHE	Standard Hydrogen Electrode
TB	Tuberculosis
TBS	Tris-Buffered Saline
TDG	Technology Development Group
3D	Three Dimensional
TIA	Transimpedance Amplifier
TSA	Tryptic Soy Agar
UTI	Urinary Tract Infection
UV-Vis	Ultraviolet Visible
Vpp	Peak-to-Peak Voltage
μTAS	Micro Total Analysis Systems

Chapter 1: Introduction

1.1 Motivation

Pathogenic bacteria are biological cells that can cause infectious diseases. Before the 20th century, bacterial infection was a significant threat due to the lack of effective treatment. In 1929, Fleming discovered the first commercial antibiotic to treat infections, which has saved many lives [1]. However, in 1944, Bigger observed that bacteria could survive even after exposure to antibiotics, which was dubbed antimicrobial resistance (AMR) [2]. Currently, clinical institutions struggle to treat many infections caused by antimicrobial resistant bacteria because they are unresponsive to at least some of the commonly used antibiotics. If necessary action is not taken, by 2050 AMR will be the largest cause of death, killing 10 million people across the world every year [3]. Antimicrobial susceptibility testing (AST) is often performed to determine the antibiotic sensitivity to bacterial pathogens isolated from clinical samples such as urine, blood, sputum or wound swabs [4]. The conventional methods used to determine the antibiotic susceptibility are disk diffusion, broth dilution, and agar dilution techniques which evaluate bacterial growth in the presence of various concentrations of antibiotics [5]. These traditional AST methods are the "gold standard" assessments of appropriate antimicrobial prescriptions in clinical testing. However, these methods are time-consuming. The number of bacteria in clinical sample will not reach the minimum detectable level unless they have been incubated for at least 16 to 20 hours [6]. The lack of rapid susceptibility diagnosis drives overuse and misuse of antibiotics and consequently accelerates the emergence of antibiotic resistant bacteria [7]. In this case, the rapid, accurate and specific antibiotic susceptibility detection of pathogenic bacteria direct from clinical sample is required to prevent inappropriate treatment and protect human health [8-11].

1.2 State-of-art diagnosis

In current AMR diagnosis systems, the testing require trained technicians and doctors need to wait for overnight to receive the diagnostic report that is needed for further treatment [12]. Long delays between "samples in" to "results out" force the antibiotics given tend to be either broad spectrum or selected empirically.

Point of care (PoC) devices aim to perform medical tests in closer proximity to the patient, such as near the patient's bed, at the GP's surgery, or at home. PoC diagnosis requires the devices to be cheap, robust and easily operated by non-professional operators [13]. Nowadays, some PoC devices are available on the market for a health check and diagnosis, such as pregnancy test strips, blood glucose monitors and blood pressure monitors. These devices enable fast and precise diagnosis, and significantly reduce the cost for hospital operations.

Most novel AMR diagnostic devices designed for PoC applications are developed on microfluidic platforms. Microfluidic platforms range in size from a few micrometres to several-hundred micrometre diameter channels and the liquid flow range from microliter to femtoliter

volumes [14]. These have been developed since the 1980s and shows numerous benefits, including lower energy consumption, single cell monitoring and the ability for smaller volume samples and reagents to be used in the assays. Moreover, devices developed on a microfluidic platform are able to improve the precision of experimental results, and they allow multiple samples to be analysed simultaneously. Now, there is a push in both academic and industrial fields to use microfluidic technology to improve the performance of current analysis systems in many areas such as biomedical engineering, biochemistry or life science fields [15].

In a microfluidic platform, several laboratory functions can be integrated into one chip. This is called a lab-on-a-chip (LoC) device, or sometimes referred to as "micro total analysis systems" (μTAS). LoC devices are one of the potential development directions for PoC diagnosis tools because LoC devices can significantly reduce the cost for laboratory support, enable faster analysis and achieve better process control due to shorter response time [16]. Many LoC devices for AMR diagnosis have been reported in the literature based either on genotype detection or phenotype detection. Genotypic methods aim to detect AMR related genes, while phenotype detection monitors the phenotypic change of bacteria when exposed to antibiotics [17]. Both genotype and phenotype diagnosis tools on microfluidic platforms could reduce the detection time, improve the detection sensitivity and reduce the cost of such tests. However, most tools are at the proof-of-concept stage, and few have been fully developed and widely used due to issues such as long preparation time, low accuracy and high manufacturing cost [18].

1.3 Research directions

This PhD thesis describes the development of rapid AMR diagnosis from clinical samples in the PoC situation. Three research directions for low-cost, high-sensitivity and easy-operation AMR diagnostic devices were pursued.

The first direction aims to detect β-lactam resistance by optical detection. Nitrocefin is a β-lactam analogue discovered in the 1970s, whose colour changes from red to yellow when mixed with β-lactamases in solution [19]. Previously, the detection of nitrocefin hydrolysis is limited by the sensitivity and the cost of bench-top plate readers and its lack of specificity for clinically important resistance mechanisms. With the advancement of microfluidic technology, low-cost high-sensitivity optical absorbance chips have been developed [20-23]. Dielectrophoresis (DEP) is a force generated on a particle in a non-uniform electric field, and is used to trap bacteria and further improve the sensitivity of bacterial diagnosis [24]. This work combines DEP enrichment, a high sensitivity optical chip and the nitrocefin indicator together to detect β-lactamase at low concentration ($<10^4$ CFU/mL).

The second direction aims to detect β-lactam resistance by monitoring pH [25]. Various pH detection tools have been developed such as pH indicators, pH glass probes and metal-metal oxide pH sensors [26]. In 2012, the Carba NP method was invented to detect carbapanemases, which is a colourimetric assay that measures a pH change when carbapenem antibiotics are hydrolysed [27]. This work replaces the colorimetric readout of pH with a solid micro pH sensor.

The third direction method aims to detect antibiotic susceptibility by monitoring the impedance of a bacterial suspension. When bacteria grow, sugars and proteins are hydrolysed to lactate, carbonate and amino acids, which results in the reduction of solution resistance [28]. Therefore, detecting the impedance reduction of a bacterial suspension solution can indicate bacterial growth [29]. Bacterial metabolism during growth differs between different bacterial species, and the speed of this is influenced by the addition of antibiotics. Therefore, the impedance reduction ratio between the chamber with antibiotics versus the chamber without antibiotics can be used to indicate the bacterial growth and subsequently the antimicrobial resistance to the antibiotics. Importantly, this method should enable the susceptibility of bacteria to be measured for all antibiotic classes.

Based on the research directions described above, three miniaturized AMR diagnosis devices have been developed in this PhD project.

1.4 Main achievements

In this project, three systems based on detecting pH, absorbance and impedance change in solution have been developed. A schematic diagram of the achievements in this project is shown in Figure 1-1.

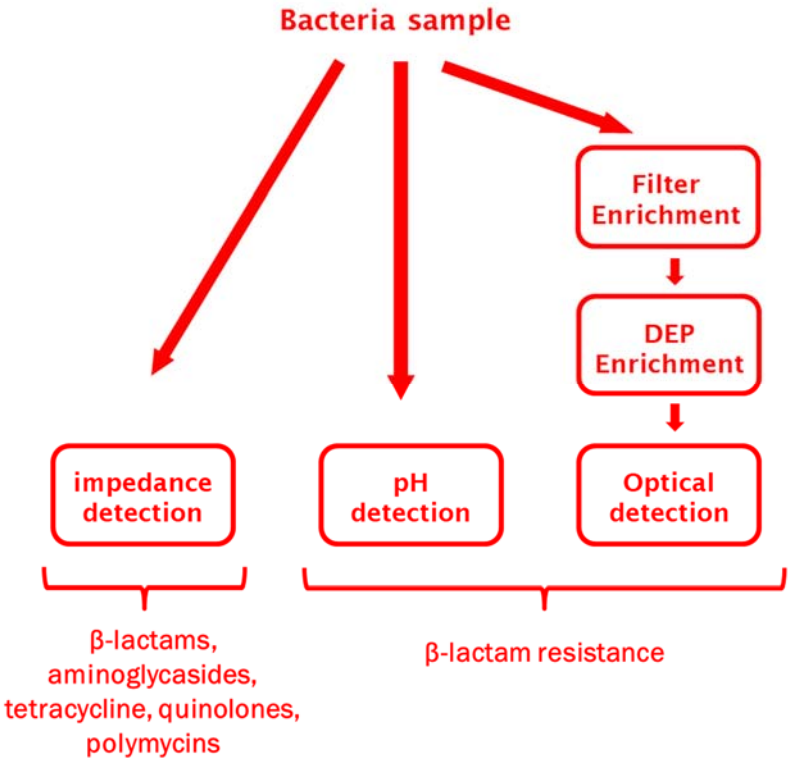

Figure 1-1: A schematic diagram of the achievements in this project. Three miniaturized platforms that aim to rapidly detect antimicrobial susceptibility are developed. The optical system and the pH device are able diagnose β-lactam resistance from low concentration samples. Impedance system demonstrates the ability to perform rapid AMR diagnosis of broadband

antibiotics and showed a high accuracy in blind tests. To improve the sensitivity of optical detection, filter enrichment and DEP enrichment steps were added.

All three rapid diagnosis systems are easy to use, robust and low-cost. Table 1-1 summarizes the performance of three rapid AMR diagnosis platforms.

Table 1-1: Summary of the DEP-enhanced optical system, pH system and impedance system for rapid AMR diagnosis.

	DEP-enhanced optical system	pH system	Impedance system
Antibiotics Selectivity	β-lactams	β-lactams	β-lactams, aminoglycasides, tetracycline, quinolones, polymycins
Sensitivity on *Escherichia Coli* TOP10	10^3 CFU/mL	10^5 CFU/mL	10^6 CFU/mL
Sample volume	10 mL	20 μL	2 μL
Clinical sample tests	66	8	60
Clinical accuracy	100%	75%	90%
Detection time	1 hour	1 hour	1 hour
Advantages	Low concentration of bacteria required	Low-cost and easy-operation	Works for many different classes of antibiotics
Disadvantages	Only β-lactam resistant strain can be detected	Only β-lactam resistant strain can be detected	Errors in bacteriostatic antibiotics

1.4.1 DEP-enhanced optical system for measuring β-lactam cleavage (DEP-enhanced optical system)

In this project, a novel DEP-enhanced colorimetric optical system has been developed to rapidly detect β-lactamases. The system is simple, robust and able to be applied in PoC situations.

The detection system consists of a filter, a DEP based concentration chamber and an optical absorbance detection chip. In the first stage, a 0.22 μm sterile filter is used to increase the bacterial concentration in the sample and to reduce the medium conductivity which is required for the DEP system. Bacteria are then concentrated using positive DEP (pDEP). The optical detection chip detects a colorimetric change that results from the hydrolysis of nitrocefin by the β-lactamases.

The experimental results showed that filters and DEP enrichment were able to concentrate bacteria 100-fold. The optical chip had a limit of detection (LoD) of 3.1 milli-AU. It can detect *Escherichia coli* with $_{bla}$*CTX-M-15* genes within 15 minutes for concentration of 10^5 CFU/mL ($5*10^5$ CFU/mL required for conventional analysis) and within 1 hour for lower concentration (10^3 CFU/mL, from sample to result) [30]. The schematic diagram of the integrated system is shown in Figure 1-2.

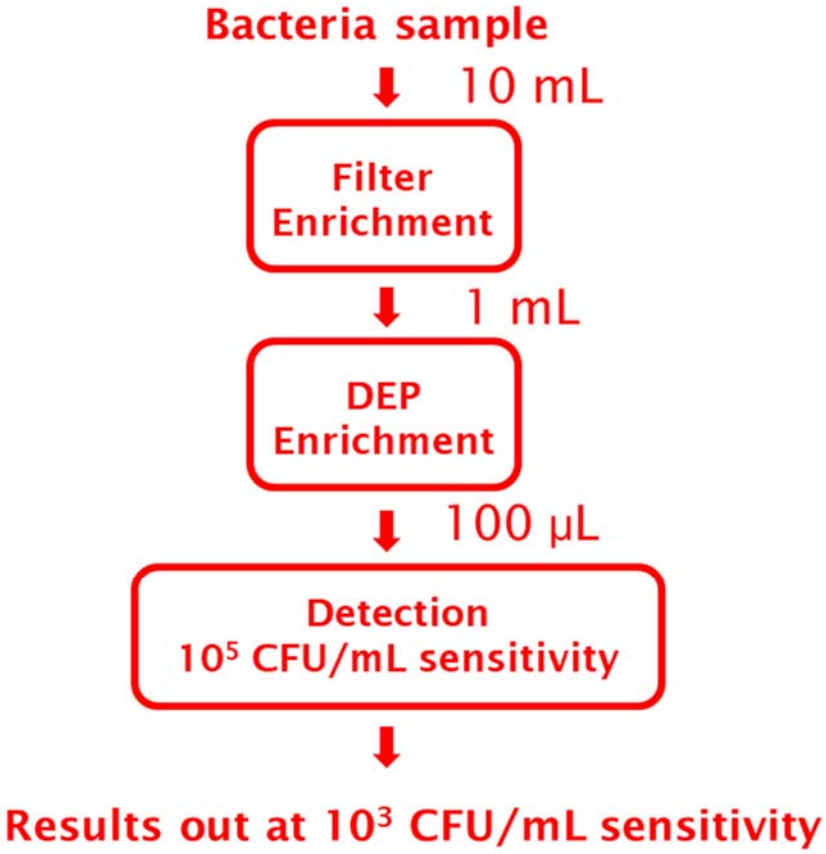

Figure 1-2: The schematic diagram of the DEP-enhanced optical system. The 10 mL bacteria sample is concentrated into 1 mL by filter, and then enriched into 100 μL of solution by the DEP chamber. Bacterial concentration is enriched by 2 orders of magnitude and the optical chip is used to detect the β-lactam susceptibility of the enriched bacteria afterwards. The integrated system has the ability to detect the β-lactam susceptibility at 10^3 CFU/mL.

1.4.2 pH detection system for measuring β-lactam cleavage (pH system)

An IrOx pH platform that aims to rapidly diagnose β-lactamases has been developed, based on detecting the pH reduction caused by β-lactam ring hydrolysis of a carbenicillin antibiotic molecule. This pH method is sensitive and easy to use, and improves on the Carba NP method by reducing experiment time (from 3 hours to 1 hour) and sample concentration (from 1010 CFU/mL to 10^5 CFU/mL). The pH sensor consists of an iridium oxide (IrOx) electrode and an Ag/AgCl reference electrode. The open circuit potential (OCP) between the detection and reference electrodes is proportional to the pH value in solution. This method could detect β-lactamases from 10^5 CFU/mL of lab safe *E. coli* TOP10 with $_{bla}$*TEM* genes and 10^8 CFU/mL of clinical *E. coli* ATCC 11560 stain within 1 hour. However, clinical blind tests showed this pH method might give "false negative" results in several β-lactamase producing samples.

1.4.3 Impedance system for assessing the susceptibility of bacteria to different classes of antibiotics (Impedance system)

In this project, a differential impedance system to rapidly assess the susceptibility of bacteria to different classes of antibiotics has been developed. The impedances of the bacterial suspensions with and without antibiotics are detected simultaneously, and the impedance ratio between the chambers is used to indicate the antibiotic effect. This impedance system significantly improves detection accuracy compared with other rapid impedance AMR diagnosis methods [31].

The differential impedance system consists of 6 impedance detection chambers placed in a customized incubator. The impedance of each chamber is monitored by a customized impedance detection kit. The experimental results demonstrated that this impedance system was able to detect antibiotic susceptibility from clinical isolates within 1 hour. In blind tests of 5 antibiotics from 10 *Klebsiella pneumoniae* strains, the antibiotic susceptibility detected by the impedance method showed 90% concordance compared with that detected by the broth dilution method. In the minimum inhibitory concentration (MIC) test of 6 antibiotics from 10 clinical isolates, 95 % MIC values detected by the impedance method were within the accepted tolerance of two fold of that detected by the conventional broth dilution method.

1.5 Novelty

1.5.1 DEP-enhanced optical system

Most optical systems used for rapid diagnosis of AMR are based on bacterium morphological observation or bacterial concentration detection, which require complex optical microscopy and image analysis systems [32-34]. The present optical system is the first sensitive β-lactamase diagnosis platform based on detection of nitrocefin hydrolysis. The sensitivity of β-lactamase detection is four orders of magnitude higher than that of normal 96-well plate assays, detected by a bench-top plate reader.

This sensitive optical chip has three main advantages. First, the longer path length design helps to increase the sensitivity of the measurement system. Second, the channel design helps to absorb reflected and refracted light in the optical chip, which reduces noise and achieves better LoD. Third, the tiny channel reduces the substrate amount used in assays.

Additionally, the application of a bacteria enrichment system helps to increase the bacterial concentration significantly and efficiently. The filter system not only enriches bacteria by one order of magnitude, but also decreases the solution conductivity because DEP systems require lower conductivity than bacterial growth media for optimum capture efficiency. The DEP chip concentrates bacteria into a small volume (100 μL), which commercial filters barely achieve because they require larger volumes to reduce sample losses during the elution stage.

1.5.2 pH detection system

Detecting pH reduction caused by bacterial metabolism has been used to diagnose antibiotic susceptibility after several hours [35]. The Carba NP method that detects the β-lactam ring hydrolysis on carbapenem antibiotics can rapidly detect carbapenamases, but needs multiple laboratory operations [27]. This method replace the colorimetric readout of pH with a solid state micro pH sensor [36]. The protein extraction step of the Carba NP method was simplified as well.

1.5.3 Impedance system

Medium resistance reduction in a period was reported to measure bacterial concentration, bacterial metabolism or susceptibility to antibiotics [28, 29, 37]. However, when using impedance changes to indicate the susceptibility on a bacterial strain, the result is usually influenced by external factors such as initial bacterial concentration or incubation temperature. Differential measurement has been widely applied in many scientific fields [38], but has never been reported in impedance AMR diagnosis before. This impedance detection system is the first microfluidic impedance detection system that aims to detect the reduction in impedance ratio between an antibiotic-present chamber and an antibiotic-absent chamber. This system can detect antibiotic susceptibility of different bacterial species and antibiotic mechanisms in a short time.

1.6 Thesis structure

This thesis describes the background, theory and achievements in the ‘miniaturised platforms for rapid diagnosis of antibiotic resistance’ project. It is divided into 9 chapters. The Chapter 1 introduces the motivation, background and aims of the project, followed by the main achievements and novelty of the devices. Then, Chapter 2 describes classification of bacteria, the action and resistance mechanisms of the different classes of antibiotics, and the golden standard methods on AMR diagnosis. The Chapter 3 and 4 summarize novel rapid AMR diagnosis methods and relevant microfluidic technology, respectively. The Chapter 5 introduces the detection theory of DEP force, impedance detection, pH detection and optical

detection. Then, the Chapter 6 simulates the impedance of an *Escherichia coli* suspension in different conditions and the DEP force on an *E. coli* bacterium. Subsequently, the methodologies of the optical system, pH system and impedance system are introduced in Chapter 7, followed by the results and discussion of the three systems in Chapter 8. In the end, the Chapter 9 summarizes the main findings and future directions for improving the current devices.

1.7 Declaration

This thesis describes the research undertaken by the author while working within a collaborative research environment. This thesis documents the original work of the author except in the following sections:

1. In the optical chip, the polymethyl methacrylate (PMMA) boards were designed and milled by Dr. Sumit Kalsi, University of Southampton.
2. In the DEP enrichment chip, the interdigitated electrodes was fabricated by Ying Denh Tran, University of Southampton.
3. In the impedance detection system, the four-terminal impedance detection electrode was fabricated by Katie Chamberlain, University of Southampton.
4. In the pH sensor, the IrOx dipping solution was prepared by Dr Roeland Mingels, University of Southampton.
5. In the moulding impedance chip, the dry-film microfluidic mould was fabricated by Josh Robertson, University of Southampton.
6. In the optical and pH system, the *E. coli* TOP10 with plasmids encoded $_{bla}$*CTX-M-15* and $_{bla}$*TEM-1* genes were prepared by Carrie Turner, Public Health England.

Chapter 2: Understanding of AMR

2.1 Bacteria

Some bacteria can cause disease, and these are termed pathogenic bacteria [39]. Tuberculosis (TB), caused by *Mycobacterium tuberculosis* bacteria, kills around 2 million people every year [40]. In the US, blood steam infection leads to more than 215 000 deaths annually [41]. In the UK, urinary tract infection (UTI) is one of the most common public health threats; >50% of women have a UTI in their lifetime [42].

Bacteria can generally be divided into two groups based on the envelope structure: Gram-positive (GP) and Gram-negative (GN), which can be distinguished using a method of staining called a Gram stain [39]. GP bacteria have a plasma membrane with an exterior peptidoglycan layer. GN bacteria have an outer membrane and a plasma membrane, divided by a periplasmic space and peptidoglycan [39]. Figure 2-1 shows the typical photos and schematic graphs of the GN and GP bacterial envelops.

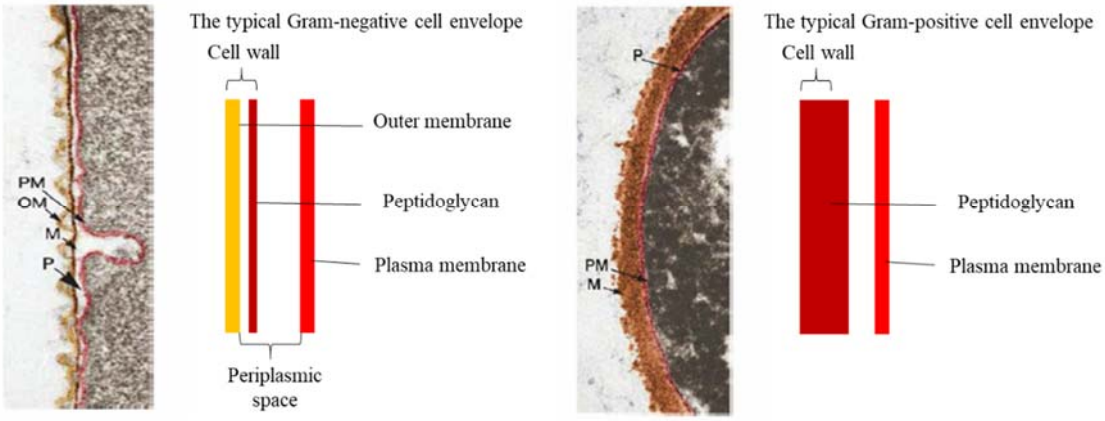

Figure 2-1: Photos and schematic diagrams of GP and GN bacterial envelop. The GP bacteria generally have three envelope layers (plasma membrane, periplasmic space, outer membrane). The GP bacteria generally have two envelope layers (peptidoglycan and membrane) [39].

Other than Gram staining, bacteria are also classified into different species according to cell structure, metabolism process or cell components such as DNA or antigens [43]. Table 2-1 lists the pathogenic bacteria described in the present thesis and the diseases they cause.

Table 2-1: Summary of common species of pathogenic bacteria described in this thesis. Their transmission, general antibiotics for treatment and gram staining are listed [39].

Species	Transmission	Treatment	Gram staining
E. coli	Gut flora, and in urinary tract	Co-trimoxazole, fluoroquinolone	GN
K. pneumoniae	Mouth, skin, and gut flora	3rd generation cephalosporins, Ciprofloxacin	GN
Pseudomonas aeruginosa	Opportunistic; infects damaged tissues	Anti-Pseudomonal penicillins, Aminoglycoside	GN
Staphylococcus aureus	Human flora	Methicillin Vancomycin	GP

2.2 Antibiotics

Antibiotics kill or inhibit the growth of certain bacteria, and are the most important discovery for fighting bacterial infections [44]. The first commercial antibiotic, penicillin, was discovered by Fleming in 1928 [1]. Since then, hundreds of antibiotics have been discovered and widely used for treating bacterial infections [45]. Antibiotics can be classified as bactericidal or bacteriostatic. Figure 2-2 shows changes in the concentration of bacteria in response to the addition and subsequent removal of bactericidal and bacteriostatic antibiotics.

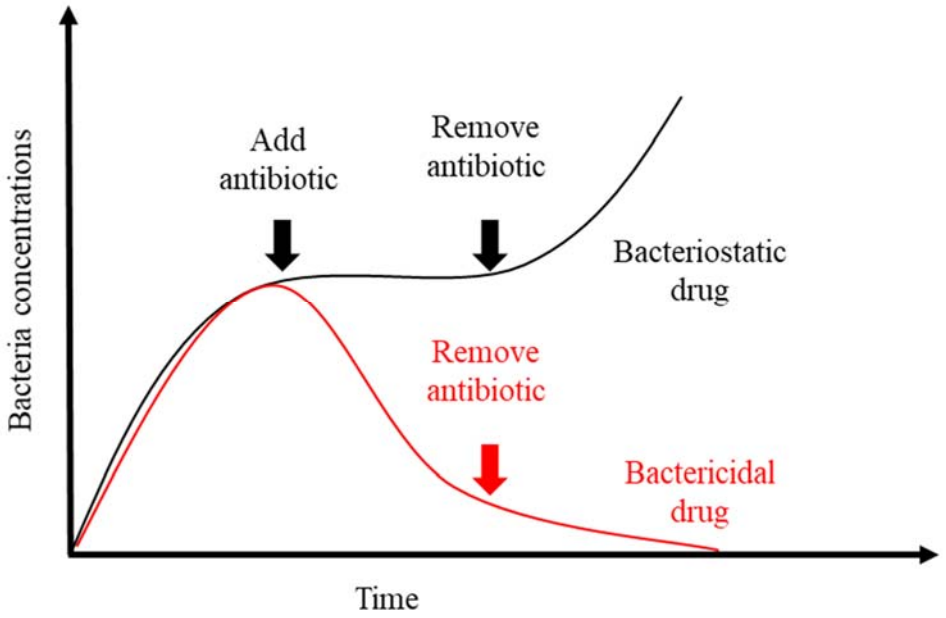

Figure 2-2: A schematic diagram of changes in the concentration of bacteria in response to the addition and subsequent removal of bactericidal and bacteriostatic antibiotics [39]. Bactericidal antibiotics kill bacteria so that the bacterial concentrations decrease after the antibiotic has been added and cannot recover after the antibiotics are removed. In contrast, bacteriostatic antibiotics inhibit bacterial growth and bacteria can still grow after the antibiotics are removed.

The bactericidal and bacteriostatic antibiotics have different mechanisms of action. For example, fluoroquinolones and tetracyclines inhibit metabolic pathways such as nucleotide synthesis or protein synthesis [46]. Polymyxins break up the cell membrane [47] and β-lactam antibiotics inhibit the crosslinking of the peptidoglycan layer to inhibit cell wall synthesis [48]. Table 2-2 summarizes the primary effects, mechanisms of action and targets of the antibiotics described in this thesis.

Table 2-2: Summary of the antibiotics described in this thesis. The primary effects, mechanisms of action, members of the antibiotics and target bacteria spectra are listed [39].

Antibiotic group	Primary effect	Mechanism of action	Members	Spectrum
Cell wall synthesis inhibition				
β-lactams	Cidal	Inhibit transpeptidation enzymes involved in cross-linking the polysaccharide chains of peptidoglycan	Pencillin, methicillin, Ceftazidime, ampicillin, carbenicillin, imipenem	Broad (GP, some GN)
Protein synthesis inhibition				
Aminoglycasides	Cidal	Bind to small ribosomal subunit (30S) and interfere with protein synthesis by directly inhibiting synthesis and causing misreading of mRNA	Kanamycin, gentamicin	Broad
Tetra-cycline	Static	Block the ability of bacteria to make proteins	Teracycline, doxycycline	Broad
Nucleic acid synthesis inhibition				
Quinolones and fluoro-quinolones	Cidal	Inhibit DNA gyrase and topoisomerase II, thereby blocking DNA replication	Cipro-floxacin	Narrow (Some GN and a few GP)
Cell membrane disruption				
Polymyxin	Cidal	Binds to plasma membrane and disrupts its structure and permeability properties	Colistin, polymixin B	Narrow (GN)

2.3 AMR

AMR is defined as 'a microorganism's resistance to an antimicrobial drug that was once able to treat an infection by that microorganism', which develops naturally in bacteria [49, 50]. In 1944, Bigger reported the first AMR case from *S. aureus* [2]. Nowadays, AMR spread has become a global issue and affected public health worldwide [51]. By 2050, if necessary action is not taken, AMR will be the greatest cause of death, killing 10 million people across the world every year [3].

Human actions accelerate the development and spread of AMR [50]. Firstly, misuse of antibiotics increase the chance of pathogenic bacteria encounter antibiotics directly [50]. For example, in up to 50% cases, the prescribed antibiotics are not necessary or not effective enough for treating the bacterial infections [3]. Moreover, different countries can have different types of resistant bacteria. With the large volume of worldwide travel, newly emerging antibiotic resistance mechanisms can quickly spread from single origin [50]. Besides that, AMR related genes may horizontal transfer between bacteria, which may spread the AMR as well [47]

2.3.1 Mechanisms of AMR

Bacteria have evolved various mechanisms to resist the effects of antibiotics [3]. For example, pathogenic bacteria may modify the antibiotic target, inactivate the antibiotic, decrease the penetration of antibiotics or overexpress efflux pumps to divert antibiotics out of the cytoplasm and into extracellular media to protect themselves [30].

Most antibiotics act on bacteria by specifically binding to one or more targets within the bacterial cell to inhibit normal function of the bacteria [52]. Structural changes in the binding targets lead to inefficient antibiotic binding, which help the bacteria to combat the effects of the antibiotic. One of the example of the antibiotic resistance caused by target modification is ciprofloxacin resistance [53].

Bacteria can produce enzymes that inactivate antibiotics to protect themselves. These enzymes can add a chemical group, such as a phosphate, a acyl or a ribitol group to the antibiotic to inactive it, or hydrolyse the antibiotic directly [54]. β-Lactam resistance is commonly caused by the production of β-lactamases that hydrolyse the β-lactam ring, inactivating the antibacterial properties of the compounds [48].

Bacteria, especially GN bacteria, can decrease the penetration of antibiotic compounds to protect themselves. GN bacteria have an outer membrane which combines a lipid bilayer with different porins, which makes it intrinsically less permeable to many antibiotics [55]. Moreover, modifications in cell wall composition can decrease the membrane permeability of antibiotic compounds and reduce the amount of active antibiotics into the pathogenic bacteria [56]. Many carbapenem resistant bacteria can modify their cell wall to decrease the penetration and help them survive in a carbapenem environment [57].

Efflux pumps are transporters localized in the bacterial membrane, which can transport the toxic components within the cell wall out of the bacteria. Overexpression of the efflux pumps divert antibiotics out of the cytoplasm and into extracellular medium, increases the rate antimicrobials are excreted [52]. Chloramphenicol resistance is caused by efflux pumps overexpression [58].

2.3.2 Horizontal gene transfer

Many pathogenic bacteria can arise resistance to antibiotics by mutation(s) in one of the target genes in the microorganism, which can be spread by plasmids who carry the AMR-related mutations. Those plasmids are transferred from antibiotic-resistant bacteria to antibiotic-susceptible bacteria to help the latter survive antibiotics, which can pass between different species of bacteria [47]. Figure 2-3 shows a schematic diagram describing horizontal gene transfer.

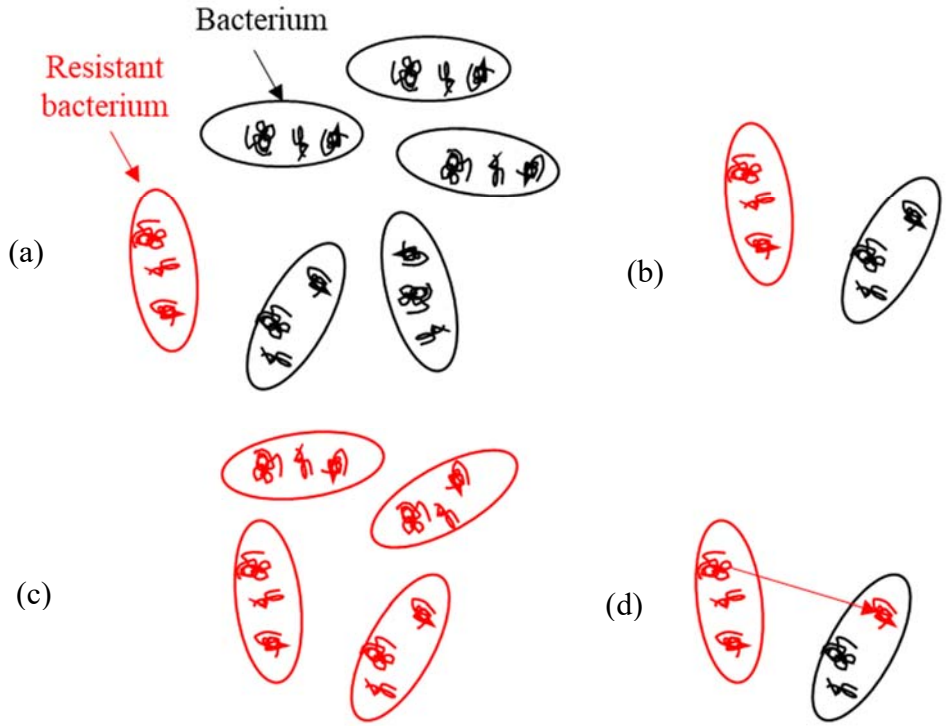

Figure 2-3: A schematic diagram describing AMR spread based on plasmid transfer. (a) A few antibiotic-resistant bacteria are present among numerous antibiotic-susceptible bacteria. (b) Most antibiotic-susceptible bacteria are killed by antibiotics but the resistant bacteria survive. (c) The resistant bacteria grow well in an antibiotic environment. (d) The resistant bacteria transfer

drug-resistance plasmids to the antibiotic-susceptible bacteria and spread the antibiotic resistance ability.

2.4 Conventional AST methods and their limitations.

Conventional methods used for determining whether patients are infected with drug-resistant bacteria involve multiple time-consuming steps. First, patients' urine or blood sample is collected. Second, the sample is plated to isolate pure cultures of bacteria (16-24 hours). Third, the bacteria has to be incubated with an antibiotic in well plates or petri dishes, which is called antimicrobial susceptibility testing (AST, 16-24 hours). Finally, the bacterial growth has to be determined [59, 60]. Figure 2-4 shows the schematic timeline of AMR diagnosis in current clinical laboratories.

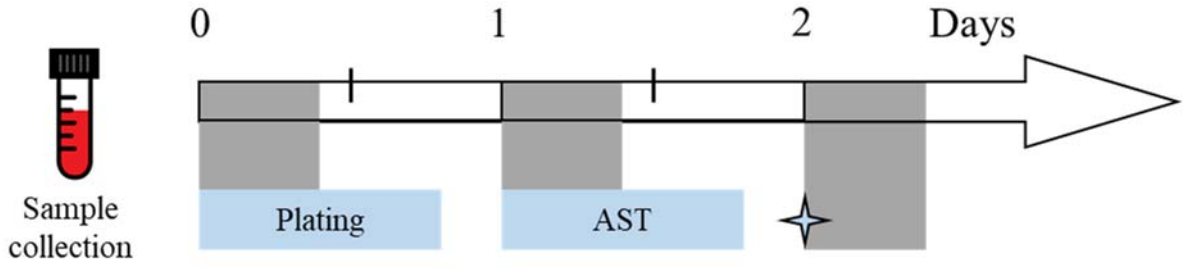

Figure 2-4: A schematic timeline of AMR diagnosis in conventional clinical laboratories. The shaded regions represent non-working time. Lengthy plating and AST steps cause AST results have to be delivered in 2 days [61].

Conventional methods of AST use either broth dilution or disk diffusion techniques to monitor bacterial growth in the presence of various concentrations of antibiotics [5]. For broth dilution, the MIC is used to describe the antibiotic's inhibitory ability against a certain bacteria, which is an important clinical evidence for the prescription of effective antibiotics. The MIC of an antibiotic is defined as the lowest concentration of the antibiotic that inhibit a significant growth of bacteria [62]. Bacterial growth is detected based on the bacterial population, which is indirectly measured by the optical density (OD) value. If the bacterial population in an antibiotic dose–pathogen culture is higher than a certain concentration, the bacterial culture medium becomes opaque and the OD increases [39]. Standard broth dilution protocol requires overnight bacterial culture for determining the MIC [63]. Table 2-3 shows the steps for the broth dilution method used in this thesis.

Table 2-3: Steps for broth dilution method used in this project. The MIC is used to describe the antibiotic susceptibility [62].

Step	Operations
1	Obtain isolated colonies of bacterial strain.
2	Take a single colony and culture overnight in Mueller-Hinton 1 (MH1) broth.

3	Add MH broth with appropriate dilution series of test antibiotic to well plates. The OD of bacterial suspensions is controlled at 0.01 absorbance unit (A.U.)
4	After overnight incubation, check culture for growth. The MIC is the minimum antibiotic concentration that inhibits OD less than 0.1 A.U.

The disk diffusion method measures the diameters of the clear zones around an antibiotic disk. A larger diameter means that the bacteria are more susceptible to the antibiotic, and a smaller diameter or no zone of clearance suggests that the bacteria are more resistant to it [39, 64]. The disk diffusion method also requires overnight culture; Table 2-4 shows the steps for the method. The disk diffusion method is usually used in clinical settings and was not used in this project.

Table 2-4: Steps for the disk diffusion method. The zone diameter around the antibiotic disk is used to indicate the antibiotic susceptibility.

Step	Operations
1	Obtain isolated colonies of bacterial strain.
2	Take a single colony and culture overnight in MH broth
3	After overnight incubation, dilute the inoculum suspension to OD at 0.01 A.U.
4	Dip a cotton swab in the inoculum suspension. Then swab over the entire surface of MH agar to give a lawn culture.
4	Place filter paper disks containing known antibiotic on the surface of inoculated MH agar.
5	Incubate the plate at 37 C overnight. Measure the zone diameter around the disk.

Breakpoints are certain MIC values or inhibition zone diameters that classify the strain's susceptibility to a certain antibiotic based on pre-defined tables. The breakpoint setting is based on distribution of MICs, clinical trials and medical experience [30]. Figure 2-5 shows a schematic diagram of the breakpoints of a hypothetical drug.

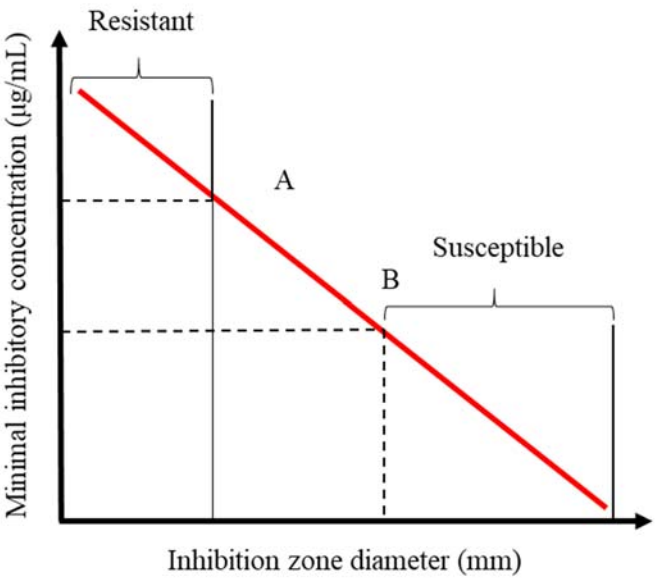

Figure 2-5: A schematic diagram of the breakpoints of a hypothetical drug. If the MIC is higher, or the inhibition zone diameter is smaller than breakpoint A, the bacteria are defined as resistant to that antibiotic. If the MIC is lower, or the inhibition zone diameter is greater than breakpoint B, the bacteria are defined as susceptible to that antibiotic. [39]

The broth dilution and disk diffusion techniques are gold standards for detecting antibiotic susceptibility, however, the conventional AST methods are subject to several disadvantages.

First, delays between sample collection and results reporting can be many days. There are a number of factors causing it, such as the delays in sample transport to hospital, purity plates, susceptibility testing and results reporting. Therefore, to avoid delaying treatment, doctors have to give prescriptions based on their previous experience upon the first visit of the patients, which may worsen a patients' condition in some cases and contribute to the emergence of drug-resistant pathogens [65].

Second, the standard diagnostic methods requires bulky, expensive supporting equipment (for example, plate readers, bio-safe cabinet), large volumes of sterile reagents and medical consumables (for example, well plates, culture broth, agar plates), which could limit their use in resource-limited conditions [66].

Third, the analysis of these assays may be subjective and variable. Technicians must be trained to correctly interpret results and the laboratories must conform to quality standards. The assay results must be standardized to the specific characteristics of the growth medium [35].

Moreover, many studies support the premise that laboratory experiment results face a significant barrier to efficient antibiotic management of infection. *In vitro* susceptibility testing in microbiology laboratories is performed under optimal growth conditions that cannot be produced in *in vivo* situations [67].

2.5 EUCAST breakpoints table

The European Committee on Antimicrobial Susceptibility Testing (EUCAST) is a standing committee jointly organized by the European Society of Clinical Microbiology and Infectious Diseases, the European Centre for Disease Prevention and Control and the European national breakpoint committees [68]. Most clinical laboratories in the European Union countries follow EUCAST guidelines for determining antibiotic susceptibility. EUCAST publishes the AST guidelines on their website with open access. The newest 'Breakpoint tables for interpretation of MICs and zone diameters Version 9.0' was published on January 1, 2019 [69]. Figure 2-10 shows the guidance on reading the EUCAST breakpoint table.

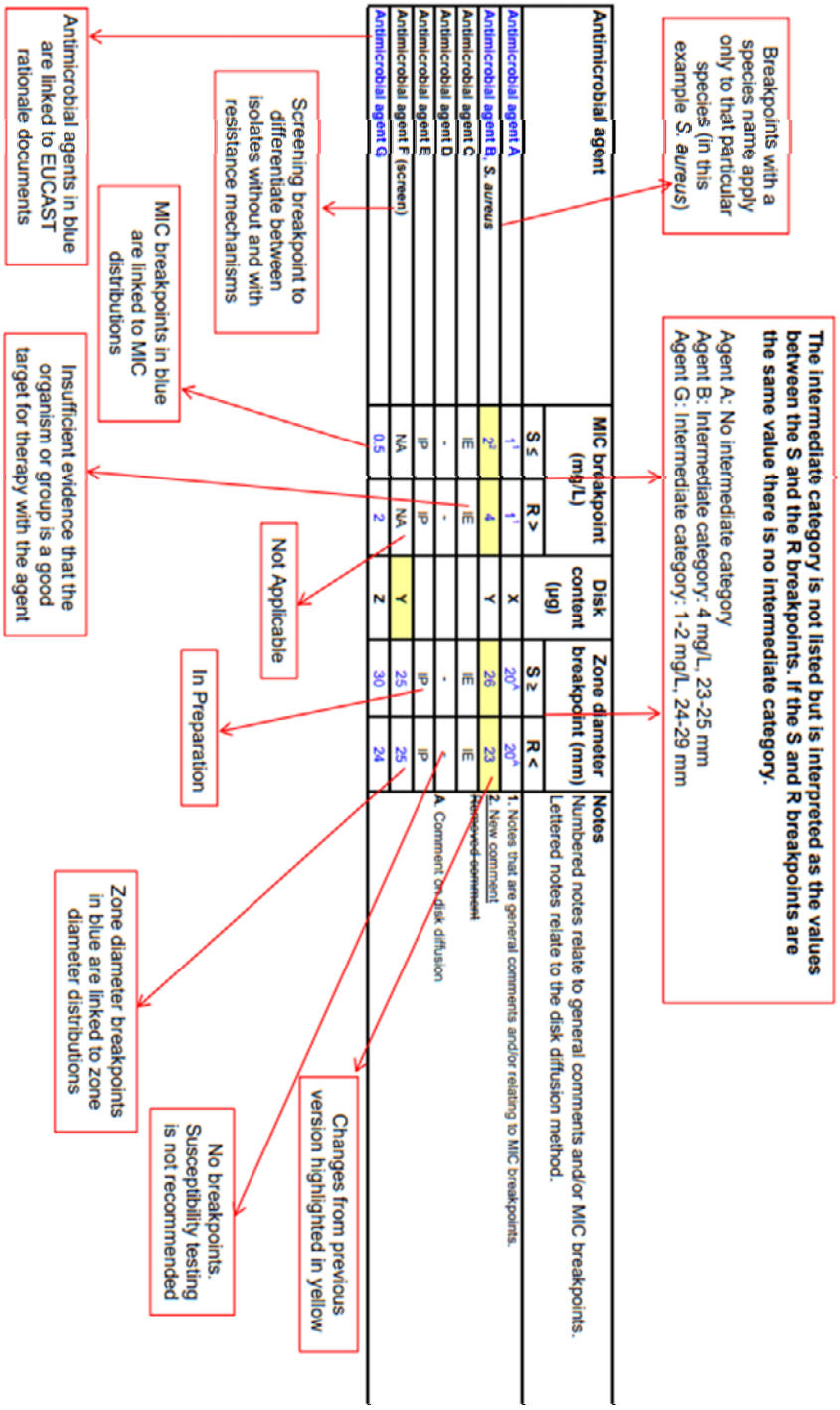

Figure 2-6: Guidance on reading the EUCAST breakpoint table. This thesis focuses on the MIC breakpoints of resistance detected by the broth dilution method [69].

In EUCAST table, readout of conventional MIC is any detectable growth within the well, observable by eye [30]. In this thesis, the readout of MIC is defined as the highest antibiotic concentration that can inhibit the OD at 600 nm less than 0.1 A.U. Table 2-5 summarizes the MIC breakpoints of resistance of different antibiotics for different bacterial species used in the assays. Most breakpoints are from the EUCAST breakpoints table. The unavailable breakpoints in the EUCAST table are referenced with the breakpoints of similar antibiotics in the same

group. If the MIC of testing bacteria is larger than the breakpoint, the strain is defined as resistance. Otherwise, it will be defined as susceptible.

Table 2-5: MIC breakpoints (μg/mL) of resistance used in this thesis. If the MIC of testing bacteria is larger than the breakpoint, the strain is defined as resistance. Otherwise, it is defined as susceptible.

Groups	Fluoro-quinolone	Amino-glycoside	Tetra-cycline	Cephalo-sporin	Poly-myxins
Antibiotics	Ciprofloxacin	Gentamicin	Doxy-cycline	Ceftazidime	Colistin
K. pneumoniae	0.5	4	2	4*	2
E. coli	0.5	4	2	4*	2
S. aureus	1	1	2	8	-
Acinetobacter baumannii	0.5	4	2*	8	2
P. aeruginosa	0.5	1	2*	8	2

* Not available from EUCAST table, taking the breakpoints of similar antibiotics in the same group.

2.6 β-Lactam resistance

2.6.1 β-Lactam antibiotics

β-Lactam antibiotics are a class of antibiotics whose chemical structures contain a β-lactam ring [70]. Based on their molecular structure, β-lactam antibiotics can be classified into four groups: penicillins, cephalosporins, carbapenems and monobactams [71]. Figure 2-11 shows the core structures of the four groups of β-lactam antibiotics, where the β-lactam ring is marked in red.

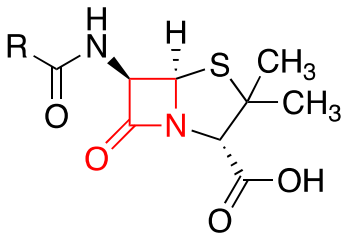

Penicillins

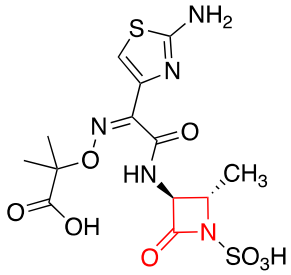

Monobactams

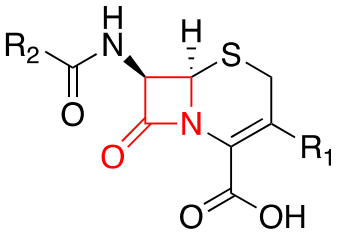

Cephalosprins

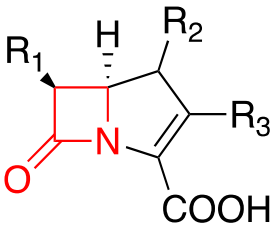

Carbapenems

Figure 2-7: Core structures of penicillins, cephalosporins monobactams and carbapenems [71]. The β-lactam ring are marked as red.

β-Lactam antibiotics kill bacteria by inhibiting peptidoglycan synthesis in the cell wall [72-74]. Penicillin-binding proteins (PBPs) are cell membrane–binding enzymes that catalyse the transpeptidation reaction that connects the peptidoglycan of the bacterial cell wall [64]. The β-lactam antibiotics bind covalently to the PBP active-site serine and inhibit peptidoglycan synthesis. Inhibition of PBPs weakens the cell wall structure by preventing the formation of cross-linkages. The cells may continue to elongate and replicate their genes, but fail to divide, which results in inhibited cell growth and finally cell death [75].

Among the various AMR cases reported, resistance to β-lactam antibiotics has received the greatest attention. β-Lactam antibiotics are the most widely used antibiotics worldwide. In 2017, based on sales, >50% of commercially available antibiotics taken in the clinic worldwide were β-lactam antibiotics [76]. Penicillins (usually in combination with a β-lactamase inhibitor) accounted for 45% of the overall antibiotics consumption in England in 2017 [77].

β-Lactam resistance is also very common worldwide. In 2011, extended-spectrum β-lactam (ESBL)-resistance genes, which make the bacteria that carry them resistant to most β-lactam antibiotics except carbapenems, were detected in 70% of *K. pneumoniae* strains in Asian countries such as India and Pakistan [78].

2.6.2 The causes of β-lactam antibiotics resistance

The production of β-lactamase(s) is the major cause of β-lactam resistance [73]. β-Lactamases are a class of enzymes that can hydrolyse the β-lactam ring in β-lactam antibiotics [64], subsequently disabling them. Many β-lactam–resistant bacteria can produce β-lactamases to

help them survive in β-lactam antibiotic-containing environment. In addition to producing β-lactamases, some β-lactam–resistant bacteria have *mecA* genes, which can produce the enzyme PBP2a [74]. PBP2a has low affinity for β-lactam antibiotics compared to normal PBPs [79]; therefore, it substitutes the essential transpeptidation function when normal peptidoglycan synthesis is inhibited by β-lactam antibiotics and helps bacteria survive. Moreover, more potential causes of β-lactam resistance, such as efflux pump overexpression, loss of porins and reduction in permeability of the membrane also impact on β-lactam resistance [80].

2.6.3 β-Lactamases

Generally, β-lactamases can be classified based on their protein structure. The majority of β-lactamases, such as TEM-1, TEM-2 and SHV-1, confer resistance to penicillins but not to cephalosporins [71]. Up to 90% of *E. coli* that demonstrate resistance to penicillins encode the TEM-1 gene [48]. In 1979, a new group of enzymes termed ESBLs was first reported by Sanders [81]. ESBL-producing bacteria are resistant to penicillins and some cephalosporins. CTX-M is a type of ESBL, which is commonly found in a number of GN species. A particular variant of CTX-M, termed CTX-M-15, is recognized as the most widespread ESBL genes among *E. coli* in the UK [82]. Another type of β-lactamase is carbapenemase. Carbapenemases are capable of breaking down all classes of β-lactam antibiotic including carbapenems, so carbapenemases-producing bacteria are resistant to all β-lactam antibiotics [83]. Carbapenem antibiotics are considered the drugs of last resort antibiotics for protecting human health from bacterial infection [77]. Therefore, the carbapenamases-producing bacteria currently threaten the global clinical system [84]. Figure 2-12 shows schematics of typical β-lactamases, ESBLs and carbapenemases.

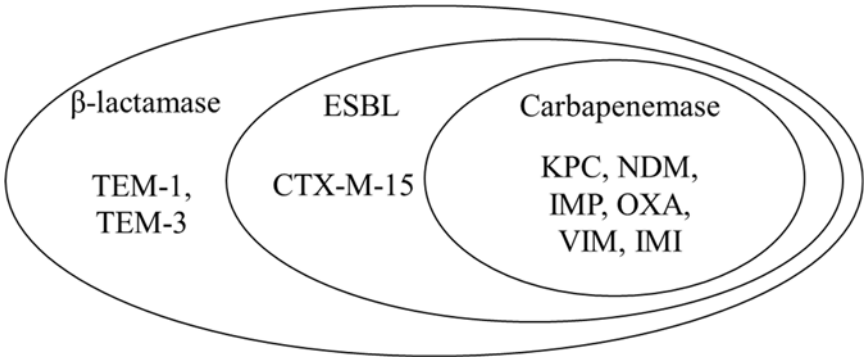

Figure 2-8: A schematics of typical β-lactamases, ESBLs and carbapenemases. TEM and SHV are β-lactamases; CTX-M is an ESBL; KPC, NDM, IMP, OXA, VIM and IMI are carbapenemases.

In this project, bacterial strains that encode TEM-1, TEM-3, SHV, CTX-M-15, KPC, NDM, IMP, OXA, VIM and IMI were used in experiments. TEM-1 and TEM-3 are β-lactamases; CTX-M-15 is an ESBL; KPC, NDM, IMP, OXA, VIM and IMI are carbapenemases. Table 2-6 demonstrates the resistance of different β-lactamases.

Table 2-6: Resistance profile of different β-lactamases to β-lactam antibiotics. β-Lactamase–producing bacteria are resistant to penicillins. ESBL-producing bacteria are resistant to penicillins and cephalosporins. Carbapenemase-producing bacteria are resistant to almost all β-lactam antibiotics.

	β-lactamase	ESBL	Carbapenemase
Typical enzymes	TEM-1	CTX-M-15	KPC, IMP, NDM
Penicillins	Resistant	Resistant	Resistant
Cephalosporins	Susceptible	Resistant	Resistant
Carbapenems	Susceptible	Susceptible	Resistant

2.6.4 Nitrocefin

Nitrocefin was invented in 1971 by O'Callaghan [63]. In solution, it is yellow, but turns scarlet once its β-lactam ring is hydrolysed by β-lactamases, producing a change in the absorbance spectrum [85]. In the laboratory, nitrocefin is commonly used to indicate the presence of β-lactamases in a test sample. Figure 2-9 (a) shows the chemical structure of nitrocefin and hydrolysed nitrocefin, and Figure 2-9 (b) shows the corresponding absorbance spectrum.

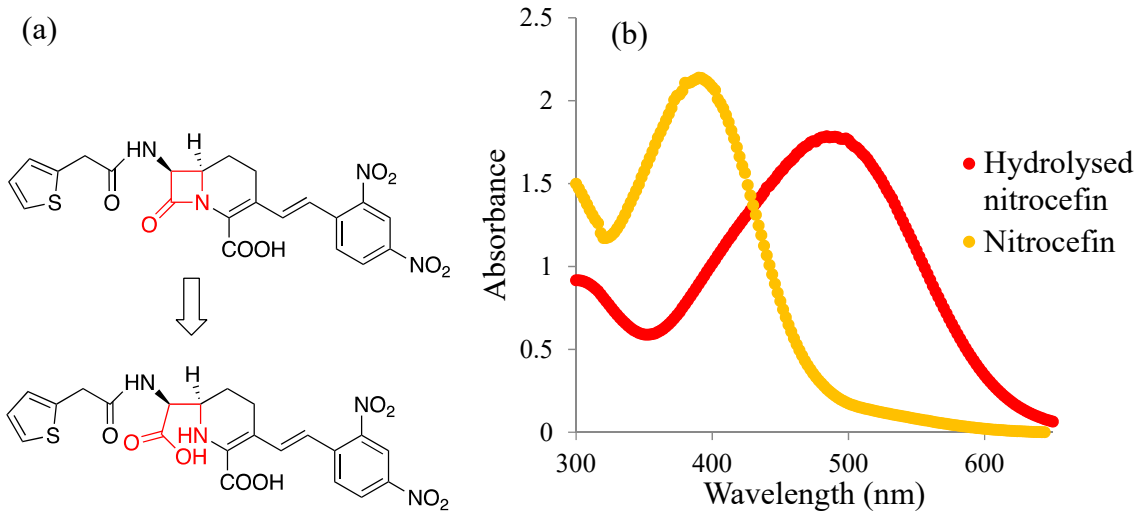

Figure 2-9: (a) Chemical structure of nitrocefin (top) and hydrolysed nitrocefin (bottom) [85]. The β-lactam ring and the broken β-lactam ring are marked in red. (b) Absorbance spectrum of 100 µg/mL nitrocefin solution before and after hydrolysis, recorded through 1-cm path length. The greatest difference in absorbance between nitrocefin and hydrolysed nitrocefin is at 482 nm.

2.6.5 pH reduction

Once a β-lactam ring is hydrolysed, the antibiotic will convert to its acid form and releases a proton [86]. The accumulation of free protons reduces the pH of the β-lactam antibiotic solution. Therefore, the pH change of a β-lactam antibiotic solution can detect the presence of β-lactamases. Figure 2-14 shows a schematic diagram of the hydrolysis of a β-lactam ring in penicillin.

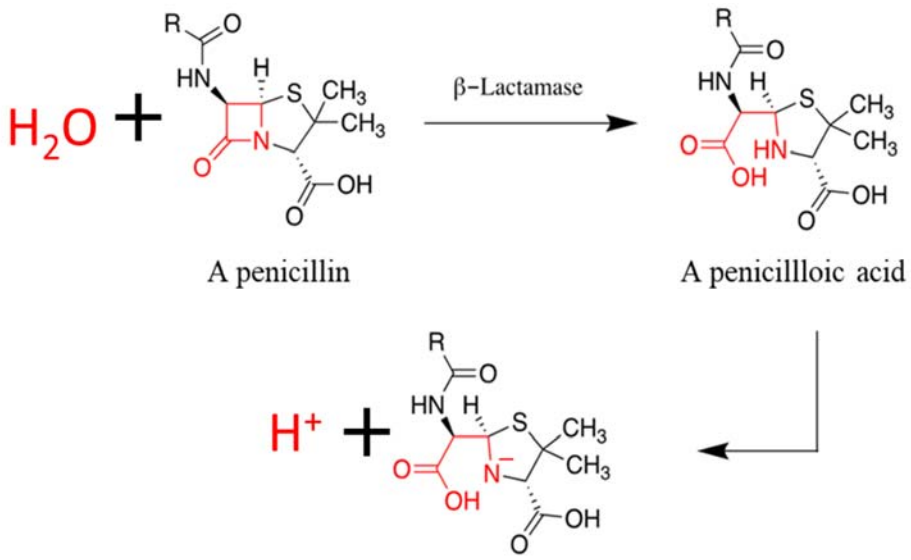

Figure 2-10: A schematic diagram of the β-lactam ring hydrolysis on a penicillin. The penicillin is hydrolysed to a penicilloic acid, which may release a proton in solution [86].

Chapter 3: Reviews of rapid AST methods

Rapid AMR diagnostic methods can be classified as genotypic or phenotypic. Genotypic methods detect AMR-related genes, while phenotypic methods monitor bacterial phenotypic changes when the bacteria are exposed to antibiotics [50]. This chapter summarizes the literature on rapid AMR diagnosis methods, especially phenotypic AMR diagnosis methods based on impedance, optical and pH detection. Next, genotypic AMR, electrochemical and DEP diagnosis methods are summarized. In the end, the commercial products that are able to perform rapid AST are introduced.

To reduce detection time, improve diagnosis sensitivity and simplify operations, most of the systems reported have been developed on microfluidics platform because microfluidic platform helps to increase the sample concentration, reduce the reagent volume and achieve automated operations [87].

3.1 Impedance methods

This section reviews the current literature on rapid AMR diagnosis using impedance. First, culture medium conductivity detection methods are reported, which detect a conductivity change during bacterial metabolism. Second, capacitance detection methods are reported, which detect the bacterial volume fraction change during bacterial growth. Then, charge transfer resistance detection methods are introduced, which detect charge transfer reactions on the surface of an immuno-impedance sensor. Subsequently, rapid AMR diagnosis based on double layer capacitance change is reported, which detects the surface area covered by the bacterial film during bacterial growth. Lastly, bacterial suspension conductivity detection methods, which detects the conductivity variation due to ion release from bacterial cytoplasm, are reported.

3.1.1 Medium conductivity detection

Stewart (1898) firstly discovered that bacterial metabolism leads to electrical conductivity change of a bacterial suspension [88]. Because of bacterial metabolism, uncharged or weakly charged substrates were transformed into highly charged products and the impedance of the bacterial suspension was reduced. For example, proteins were metabolised to amino acids, carbohydrates were hydrolysed to lactate and lipids were transformed to acetate [28]. Therefore, by monitoring the conductivity of a solution, the metabolism of a suspension can be monitored.

Stewart collected dog blood and serum samples and incubated them at 37–39°C for 6 weeks. He found that the solution conductivity was reduced and the osmotic pressure was increased during the experiment. Those changes were related with bacterial concentrations. Parsons *et al.* (1926) monitored the conductivity, pH value, ammonia (NH_3) and amino acid concentrations of *Clostridium sporogenes* and *Clostridium flabelliferum* suspensions in various mediums for 20 days at 35°C [89]. They found that the increased conductivity resulted from

the accumulation of protons and ionic production such as that for nitrogen. Allison *et al.* (1938) confirmed that the increased conductivity during bacterial growth was proportional to the amount of ammonia being produced [90]. Moreover, the production of CO_2 also contributed to the conductivity change. Therefore, the ratio between the amount of increase in ammonia and CO_2 aided investigation of the mechanism of bacterial metabolism. Additionally, they concluded that the conductivity change of the medium was proportional to the pH reduction until a certain point, when the hydrolysis of certain proteins ended. After that, the pH remained stable but the conductivity continued to increase.

The innovation of the electronic systems led to breakthroughs in impedance detection of bacterial suspensions. Ur and Brown (1975) used a capillary tube to detect the medium impedance of an *E. coli* suspension over 10 hours and compared the impedance change with bacterial concentration [29]. The results revealed a high-concordance relationship between impedance change and cell concentration. They confirmed that the broth medium, bacterial species and presence of antibiotics influenced the reduction of both impedance and pH, which suggested that the changes in pH and conductivity are based on similar bacterial activities. Figure 3-1 (a) shows the experiment device and Figure 3-1 (b) shows the plot of impedance change against time and bacteria number against time. After 5 hours culture, the impedance of the bacterial suspension continue increase due to bacterial metabolism, but the viable bacterial concentration reached the peak and would not increase further.

(a)

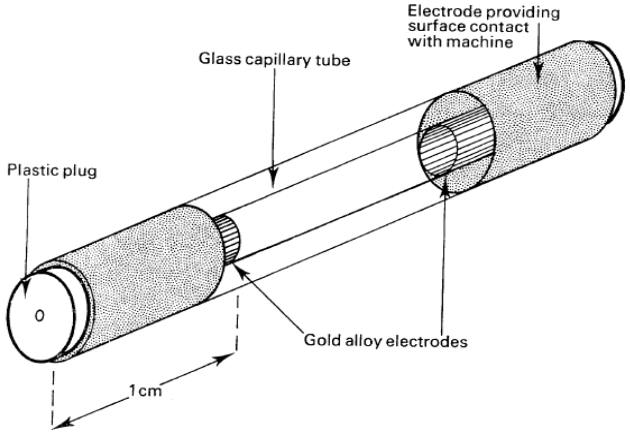

(b)

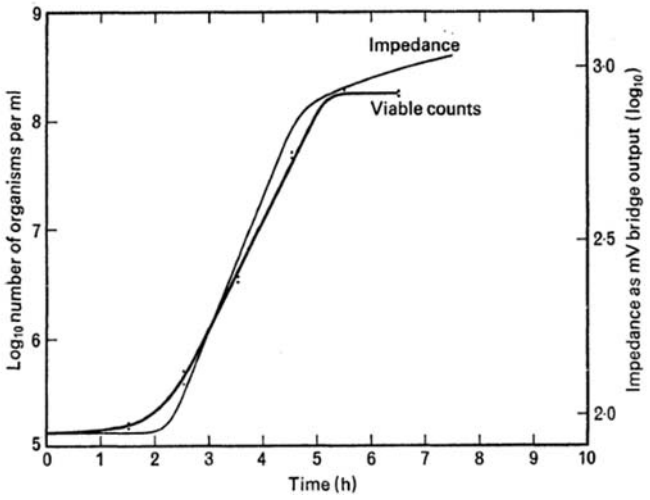

Figure 3-1: (a) The experiment device by Ur and Brown (1975) and *E. coli* concentration detected visually against time compared with impedance reduction against time. A high-concordance relationship between impedance change and cell concentration was identified.

Cady *et al.* (1975) mixed bacterial samples at initial bacterial concentrations of 10^5 CFU /mL and antibiotics gradients together, and monitored the impedance reduction over 20 hours [37]. They reported that the MIC detected by the impedance method at 5 hours was within a 2-fold difference with the MIC detected by the broth dilution method in 20 hours. Colvin *et al.* (1977) and Richards *et al.* (1978) reported similar results [91, 92]. Figure 3-2 demonstrates (a) a schematic diagram of testing device and (b) the typical result of impedance reduction against time by Colvin *et al.* (1977). These experiments verified the possibility of rapid AMR diagnosis by impedance detection.

(a)

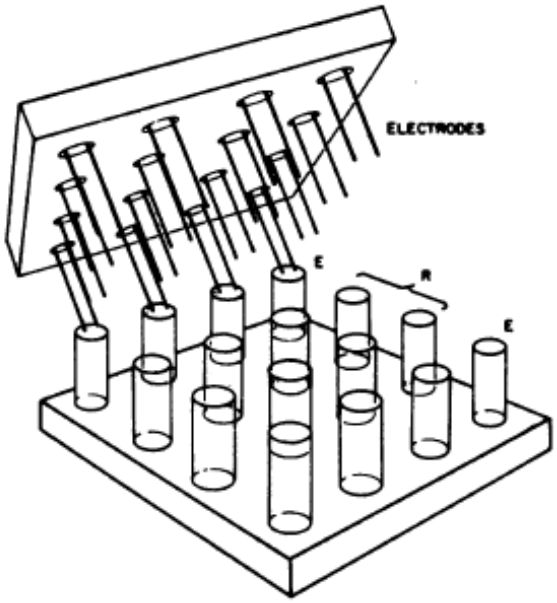

(b)

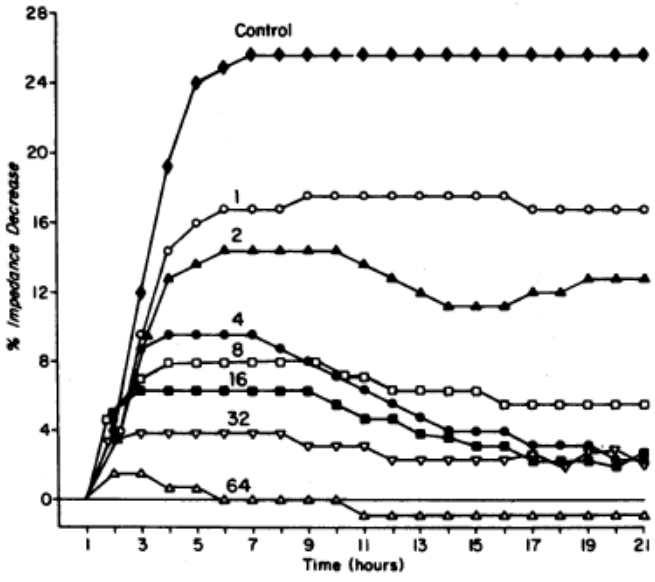

Figure 3-2: (a) A schematic diagram of the testing device and (b) the typical results of impedance reduction by Colvin *et al.* (1977). A 16-chamber impedance detection system was used to detect the medium resistance of bacterial suspensions. The impedance reduction was used to indicate the bacterial metabolism. The MIC detected by this method at 5 hours was within 2-fold difference with the MIC detected by the broth dilution method in 20 hours.

Cady *et al.* (1978) diluted bacterial samples to different-concentration suspensions and monitored the impedance of each suspension, setting 0.8% of initial impedance as a threshold [93]. The interval from start to when the impedance reduced to a threshold point was recorded as the detection time. Figure 3-3 shows the initial bacterial concentration against the detection time of *E. coli* and *S. aureus*.

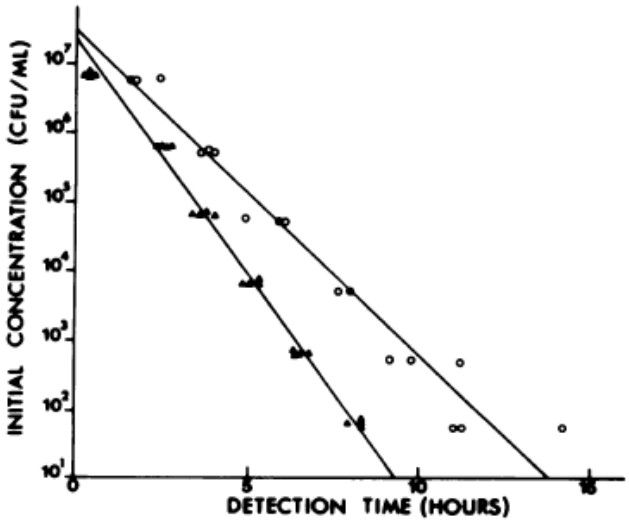

Figure 3-3: The initial bacterial concentrations against detection time of *E. coli* (black triangles) and *S. aureus* (circles). When initial concentrations reached 10^6 CFU/mL, the detection time was within 1 hour. Different bacterial species had different metabolism mechanisms and the detection time were variable in the same initial bacterial concentrations.

Eden and Eden (1984) built a simplified model of an electrochemical chamber to describe the impedance change caused by bacterial metabolism [28]. Figure 3-4 (a) shows the electrochemical chamber model and Figure 3-4 (b) shows the corresponding electrical circuit.

(a)

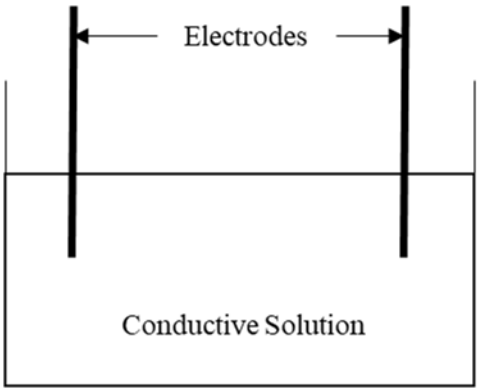

(b)

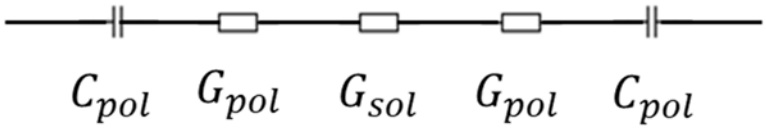

Figure 3-4: (a) A simplified model of an electrochemical well and (b) the corresponding circuit for describing the impedance change caused by bacterial metabolism. Cpol and Gpol are the polarization capacitance and conductance of each electrode, respectively. Gsol is the conductance of the solution, which is related to the metabolism in the bacterial suspension. The circuit was developed by Eden and Eden (1984).

Microfluidic technology enabled smaller sample volumes to be measured. Furthermore, pH electrodes could be integrated into the same measurement chamber. Yang *et al.* (2005) incubated an *E. coli* suspension at an initial bacterial concentration of 10^5 CFU/mL for 20 hours and monitored the medium resistance and pH of the suspension simultaneously [94]. They found that the pH and solution resistance reduction rates peaked at 10^7 CFU/mL. When the bacterial concentration was $>10^7$ CFU/mL, the bacterial metabolism slowed down due to the lack of essential nitrogen supply in the medium. Safavieh *et al.* (2017) demonstrated that the medium resistance of an *E. coli* suspension or a methicillin-resistant *S. aureus* (MRSA) suspension could reduce by >50% within 1 hour at 10^8 CFU/mL starting concentration [31]. Moreover, mixing antibiotics with the bacterial samples could significantly slow down the conductivity change and be used to detect antibiotic susceptibility of *E. coli* and *S. aureus* within 1 hour. Figure 3-5 shows the normalized impedance against time for (a) *E. coli* and (b) MRSA.

(a)

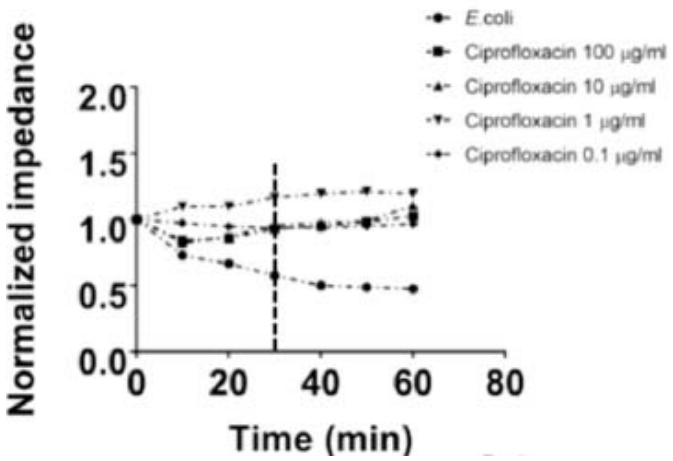

(b)

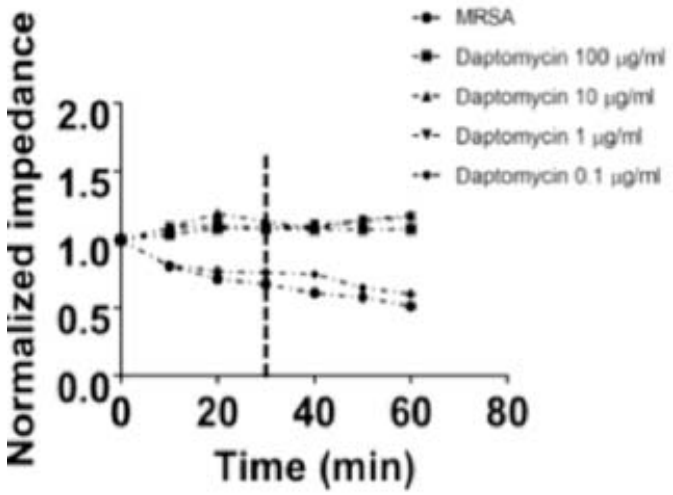

Figure 3-5: The normalized impedance against time for (a) *E. coli* and (b) MRSA. The impedance reduced by >50% within 1 hour at 10^8 CFU/mL initial bacterial concentration. Mixing antibiotics with test bacteria could significantly slow the medium conductivity change [31].

Using impedance detection to monitor bacterial metabolism with additional antibiotics is convenient for detecting the effect of antibiotics on a bacterial strain. The sensitivity of the impedance detection method is roughly 10^6 to 10^7 CFU/mL and generally spans several hours from 'sample in' to 'results out'. However, current metabolism detection methods are based on detecting conductivity reduction in a single chamber within a certain interval. The bacterial species, temperature, and medium type influence the diagnosis results. This thesis describes a differential impedance detection method to remove the impact of these external factors.

3.1.2 Growth medium permittivity detection

The medium capacitance of a bacterial suspension can be used to indicate the bacterial concentration because the medium capacitance is proportional to the bacterial volume fraction in solution, (simulations are in Chapter 6). Compared with the indirect metabolism-based methods, the bacterial volume fraction based methods can be used to detect bacterial concentrations directly.

Harris *et al.* (1987) measured dielectric properties of yeast solutions in the radio frequency (RF) range and found that at 300 kHz, the capacitance of yeast suspensions was proportional to the OD of the solution at 600 nm [95]. Carvell and Eowd (2006) monitored the capacitance of cell suspensions in RF range and demonstrated that the capacitance of cell suspensions was proportional to the viable cell densities with $R^2 = 0.999$. The capacitance of bio-particle suspensions can be used to monitor particle density accurately [96]. Sengupta *et al.* (2006) measured the impedance of a bacterial suspension and used the medium capacitance to indicate the bacterial concentration in solution [97]. Puttaswamy and Sengupta (2010) detected the capacitance of *E. coli* suspensions in milk, apple juice or Tris-buffered saline (TBS) medium and demonstrated that the sensitivity of real-time bacterial concentration detection was 10^3 CFU/mL and that the medium type does not influence the detection sensitivity [98]. Puttaswamy *et al.* (2013) mixed antibiotics with *E. coli* and used an ultra-precision impedance analyser to detect the resistance and reactance of the bacterial suspension [99]. The medium capacitance could indicate the antibiotic susceptibility and primary effect (bacteriostatic and bactericidal) of the tested *E. coli* in 4 hours. Grossi *et al.* (2010) designed a portable impedance detection system for detecting the resistance and capacitance of bacterial suspensions in PoC settings [100]. They were able to detect bacterial concentrations of $>10^6$ CFU/mL within 3 hours. Luchterhand *et al.* (2015) designed an impedance detection system to monitor medium capacitance [101]. Four circular electrodes in rotation-symmetrical design were immersed in chambers of a standard-size well plate and medium capacitance could be detected.

Capacitance detection can detect bacterial concentrations in high-conductivity medium directly. However, because the shape and size of pathogen bacteria are various, the relationship between the medium capacitance and the bacterial concentration in solution are variable. In clinical situations, the species of pathogens are unknown, so the the application of using capacitance detection method for rapid AST is limited.

3.1.3 Charge transfer resistance detection

An immunoassay is a plate-based biochemical method that detects and quantifies substances such as peptides, proteins or antibodies in solution, and is generally analysed based on optical absorbance or fluorescence [59]. Impedance immunosensors are impedance sensors with specific antigens at an electrode surface, and can analyse immunoassays rapidly and efficiently. Several groups have developed impedance immunosensors for detecting antibiotic susceptibility, based on detecting charge transfer at the electrode–electrolyte interface. First, bacteria are exposed to a certain antibiotic concentration. Then, the antibiotic-treated bacteria are flowed across the antibody-immobilized electrode, where specific antigens on the bacteria surface will bond to the antibodies on the electrode. The antibiotic-resistant strains usually have higher bacterial concentrations than susceptible strains, so the charge transfer resistance varies according to the antibiotic susceptibility of the test bacterial strain.

Ruan *et al.* (2002) first developed an electrochemical impedance immunosensor for rapid detection of *E. coli* concentrations with LoD at 10^3 CFU/mL [102]. Antibodies were immobilised onto the surface of indium–tin oxide (ITO) interdigitated electrodes, and a $Fe(CN)_6^{3-/4-}$ redox probe was used to indicate the binding between the immobilized antibodies

and *E. coli*. The charge transfer resistance at the electrode surface is influenced by the charge transfer reactions of the redox probe. The Randles model was used to analyse the electrode–electrolyte interface and the impedance spectrum was plotted as a Nyquist plot for mathematic analysis. Figure 3-6 shows: (A) The schematic diagram of the impedance immunosensor and (B) the Nyquist plots of (a) the bare interdigitated ITO electrode, (b) after antibody immobilization and (c) after *E. coli* binding. Yang *et al.* (2004) demonstrated that the charge transfer impedance on the impedance immunosensor surface was proportional to the bacterial concentration in solution [103].

(A)

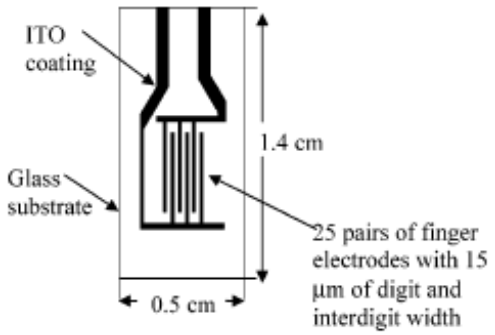

(B)

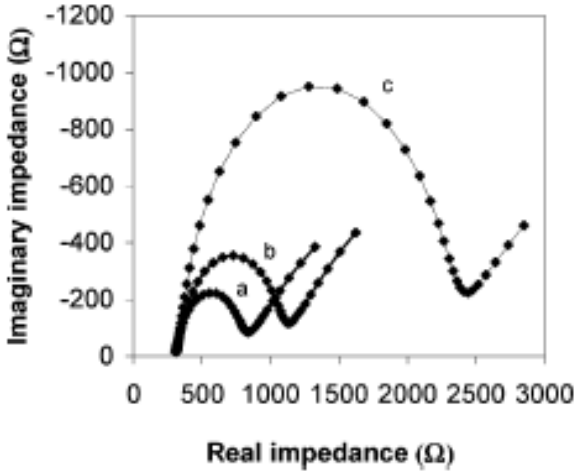

Figure 3-6: (A) The schematic diagram of interdigitated ITO impedance immunosensor and (B) Nyquist plots of (a) the bare interdigitated ITO electrode, (b) after antibody immobilization and (c) after *E. coli* binding. The antibody–*E. coli* binding altered the charge transfer resistance.

Subsequent to that, impedance immunosensors were developed with improved sensitivity. Radke *et al.* (2005) designed an interdigitated Au impedance immunosensor for detecting *E. coli* at 10^4 to 10^7 CFU/mL [104]. Varshney *et al.* (2007) bound magnetic nanoparticle–antibody conjugates on interdigitated electrodes to detect *E. coli* at 10^2 CFU/mL [105]. Barreiros-dos-Santos *et al.* (2015) then improved the LoD of *E. coli* detection to 1 CFU/mL [106]. Mannoor *et al.* (2010) attached antimicrobial peptides (AMP) on an Au electrode surface to capture *E. coli* and *Salmonella* [107]. Figure 3-7 (a) and (c) are the schematic diagrams of the system before and after bacterial binding, respectively. Figure 3-7 (b) shows the structure of the AMP. Figure 3-7 (d) is a photo of the interdigitated Au electrodes developed by Mannoor *et al.* (2010).

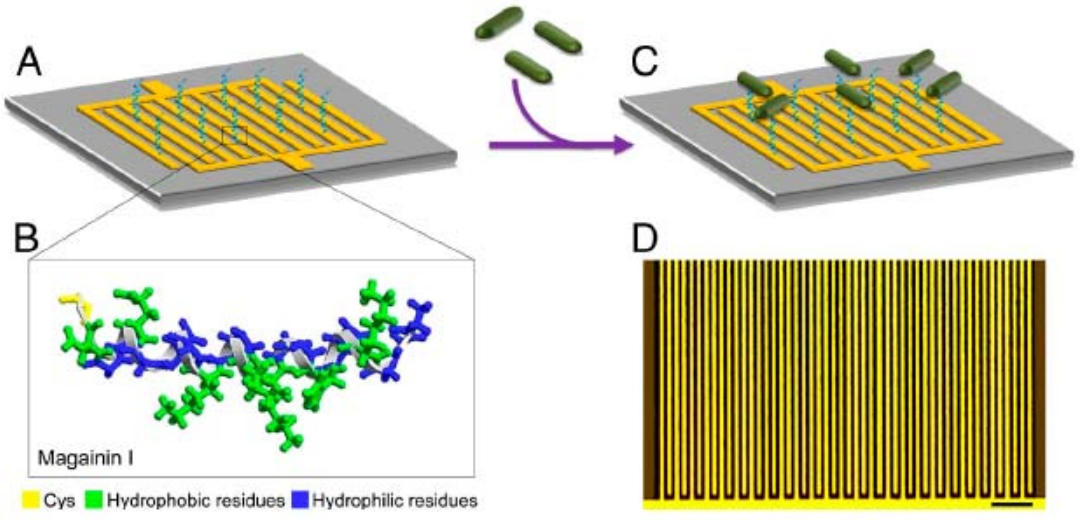

Figure 3-7: (a) The schematic diagram of the system before bacteria binding. (b) The AMP structure. (c) The schematic diagram of the system after bacteria binding. (d) A photo of the interdigitated Au electrodes developed by Mannoor *et al.* (2010). This immunosensor can distinguish pathogenic bacterial species and detect bacterial concentrations at 10^3 CFU/mL.

Cui *et al.* (2013) used an impedance immunosensor to test the antibiotic susceptibility of 11 human TB and 10 bovine TB serum samples [108]. Etayash *et al.* (2014) improved the AMP immunosensor by Mannoor *et al.* (2010) and extended the testing strains to *Listeria monocytogenes*, *Enterococcus faecalis*, *L. innocua* and *S. aureus* [109]. When the bacterial concentrations reached 10^3 CFU/mL, the sensor could detect the bacterial species and concentration in 5 minutes. Jiang *et al.* (2014) designed an integrated filter–impedance microfluidic system for detecting bacterial concentrations in flow with the LoD at 10 CFU/mL [110]. Bacterial suspensions were trapped by a filter, and then the impedance of the enriched bacterial samples was detected. The impedance magnitude was recorded as Nyquist plots and analysed by the Randles model. They found that the charge transfer resistance and double layer capacitance could indicate the bacterial concentration in deionized (DI) water. Figure 3-8 shows diagrams of (a) the Randles model, (b) the corresponding Nyquist plot, (c) the cross-view of the device and (d) a three-dimensional (3D) schematic diagram of the device.

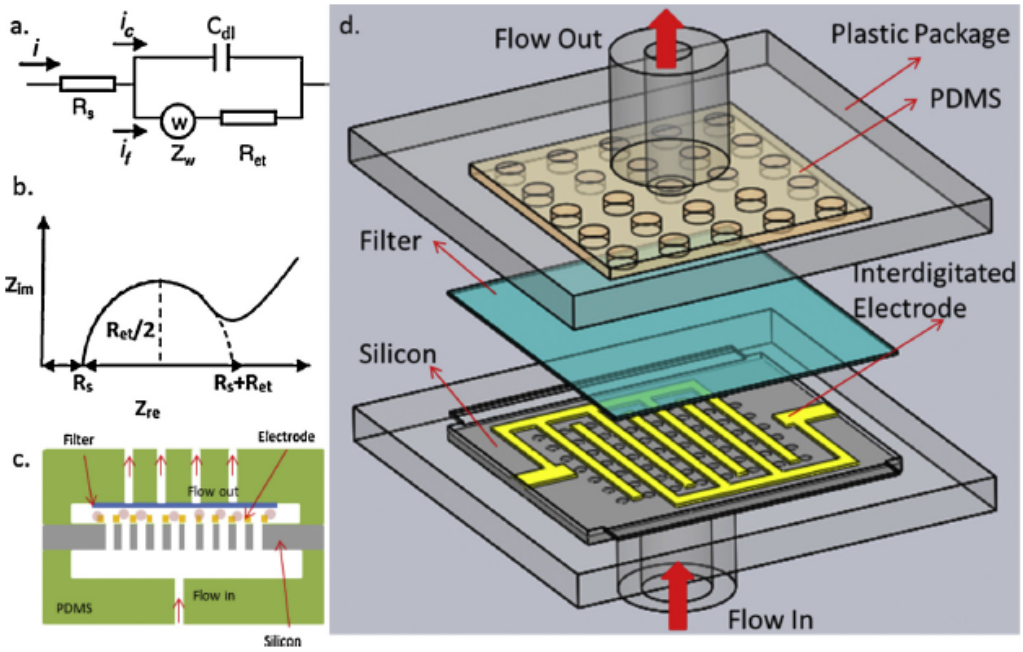

Figure 3-8: Diagrams of (a) the Randles model, (b) the corresponding Nyquist plot, (c) the cross-view of the device and (d) a 3D schematic diagram of the device by Jiang *et al.* (2014). Their results demonstrate that a filter can be used to trap bacteria and improve the sensitivity of impedance detection.

In conclusion, impedance immunosensors are sensitive for detecting specific bacterial concentrations, with the LoD being highest at 1 CFU/mL [106]. However, antibodies can attach only to some specific bacterial strains, which may provide false negative results in clinical testing. Moreover, immunosensors are expensive and rarely reused because of the irreversible binding between the antibodies and bacteria, which limit its application in PoC situation [111].

3.1.4 Double layer capacitance detection

In an impedance detection chamber that contains a large amount of bacterial suspensions, some parts of the electrode surface may be covered by bacteria and the double layer capacitance of the chamber may be altered. Therefore, the double layer capacitance of the chamber can be used to indicate the bacterial concentration in solution. Paredes *et al.* (2014) detected the impedance magnitude at low frequency during *E. coli* growth in Luria-Bertani (LB) broth [112]. They demonstrated that at 10 Hz, the impedance increased after 10-hour incubation. Settu *et al.* (2015) reported similar results [113]. Figure 3-9 shows the impedance spectrum of *E. coli* growth in LB broth from Settu *et al.* (2015).

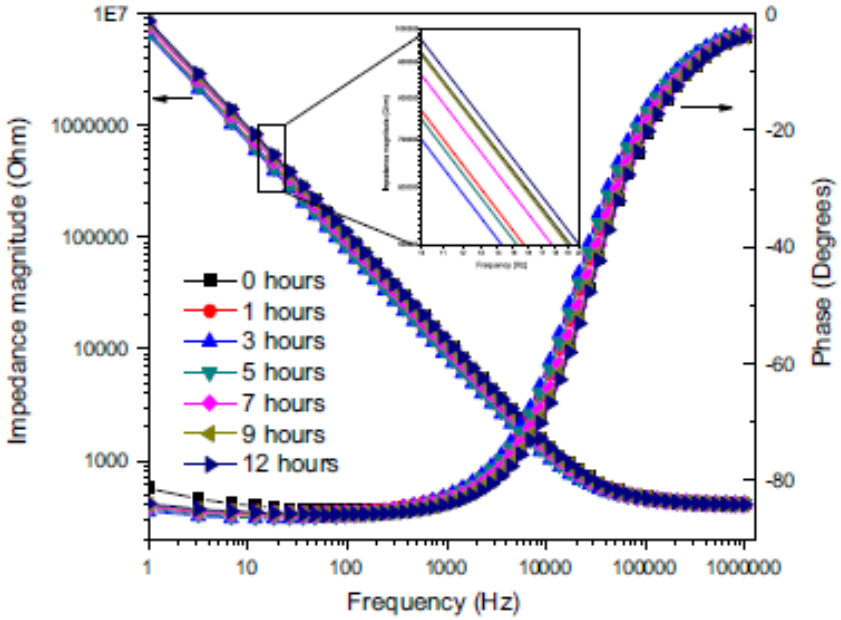

Figure 3-9: Impedance spectrum of *E. coli* growth in LB broth in 12 hours from Settu *et al.* (2015). Impedance magnitude was increased at low frequencies, which indicated reduced double layer capacitance during *E. coli* growth. After long-term incubation, a large amount of *E. coli* covered some part of the electrode surface and reduced the double layer capacitance.

Using double layer capacitance to indicate the bacterial concentration in solution is easy and simple. However, a long time is needed for incubating a large amount of bacteria on an electrode surface; generally, >10 hours is needed from sample to results. Therefore, detecting double layer capacitance to diagnose AMR in PoC settings is not quick enough.

3.1.5 Ion release detection

Bacterial cytoplasm contains high-conductivity (approximately 2.2 S/m) solution [114]. If the bacteria are lysed, the ions will be released into the suspending medium. If the suspending medium is of lower conductivity, the overall conductivity will increase.

Yang (2008) diluted *E. coli* from 10^4 CFU/mL to 10^9 CFU/mL in deionized (DI) water (conductivity = 0.001 S/m) and phosphate-buffered saline (PBS, conductivity = 1.8 S/m) [115]. Then, the impedance spectra of different bacterial suspensions were detected. The ion release from *E. coli* in DI water could alter the medium conductivity significantly. In contrast, the impedance spectrum in PBS did not change when bacterial concentration increased. Figure 3-10 shows the impedance spectrum of *E. coli* suspensions in (a) DI water and (b) PBS solution.

(a)

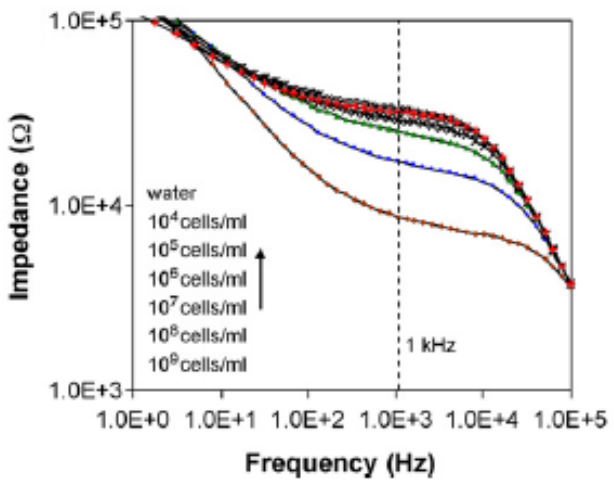

(b)

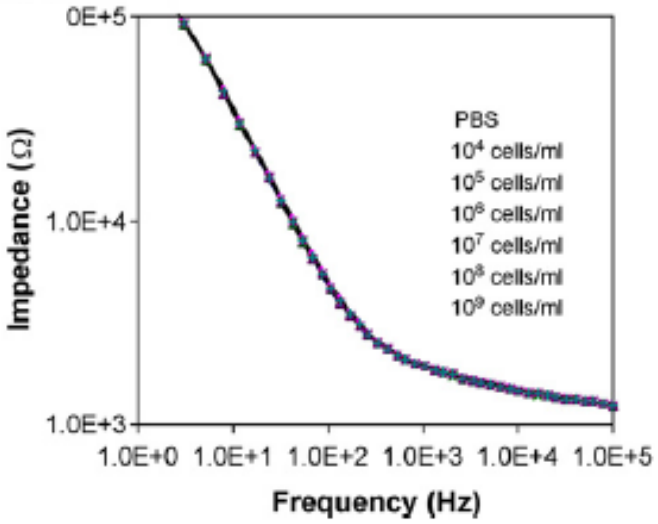

Figure 3-10: Impedance spectra (1 Hz to 100 kHz) of *E. coli* suspensions in (a) DI water and (b) PBS from Yang (2008). Ion release in the DI water caused significant medium resistance reduction. The impedance spectrum in PBS did not change when bacterial concentration increased.

Mortari *et al.* (2015) used bacteriophages to hydrolyse bacteria and detected the reduced impedance to indicate the bacterial concentration in solution. The method could detect the bacteria at 10^4 to 10^8 CFU/mL [116]. Ebrahimi *et al.* (2017) used a droplet-based impedance sensor to detect ampicillin susceptibility. A droplet containing 10^9 CFU/mL *E. coli* and ampicillin was pipetted on a microfluidic electrode array [117]. If the bacteria were dead, ions in their cytoplasm would be released and the medium conductivity would increase. They demonstrated that the ion release method could detect ampicillin susceptibility in 1 hour. However, high–bacterial concentration test bacterial samples are needed. Moreover, the method could not be applied for bacteriostatic antibiotics.

3.2 Optical methods

This section reviews rapid AMR diagnosis by optical methods. First, morphological observation methods are reviewed, followed by the review of bacterial length monitoring techniques. Next, a general introduction to fluorescence observation follows. Lastly, novel optical droplet methods for AMR diagnosis are introduced.

3.2.1 Morphological observation

When exposed to antibiotics, the bacterial morphological patterns may indicate its antibiotic susceptibility. However, conventional morphological observation requires trained technicians using a high-resolution microscope, which cannot be applied in PoC situation. Recently, automatic image analysis has been developed to monitor bacterial morphological patterns, which has significantly reduce the difficulty in morphological observation.

Peitz *et al.* (2010) reported that DEP force could be used to immobilise bacteria between interdigitated electrodes so that single-cell morphological monitoring could be achieved [34]. The bacterial number in the camera field was automatically counted. The MIC and IC50 (median inhibition concentration) could be determined in 4 hours. Choi *et al.* (2013, 2014) developed an auto-analysis system that could detect antibiotic susceptibility within 4 hours [32, 33]. Their system could not only automatically count the bacteria numbers in the camera field, but could also observe the morphological patterns of the bacteria, for example, division, swelling formation and filamentary formation. Figure 3-11 shows the image processing steps.

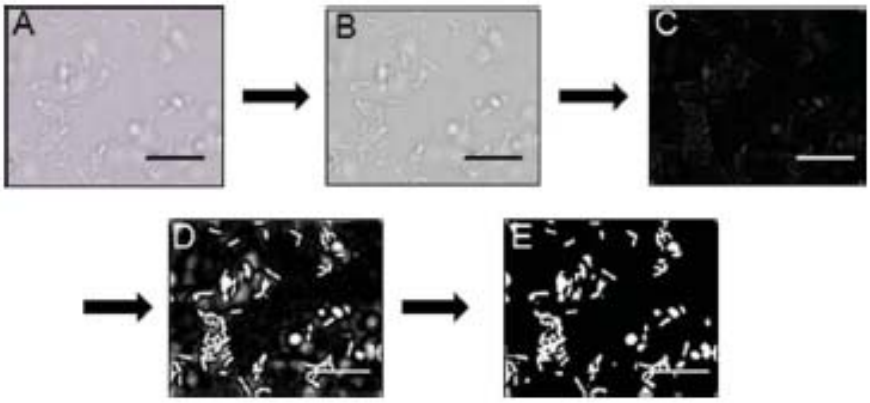

Figure 3-11: Image processing steps from Choi *et al.* (2013). An RGB photo was transformed to grey format and the background was eliminated. The photo quality was optimized and the photo was converted to binary format to enhance the image contrast.

Price *et al.* (2014) designed a multi-chamber microfluidic chip to detect the growth rate of bacteria in different antibiotic environments [118]. The bacterial numbers in each chamber was counted by a camera in certain time intervals and the bacterial growth rate was calculated. The device could distinguish MRSA and methicillin-susceptible *S. aureus* (MSSA) with >95% accuracy within 4 hours.

Optical observation is direct and conventional, but still relies on high-resolution microscopes and requires several hours from ‘sample in’ to ‘results out’. Therefore, several groups have aimed to simplify optical observation and reduce the cost of microscopes.

3.2.2 Length monitor

Several groups have reported that bacterial morphological patterns in three dimention can be simplified into a one-dimensional measurement. Therefore, the complexity of optical observation can be reduced.

Lu *et al.* (2013) designed a microfluidic system that could detect the MIC in 30 minutes [119]. In their system, single bacterium was loaded into a millimetre-scale channel filled with a certain concentration of antibiotic. The bacterium length in the channel was monitored by a camera and was used to indicate the bacterial growth. Baltekin *et al.* (2017) reported a similar microfluidic chip that could diagnose AMR in 30 minutes [120]. The detection chamber fitted with 2000 cell traps placed in parallel. The width and height of each trap was 1.25 μm. Therefore, the bacterium was forced into a rod shape in the trap. Figure 3-12 shows a schematic diagram of the device.

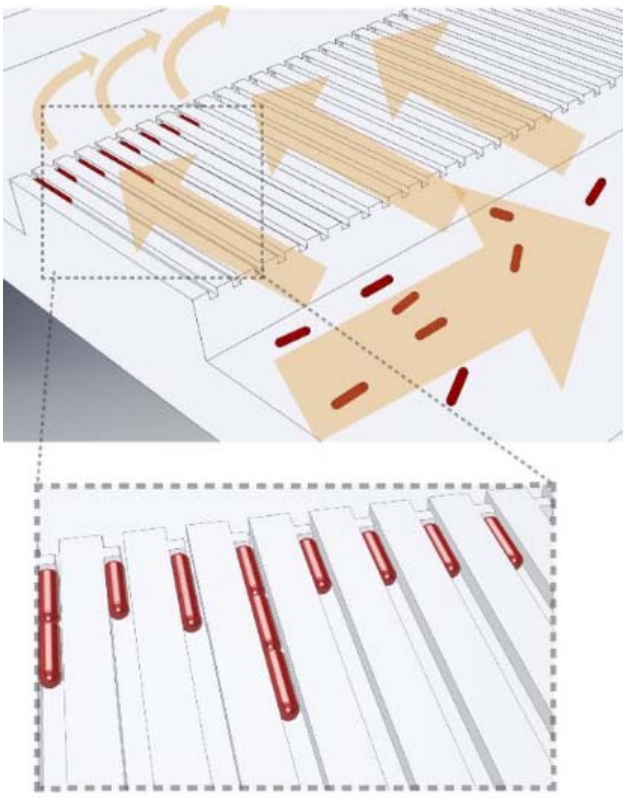

Figure 3-12: A schematic diagram of rod-shaped bacteria loaded in a cell trap (Baltekin *et al.*, 2017). Test bacteria were mixed with antibiotics in the chamber and a charge-coupled device (CCD) camera monitored the bacterial length of each trap, which was used to show the antibiotic susceptibility.

3.2.3 Fluorescence observation

Fluorescence observation is widely used in bacterial observation because the fluorescence signal can not only indicate bacterial concentrations or morphological properties, but also indicate the bacterial viability.

Tsou *et al.* (2010) reported an AMR diagnosis device that could distinguish MRSA and MSSA according to fluorescence [121]. Test bacteria were exposed to antibiotics for 1 hour and flowed through a porous membrane filter, where the bacteria were trapped. Then, a fluorescence dye stain was used to count the surviving bacterial number and further indicate the antibiotic susceptibility. Kim *et al.* (2010) used a fluorescence dye stain method to detect the antibiotic susceptibility of a biofilm [122]. The biofilm was first incubated on polydimethylsiloxane (PDMS) chamber, and then the chamber was filled with gradient of antibiotic. A fluorescence camera was used to monitor the area of surviving biofilm. Resistant bacteria could survive in high–antibiotic concentration areas while susceptible bacteria could only survive in low–antibiotic concentration areas. Sun *et al.* (2011) designed a microfluidic device for long-term bacteria growth monitoring [123]. A fluorescence camera was used to monitor the growth rate of green fluorescent protein (GFP)-labelled *E. coli*. The fluorescence output was proportional to the *E. coli* numbers in the chamber and changed when the testing *E. coli* were exposed to antibiotics. Kalashnikov *et al.* (2012) used a fluorescent dye that could permeate the cell membrane only when the bacteria were dead and produce fluorescence when it intercalate to bacterial DNA. In this system, the methicillin susceptibility of *S. aureus* could be detected within 1 hour [124]. Figure 3-13 shows the optical and fluorescence images of the experiment reported by Kalashnikov *et al.* (2012).

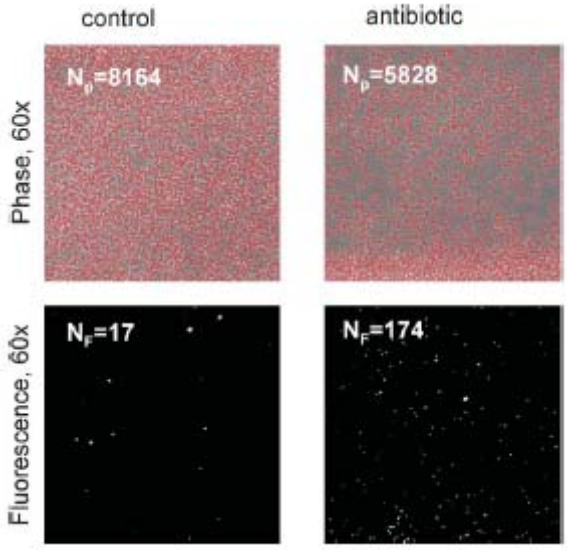

Figure 3-13: Kalashnikov *et al.* (2012) detected antibiotic susceptibility using fluorescence. In one chamber, test bacteria were mixed with a fluorescent dye and an antibiotic. In another chamber, test bacteria were mixed with a fluorescent dye without antibiotics (control). The fluorescence signals of the two chambers were observed simultaneously. The antibiotic susceptibility was calculated based on the ratio of the death rates of the antibiotic-present and antibiotic-absent chambers.

Jiang *et al.* (2014) used a fluorescence image system to monitor dynamic β-lactamase presence [80]. They intercalated a GFP gene with an ESBL expression gene and then transported it into an *E. coli*. The *E. coli* was exposed to cephalosporin to induce β-lactamase expression. Thus, the fluorescence intensity was proportional to β-lactamase production. The fluorescence image system could perform single-cell monitoring and aided quantification of β-lactamase expression. Dong and Zhao (2015) designed an immunosorbent bioluminescence sensor for performing AMR diagnosis [125]. Antibodies were immobilized on the bottom of the chip to capture antibiotic-treated bacteria. The fluorescence intensity was proportional to the captured bacterial concentrations. The system could identify UTI pathogen species in 20 minutes and detect the AST of eight antibiotics in 3–6 hours.

The fluorescence observation methods can observe bacterial viability directly, but still rely on high-resolution fluorescence microscopes and cannot provide accurate diagnosis in low-concentration bacterial samples. Therefore, several groups have developed single-cell fluorescence methods for diagnosing antibiotic susceptibility.

3.2.4 Droplet fluorescence observation

Droplet or digital microfluidics can provide better mixing, sorting and sensing performance, and eliminate the need for pre-incubation. Combining droplet microfluidics and optical observation systems makes it possible to detect antibiotic susceptibility directly from patient urine or blood samples.

Boedicker *et al.* (2008) designed a droplet microfluidic system to rapidly diagnose AMR [126]. Single bacterium was captured in plugs and cultured with antibiotics and fluorescent dye for 2.8 hours in 37 ˚C. Then, the fluorescence intensity of each plug was scanned. Resistant bacterium showed high fluorescence signal while the susceptible bacterium cannot. Figure 3-14 shows a schematic diagram of the droplet microfluidic device. Eun *et al.* (2011) and Churski *et al.* (2012) designed similar droplet microfluidic systems for rapid AST diagnosis [127, 128].

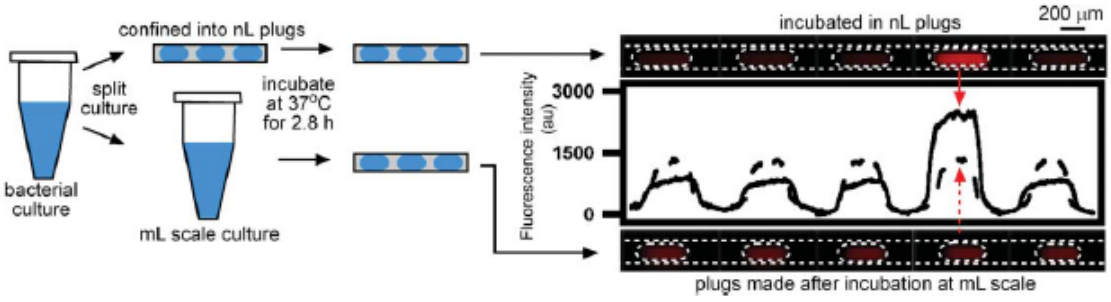

Figure 3-14: Boedicker *et al.* (2008) designed a droplet microfluidic system to rapidly diagnose AMR. Single bacterium is mixed with antibiotics in a capsule and then incubated for 2.8 hours. The resistant bacteria emit a strong fluorescent signal after 2.8-hour incubation.

Resazurin is a bacterial metabolism indicator that is converted to resorufin during bacterial growth and emits fluorescent light. Avesar *et al.* (2017) designed a static droplet system to detect bacterial metabolism in an antibiotics environment [61]. Test bacteria were mixed with antibiotics and resazurin in an Eppendorf tube, and then injected into a microfluidic static

droplet system. The resistant testing strain had stronger metabolism and exhibited higher fluorescence intensity at the same time. The device could detect antibiotics susceptibility within 8 hours.

3.3 pH methods

This section reviews pH-detection based AMR diagnosis methods results from two working mechanisms. The metabolism monitoring methods are reported first. Living bacteria release protons during metabolism and reduce pH, which be used to demonstrate broadband antibiotics susceptibility. However, this process requires a long time for proton accumulation because metabolism process is relative slow. Next, a pH method based on detecting β-lactam ring hydrolysis is reported. When a β-lactamase hydrolyses the β-lactam ring of a β-lactam antibiotic, a proton is released and the pH is reduced. The enzyme reaction is relative fast and reliable, so β-lactamases can be detected in a short time.

3.3.1 Metabolism detection

During bacterial growth, sugars are hydrolysed into organic acids. The accumulation of organic acids leads to increased medium acidity. Therefore, pH detection is widely used in bacterial metabolism monitoring. For example, Yang *et al.* (2005) demonstrated that *L. monocytogenes* growth in a low-conductivity growth medium could be detected by both pH measurement and solution conductivity measurement [94]. Using the pH method, bacterial growth could be detected after approximately 12 hours for samples with initial bacterial concentrations of 10^2 CFU/mL and after 2 hours for samples with initial bacterial concentrations of 10^7 CFU/mL. Changed in the conductivity of the medium could be detected 1 hour earlier than the changes in the medium pH. Cira *et al.* (2012) used a phenol red indicator to monitor the pH change during bacterial growth. Phenol red is a commonly used pH indicator. If the pH value of a phenol red solution is >7.5, the solution would be pink; if the pH value is <7.5, the solution would be yellow/orange [35]. In that study, the authors fabricated a microfluidic chip with 11 chambers along a central channel. The phenol red indicator was first mixed with different concentrations of antibiotics, and the mixing solutions were then placed in specific chambers. The test bacterial strains were then pipetted from the end of the channel and flowed to each chamber by capillary force. Bacterial growth was reflected by the solution colour. Yellow indicated a lower solution pH due to the products of metabolism, indicating bacterial growth and hence resistance to the antibiotic. In contrast, red indicated that bacterial growth was inhibited in that antibiotic concentration. Figure 3-15 (A) and (B) are photos of *E. coli* MG1655 mixed with different concentrations of kanamycin at the start and after 18 hours, respectively.

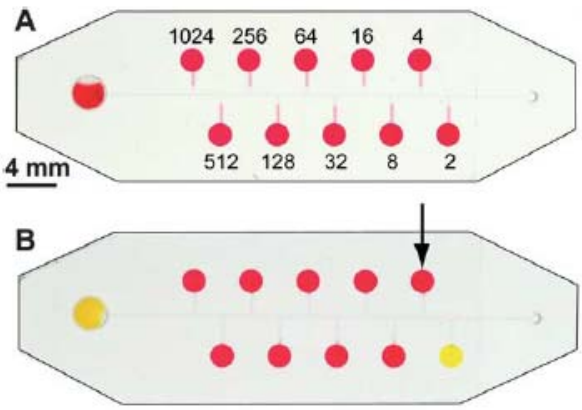

Figure 3-15: *E. coli* MG1655 mixed with different concentrations (µg/mL, indicated on the chip) of kanamycin at (A) the start and (B) after 18 hours (Cira *et al.*, 2012). After 18-hour incubation, bacteria in chambers with kanamycin concentration > 4 µg/mL showed inhibited growth. In contrast, bacterial growth was observed in the presence of 2 µg/mL kanamycin and no kanamycin. Thus, the chip indicates that the MIC of kanamycin for *E. coli* MG1655 is 4 µg/mL.

Tang *et al.* (2013) monitored the pH value of a bacterial suspension using a pH-sensitive chitosan gel, whose thickness was correlated with the pH [129]. The test bacteria strain was first mixed with an antibiotic, and then injected into a channel formed by the special gel. The device could rapidly diagnose antibiotic susceptibility within 1 hour when the initial bacterial concentration reached 10^6 CFU/mL. Figure 3-16 shows a schematic diagram of the pH monitoring system and typical results from the device.

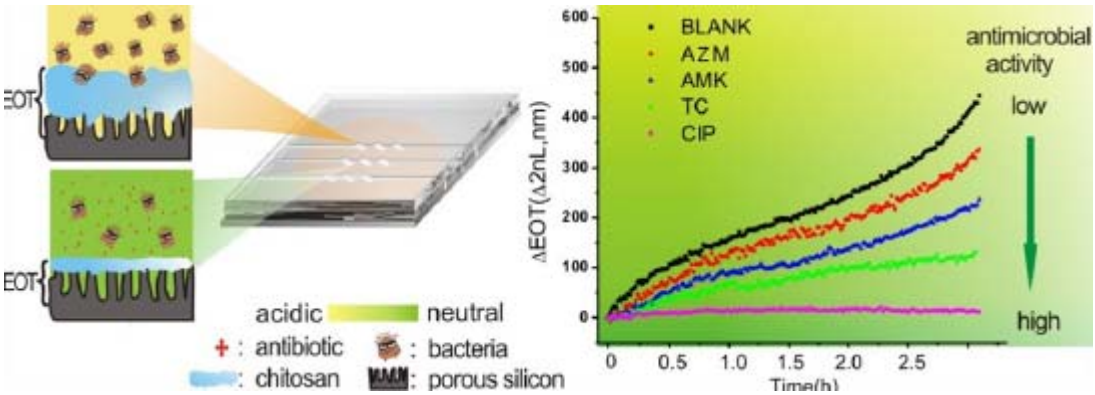

Figure 3-16: A schematic diagram of the pH monitoring system and typical results from the device (Tang *et al.*, 2013). A pH-sensitive chitosan gel was used to monitor bacterial metabolism. The effective thickness (EOT) of the channel was monitored by an optical microscope and the pH value was calculated in real-time.

Measuring pH to monitor bacterial metabolism is convenient for detecting the effect of antibiotics on bacteria. However, pH detection has lower sensitivity than impedance detection in the same interval [94]. Moreover, the bacterial species, temperature and buffer capacity of the suspended media influence the pH detection results.

3.3.2 β-Lactam ring hydrolysis

The Carba NP test was developed by Nordmann, Poirel and Dortet in 2012, and can rapidly detect carbapenemase producers based on pH [130]. The Carba NP method is based on detecting the pH reduction when the β-lactam ring on imipenem, a carbapenem antibiotic, is hydrolysed by carbapenemases. In operation, one loop (10 μL) of test strain was suspended in bacteria protein extraction reagent (B-PER) and vortexed to extract proteins from the bacteria. The lysate was centrifuged and the supernatant was mixed with the imipenem solution. Phenol red indicator was added and the solution pH was adjusted to pH 7.8 by adding drops of 1 N NaOH. The mixture was incubated at 37°C for 2 hours, and the presence of carbapenemases was indicated by the solution colour. Figure 3-17 shows the representative test results of the Carba NP method.

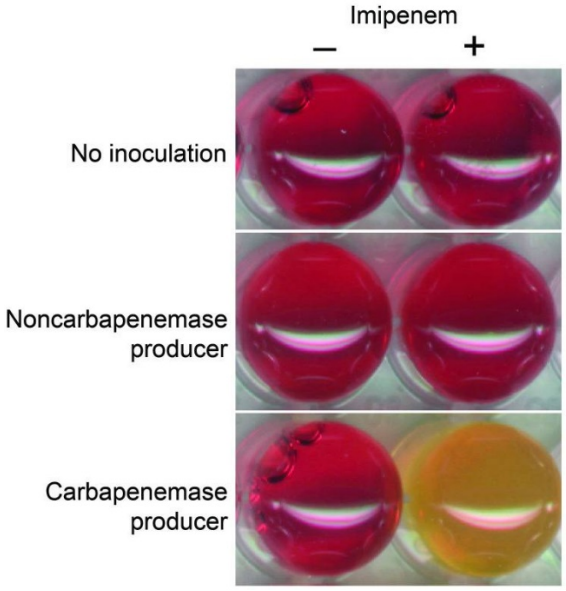

Figure 3-17: Representative results of the Carba NP test [130]. Red indicates that the solution pH is unchanged. In contrast, yellow indicates reduced solution pH. If the imipenem-present and imipenem-absent chambers are both red, the testing strain might not have been inoculated or the testing strain might be a carbapenemase non-producer. If the imipenem-present chamber changes colour but the imipenem-absent chamber remains red, then the testing strain is a carbapenemase producer.

Carba NP yields visual positive/negative results for detecting imipenem susceptibility. It is rapid, sensitive, inexpensive and suitable for testing urine [27] and blood samples [131]. However, sample preparation is relatively complicated and time-consuming, which renders the method unsuitable in PoC settings. In this thesis, a pH system is developed to detect β-lactamases using the Carba NP method with a metal-metal oxide pH sensor.

3.4 Other rapid AMR diagnosis methods

In addition to the rapid AMR diagnosis methods described above, there are many other rapid AMR diagnosis devices. This section summarizes genotypic AMR diagnosis methods, electrochemical diagnosis methods and other rapid AMR diagnosis platforms.

3.4.1 Genotypic diagnosis

Genotypic AMR diagnosis methods are rapid and sensitive, but the presence of resistance genes may not always coincide with phenotypic resistance test results due to the varied resistance mechanisms [132] and continuous evolution of antibiotic-resistant bacteria [124]. The general process of the genotypic method involves three steps. First, bacteria are lysed and the DNA is extracted. Second, unique DNA sequences are amplified to obtain sufficient copies. Third, the amplified DNA sequences are analysed. Recently, novel LoC DNA amplification methods, such as on-chip polymerase chain reaction (PCR) [133], on-chip recombinase polymerase amplification (RPA) [134] and on-chip loop-mediated isothermal amplification (LAMP) [11] have been developed. Those methods simplify bench-top operations and demonstrate the potential for use in PoC settings. Moreover, DNA analysis methods other than conventional slab gel electrophoresis or capillary electrophoresis have recently been developed. Absorbance signals[11], fluorescence signals [133-135], pH change [136] and electrochemical signals [65] can be used to determine DNA amplification production.

Mach *et al.* (2011) used electrochemical biosensors to detect the concentrations of specific amplified RNA [65]. 16S rRNA from test bacteria strains were first amplified, and the amount of amplified 16S rRNA was detected using an electrochemical method. The chip could identify bacterial species or initial bacterial concentrations in the testing strain in 3.5 hours with 95% accuracy. Wang *et al.* (2011) designed an optical-based LoC system to rapidly distinguish MRSA and MSSA [11]. Test samples were lysed and the extracted DNA was amplified by LAMP. The amplified DNA was bound to tiny beads whose concentration was proportional to the absorbance at 260 nm. This method could diagnose MRSA with 1000-fold better sensitivity than conventional PCR. Toumazou *et al.* (2013) developed a pH sensor for monitoring DNA amplification that was based on the fact that the nucleotide incorporation could reduce the pH of the DNA-containing solution [136]. The pH change during PCR or LAMP was monitored using an ion-sensitive field effect transistor (ISFET) sensor. This method could diagnose antimicrobial susceptibility in saliva samples in 30 minutes. Cheng *et al.* (2013) designed a fluorescence-based LoC system to rapidly diagnose AMR [133]. The DNA of test strains were amplified by on-chip PCR and then pumped to an on-chip ligase detection reaction (LDR) chamber, where specific DNA might generate fluorescence signals during ligation. The system could distinguish MRSA and MSSA in <40 minutes. Kang *et al.* (2014) used a droplet microfluidic system to diagnose AMR via a single bacterium in unprocessed blood samples [135]. The single bacterium was lysed in a droplet and a DNAzyme was used to generate a fluorescence signal when it bound with the target DNA. The DNA is negatively charged due to the phosphate ions in its structure. Therefore, DNA-labelled beads may have different electrical parameters from the pristine beads and can be distinguished by the DEP force.

Nakano *et al.* (2014) used beads to detect the DNA amount after amplification [137]. The DNA released from test samples were amplified by PCR and then mixed with beads. In a DEP impedance measurement (DEPIM) system, pristine microbeads were trapped by negative DEP (nDEP) force, while the DNA-labelled microbeads were trapped by pDEP force. Impedance detection was used to detect the DNA-labelled beads and diagnose the presence of AMR-related genes. Kalsi *et al.* (2015) used an active matrix electrowetting-on-dielectric (AM-EWOD) device to detect the presence of β-lactamase–related genes [134]. The target DNA was amplified with RPA and the amount of amplified DNA was indicated by fluorescence intensity. Lysed test bacterial strains, RPA reagents and fluorescent probes were capsuled in tiny droplets and manipulated by the AM-EWOD method. The fluorescent probe emitted fluorescence when bound with certain DNA. The system could detect single copies of CTX-M-15, NDM-1 and KPC in 15 minutes.

3.4.2 DEP method

The dielectric properties of non-viable bacteria are often different from that of live bacteria because they have no intact membranes, so their internal conductivity decreases in a low-conductivity medium. Chung *et al.* (2011) and Su et al. (2017) designed a quadrupole-electrode DEP system for diagnosing antibiotic susceptibility [138, 139]. Bacteria were first mixed with antibiotics, and then incubated at 37°C for 1 hour. Then, the antibiotic-treated bacteria were pipetted into the quadrupole-electrode DEP system. The positions of the bacteria indicated the antibiotic susceptibility because the viable bacterium suffered negative-DEP (nDEP) force but non-viable bacterium suffered positive-DEP (pDEP) force. Figure 3-18 shows a schematic diagram of the quadrupole-electrode array for rapid AMR diagnosis.

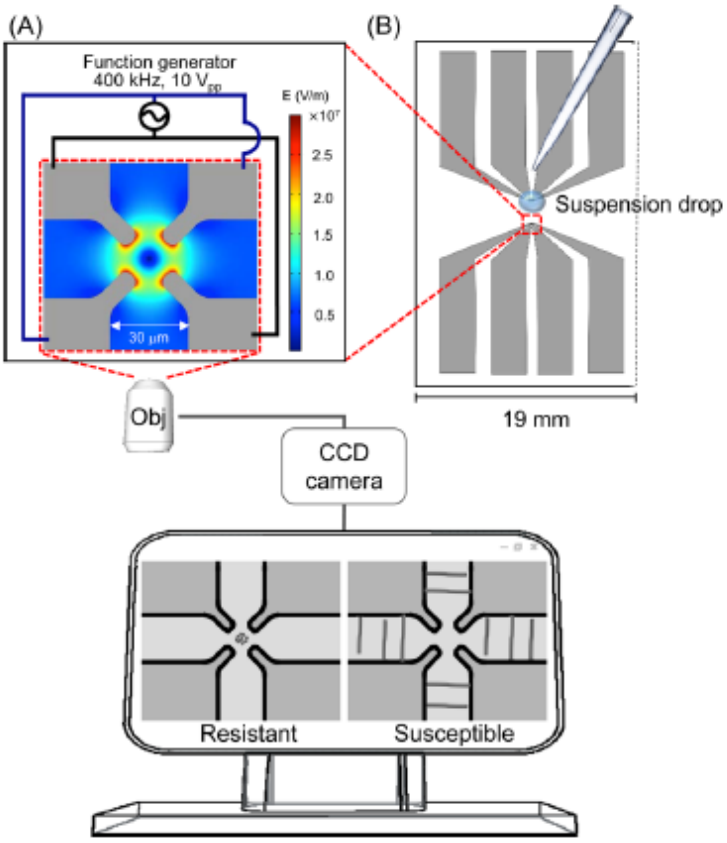

Figure 3-18: A schematic graph of a quadruple-electrode array for rapid diagnosis of antibiotic susceptibility from Chung *et al.* (2011) [138]. Resistant bacteria were concentrated at the centre of the electrode array while susceptible bacteria were concentrated at the gaps between the electrodes.

3.4.3 Electrochemical methods

Resazurin has a specific electrochemical signal in the voltammetry spectrum, which may change once metabolically active bacteria hydrolyse resazurin to resorufin. Therefore, an electrochemical method with a resazurin indicator can be used to detect antibiotic susceptibility. Besant *et al.* (2015) used a stationary droplet microfluidic electrochemical chip to detect the antibiotic susceptibility of *E. coli* and *K. pneumonia* [140]. The test bacteria and resazurin indicator were mixed with antibiotics in the detective chamber and incubated at 37°C for 1 hour. Then, the electrochemical detection was performed. This system could be used to detect the antibiotic susceptibility of *E. coli* and *K. pneumoniae* for ampicillin and ciprofloxacin in 1 hour with a sensitivity of 10^3 CFU/mL.

3.5 Commercial Devices

Nowadays, many rapid AMR diagnosis devices have been applied in clinical laboratories, which are summarized in this section. Table 3-1 shows the steps of AMR diagnosis by novel clinical diagnostic devices [141].

Table 3-1: The steps of AMR diagnosis by novel clinical diagnostic devices [141].

Steps	Operations
1	Confirmation and identification of infection
2	Introduction of pathogens into assay
3	Exposure to antibiotics
4	Susceptibility monitored over time
5	Data processing for MIC determination

Bacteria species identification can cut down the number of possible effective antibiotics for AST [142]. Many clinical laboratories used Matrix Assisted Laser Desorption Ionization Time of Flight (MALDI-TOF) mass spectroscopy (MS) for pathogenic species identification [142]. Different species of bacteria can synthesize unique proteins during their metabolism. Those proteins have specific peaks in the MALDI-TOF MS. This method is rapid, sensitive and economic. Commercial MALDI-TOF MS manufactures include Bruker [143], bioMérieux [144] and Simadzu [145]. PCR technology is also widely used for pathogenic identification. The common method is to detect the unique 16s RNA in bacteria to identify the pathogenic species [146].

Many rapid AST methods are used for MIC detection in clinical laboratories. Etest (bioMérieux) is a commonly used manual diagnostic device [147]. It is based on a disk with a gradient in antibiotic concentrations that can provide the MIC value. The Etest requires 16–20 hours to yield AST results. Figure 3-19 shows a photo of an Etest plate.

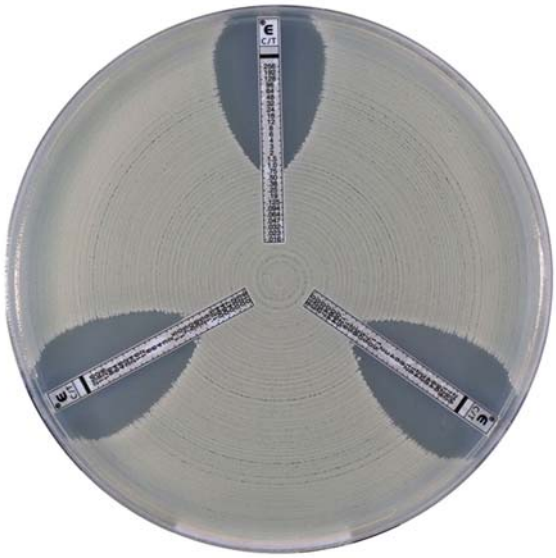

Figure 3-19: A photo of an Etest plate. MIC values are determined by the minimum antibiotic concentration where the bacterial growth is not separated from the antibiotic disk.

Automatic devices for rapid MIC detection are widely used in hospitals. In United States, the Food and Drug Administration (FDA) has cleared 5 automatic AST systems for clinical use [141]. They are Accelarate Pheno (Accelarate Diagnostics) [148], Vitek 2 System (bioMérieux) [149], MicroScan WalkAway system (Siemens Healthcare Disgnostics) [150], BD Phoenix Automated Microbiology System (BD Diagnostics) [151] and Sensititre ARIS 2X (Trek Diagnostic systems) [152].

Accelarate Pheno (Accelarate Diagnostics) integrates multiple phenotypic diagnostic methods to rapidly identify bacterial species in a sample and to measure the MIC [148]. Cells are electro-kinetically concentrated on a glass substrate and fluorescent *in situ* hybridization (FISH) technology is used to identify the pathogenic species. After species identification, the concentrated cells are analysed by automated dark field microscopy for changes in morphology over time. Machine learning and computer algorithms are used for data analysis. Blood samples can be used directly and the device can identify species in 1 hour and yield an MIC in 7 hours. This device is the first fully automated solution approved by the FDA for quantitative AST directly on patient samples. However, in 2018, it was recalled due to the high number of false detection in *S. aureus* [153]. The VITEK 2 system (bioMérieux) uses a microfluidic turbidimetric detection system to detect bacterial growth [149]. Dilutions of antibiotics and bacteria are mixed in a credit card–sized plastic reagent card. The instrument can accommodate 30–240 tests simultaneously. The antibiotic susceptibility of >100 organisms can be detected within 8 hours. The MicroScan WalkAway system (Siemens Healthcare Diagnostics) uses a photometer and a fluorimeter to detect bacterial growth in 40–96 standard-size well plates simultaneously [150]. The well plates need to be prepared manually and then placed in one of the incubation slots in the instrument. The antibiotic susceptibility of GN strains containing fluorogenic substrates can be detected in 3.5–7 hours. Turbidimetric-based detection can determine the antibiotic susceptibility of GP and GN strains in 4.5–18 hours. BD Phoenix Automated Microbiology System (BD Diagnostics) uses an oxidation-reduction indicator to

determine the bacterial growth in an antibiotic environment [151]. Antibiotic dilutions are placed in an 84-well plate and mixed with test bacteria and the oxidation-reduction indicator. The absorbance of each well is monitored in 20-minute intervals. The system can detect antibiotic susceptibility from 99 test strains and the MIC results can be detected in 6–16 hours. The Sensititre ARIS 2X (Trek Diagnostic Systems) can prepare antibiotic dilutions in a 96-well plate automatically [152]. Bacterial growth is determined by measurement of fluorescence. The antibiotic susceptibility of the 64 testing strains can be detected after 18–24-hour incubation.

Besides the FDA approved automated clinical devices, many other commercial machines are available in market to rapid detect ARM. For example, oCelloScope (SioSENSE solution) [154] and QMAC-dRAST (QuantaMatrix) [155].

oCelloScope (SioSENSE solution) is based on real-time microscopy for rapid AST [154]. This system combines phase contrast, bright-field and confocal-like microscopy. By change the plane of focus, bacterial morphological data are extracted from images acquired over time. It is a rapid, sensitive and real-time microscopy, which can provide MIC in 6 hours. QMAC-dRAST (QuantaMatrix) uses a similar real-time microscopy technology but the test bacteria grow in agar [155]. An agarose matrix is incorporated into each well on a 96-well plate. Blood samples can be directly injected into the agarose matrix for test. Automated optical microscope imaging allows for analysis of the microcolony area over time. This system needs 6 hours from "sample in" to "results out".

Some general-purpose scientific equipment can also be used for rapid AST. For example, Attune Acoustic Focusing Cytometer (Thermalfisher) [156] and Forward Laser Light Scatter System (BacterioScan) [157].

Attune Acoustic Focusing Cytometer (Thermal Science) uses live/non-viable staining of a drug-treated bacterial panel for rapid antimicrobial resistance diagnose [156]. Usually, two fluorescent dyes (DMAO and EtD-III) are mixed with bacteria and antibiotics. DMAO is a green-fluorescent nucleic acid dye that stains both live and dead bacteria with intact and damaged cell membranes; EtD-III is a red-fluorescent nucleic acid dye that only stains dead bacteria with damaged cell membranes. With an appropriate mixture of DMAO and EtD-III, bacteria with intact cell membranes stain fluorescent green, whereas bacteria with damaged cell membranes stain fluorescent red [158]. This method can provide the antibiotic susceptibility for certain antibiotics (for example, carbapenems) in 2 hours. Forward Laser Light Scatter System (FLLS, BacterioScan) is also reported for rapid AST in many clinical laboratories [157]. This system is able to detect the information such as cell shape, size and density in a bacterial suspension. Compared with conventional OD based measurement, the sensitivity of using FLLS system for AST is improved [159]. The MIC can be detected within 6 hours by FLLS technology.

3.6 Discussion and conclusion

This section summarises the performance of rapid AMR diagnosis methods and the related commercial devices. Compared with conventional broth dilution and disk diffusion methods,

most of novel AMR diagnosis methods can determine antibiotic susceptibility from low-concentration bacterial samples in several hours. Table 3-2 shows the minimum bacterial concentration required, detection time, and advantages and disadvantages of each novel AMR diagnosis method.

Table 3-2: The minimum bacterial concentration required, detection time, and advantages and disadvantages of the novel AMR diagnosis methods.

Detection principle	Minimum bacterial concentration (CFU/mL)	Detection time (hour)	Advantages	Disadvantages
Impedance methods				
Medium resistance (Metabolism)	10^6 to 10^7	1 to 5	Simple device and easy operation	Influenced by bacterial metabolism mechanisms
Medium capacitance	1 to 10^4	1 to 4	Real-time bacteria concentration detection	Complex impedance analysis
Charge transfer resistance	1 to 10^3	<1	High sensitivity	Chips are expensive and hard to be reused
Double layer capacitance	10^5	>10	Simple device and easy operation	Long detection time
Medium resistance (Ion release)	10^9	1	Simple device	Low sensitivity
Optical methods				
Morphological patterns	10^5	4	Single cell observation	Complex optical device
Bacterial length	10^5	<1	High sensitivity	Lack clinical tests

Fluorescence	1 to 10^5	1 to 6	Bacterial viability detection	Complex fluorescence observation
pH methods				
Metabolism	10^5 to 10^7	1 to 12	Simple operation	Influenced by bacterial metabolism mechanisms
β-lactam ring hydrolysis	$>10^9$	<1	High sensitivity	Only suitable for β-lactam resistance
Other methods				
Genotypic Methods	1	<1 to 4	High sensitivity	Not always coincide with phenotypic resistance test
DEP Method	10^5	2	Bacterial electrical property observation	Complex DEP and optical device
Electro-chemical Method	10^3	1	High sensitivity, simple device	Influenced by bacterial metabolism mechanisms

Those novel methods demonstrate the potential for rapidly diagnosing AMR in PoC settings, and are sensitive, labour-saving and low-cost. However, they still face challenges such as low reliability, low accuracy and long sample preparation time [17], and rely on future research to improve their performance and replace conventional AST methods in clinical settings.

Chapter 4: Reviews of microfluidic platforms

This chapter introduces the literature on the dielectric properties of bacteria suspension, bio-particle manipulation by DEP, novel sensitive absorbance chips and pH sensors. The DEP force is used to separate or enrich bacteria. Sensitive absorbance chips are used to improve sensitivity and reduce the cost of absorbance detection. Novel pH sensors are robust and miniaturized, and can be used for detecting β-lactamases in the PoC setting.

4.1 Dielectric dispersion

Dispersion is a measure of polarization loss when frequency increases, which occurs typically over 2 decades in frequency [160]. Two important dispersions are observed in a dielectric spectrum of a bio-particle suspension, namely α- and β-dispersion. In general, α-dispersion is of a lower frequency than β-dispersion. The α-dispersion is caused by the relaxation of counterions; β-dispersion is caused by particle interfacial polarization. Interfacial polarisation is important in bacterial concentration detection, bacterial viability detection and bacteria manipulation by DEP, so the literature on β-dispersion will be introduced first, followed by the literature on α-dispersion.

4.1.1 Interfacial polarization (β-dispersion)

In 1873, Maxwell published the famous 'a treatise on electricity and magnetism', modelling the dielectric property of a diluted suspension of spherical particles in a medium. He showed that the particle suspension could be modelled with a uniform material that had a different dielectric property. He derived an expression for the permittivity and conductivity of suspension of spheres, termed the Maxwell mixture theory (MMT) [161]. In 1914, Wagner introduced complex conductivities into the MMT and simplified Maxwell's mixing equation [162]. Therefore, interfacial polarization is also termed Maxwell-Wagner polarization.

Between 1910 and 1913, Hober measured the impedance of red blood cell suspensions [163]. He found that the suspensions had lower conductivity at low frequency than at high frequency, but had higher permittivity at low frequency than at high frequency. These were the first reports of β-dispersion in bio-particles. Moreover, he concluded that a red blood cell could be modelled as a conducting cytoplasm surrounded by a thin insulating membrane. Fricke (1925) found that the membrane capacitance of a red cell was 0.8 μF/cm^2 [164]. The red cell membrane acted as a good dielectric because the capacitance was independent of frequency from 3.6 kHz to 4.5 MHz. He also determined that the membrane thickness of a red cell was 3.3 nm when the relative permittivity of membrane was set as 3. Subsequently, Fricke *et al.* (1956) reported that the thickness of the *E. coli* membrane was the same as that of a red cell (3 nm), and estimated the membrane capacitance as 0.7 μF/cm^2 [165]. Cole (1932) reviewed several papers on impedance measurements in bio-particle suspensions and found that the resistance and capacitance of a cell membrane commonly varied with frequency [166]. He found that the phase angle of a bio-particle suspension remained relatively constant despite frequency change.

He improved the electrical model of Hober and Fricke by replacing a capacitance with a constant-phase angle component to represent the electrical properties of the cell membrane. Furthermore, he placed reactance and resistance (Ω) in Cartesian coordinate plots to present the data of Fricke (1925) and Lullies (1930) on impedance detection in bio-particle suspensions, and verified that the constant-phase element model was accurate for demonstrating the impedance spectrum of a cell solution. This plot was developed into the well-known Cole–Cole plot (1941), where the real part (ε') and imaginary part (ε'') of the complex permittivity was plotted in a Cartesian coordinate system to describe the dielectric relaxations [167]. From 1965 to 1973, Carstensen *et al.* published a series of important papers on bacterial impedance detection [168-172]. They found that when using the conventional single-shell model to simulate the impedance magnitude of a bacterial suspension, there was a 20% difference between experiment and simulation. To correct the errors, they proposed a 2-shell sphere model, in which a bacterium had a conductive cell wall outside the plasma membrane. The outer shell was termed the cell wall, which acted as an ion exchanger. The conductivity of the cell wall remained constant in low–ion concentration solutions but might increase rapidly if the medium ion concentrations exceed that of the cell wall. Asami *et al.* (1980) extended the spherical model to an ellipsoid model, which was more accurate for describing the rod shape of the *E. coli* bacterium [173]. The bacterial model was developed into a 3-shell ellipsoid model, which had an outer membrane, a periplasmic shell and an inner membrane outside the cytoplasm [114]. The 3-shell ellipsoid model is used in this thesis to simulate the bacterium electrical properties in different conditions.

4.1.2 Relaxation of attracted counter-ions (α-dispersion)

When bio-particles are immersed in ionic salt solutions, the surface charges on the particle attracts ions to form an electrical double layer. The conductivity of bio-particle suspensions in low frequency ranges is therefore higher than expected [174], and a dispersion with a lower frequency than β-dispersion is detected [175], termed the α-dispersion.

O'Konski (1960) explained the cause of the α-dispersion by surface conductance [176]. He explained that negative charges exist on the cell membrane, so counterions are attracted and the charge transport causes a charge flux. Schwarz (1962) then demonstrated that the counterions on the cell surface are strongly bound by electrostatic attraction, and are difficult to move in a radial direction but easy to move in a tangential direction, so that a counterion atmosphere forms over the cell [177]. If an external electric field is applied, the ions will move around the sphere and polarise. The polarisation of the counterion layer has a longer relaxation time compared with interfacial polarisation. Therefore, the dispersion frequency is lower than that of interfacial polarisation. However, this explanation is inadequate because it does not include the diffusion effects of the double layer. Einolf and Carstensen (1969) detected the α-dispersion from *Micrococcus lysodeikticus* suspension below 10 kHz [171]. In 1973, they improved Schwarz's model to count for counterion movement both inside and outside the bacterial wall because the bacterial wall behaves like a porous structure for ions [172]. Dukhin and Shilov (1974) proposed a theory termed the Dukhin-Shilov model [178]. Ions on the cell surface attract counterions, which form a bound layer and a diffusion layer in solution. They developed mathematical expressions for calculating the double layer capacitance around bio-

particles and introduced the Dukhin number, the ratio of the surface conductance to that of the bulk solution. Grosse and Zimmercan (2005) used the Dukhin-Shilov model to calculate the impedance spectrum of lipid vesicle suspensions [179]. They provided an analytical solution suitable for simulating the complete dielectric spectrum including both α- and β-dispersion based on a model of a single-shell sphere covered by a charged surface.

Farrow *et al.* (2012) measured the impedance spectrum of *S. aureus* solutions in 16 hours and found that the counterion diffusion effect and capacitive charging at the cell wall might cause phase shift at low frequencies [180]. Asami (2014) measured the dielectric spectrum of a live *E. coli* suspension and a heat-killed *E. coli* suspension, respectively [181]. He showed that α-dispersion did not change once the bacteria had been killed by heating. The α-dispersion is not commonly used in bacterial concentration detection because the α-dispersion is influenced by the electrode double layer [181]. Rapid AMR diagnosis by observation of α-dispersion has not been explored.

4.2 Bio-particle manipulation by DEP

Many groups have developed DEP-based technologies for enriching and separating bacteria. Markx *et al.* (1994) used four-terminal polynomial electrodes or castellated electrodes to generate a non-uniform electric field to separate bio-particles [182]. Figure 4-1 (a) shows a photo of bio-particle separation in polynomial electrodes and Figure 4-1 (b) shows a photo of bio-particle separation in castellated electrodes.

(a)

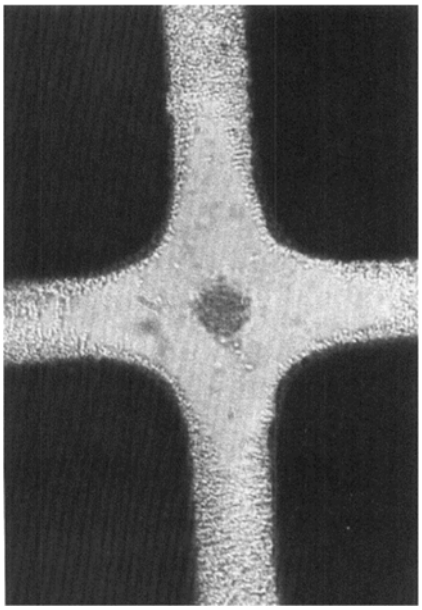

(b)

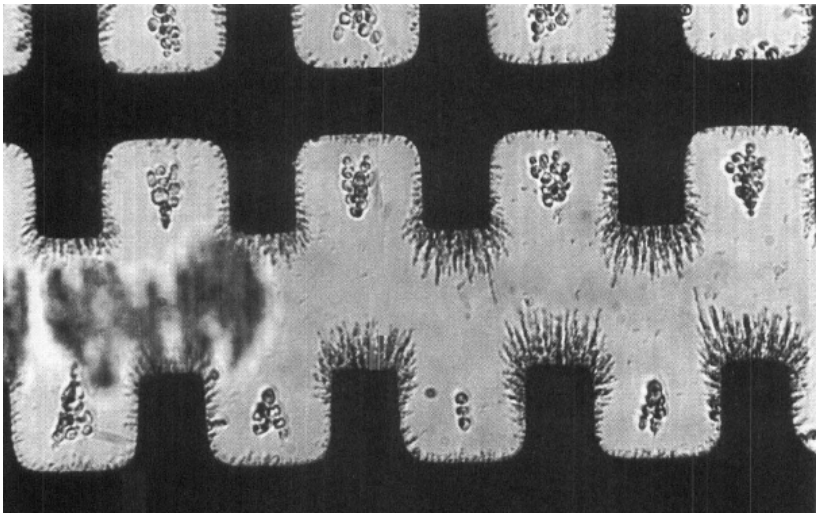

Figure 4-1: Photos of bio-particles DEP separation by (a) a polynomial electrode system and (b) a castellated electrode system (Markx *et al.*, 1994). In a polynomial electrode system, *E. coli* (experiencing nDEP) are concentrated in the middle and *M. lysodeikticus* (experiencing pDEP) are concentrated at the edge of the electrodes. In a castellated electrodes system, *M. lysodeikticus* (experiencing pDEP) are concentrated at the edge of the electrodes and yeast (experiencing nDEP) are concentrated at the gap between each castellated electrode.

Markx *et al.* (1996) used DEP to separate different bacterial species according to a conductivity gradient [183]. First, all bacteria were trapped by pDEP force at the edge of the electrodes in low-conductivity medium. Then, the conductivity of the medium was increased gradually and particles with different dielectric properties were released from the electrodes at different times. Based on this principle, *Bacillus subtilis*, *E. coli* and *M. luteus* were successfully separated. Brown *et al.* (1999) used DEP to trap bacteria and then used a camera to monitor the number of trapped cells [184]. They demonstrated that the captured bacterial concentrations in the camera field was proportional to the initial bacterial concentrations go through the DEP electrodes.

Elitas *et al.* (2014) used 3D carbon electrode arrays to generate a non-uniform electric field to separate live and dead bacteria [185]. *Mycobacterium smegmatis* cells were treated with drugs for 24 hours, which killed 90% of the bacteria. The drug-treated bacteria were pumped in to the non-uniform electric field and live bacteria were trapped by pDEP force, while the dead bacteria were flowed away. This method could purify the living bacteria with 99% maximum recovery ability at the bacterial concentration of 3×10^4 CFU/mL. A DEPIM system is a combination of a DEP system and impedance spectroscopy for impedance detection. A DEP force can enrich bacteria and the impedance of the channel is measured. Suehiro *et al.* (1999) designed a DEPIM system that consists of two pairs of interdigitated electrodes in a channel [186]. The system detected *E. coli* at 10^5 CFU/mL in 10 minutes. Figure 4-2 (a) shows the schematic diagram of the device and Figure 4-2 (b) shows the detected conductance against time.

(a)

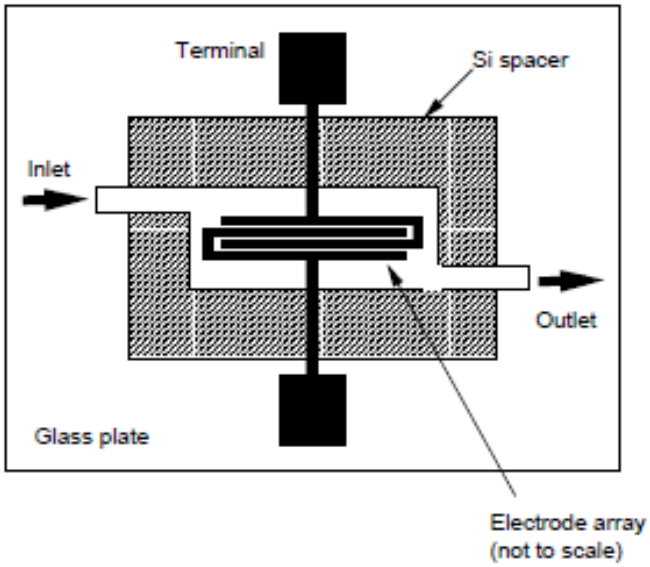

(b)

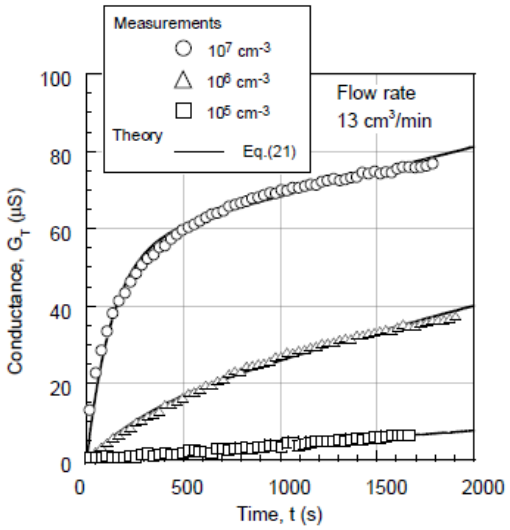

Figure 4-2: (a) The schematic diagram of the DEPIM device by Suehiro *et al.* (1999) and (b) the results of conductance against time for different concentrations of *E. coli*. Parallel *E. coli* pearl chains connected in the channel, which led to increased channel conductance and capacitance.

In 2003, Suehiro *et al.* replaced the interdigitated electrodes with castellated electrodes to enhance the electric field strength between pairs of electrodes [187]. They heat-treated an *E. coli* suspension, and then pumped the dead and live *E. coli* into the improved DEPIM system. The system could detect the viability of *E. coli* at 10^7 CFU/mL. In another paper they added *E. coli*–specific antibodies and mixed species bacterial suspensions into the detection chamber [188]. *E. coli* were bound by the antibody and formed pearl chains in the channel, while the other bacterial species were washed out. The method could specifically detect *E. coli* concentrations in a mixed bacteria sample. In 2005, Suehiro *et al.* incorporated DEPIM detection with electropermeabilization (EP) technology and created an EP-assisted DEPIM (EPA-DEPIM) system [189]. The system could detect *E. coli* at 10^2 CFU/mL in 3 hours. Hamada and Suehiro (2011) miniaturized the DEPIM devices and achieved *E. coli* detection in a PoC setting. The system could detect oral bacteria at 10^5 CFU/mL in 10 minutes [190]. Hamada *et al.* (2011) added pairs of interdigitated electrodes to improve the performance of the EPA-DEPIM system [191]. The extra interdigitated electrodes were used to generate a non-uniform electric field to push the bacteria to the surface of the system by nDEP force. Figure 4-3 (a) shows the electric field strength generated by the interdigitated electrodes and Figure 4-3 (b) shows a schematic diagraph of the DEP-enhanced EPA-DEPIM system. Their results demonstrate that the DEP-enhanced system had improved sensitivity compared with the original EPA-DEPIM system.

(a)

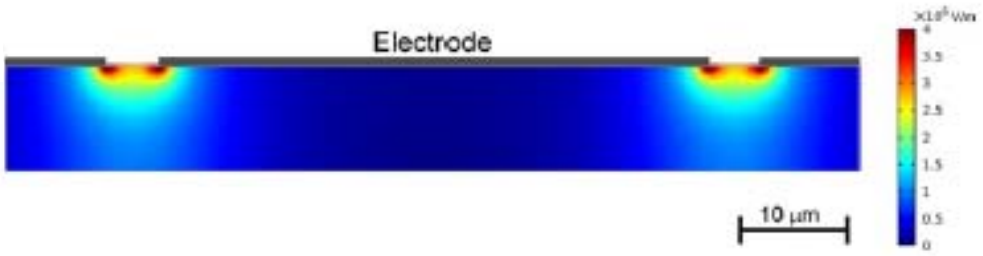

(b)

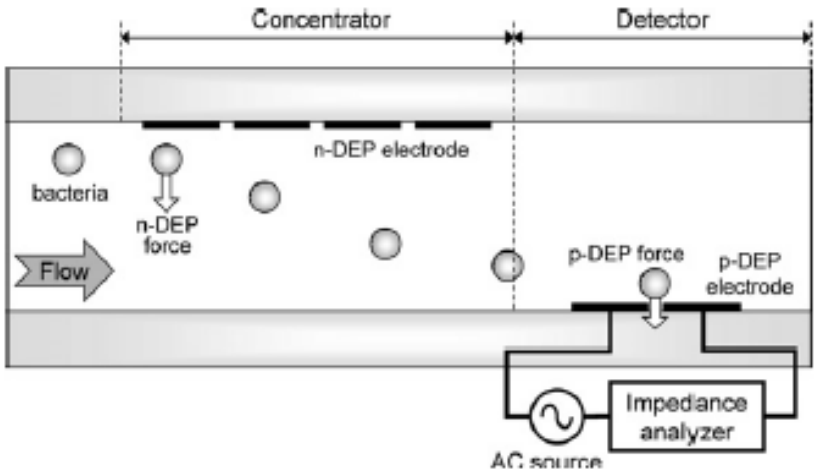

Figure 4-3: (a) The electric field strength of the nDEP assistance electrodes and (b) a schematic diagraph of the DEP-enhanced EPA-DEPIM system for *E. coli* concentration detection (Hamada *et al.*, 2011). In the experiment, the bacteria were pre-enriched at the bottom of the channel before EPA-DEPIM detection.

Sabounchi *et al.* (2008) used insulator-based DEP (iDEP) to separate particles and then detected the impedance of the concentrated suspension to detect particle concentrations of $>10^4$ particles/mL [192]. Rather than the commonly used AC signal, the authors used DC voltage to generate a non-uniform electric field in their system. Kim *et al.* (2015) designed a DEPIM platform to detect bacteria in DI water [193]. The device could detect bacteria at 300 CFU/mL. Figure 4-4 shows a schematic diagram of the device, a photo of the DEP enrichment electrodes and a photo of the impedance detection electrodes.

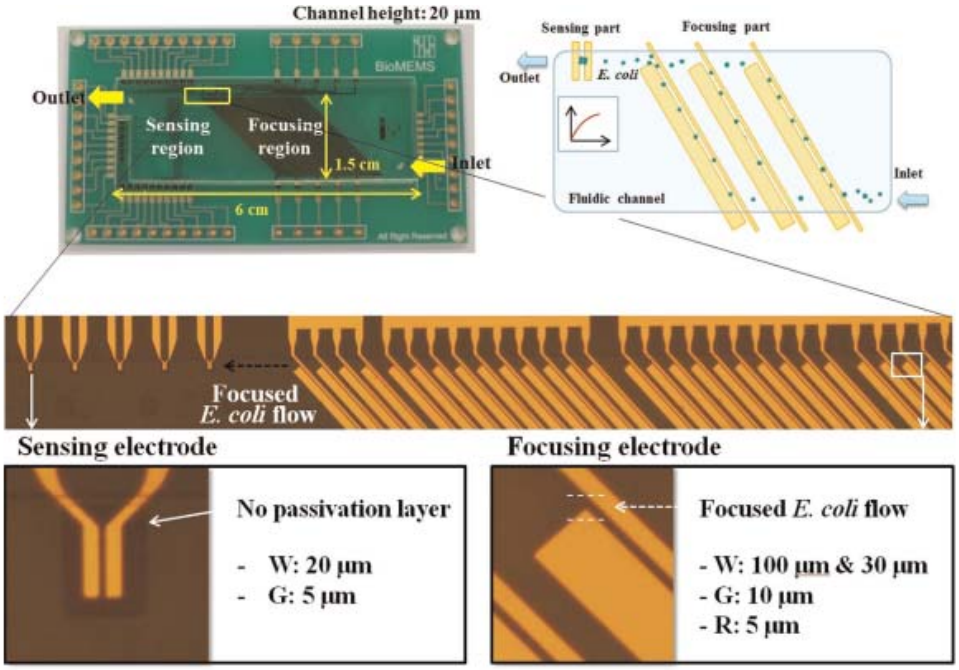

Figure 4-4: A schematic diagram of the device (top), a photo of the DEP enrichment electrodes (middle) and a photo of the impedance detection electrodes (bottom) (Kim *et al.*, 2015). Asymmetric interdigitated electrodes were used to enrich bacteria, and the concentrated bacteria were flowed to impedance-sensing electrodes for impedance detection.

Páez-Avilés *et al.* (2016) designed a four-terminal DEPIM system to detect bacteria in DI water [194]. Interdigitated electrodes were used to generate a non-uniform electric field. First, bacterial suspensions were pumped in to the chamber and the bacteria were trapped at the edge of the electrodes. Then, the impedance of the trapped bacteria was detected by a four-terminal impedance system. The DEP enrichment step increased the bacterial concentrations by 20 fold, and impedance detection sensitivity was improved significantly. The DEP enrichment chip used in this thesis is an improvement on this design.

4.3 Sensitive absorbance chips

Colorimetric detection is widely used in microbiology assays, generally performed in 96- or 384-well plates, with absorbance or fluorescence detected by a plate reader. The typical path length of the standard well plates are 3 to 4 mm. According to the Beer-Lambert law (see Chapter 5), the sensitivity of colorimetric detection is proportional to the path length of the solution. The short path length of commercial well plates limits the sensitivity of many colorimetric assays. Therefore, a long path length design improves the detection sensitivity. In the last two decades, the development of microfluidic technology has greatly reduced the manufacturing price of sensitive optical chips. Therefore, low-cost sensitive absorbance chips have been widely reported.

Jiang and Pau (2007) reported a compact optical sensor with spiral geometry optical guide for detecting absorbance [195]. The path length of the device was 110 mm, 24.4 times longer than that of commercial 96-well plates. However, its fabrication required photolithography technology, and the cost of the absorbance detection chip was high. Sieben *et al.* (2010) demonstrated a tinted plastic-based absorbance chip with a 25-mm path length was able to detect the absorbance with high sensitivity [20]. Floquet *et al.* (2011) used PMMA boards with different colours to fabricate the optical chip developed by Sieben *et al.* and found the grey PMMA chip demonstrated the highest LoD [21]. Figure 4-5 shows the cross-view of the optical detection cell.

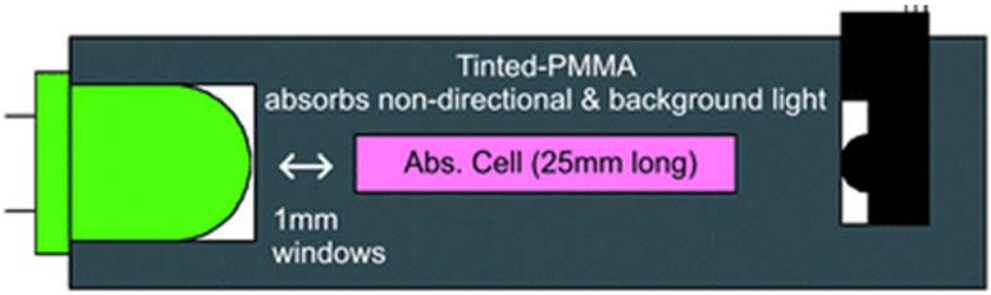

Figure 4-5: The cross-view of the optical detection cell by Sieben *et al.* (2010). A light-emitting diode (LED, green) and a photodiode (black) are glued on either side of a 25-mm path length channel. The LoD could reach 4.1 mA.U.

Sansalvador *et al.* (2016) developed a high-sensitivity optical chip for detecting pH [23]. The sensor had several channels and could perform multi-channel detection simultaneously. Figure 4-6 shows a picture of the microfluidic absorption cell. Feng *et al.* (2016) developed an automated absorbance detection device in a cell phone, which replaced the bench-top plate reader [196]. Pictures of a 96-well plate were recorded and the solution absorbance was detected by pixels on the image.

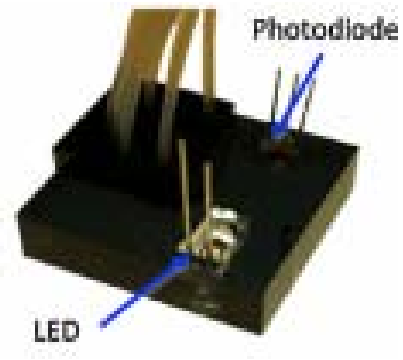

Figure 4-6: A photo of the device by Sansalvador *et al.* (2016). An LED and a photodiode are glued to either side of a 1-cm path length channel. The absorbance of the medium is determined by the voltage output of the photodiode.

In conclusion, the development of a low-cost microfluidic optical chip deliver high-sensitivity, low-cost absorbance detection in the PoC setting. The optical chip described in thesis is improved from Sieben *et al.* (2010) with modifications. A decoupling channel is used for improving the signal-to-noise ratio, and the LED at 470 nm is used for hydrolysed nitrocefin detection.

4.4 pH detection

pH is a measure of the proton concentration, calculated as log10 of the reciprocal of the hydrogen ion activity (see Chapter 5). pH can be detected by various methods such as glass pH meters, pH indicators [27], ISFET sensors [197] and metal–metal oxide pH sensors [36]. Here, conventional pH detection by pH indicator and glass pH meter is reviewed. Then, the applications of ISFET are listed. Lastly, the literature on metal–metal oxide pH sensors is summarized.

4.4.1 Conventional pH detection

A pH indicator is a chemical component whose colours changes with pH of the surrounding environment [25]. Some pH indicators are concentrated on a paper substrate, forming a pH test paper. A glass pH probe consists of an ion-selective electrode and a reference electrode. The ion-selective electrode is made of a doped glass membrane that is sensitive to hydrogen ions [198]. Figure 4-7 shows a cross-view of a typical glass pH probe. The results from a glass pH meter are accurate and stable, but the device is complicated, fragile and hard to miniaturize.

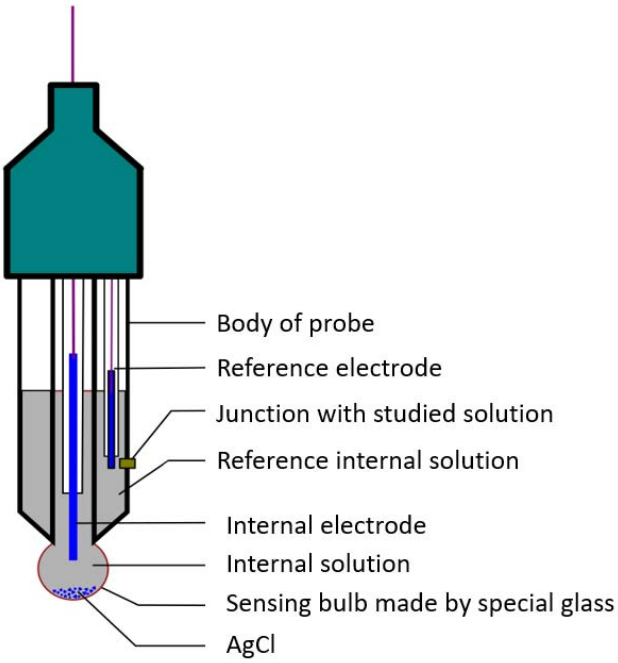

Figure 4-7: A schematic diagram of a glass pH probe, where a bulb made from specific glass forms the sensing part of the probe [198]. The reference electrode is embedded in the probe body and the OCP between the internal and reference electrodes is proportional to the pH of the test solution.

4.4.2 ISFET pH detection

ISFET is a miniaturized device for converting a pH value to an electronic signal and has been used in many biomedical fields such as DNA sensing [199], protein sensing [200] and enzyme detection [201]. Figure 4-8 shows a cross-view of a typical ISFET sensor. An ISFET consists of a gate, source and drain, with gate oxide such as Si_3N_4, Al_2O_3 and Ta_2O_5. ISFETs are easy to miniaturize, but suffer from drift [197]. Moreover, ISFET fabrication is complicated and they are difficult to integrate with reference electrodes [202].

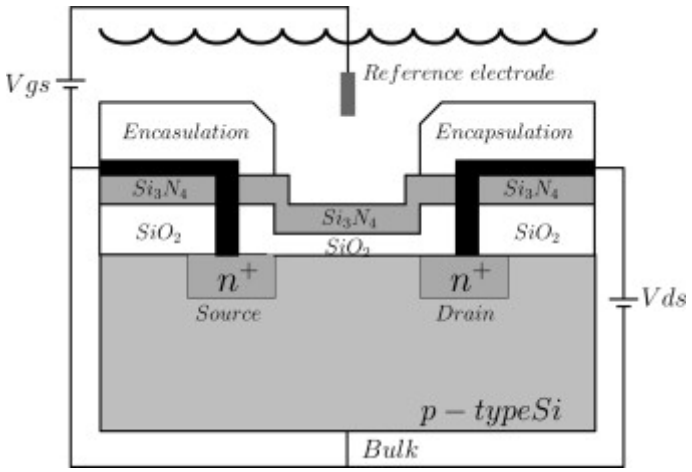

Figure 4-8: The cross-section of a typical ISFET sensor [floating gate (Si_3N_4), source, drain] [203]. The pH value of the aqueous solution affects the formation of metal-OH groups on the gate and changes the gate potential, which alternates the current through the transistor accordingly.

4.4.3 Metal-Metal Oxide pH detection

Various solid-state materials have been investigated for metal–metal oxide pH-sensing electrodes, including PtO_2, IrOx [204], RuO_2 [205, 206], OsO_2, Ta_2O_5 [207], RhO_2, TiO_2 [26] and SnO_2 [208]. When the metal–metal oxide electrode is immersed in an aqueous solution, insoluble hydroxide groups form on the metal surface and proton displacement occurs [36]. Protons on the electrode surface transfer in the solution and cause a surface potential change. The pH value of metal–metal oxide pH sensors can be determined by the OCP between the metal–metal oxide electrode and the reference electrode.

IrOx is a metal–metal oxide material with a wide pH response range, fast response time, high pH sensitivity and low potential drift [209]. The IrOx sensing film can be formed by techniques such as sol-gel dipping [210], thermal oxidation [211], sputtering [212] and electrochemical deposition [213]. Here, IrOx was fabricated using the sol-gel method and used to detect β-lactamases.

4.5 Discussion and conclusion

This chapter summarizes the literature on dielectric dispersions and on DEP chips, novel absorbance chips and pH detection sensors.

Interfacial polarization is the origin of the β-dispersion and results in a DEP force on a bio-particle in a non-uniform electric field. The DEP force is used in bacterial separation and enrichment. In this project, a DEP enrichment chip is developed based on the literature. The α-dispersion results from the relaxation of counterions, and can occurs in the low-frequency part of a dielectric spectrum.

Novel optical chips can achieve low-cost and high-sensitivity absorbance detection in the PoC setting. The path length of novel optical chips are between 10 mm and 25 mm. In this project, a novel 25-mm optical chip is developed based on the literature. pH indicators, glass pH probes, ISFETs and metal–metal oxide pH sensors can detect pH. A metal–metal oxide pH sensor is sensitive, requires no power supply and can be easily miniaturized. IrOx is a suitable material for fabricating such a sensor, which has high sensitivity, low drift voltage and fast response. In this project, an IrOx electrode is fabricated using the sol-gel method based on the literature.

Chapter 5: Theory

5.1 Interfacial polarisation and its applications

5.1.1 Complex permittivity

Consider two electrodes of area A, separated by distance d. If the material between the electrodes is a pure conductor, as shown in Figure 5-1 (a), the impedance between the electrodes is:

$$Z = R = \frac{d}{A} \times \frac{1}{\sigma} \tag{5.1}$$

If the material between the electrodes is an ideal dielectric material, as shown in Figure 5-1 (b), the capacitance between the electrodes is:

$$C = \frac{\varepsilon_0 \varepsilon_r A}{d} \tag{5.2}$$

and the impedance between two electrodes becomes

$$Z = \frac{1}{j\omega C} = \frac{d}{j\omega \varepsilon_0 \varepsilon_r A} \tag{5.3}$$

If the material between the parallel electrodes is a dielectric material that contains unbounded charge, as shown in Figure 5-1 (c), the complex impedance between two electrodes is

$$\mathrm{Z}^* = \frac{d}{A(\sigma + j\omega \varepsilon_0 \varepsilon_r)} \tag{5.4}$$

Sometimes it can be expressed as

$$\mathrm{Z}^* = \frac{d}{A(j\omega \varepsilon_0 \varepsilon^*)} \tag{5.5}$$

where ε^* is the complex relative permittivity [214]

$$\varepsilon^* = \varepsilon_r - j\frac{\sigma}{\varepsilon_0 \omega} \tag{5.6}$$

The complex relative permittivity is important in the calculations of interfacial polarisation.

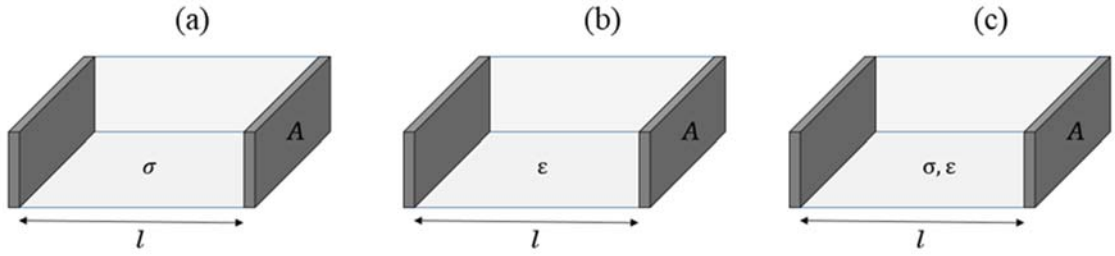

Figure 5-1: The schematic diagram of two parallel electrodes, each covers area A, separate with distance d with (a) pure conductor, (b) ideal dielectric material and (c) dielectric material contains unbounded charges in the middle.

5.1.2 Dielectric relaxation

If an electric field is applied across a dielectric material, the material will be polarised. The polarisation process takes a finite time. Likewise, if a material is polarised but the electric field is removed suddenly, the material will also need some time to reach a random situation. This time is called relaxation time, written as τ [215]. When the frequency of an AC electric field is low enough, the polarisation is maximum. If the frequency of the applied electric field increases, the polarisation may reduce because the material cannot be fully polarized [214]. The polarisation at sufficient high frequency is written as P_{hf}, and polarisation at sufficient low frequency is written as P_{lf}, given by

$$\boldsymbol{P_{hf}} = \varepsilon_0 \chi_{hf} \boldsymbol{E} \tag{5.7}$$

$$\boldsymbol{P_{lf}} = \varepsilon_0 \chi_{lf} \boldsymbol{E} \tag{5.8}$$

where χ_{hf} and χ_{lf} are the electric susceptibility at sufficient high frequency and sufficient low frequency of the material, ε_0 is the vacuum permittivity with a constant value 8.85×10^{-12} in the unit (F/m). $\boldsymbol{E}$ is the electric field.

The frequency dependent polarisation of the material can be written as [214]

$$\boldsymbol{P} = \varepsilon_0 (\chi_{hf} + \frac{\chi_{lf}}{1+\omega\tau}) \boldsymbol{E} \tag{5.9}$$

If χ_{hf} and χ_{lf} are related to permittivity ε_{hf} and ε_{lf} as

$$\varepsilon_{hf} = \chi_{hf} + 1 \tag{5.10}$$

$$\varepsilon_{lf} = \chi_{lf} + 1 \tag{5.11}$$

where ε_{lf} is the relative permittivity measured in a low frequency electric field and ε_{hf} is the relative permittivity at sufficient high frequency electric field, the complex permittivity of the material can be written as

$$\varepsilon^* = \varepsilon_0(\varepsilon_{hf} + \frac{\varepsilon_{lf} - \varepsilon_{\mathrm{hf}}}{1 + j\omega\tau}) - j\frac{\sigma}{\omega} \tag{5.12}$$

The complex permittivity consists of a real part ε' and imaginary part ε''.

$$\varepsilon^* = \varepsilon' - j\varepsilon'' \tag{5.13}$$

The real part ε' is

$$\varepsilon' = \varepsilon_0(\varepsilon_{hf} + \frac{\varepsilon_{lf} - \varepsilon_{hf}}{1 + j\omega^2\tau^2}) \tag{5.14}$$

and the imaginary part ε'' is

$$\varepsilon'' = \varepsilon_0\left(\frac{(\varepsilon_{lf} - \varepsilon_{hf})\omega\tau}{1 + j\omega^2\tau^2}\right) + \frac{\sigma}{\omega} \tag{5.15}$$

These equations are called Debye dispersions [216].

5.1.3 Interfacial polarisation

For the same system, consider two different dielectric materials with different permittivity and conductivity in the middle of the electrodes, as shown in Figure 5-2.

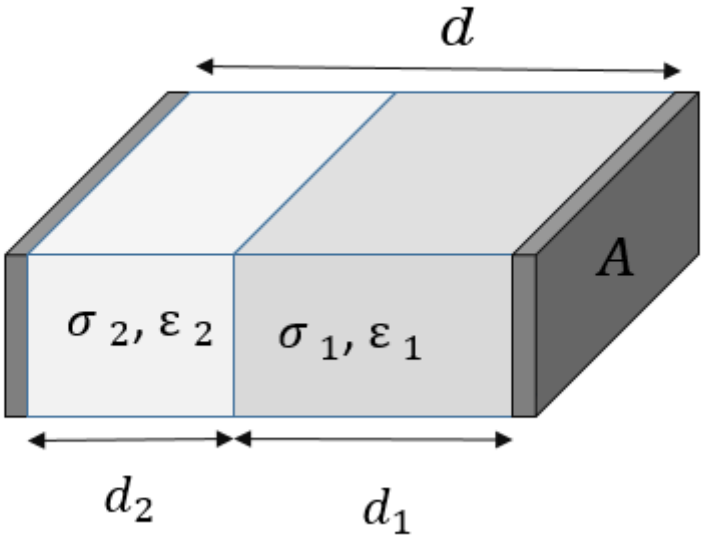

Figure 5-2: A schematic diagram of two parallel electrodes, each covers area A, separate with distance d. Two different dielectric materials with different width (d_1 and d_2), different permittivity (ε_1 and ε_2) and different conductivity (σ_1 and σ_2) are in the middle of the parallel electrodes.

The total impedance between the electrodes is:

$$Z = Z_1 + Z_2 = \frac{R_1}{1 + j\omega R_1 C_1} + \frac{R_2}{1 + j\omega R_2 C_2} \tag{5.16}$$

The two materials can be seen as a single material with different complex relative permittivity. The complex relative permittivity of the single material can be calculated by Debye formulations as

$$\varepsilon^* = \varepsilon' - i\varepsilon'' = \varepsilon_0 \left[\varepsilon_{hf} + \frac{\varepsilon_{lf} - \varepsilon_{hf}}{1 + \omega^2\tau^2}\right] - j\varepsilon_0[\frac{(\varepsilon_{lf} - \varepsilon_{hf})\omega\tau}{1 + \omega^2\tau^2} + \frac{\sigma}{\omega\varepsilon_0}] \tag{5.17}$$

where ε_{hf} is the high frequency permittivity of the material and ε_{lf} is the low frequency permittivity of the material. τ is the relaxation time and σ is the system conductivity. Those parameters are:

$$\varepsilon_{hf} = \frac{d\varepsilon_1\varepsilon_2}{d_1\varepsilon_2 + d_2\varepsilon_1} \tag{5.18}$$

$$\varepsilon_{lf} = \frac{d(d_1\varepsilon_1{\sigma_2}^2 + d_2\varepsilon_2{\sigma_1}^2)}{(d_1\sigma_2 + d_2\sigma_1)^2} \tag{5.19}$$

$$\tau = \varepsilon_0 \frac{d_1\varepsilon_2 + d_2\varepsilon_1}{d_1\sigma_2 + d_2\sigma_1} \tag{5.20}$$

$$\sigma = \varepsilon_0 \frac{d\sigma_1\sigma_2}{d_1\sigma_2 + d_2\sigma_1} \tag{5.21}$$

This polarization is called interfacial polarization, or Maxwell-Wagner polarization [160].

5.1.4 The effective dipole moment of a sphere or an ellipsoid particle

If a homogeneous solid dielectric sphere, for example, a polystyrene bead is placed in an electrolyte and an electric field is applied across the electrolyte, the effective dipole moment of the sphere results from interfacial polarisation is

$$\boldsymbol{P} = 4\pi\varepsilon_m \frac{\varepsilon_p^* - \varepsilon_m^*}{\varepsilon_p^* + 2\varepsilon_m^*} r^3 \boldsymbol{E} \tag{5.22}$$

where r is the radius of the sphere, ε_m is the relative permittivity of the medium, ε_p^* is the complex relative permittivity of the particle, ε_m^* is the complex relative permittivity of the medium. This formula is sometimes re-written as

$$\boldsymbol{P} = v\alpha^*\boldsymbol{E} \tag{5.23}$$

where v is the volume of the dielectric sphere;

$$v = \frac{4}{3}\pi r^3 \tag{5.24}$$

and α^* is the effective polarizability;

$$\alpha^* = 3\varepsilon_m\left(\frac{\varepsilon_p^* - \varepsilon_m^*}{\varepsilon_p^* + 2\varepsilon_m^*}\right) = 3\varepsilon_m f_{CM} \tag{5.25}$$

f_{CM} is called the Clausius-Mossotti factor [217], which is

$$f_{CM} = \frac{\varepsilon_p^* - \varepsilon_m^*}{\varepsilon_p^* + 2\varepsilon_m^*} \tag{5.26}$$

The effective polarizability of a homogeneous ellipsoid is the average of the effective polarizability for the three different axes [218]. For an ellipsoid, K is a frequency dependent factor, which is equivalent to the Clausius-Mossotti factor, given by

$$K = 1/3\sum K_i \tag{5.27}$$

where $i = x, y, z$. The frequency dependent factor in each axes (K_i) is

$$K_i = \frac{1}{3}\frac{\left(\varepsilon_p^* - \varepsilon_m^*\right)}{\varepsilon_m^* + Ai\left(\varepsilon_p^* - \varepsilon_m^*\right)} \tag{5.28}$$

where Ai is a depolarising factor, given by

$$Ai = \frac{1 - e^2}{2e^3}\left[\log\left(\frac{1+e}{1-e}\right) - 2e\right] \tag{5.29}$$

For an ellipsoid, the depolarising factor for three direction is

$$A_z = A_y = (1 - A_x)/2 \tag{5.30}$$

with e the eccentricity, given by

$$e = \sqrt{1 - \left(\frac{b}{a}\right)^2} \tag{5.31}$$

5.1.5 DEP force

The force on a dipole in an electric field is [214]

$$\boldsymbol{F} = (\boldsymbol{p} \cdot \nabla)\boldsymbol{E} \tag{5.32}$$

The DEP is a phenomenon in which a force is exerted on a particle produced by the interaction of an electric field with the effective dipole moment of the particle [24]. In a uniform electric field, there is no net force generated on a particle. In a non-uniform electric field, the strength on each side of the particle is not equal, so the result average force may cause the particle move [214].

If the particle is sphere, the effective dipole moment is given by equation (5.22), and the time average of the DEP force is

$$\langle \boldsymbol{F}_{\boldsymbol{DEP}} \rangle = 2\pi\varepsilon_m r^3 Re\{f_{CM}\}\nabla \boldsymbol{E}^2(rms) \tag{5.33}$$

where $\nabla \boldsymbol{E}^2(rms)$ is the local field strength gradient in (V^2/m^3).

If $Re\{f_{CM}\} > 0$, the DEP force is called positive DEP (pDEP) force and the particle moves from low electric field to high electric field. If $Re\{f_{CM}\} < 0$, the DEP force is called negative DEP (nDEP) force and the particle move from high electric field to low electric field [214].

5.1.6 MMT of a particle suspension

In the middle of two parallel electrodes, a uniform electric field is applied between a diluted suspension of particles. Figure 5-3 (a) is a schematic diagram of a particle suspension. The dielectric property of the particle suspension is equivalent to a new material with different dielectric property [219] - see Figure 5-3 (b).

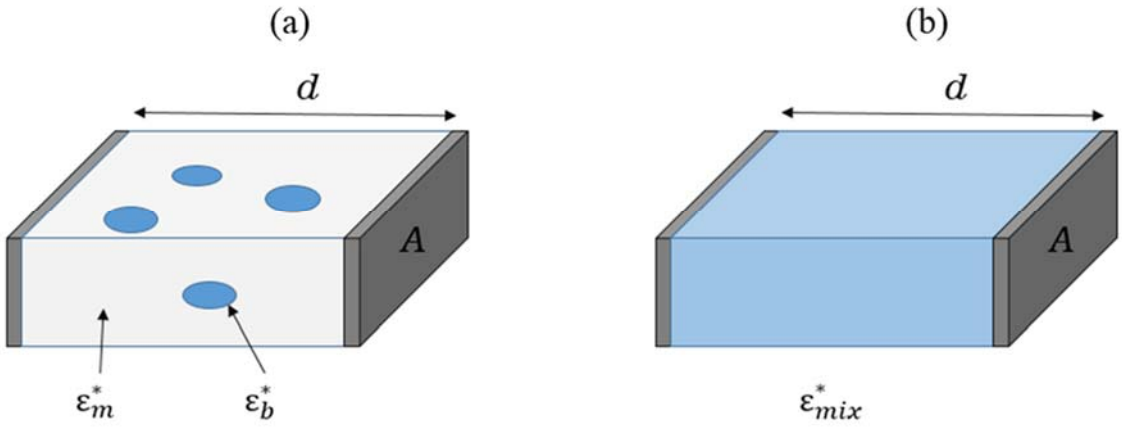

Figure 5-3: A schematic diagram of MMT of a particles suspension. (a) In the middle of two parallel electrode, a uniform electric field is applied between a particles suspension. (b) The dielectric property of the particles suspension can be seen as a new material with different dielectric property. ε_m^* is the complex permittivity of the medium, ε_b^* is the complex permittivity of the particle and ε_{mix}^* is the complex permittivity of the new material.

The complex relative permittivity of the mixture is

$$\varepsilon_{mix}^{*} = \varepsilon_{m}^{*} \frac{1 + 2\psi f_{CM}}{1 - \psi f_{CM}} \tag{5.34}$$

where ψ is the volume fraction of the particles, written as

$$\psi = \frac{v}{Ad} \tag{5.35}$$

where v is the total volume of particles, A is the area of each electrode and d is the distance between two parallel electrodes [219].

5.2 Impedance detection

5.2.1 Electrode double layer and parasitic capacitance

When a potential is applied between two electrodes immersed in a liquid, an electric field is generated in the bulk solution that attracts counterions to the surfaces [220]. The attracted ions create an electrode double layer at the electrode-electrolyte interface. Figure 5-4 demonstrates a schematic diagram of an electrical double layer.

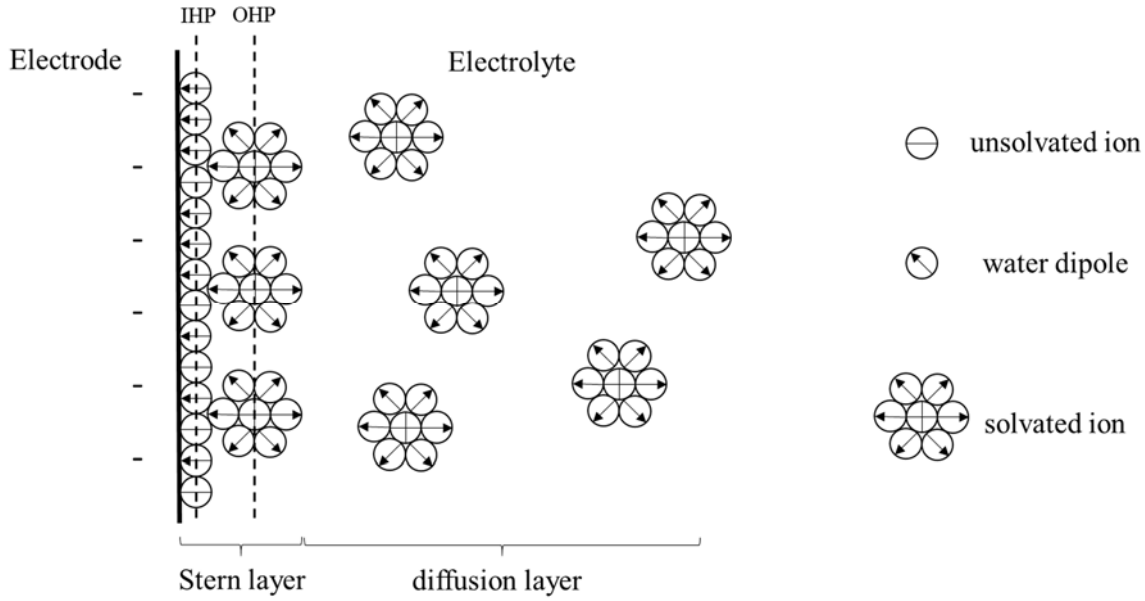

Figure 5-4: A schematic diagram of an electrical double layer [221]. A Stern layer consists of two layers formed by unsolvated ions, solvated ions and water. The inner layer is formed by specifically adsorbed ions (both co and counter ions). The locus of electrical centres of these ions is call inner Holmholtz plane (IHP). The outside layer is formed by solvated ions. The locus of these nearest solvated ions centres is called outer Holmholtz plane (OHP). Outside the Stern layer, a diffusion layer is formed by solvated ions that not specific adsorbed but affected by the electric attraction [220].

The electric double layer is usually described as the double layer capacitance C_{DL}. C_{DL} is seen as a series combination of the capacitance C_H from the Stern layer and capacitance C_G from diffusion layer:

$$\frac{1}{C_{DL}} = \frac{1}{C_H} + \frac{1}{C_G} \tag{5.36}$$

The Stern layer capacitance C_H is

$$C_H = \frac{\varepsilon_0 \varepsilon_r A}{d_{OHP}} \tag{5.37}$$

ε_r is generally between 6 to 20, so C_H/A is estimated to be 10 to 40 μF/cm^2 [221].

The capacitance of the diffusion layer depends on Debye length λ:

$$\lambda = \sqrt{\frac{\varepsilon_0 \varepsilon_r kT}{2z^2 e^2 n_0}} \tag{5.38}$$

where z is the valence of the ions, k is the Boltzmann constant, T is absolute temperature, e is the electron charge, and n_0 is the solvated ion concentration.

In the impedance system, the area of an electrode is 0.08 mm^2, the double layer capacitance of the electrode in MH1 broth is roughly 6 μF [221].

A parasitic capacitance (also termed pass or stray capacitance) occurs from the crosstalk between wires connected to the electrodes. The parasitic capacitance between two ribbon cables is 46 pF/m [222]. In the impedance system, a 0.2 m ribbon cable is used to connect the electrodes to the impedance analyser and the parasitic capacitance is roughly 10 pF.

In a microfluidic channel, two parallel, planar electrodes are placed at the bottom of a channel and connected to an impedance analyser, giving a two-terminal impedance detection system. Figure 5-5 shows the circuit diagram of this two-terminal detection system.

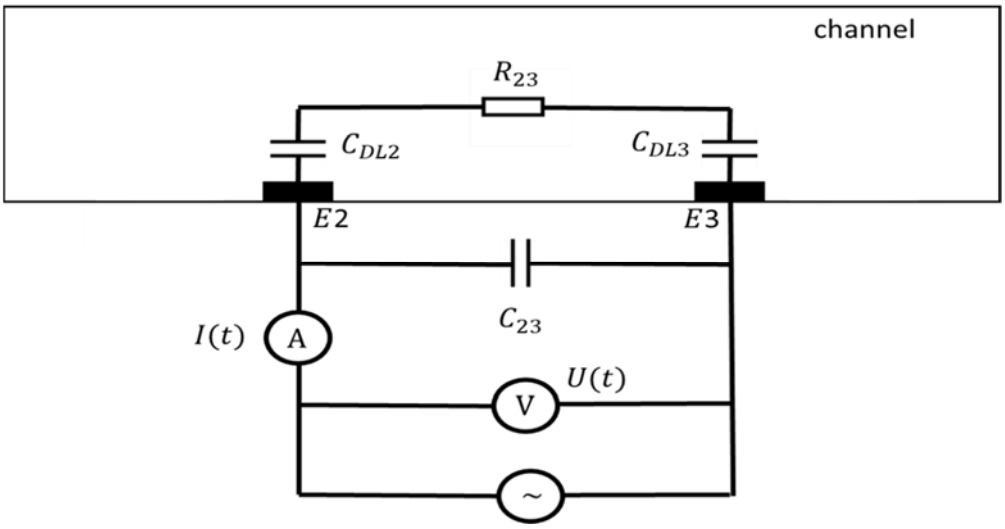

Figure 5-5: A schematic diagram of a microfluidic channel with two planer, parallel electrodes placed at the bottom. The two electrodes (named electrode E2 and E3, respectively) are connected to an impedance analyser and build a two-terminal impedance detection system. The simplified electric circuit of the two-terminal impedance detection system is shown. R_{23} and C_{23} are solution resistance and parasitic capacitance. C_{DL2} and C_{DL3} are double layer capacitance on electrode E2 and electrode E3.

Usually, the impedance magnitude detected from two-terminal impedance system can be divided into 3 different regions. In the low frequency range, the impedance is dominated by the double layer (C_{DL2} and C_{DL3}). As the frequency increases, the reactance of the double layer capacitance reduces and the impedance magnitude is dominated by bulky resistance (R_{23}). As the frequency of applied AC signal increases further, a part of the current goes through the parasitic capacitance (C_{23}) and the impedance of the system reduces.

5.2.2 Electrode polarisation: Pt black

Electrode polarisation phenomenon introduces errors in bulk resistance detection by a two-terminal detection system because of the presence of double layer capacitance. Electrode polarisation correction aims to reduce the influence of double layer capacitance [223].

Equation (5.2) and (5.37) show that an increase in electrode surface leads to an increase in double layer capacitance and a decrease in corresponding impedance. Therefore, electrode coating, such as roughening of the electrode surface (e.g., sandblasting [224]) or producing a porous electrode surface (e.g. electrodeposition [225]) is used to maximise the double layer capacitance.

When Pt electrodes are used, the most common coating material is Pt black. Porous Pt black is usually coated by an electrochemical process onto planar Pt electrodes according to

$$PtCl_4 + 2H_2 \rightarrow Pt \downarrow + HCl \tag{5.39}$$

To compare the double layer capacitance on a Pt black electrode and a bright Pt electrode, 10 pairs of interdigitated Pt electrodes (400 μm length, 20 μm width and 20 μm gaps) were

immersed in 0.025M HCl, 0.3% $PtCl_4$ and 0.025% $PbAc_4$ solution. 30 mA/cm^2 current flowed through the electrodes for 40 minutes to coat a Pt black layer [226]. Figure 5-6 shows the impedance magnitude and phase of LB broth for a 400 µm wide, 125 µm deep channel detected by integrated bright Pt and Pt black electrodes, respectively.

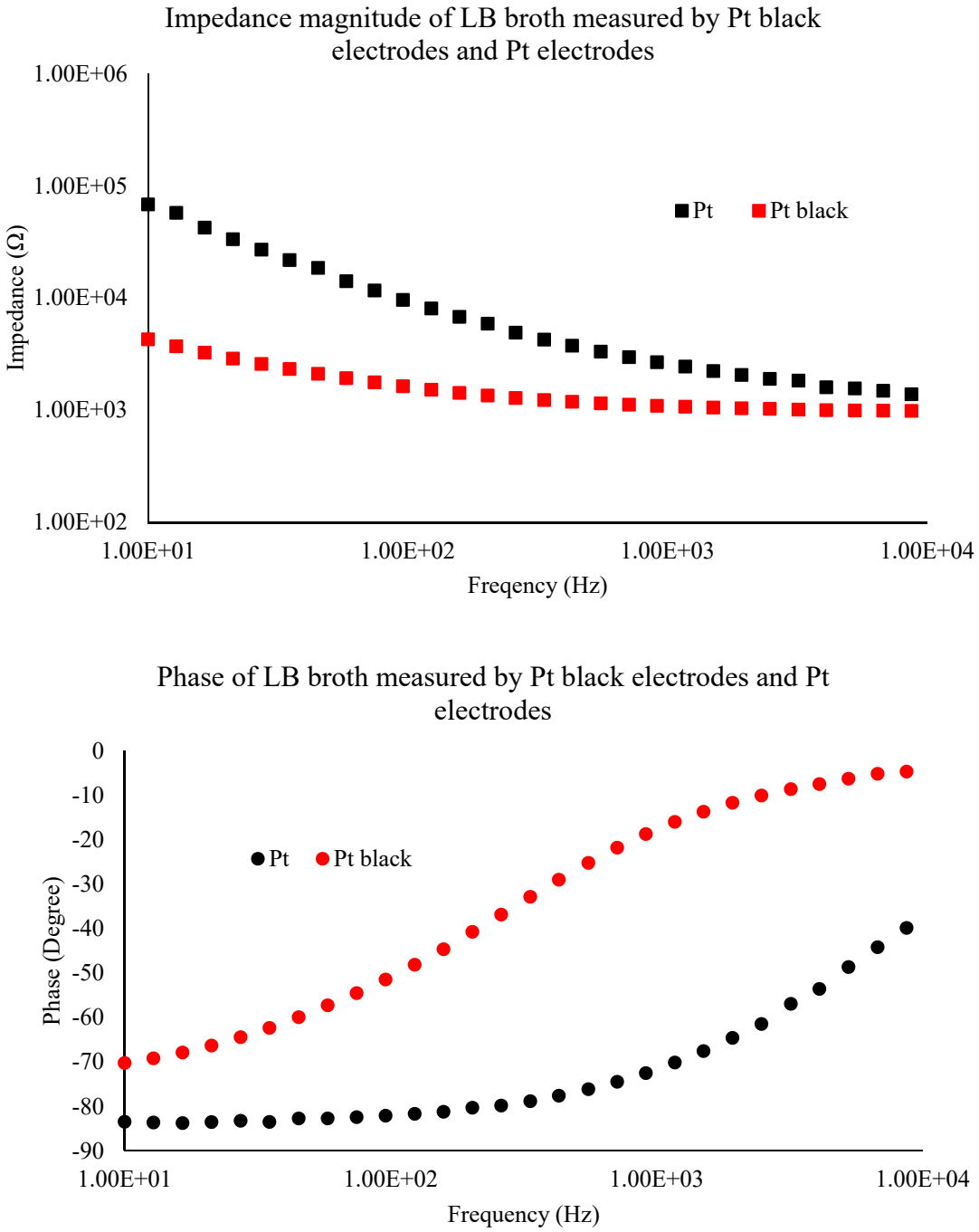

Figure 5-6: The impedance magnitude and the phase of LB broth measured by 10 pairs interdigitated Pt (black dots) and Pt black (red dots) electrodes (400 µm length, 20 µm width and 20 µm gaps) from 10 Hz to 10 kHz. The width and depth of the channel were 400 µm and 125 µm, respectively. The applied voltage of two-terminal detection (PalmSence 3 impedance analyser, Netherland) was 0.1 peak-to-peak voltage (Vpp).

In the low frequency range, the impedance magnitude and phase measured by the Pt black electrode were lower than that for bright Pt electrode, indicating that the double layer capacitance for the Pt black electrode was larger than the bright Pt electrode. The bulk resistance detected by Pt black electrodes is more accurate than that detected by Pt electrodes.

5.2.3 Electrode polarisation: four-terminal system

Developed by Schwan *et al.* in 1968, the four-terminal measurement technique provides an extra pair of non-current-carrying electrodes to detect the voltage [227]. Figure 5-7 demonstrates a four-terminal sensing system.

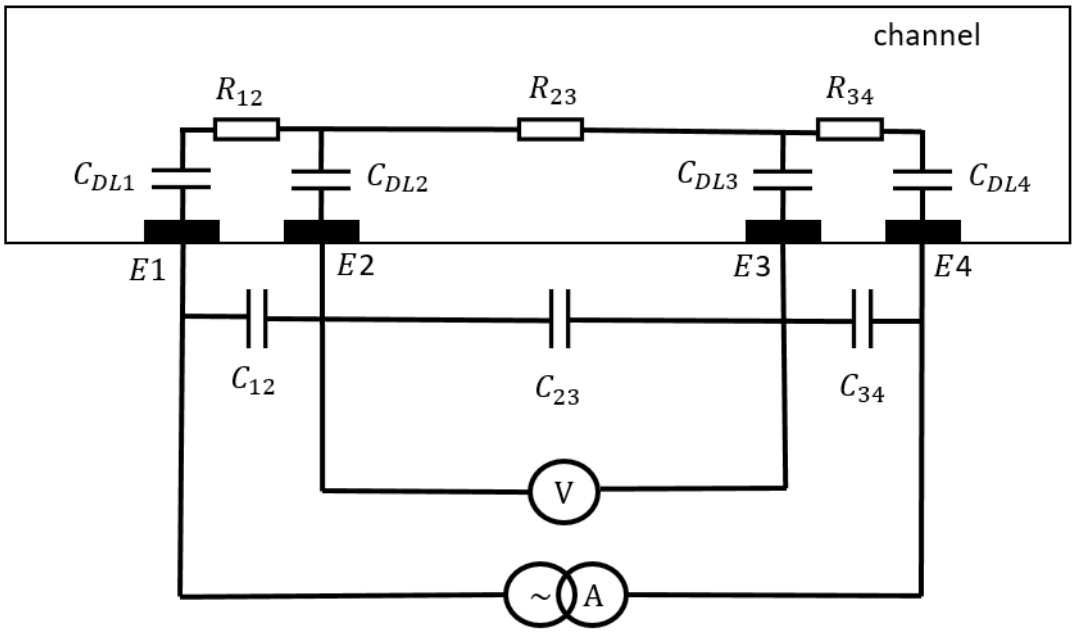

Figure 5-7: A schematic diagram of a microfluidic channel with four planar, parallel electrodes placed at the bottom of the channel. The inner two electrodes (named electrode E2 and E3, respectively) are connected to a voltage detection component and outer two electrodes (named electrode E1 and E4, respectively) are connected to a constant current injection, which build a four-terminal impedance detection system. The simplified electric circuit of the four-terminal impedance detection system is shown. The voltage detection component between E2 and E3 has very high impedance, so no current is able to flow through the double layer capacitance on E2 and E3 (C_{DL2} and C_{DL3}). Therefore, no voltage drops on C_{DL2} and C_{DL3}. The differential voltage between E2 and E3 is given by the bulk resistance (R_{23}).

A constant excitation current is injected by electrodes E1 and E4, and the differential voltage between electrodes E2 and E3 is measured. The differential voltage between E2 and E3 is directly from the bulk resistance (R_{23}) and the electrode polarisation is corrected. A four-electrode chip was fabricated and compared to the two-terminal detection chip. Figure 5-8 shows the impedance spectrum of MH1 broth measured by two-terminal and four-terminal chip in a 400 μm wide and 125 μm deep channel.

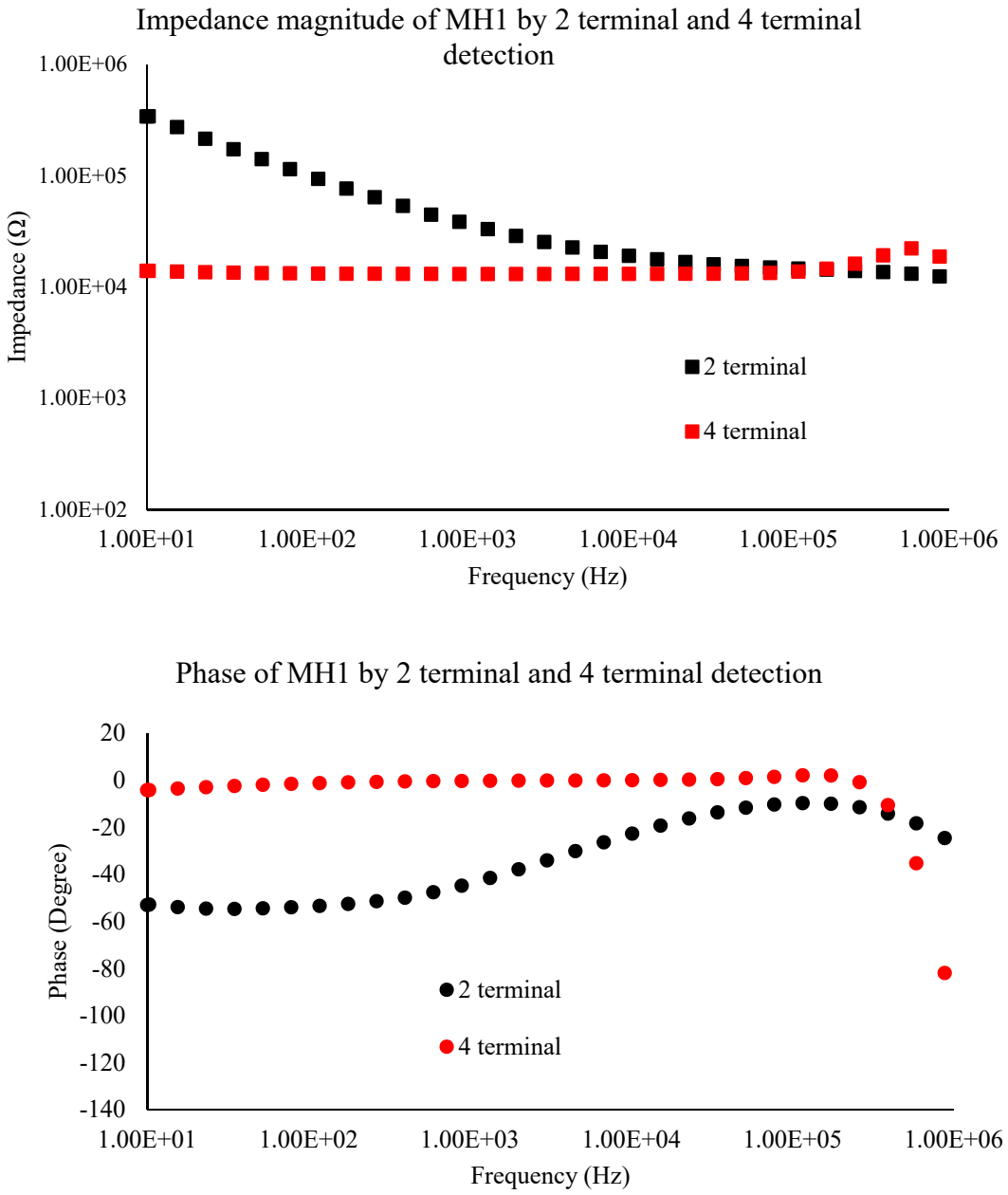

Figure 5-8: The impedance magnitude and the phase from 10 Hz to 1 MHz of MH1 detected by the four-terminal (red dots) method and the two-terminal (black dots) method. The width and depth of the channel were 400 µm and 125 µm, respectively. The inner two electrodes (E2 and E3) covered 0.08 mm^2 each and had 1 mm separation. The outer two electrodes (E1 and E4) covered 0.08 mm^2 each with 200 µm gap to E2 or E3, respectively. The applied voltage of the two-terminal detection (Novocontrol Gmtd, Germany) was 0.1 Vpp. E2 and E3 were connected to the impedance analyser while E1 and E4 were floating. The injection current of the four-terminal detection (Novocontrol Gmtd, Germany) was 10 µA. E2 and E3 were connected to the voltage detection component and E1 and E4 were connected to the current injection component.

In the frequency range <100 kHz, the four-terminal chip provided accurate detection of the bulk resistance. In contrast, the two-terminal setting could only measure the bulk resistance in

the frequency range >10 kHz and <100 kHz. In the frequency >100 kHz, the four-terminal chip suffered high-frequency induction, which leads to an increase in impedance magnitude. In the frequency >500 kHz, the impedance of the parasitic capacitance reduced in both the four-terminal system and the two-terminal system.

5.2.4 Transconductance amplifier

A transconductance amplifier (TCA) is used as a voltage-to-current converter with the bulk resistance in the feedback loop [228] as shown in Figure 5-9.

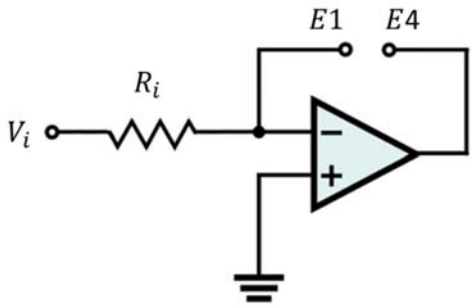

Figure 5-9: The circuit diagram of a TCA used in the four-terminal impedance detection system. The current between E1 and E4 is set by the voltage source V_i and resistor R_i. It is independent of any resistance between E1 and E4 within limites.

The current flow through the sensor (I) is:

$$I = \frac{V_i}{R_i} \tag{5.40}$$

which is independent of the bulk resistance between E1 and E4.

5.3 Ideal electrodes

5.3.1 Nernst equation

The open circuit electrode potential is given by the Nernst equation as:

$$V_{eq} = \Phi^0 + \frac{RT}{nF}\ln\frac{C_O}{C_R} \tag{5.41}$$

where Φ^0 is the standard electrode potential based on a normal hydrogen electrode. R is the universal gas constant, F is Faraday's constant, T is absolute temperature and n is the number of electrons transferred in the reaction. C_O and C_R are the oxidation concentration and reduction concentrations in the electrode, respectively.

5.3.2 Ideal non-polarisable electrode: Ag/AgCl electrode

An ideal non-polarisable electrode is an electrode whose potential does not change no matter how much current passes through it. Figure 5-10 shows the voltage-current plot of an ideal non-polarisable electrode [220].

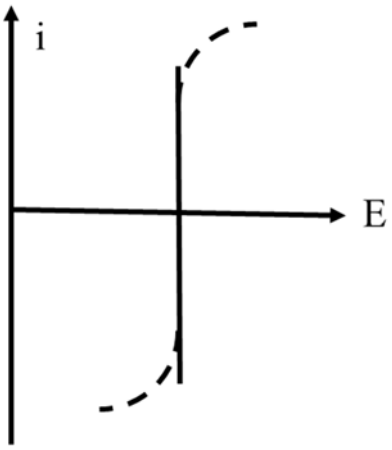

Figure 5-10: The current-potential curve of an ideal non-polarisable electrode. Dashed line shows the behaviour of actual electrodes that over the limited ranges of current [220].

The Ag/AgCl electrode is an ideal non-polarisable electrode with the reaction:

$$AgCl + e^- \leftrightarrow Ag + Cl^- \qquad \Phi = 0.230\,V$$

On the Ag/AgCl electrode surface, when the equilibrium is broken by a voltage V ($> V_{eq}$), Ag and Cl^- will be consumed and the net current will reach its maximum when no Ag or Cl^- is on electrode surface. Because Ag is the electrode material, if Cl^- are constant around the electrode, the net current will never reach its maximum.

When the equilibrium is broken by a voltage V ($< V_{eq}$), AgCl will be consumed and the current will reach its minimum when AgCl are all consumed. AgCl can be seen as infinite because it is the material of the electrode, the net current can never reach its minimum, either.

The Ag/AgCl electrode allows large current transfer, and it has a narrow range of potential as long as the Cl^- concentration around the electrode is constant stable. If the Ag/AgCl is immersed in a 3 M NaCl solution at 25° C.

$$V_{eq} = 0.230 + 0.059 \times 0.477 = 0.258\ \text{V}$$

i.e, the potential of a Ag/AgCl electrode is 0.258V in a 3 M NaCl solution at 25 C [229].

5.3.3 Ideal polarisable electrode: Pt electrode

An ideal polarisable electrode is an electrode where there is no DC current across the electrode-electrolyte interface regardless of the applied potential [230]. Figure 5-11 demonstrates the current-potential curve of an ideal polarisable electrode [220]. Although no real electrode

performs as an ideal polarisable electrode, some electrodes can approach the ideal in limited potential ranges, for example, Pt electrode.

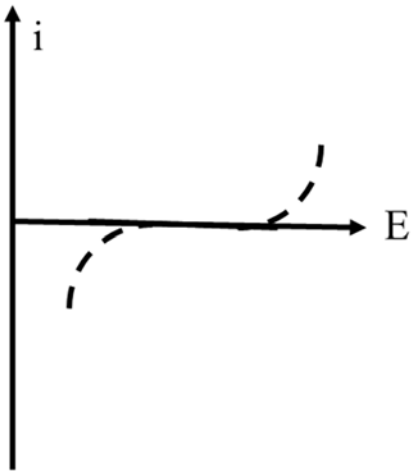

Figure 5-11: The current-potential curve for an ideal polarisable electrode. Dashed line shows the behaviour of actual electrodes that over the limited ranges of applied potential [220].

The reaction for the Pt electrode is:

$$PtO(s) + 2H^+ + 2e^- \leftrightarrow Pt + H_2O \qquad \Phi = 0.980\ V$$

In this reaction, the oxide PtO is in a solid form that covers the Pt electrode surface and prevents the remaining Pt from being oxidised [231].

In the impedance detection chamber, the pH of MH1 broth is 7.3 ± 0.1. The potential range for a Pt electrode to behave as an ideal polarisable electrode is limited by the reactions involving O_2 and H_2.

In an aqueous solution, soluble O_2 may react as:

$$O_2 + 4H_3O^+ + 4e^- \leftrightarrow 6H_2O \qquad \Phi = 1.229\ V$$

The equilibrium potential of the charge transfer reaction in MH1 broth is

$$V_{eq}^* = 1.229\ V + \left(\frac{8.314 \times 298}{4\ mol \times 96485}\right) \ln\left(\frac{[O_2] \times [H_3O^+]^4}{1^6}\right) = 1.229 - 0.0257 \times 2.303 \times pH$$
$$= 0.797\ V$$

Furthermore, H_2 may be generated from the reaction:

$$2H_3O^+ + 2e^- \leftrightarrow H_2 + 2H_2O \qquad \Phi = 0\ V$$

The equilibrium potential of H_2 generation in MH1 broth can also be calculated as

$$V_{eq}^* = 0V + \left(\frac{8.314 \times 298}{2\ mol \times 96485}\right) \ln\left(\frac{[H_3O^+]^2}{[H_2] \times 1^2}\right) = -0.0257 \times 2.303 \times pH = -0.432\ \text{V}$$

If the potential applied to a Pt electrode is limited within -0.43 V to 0.79 V, the Pt electrode may work as an ideal polarisable electrode.

5.4 pH detection

5.4.1 Definition of pH value

pH is given by[25]:

$$pH = -\log_{10}([H^+]) = \log_{10}\left(\frac{1}{[H^+]}\right) \tag{5.42}$$

where $[H^+]$ is the hydrogen ion concentration.

5.4.2 pH buffer

A pH buffer aims to keep the pH of an aqueous solution stable [232]. The mechanism of pH buffers is given as

$$HA \leftrightarrow H^+ + A^- \tag{5.43}$$

where HA represents a chemical species. A^- is the salt from HA.

An acid dissociation constant K_a is a quotient of the equilibrium concentrations (mol/L) in solution, written as,

$$K_a = \frac{[A^-][H^+]}{[HA]} \tag{5.44}$$

where [HA], [A^-] and [H^+] are the concentrations of HA, A^- and H^+, respectively.

In many practical cases, it is more convenient to discuss *pKa*, written as [232]

$$pK_a = -\log_{10} K_a \tag{5.45}$$

For a buffer solution consisting of a weak acid and its conjugate base, *pH* and *pKa* are related by

$$pH = pK_a + \log_{10}\frac{[A^-]}{[HA]} \tag{5.46}$$

In an equilibrium HA aqueous solution, $[A^-]$ and $[H^+]$ are stable. If extra H^+ are added into the solution, A^- will bind with H^+ and generates extra HA, which leads to a reduction in $\log_{10}\frac{[A^-]}{[HA]}$. The pH change of this aqueous solution is related with its buffer type and concentration.

5.4.3 IrOx pH sensor

The potentiometric response of the IrOx to pH is a function of transition between two oxidation states, Ir(III) oxide and Ir(IV) oxide, which can is given as follow [198]:

$$Ir(IV)oxide + qH^+ + ne^- \leftrightarrow Ir(III)oxide + rH_2O \tag{5.47}$$

The proposed reaction at a hydrous IrOx electrode can be described as [233]

$$2[IrO_2(OH)_{2-x}(2+x)H_2O]^{(2-x)-} + (3-2x)H^+ + 2e^- \leftrightarrow [Ir_2O_3(OH)_3 3H_2O]^{3-} + 3H_2O \tag{5.48}$$

where x differs depending on the IrO*x* electrode preparation and electrode age [234]. The Nernst equation can be expressed in terms of $\log_{10}$ as:

$$V_{eq} = \Phi^0 + \frac{2.3026RT}{nF}\log_{10}\frac{C_O}{C_R} \tag{5.49}$$

Thus, the equilibrium potential from equation (5.49) can be calculated as [235]

$$E = E^0 - \frac{2.3026RT}{2F}\log_{10}\frac{[IrO_2(OH)_{2-x}(2+x)H_2O^{(2-x)-}]^2[H^+]^{3-2x}}{[Ir_2O_3(OH)_3 3H_2O^{3-}]} \tag{5.50}$$

$$= E^0 - \frac{2.3026RT}{2F}\log_{10}\frac{[IrO_2(OH)_{2-x}(2+x)H_2O^{(2-x)-}]^2}{[Ir_2O_3(OH)_3 3H_2O^{3-}]} + \frac{2.3026(3-2x)RT}{2F}\log_{10}[H^+] \tag{5.51}$$

$$= E^0 - \frac{2.3026RT}{2F}\log_{10}\frac{[IrO_2(OH)_{2-x}(2+x)H_2O^{(2-x)-}]^2}{[Ir_2O_3(OH)_3 3H_2O^{3-}]} - (1.5-x)0.05916pH \tag{5.52}$$

If $E^{0\prime}$ is defined as

$$E^{0\prime} = E^0 - \frac{2.3026RT}{2F}\log_{10}\frac{[IrO_2(OH)_{2-x}(2+x)H_2O^{(2-x)-}]^2}{[Ir_2O_3(OH)_3 3H_2O^{3-}]} \tag{5.53}$$

the surface potential of IrOx film is

$$E = E^{0\prime} - (1.5-x)0.05916pH \tag{5.54}$$

If $x = 0.5$, the slope of potential against pH is -59.16 mV/pH, which is a Nernstian response [92]. The pH detection sensitivity that larger than 59.16 mV/pH is called super-Nernstian response [36].

5.5 Beer-Lambert law

The Beer-Lambert law demonstrates that the optical absorbance is proportional to the path length, the concentration of an absorbing molecule and the molar absorption coefficient in the solution [236], according to

$$A = -\log_{10}\left(\frac{I}{I_0}\right) = \varepsilon(\lambda)cl \tag{5.55}$$

where A is the absorbance, I_0 is the intensity of monochromatic light incident upon the substance, I is the intensity of measured monochromatic light after absorbance, $\varepsilon(\lambda)$ is the molar absorption coefficient, l is the absorption path length and c is the concentration of the sample. The Beer-Lambert law shows that longer path length leads to higher sensitivity ($\frac{dA}{dc}$), which means low concentration samples can be easier to measure. The path length of the optical chip used in this project (25 mm) is 6.5 times than the path length of a well in a 96-well plate (3.8 mm) with 200 µL solution.

5.6 Summary

This chapter summarizes the theory underlying the devices developed in this thesis. In the two-terminal impedance detection system, the applied voltage should be less than ± 0.4 V_{pp} to avoid charge transfer reactions on Pt electrode surface. The four-terminal detection system can correct for electrode polarisation (electrode double layer) efficiently, and was used in the impedance system to rapidly detect the antimicrobial susceptibility.

In the pH sensing system, an Ag/AgCl electrode is chosen to be the reference electrode. Therefore, Cl^- is essential in the solution to maintain the potential of Ag/AgCl electrodes stable. Extra KCl or NaCl need to be added into the solution manually if the detection medium lacks Cl^-.

Chapter 6: Electrical properties of *E. coli* suspension: simulations

6.1 Three-shell ellipsoid *E. coli* model

Castellarnau *et al.* (2006) used a two-shell ellipsoid model to simulate the electrical properties of *E. coli*, where the two shells were cell membrane and cell wall, respectively. Their simulation results were verified with experimental results [237].

Bai *et al.* (2006) improved the simulation by using a three-shell model, named outer membrane, periplasmic and inner membrane, respectively [114]. The three-shell model is more accurate to describe an *E. coli* because the cell envelope of a GN bacterium has three layers with different dielectric properties - see Figure 6-1. However, their simulations modified the permittivity and conductivity of outer membrane, periplasmic, inner membrane and cytoplasm based on assumption rather than experimental microbiological results. The simulation in this thesis is improved from Bai *et al.* with consideration of the bacterial phenotypical changes resulting from bacterial growth and the impacts of antibiotics.

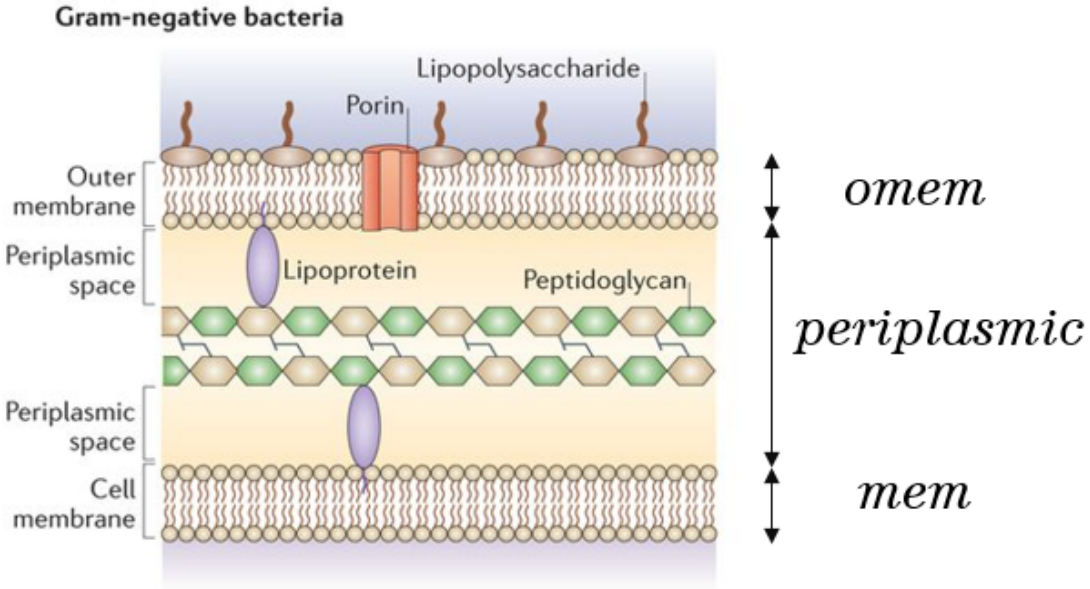

Figure 6-1: A schematic diagram of the cell envelop structure of a GN bacterium and the corresponding names used in the simulations. For GN bacteria, the cell envelop can be classified as three different shell layers with different dielectric properties: the outer membrane (omem), periplasmic area (periplasmic) and inner membrane (mem) [238].

Figure 6-2 shows a schematic diagram of a three-shell ellipsoid *E. coli* model.

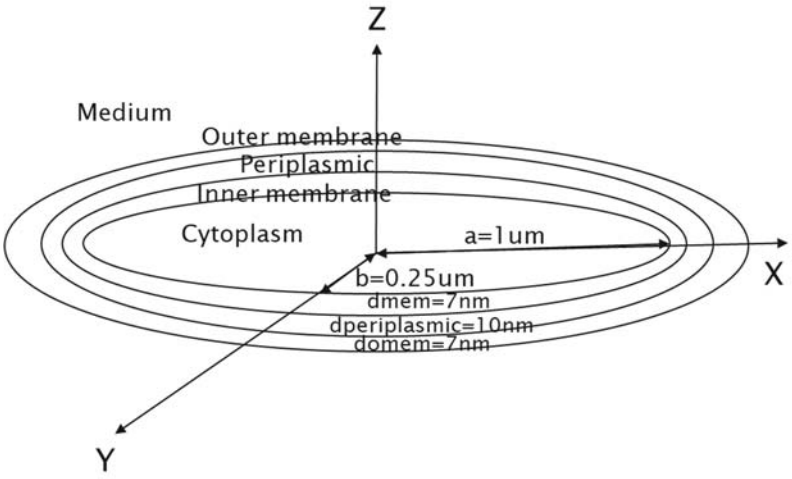

Figure 6-2: The schematic graph of a three-shell ellipsoid *E. coli* model. The bacterium is 2.048-μm long and 0.548-μm wide. The outer membrane and (inner) membrane are 7 nm thick and the periplasmic layer is 10 nm thick.

This simulation used five materials with different electronic properties: medium, outer membrane, periplasmic, membrane and cytoplasm. Table 6-1 lists the default electrical parameters of the materials.

Table 6-1: The default electrical parameters used in this simulation. Five materials with different electronic properties were used in this simulation: medium, outer membrane, periplasmic, inner membrane and cytoplasm. The parameters are from Bai *et al.* (2006) [114].

	$\varepsilon/\varepsilon_0$	σ (S/m)
Medium	81	0.35
Outer membrane	10	0
Periplasmic	60	3
Membrane	6	0
Cytoplasm	100	0.22

6.2 Simulations of the impedance of an *E. coli* suspension

6.2.1 Permittivity and conductivity of an *E. coli* suspension

The permittivity and conductivity of an *E. coli* suspension during 30-minute bacterial growth are calculated. The permittivity and conductivity are calculated from the complex permittivity of the suspension, given as:

$$\varepsilon_{mix} = Re\{\varepsilon^*_{mix}\} \tag{8.1}$$

$$\sigma_{mix} = Im\{\varepsilon^*_{mix}\} \times \omega \times \varepsilon_0 \tag{8.2}$$

where ε^*_{mix} is calculated from equation (5.34).

The MATLAB codes are attached in the Appendix.

The volume fraction of *E. coli* is set as 0.1. The bacterial concentration can be calculated as

$$volume\ fraction = 0.1 = x \times \frac{\frac{4}{3}\pi \times (1.024 \times 10^{-6}m) \times (0.274 * 10^{-6}m)^2}{1 \times 10^{-6}m^3} \tag{8.3}$$

where x is the bacterial number in 1 mL solution and calculated as 10^{11} CFU/mL.

The length of *E. coli* increases during its growth. Reported by Cullum *et al.* (1978), in half an hour, the length of *E. coli* normally increases from around 1 μm to around 2 μm [239]. Figure 6-3 shows the permittivity and conductivity of an *E. coli* suspension where the bacterium length of *E. coli* is increased from 1.048 μm to 2.048 μm (from a = 0.5 μm to a = 1 μm) and the volume fraction (P) of *E. coli* increases from 0.05 to 0.1 correspondently. The simulation assumes that the bacterial concentration keeps the same.

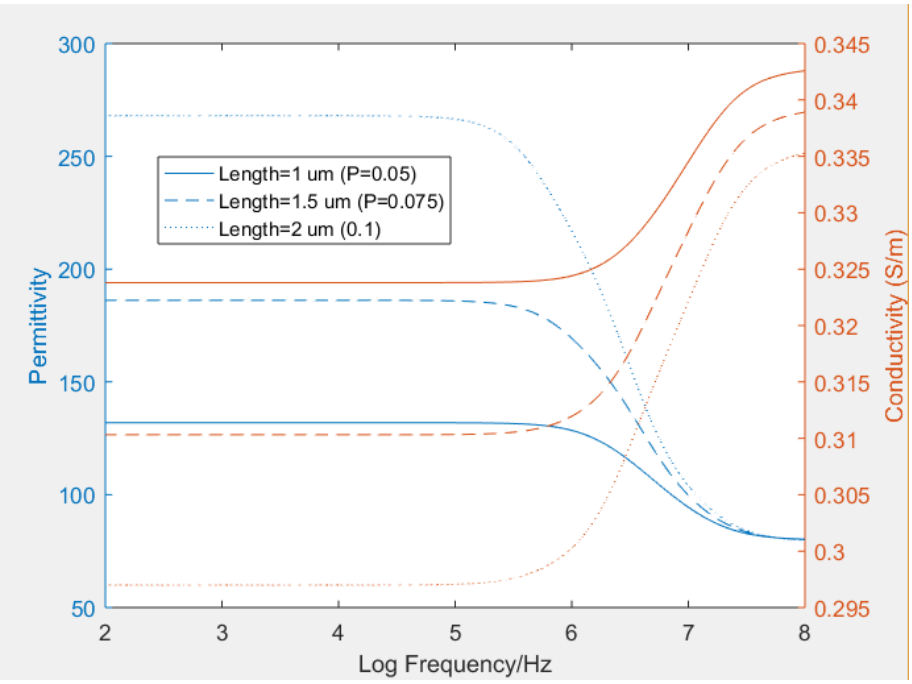

Figure 6-3: The conductivity and permittivity of an *E. coli* suspension where the length of *E. coli* is changed. The bacterium length is changed from 1.048 μm to 2.048 μm (from a = 0.5 μm to a = 1 μm), so the volume fraction (P) is changed from 0.05 to 0.1. Other parameters remain the same. The permittivity is increased significantly and the conductivity is reduced significantly at <1 MHz.

This simulation result shows that where the bacterial length is increased from 1.048 µm to 2.048 µm, the permittivity of the bacterial suspension will increase 85% at <100 kHz, and the conductivity of the bacterial suspension will reduce 9% at <100 kHz. The medium capacitance and the medium resistance of the bacterial suspension are influenced by the bacteria length, which can be used to monitor the bacterial growth.

Bacterial metabolism alters the medium conductivity. Reported by Safavieh *et al.* (2017), when the initial bacterial concentration is 10^8 CFU/mL, the medium conductivity changes about 30 % in half an hour [31]. The current setting of 10^{11} CFU/mL bacterial concentration is higher than the *E. coli* concentration in an overnight culture. Therefore, in this simulation, the medium conductivity increases from 0.3 S/m to 0.4 S/m (33%) to fit a practical condition. Figure 6-4 shows the permittivity and conductivity of an *E. coli* suspension where the medium conductivity is altered.

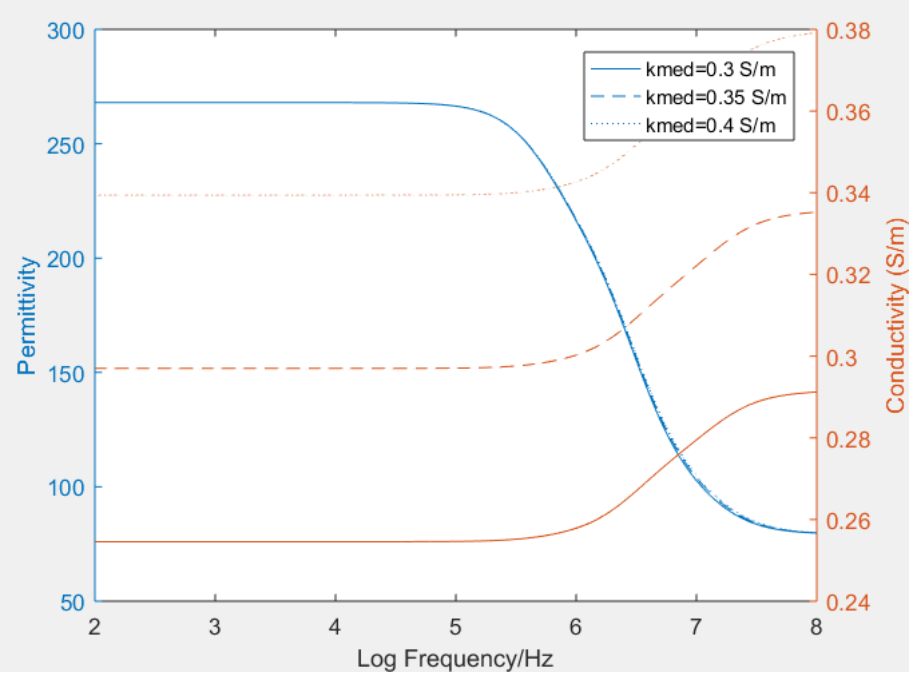

Figure 6-4: The permittivity and conductivity of an *E. coli* suspension where the medium conductivity (kmed) is altered. The medium conductivity is changed from 0.3 S/m to 0.4 S/m and the other parameters remain the same. The conductivity is significantly changed in all frequency ranges but there is hardly any change to the permittivity.

This simulation result shows that where the medium conductivity is increased from 0.3 S/m to 0.4 S/m by bacterial metabolism, the permittivity of the bacterial suspension will keep the same but the conductivity of the bacterial suspension will increase 28% at <100 kHz. The medium resistance of the bacterial suspension is influenced by the bacterial metabolism, which can be used to monitor the bacterial growth.

In an aerobic, nutrient-rich condition, the doubling time of *E. coli* is around 20 minutes [240]. Meanwhile, the bacterial volume fraction increases if the size of single *E. coli* remains the same. Reported by Gibson *et al.* (2018), the doubling time of *E. coli* in wild may be longer than that in the optimized situation [241]. In this simulation, the volume fraction is changing from

0.06 (rather than 0.05) to 0.1 to fit a practical growing condition. Figure 6-5 shows the relative permittivity and conductivity of an *E. coli* suspension where the volume fraction is changed (bacterial concentration is changed but the bacterium size keeps the same).

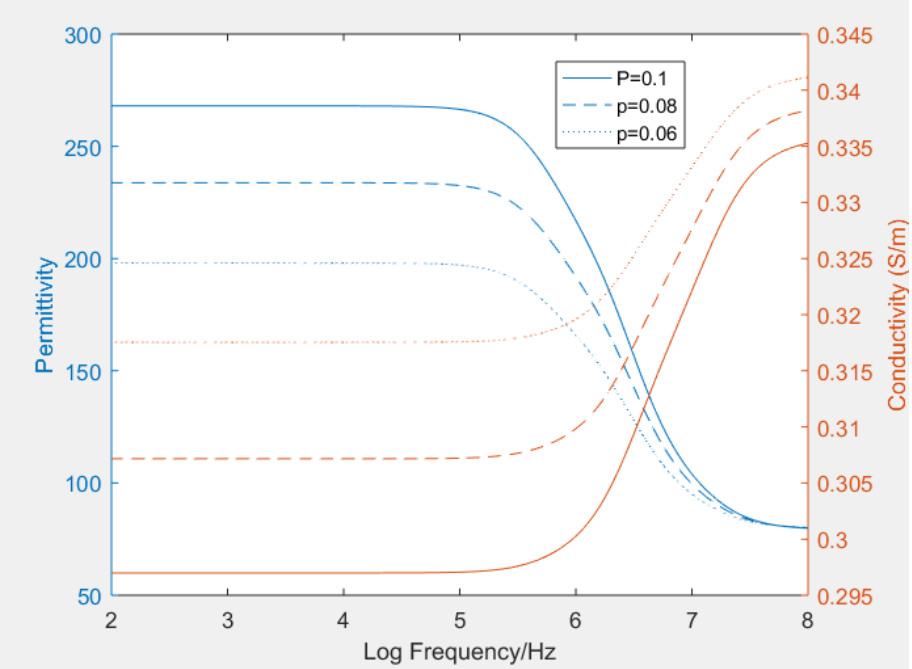

Figure 6-5: The permittivity and conductivity of an *E. coli* suspension where the volume fraction (P) is altered. The volume fraction is increased from 0.06 to 0.1. Other parameters remain the same. The permittivity is increased significantly and the conductivity is reduced significantly at <1 MHz.

This simulation result shows that where the volume fraction is increased from 0.06 to 0.1, the permittivity of the bacterial suspension will increase 30%, and the conductivity of the bacterial suspension will reduce 7% at <100 kHz. The medium capacitance and medium resistance of the bacterial suspension are influenced by the volume fraction, which can be used to monitor the bacterial growth.

Reported by Yu *et al.* (2015), colistin works on penetrating the outer membrane of an GN bacterium, disrupting the physical integrity of the phospholipid bilayer on the inner membrane and then leaking the cytoplasm through the bacterial membrane and wall [242]. Therefore, both outer and inner membrane conductivity of a colistin treated *E. coli* increase and the cytoplasm conductivity of a colistin treated *E. coli* reduces. Meanwhile, colistin can reduce protein incorporation in the outer membrane [55]. As a result, the permittivity of the outer membrane reduces. The permittivity and conductivity of an *E. coli* suspension after exposing to colistin for half an hour are simulated.

Figure 6-6 shows the permittivity and conductivity of an *E. coli* suspension where the conductivity of the *E. coli* outer membrane is increased, caused by outer membrane penetration.

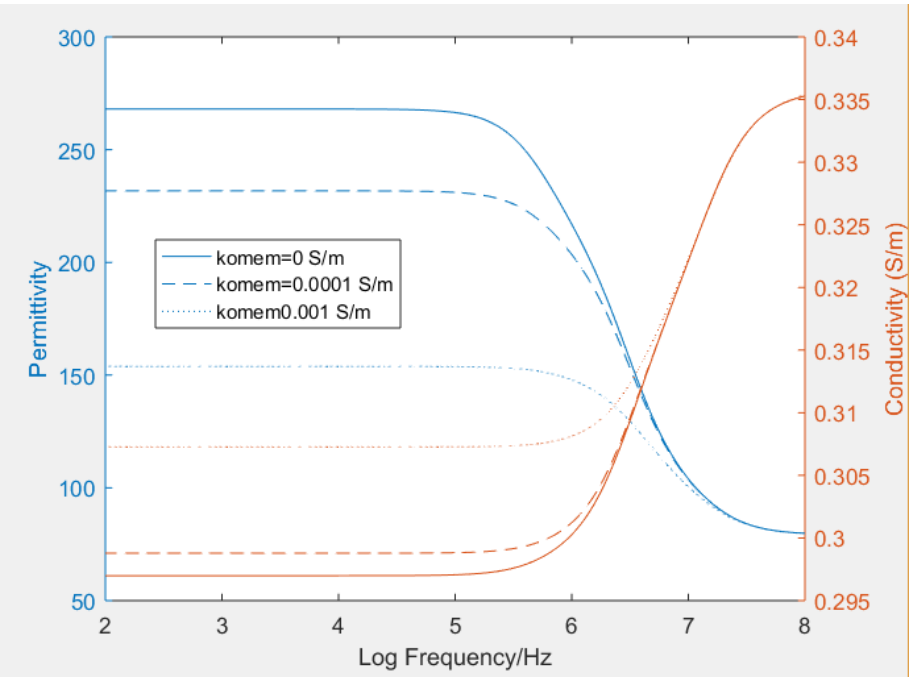

Figure 6-6: The permittivity and conductivity of an *E. coli* suspension where the conductivity of the *E. coli* outer membrane (komem) is changed. The outer membrane conductivity is increased from 0 to 0.001 S/m. Other parameters remain the same. The permittivity is reduced significantly at <1 MHz and the conductivity is increased significantly at <10 MHz.

This simulation result shows that where the outer membrane conductivity is increased from 0 to 0.001 S/m by the effect of colistin, the permittivity of the bacterial suspension will reduce 57% and the conductivity of the bacterial suspension will increase 4% at <100 kHz. The medium capacitance of the bacterial suspension is influenced by the outer membrane conductivity, which can be used to monitor the effect of colistin.

Figure 6-7 shows the permittivity and conductivity of an *E. coli* suspension where the conductivity of the *E. coli* membrane is changed, caused by inner membrane penetration.

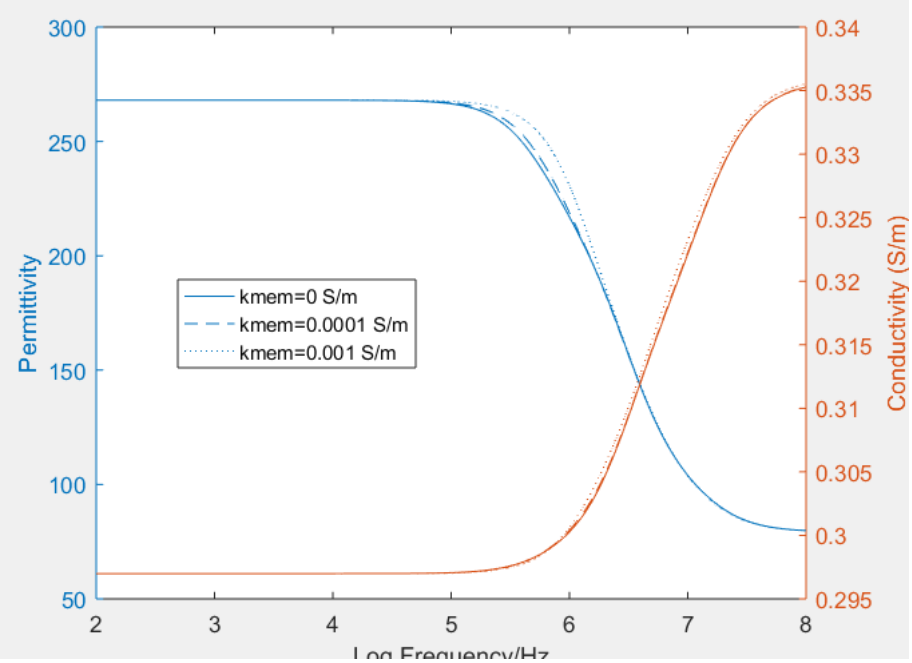

Figure 6-7: The permittivity and conductivity of an *E. coli* suspension where the conductivity of the *E. coli* membrane (kmem) is changed. The membrane conductivity is changed from 0 S/m to 0.001 S/m. Other parameters remain the same. The permittivity is increased slightly between 100 kHz and 1 MHz and the conductivity is increased slightly at >100 kHz.

This simulation result shows that where the membrane conductivity is increased from 0 S/m to 0.001 S/m by the effect of colistin, the permittivity of the bacterial suspension will increase 8% at 500 kHz and the conductivity of the bacterial suspension will increase <1% at >1 MHz. The medium capacitance of the bacterial suspension can be used to measure the membrane conductivity at 500 kHz, which can indicate the effect of a drug on the membrane.

Pethig (2017) concluded that after a high-dose colistin treatment, the cytoplasm conductivity of *K. pneumoniae* drops 60 % in 1 hour [163]. Figure 6-8 shows the permittivity and conductivity of an *E. coli* suspension where the conductivity of the *E. coli* cytoplasm is reduces from 2.6 S/m to 1.8 S/m (30%), resulting from cytoplasm leakage after 30 minutes colistin treatment

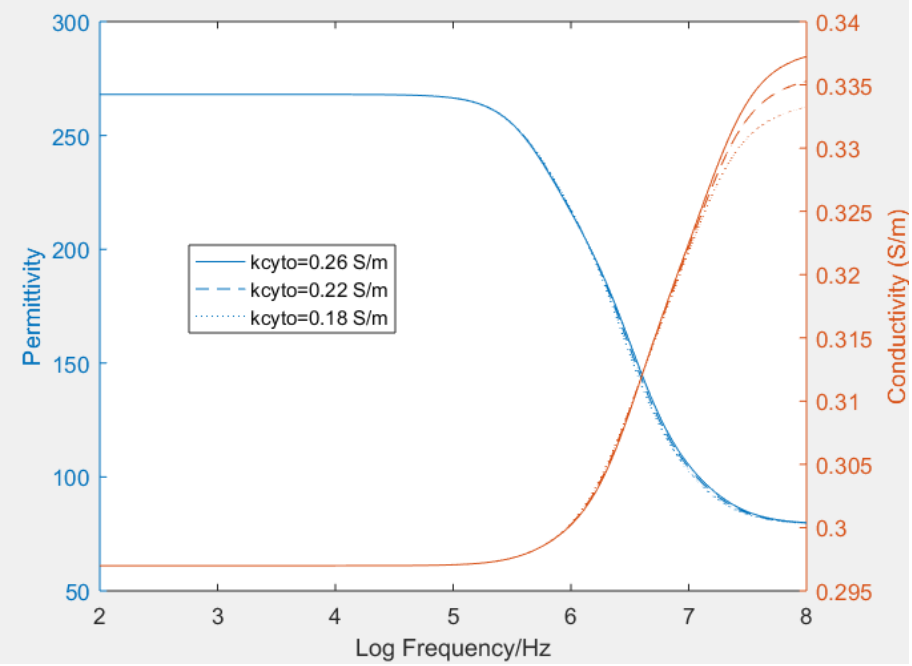

Figure 6-8: The permittivity and conductivity of an *E. coli* suspension where the conductivity of the *E. coli* cytoplasm (kcyto) is changed. The cytoplasm conductivity is changed from 0.26 S/m to 0.18 S/m. Other parameters remain the same. The permittivity is reduced slightly between 1 MHz and 100 MHz and the conductivity is reduced slightly at >10 MHz.

This simulation result shows that where the cytoplasm conductivity is reduced from 0.26 S/m to 0.001 S/m by the effect of a drug, the permittivity of the bacterial suspension will reduce <1% at 5 MHz and the conductivity of the bacterial suspension will reduce 1.5% at 100 MHz. The cytoplasm conductivity change can be detected by a precision impedance analyser at >10 MHz.

The outer membrane permittivity is reduced from 10 to 6 to simulate the incorporation of proteins on the outer membrane caused by colistin. Figure 6-9 shows the relative permittivity and conductivity of an *E. coli* suspension where the permittivity of the *E. coli* outer membrane is reduced.

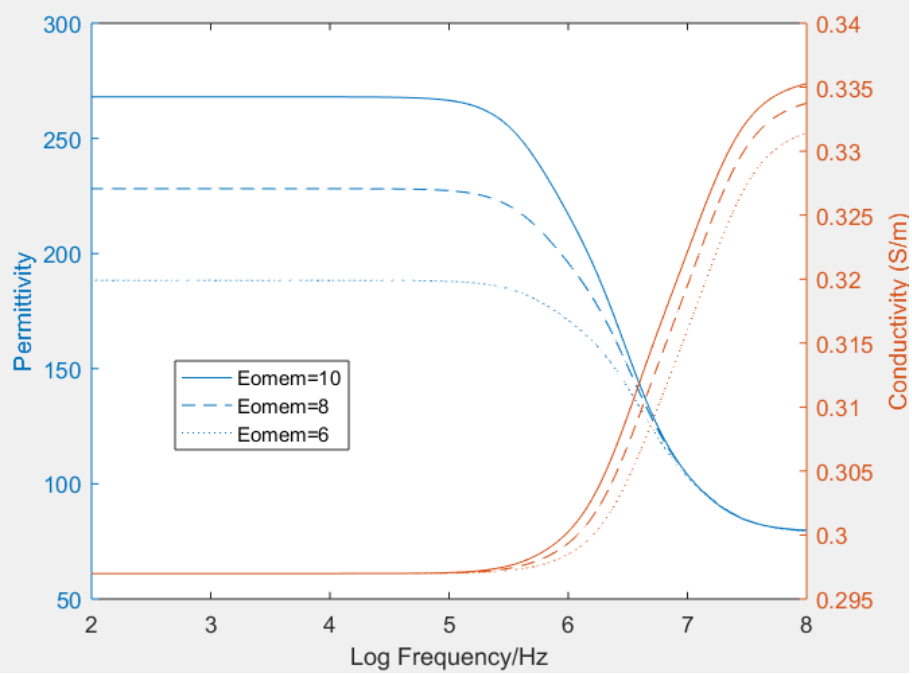

Figure 6-9: The permittivity and conductivity of an *E. coli* suspension where the permittivity of the *E. coli* outer membrane (Eomem) is reduced. The outer membrane permittivity is reduced from 10 to 6. Other parameters remain the same. The permittivity is reduced significantly at <100 kHz and the conductivity is reduced slightly at >1 MHz.

This simulation result shows that where the outer membrane permittivity is reduced from 10 to 6 by the effect of colistin, the permittivity of the bacterial suspension will reduce 36% at <100 kHz, and the conductivity of the bacterial suspension will reduce 1% at 100 MHz. The medium capacitance of the bacterial suspension is influenced by the outer membrane permittivity, which can be used to monitor the effect of colistin. The medium resistance is rarely influenced by the outer membrane permittivity.

From the simulations described above, the changes of the permittivity and the conductivity of the bacterial suspension in different frequency can reflect the variations in the bacterial outer membrane, inner membrane and cytoplasm. Volume fraction, medium conductivity, outer membrane permittivity and outer membrane conductivity can alter the permittivity and conductivity of an *E. coli* suspension significantly. However, the simulations are based on a very high bacteria volume fraction (0.1, roughly 10^{11} CFU/mL bacterial concentration), which is not possible in a practical setting. Next, the impedance spectrum of bacterial suspensions at 10^7 CFU/mL is simulated, which is more accurate in practical impedance-based measurement.

6.2.2 Normalized impedance change ratio (NICR)

The normalized impedance reduction ratio (NICR) is usually used to quantify bacterial growth, as reported by Colvin *et al.* (1977) [92] and Safavieh *et al.* (2017) [31]. The NICR is defined as:

$$Normalized\ impedance\ change\ ratio\ (NICR) = \frac{|Z_i| - |Z_0|}{|Z_0|} \times 100\% \quad (8.4)$$

where $|Z_i|$ is the impedance magnitude after time i and $|Z_0|$ is the initial impedance magnitude.

In the experiment setting, two electrodes cover area A separately, with distance d in parallel. The impedance magnitude of the bacterial suspension placed in the parallel electrodes can be calculated as:

$$|Z| = \frac{d}{A}\left|\frac{1}{\omega\varepsilon_0\varepsilon^*_{mix}}\right| \quad (8.5)$$

In this thesis, the NICR of an *E. coli* suspension after 1-hour incubation was simulated. The initial OD in a conventional broth dilution method was set as 0.01, which generally equals 10^7 CFU/mL *E. coli* [243]. The volume fraction of *E. coli* at 10^7 CFU/mL can be calculated as

$$volume\ fraction = \frac{10^7 \times \frac{4}{3}\pi \times 1.024 \times 10^{-6} \times (0.274 \times 10^{-6})^2}{1 \times 10^{-6}} * 100\% \quad (8.6)$$
$$= 0.0026\%$$

Therefore, the volume fraction of 0.0026% is used in this simulation.

Assuming a starting concentration of 10^7 CFU/mL and a doubling time of 20 minutes, the concentration will reach 8×10^7 CFU/mL after a 1-hour incubation period [241].

At the same time, the medium conductivity of the *E. coli* suspension may increase by 20% because of bacterial metabolism in MH1 broth, whose medium conductivity may increase from 0.35 S/m to 0.42 S/m [28].

Figure 6-10 shows a simulation of NICR for an *E. coli* suspension where the medium conductivity changes from 0.35 S/m to 0.42 S/m, and the bacterial concentration increases from 10^7 CFU/mL to 8×10^7 CFU/mL.

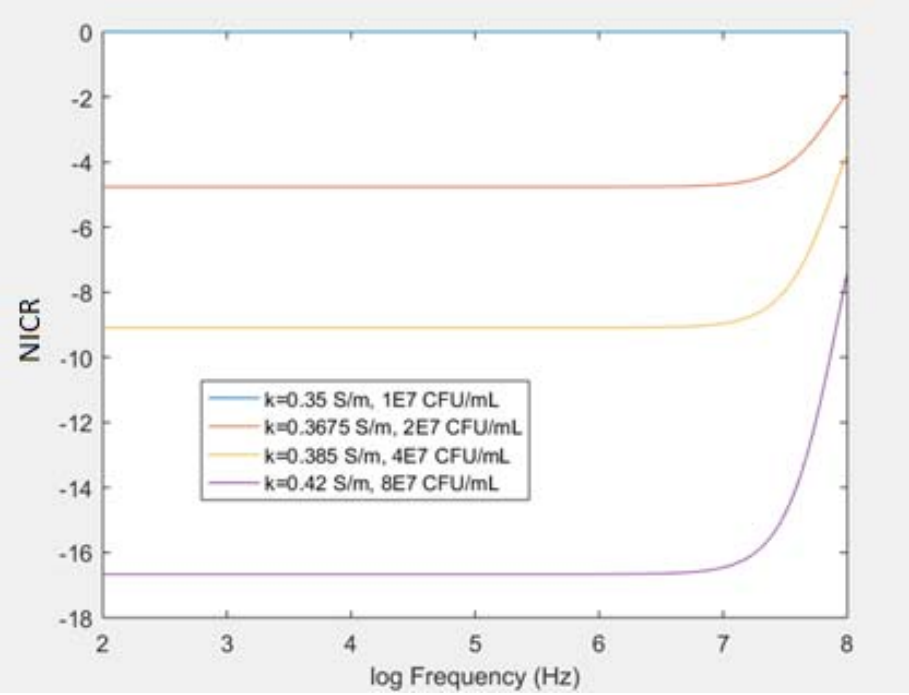

Figure 6-10: The NICR (%) of an *E. coli* suspension where medium conductivity (k) is changed from 0.35 S/m to 0.42 S/m and the bacterial concentration increases from 10^7 CFU/mL to 8×10^7 CFU/mL. This simulation shows the NICR results from bacterial concentration change and bacterial metabolism together. During bacterial growth, the cell number doubles every 20 minutes in 1 hour. Therefore, the *E. coli* concentration is 2×10^7 CFU/mL, 4×10^7 CFU/mL and 8×10^7 CFU/mL at 20 minutes, 40 minutes and 1 hour, respectively. The corresponding medium conductivity is 0.3675 S/m, 0.385 S/m and 0.42 S/m, respectively.

In 20 minutes, the NICR is reduced by around 5% at <10 MHz (10^7 Hz); in 40 minutes, it is reduced by 9% at <10 MHz; in 1 hour, it is reduced by 17% at <10 MHz. The impedance change is very significant and can be detected within 1 hour. The change in NICR is from conductivity change of the bacterial suspension and the volume fraction change of bacteria.

Figure 6-11 shows the NICR of an *E. coli* suspension where the medium conductivity changes from 0.35 S/m to 0.42 S/m, but the bacterial concentration remains stable at 10^7 CFU/mL. It describes the NICR from the conductivity change of the bacterial suspension without the volume fraction change of bacteria.

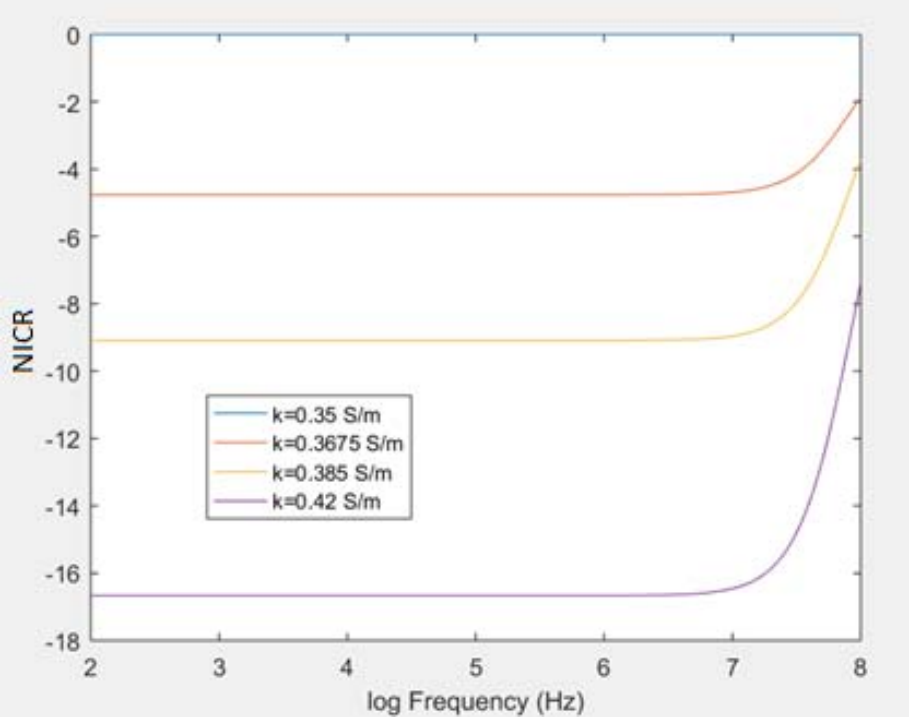

Figure 6-11: The NICR (%) of an *E. coli* suspension where medium conductivity (k) changes from 0.35 S/m to 0.42 S/m but the bacterial concentration remains stable at 10^7 CFU/mL. The impedance change is very similar to that caused by both bacterial metabolism and bacterial concentration change together.

The change in NICR is from conductivity change of the bacterial suspension without the volume fraction change of bacteria, which can also be detected within 1 hour.

Figure 6-12 shows the NICR of an *E. coli* suspension where bacterial concentration changes from 10^7 CFU/mL to 8×10^7 CFU/mL, and the medium conductivity remains stable at 0.35 S/m. It describes the NICR from the volume fraction change of bacteria without the conductivity change of the bacterial suspension.

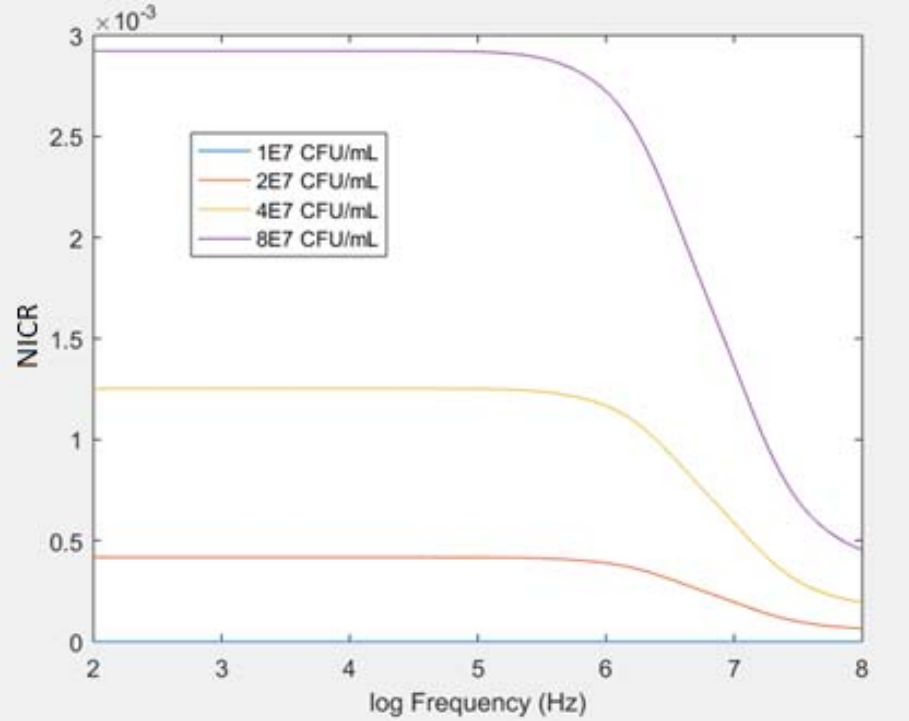

Figure 6-12: The NICR (%) of an *E. coli* suspension where the bacterial concentration increases from 10^7 CFU/mL to 8×10^7 CFU/mL, but the medium conductivity remains stable at 0.35 S/m. This simulation shows the impedance change caused by bacterial concentration change without bacterial metabolism.

The change in NICR is from the volume fraction change of bacteria without the conductivity change of the bacterial suspension. In 20 minutes, the NICR is increased by around 0.0005% at <1 MHz (10^6 Hz); in 40 minutes, it is increased by 0.00125% at <1 MHz; in 1 hour, it is increased by around 0.003% at <1 MHz. Therefore, it is difficult to detect the NICR caused by bacterial concentration change within 1 hour.

Based on the simulations above, the impedance detection system is focused on detecting the impedance change caused by bacterial metabolism during bacterial growth.

6.2.3 Quotation of normalized impedance change ratio (QNICR)

When using NICR to indicate the antibiotic effect, external impacts such as temperature, bacterial species or initial bacteria concentrations rather than antibiotics may influence the results. Simulation of the quotation of NICR (QNICR) between antibiotic-present and antibiotic-absent (blank) chambers is described in this section. Differential measurement can minimize the external influences on impedance such as bacterial metabolism, temperature or bacterial concentration. The QNICR is defined by the impedance change between two different chambers by

$$QNICR = \frac{\frac{|Z_{t,antibiotics}| - |Z_{0,antibiotics}|}{|Z_{0,antibiotics}|}}{\frac{|Z_{t,blank}| - |Z_{0,blank}|}{|Z_{0,blank}|}} \times 100\% \quad (8.7)$$

where $|Z_0|$ is the initial impedance magnitude of each chamber. $|Z_t|$ is the impedance magnitude of each chamber after t. $|Z_{blank}|$ is the impedance magnitude of the antibiotic-free chamber and $|Z_{antibiotics}|$ is the impedance magnitude of the chamber with antibiotics.

In this simulation, t is set as 1 hour. $|Z_0|$ is the impedance magnitude when the medium conductivity is 0.35 S/m and the bacterial concentration is 10^7 CFU/mL. $|Z_{t,blank}|$ represents the impedance magnitude where the bacteria have optimized growth and duplication, the medium conductivity is 0.42 S/m and the bacterial concentration is 8×10^7 CFU/mL. $|Z_{t,antibiotics}|$ represents an antibiotic inhibits bacterial metabolism and duplication, the medium conductivity remains stable at 0.35 S/m and the bacterial concentration remains stable at 10^7 CFU/mL.

Antibiotics can not only inhibit metabolism and duplication, but also alter bacterial phenotypic parameters (e.g. bacterial length) or electrical properties (e.g. the conductivity of the outer membrane or cytoplasm). Different groups of antibiotics have different mechanisms of action. For example, the β-lactam antibiotics inhibit peptidoglycan synthesis, so they can inhibit bacterial division [39]. Therefore, a β-lactam antibiotic–treated *E. coli* will be longer than an untreated *E. coli*. Figure 6-13 shows the QNICR of two *E. coli* suspensions where the length of a single *E. coli* in the antibiotic chamber changes from 1.048 μm (a=0.5 μm, simplified as l =1 um) to 2.048 μm (a=1 μm, simplified as l =2 um) but bacterial concentration and medium conductivity remain stable.

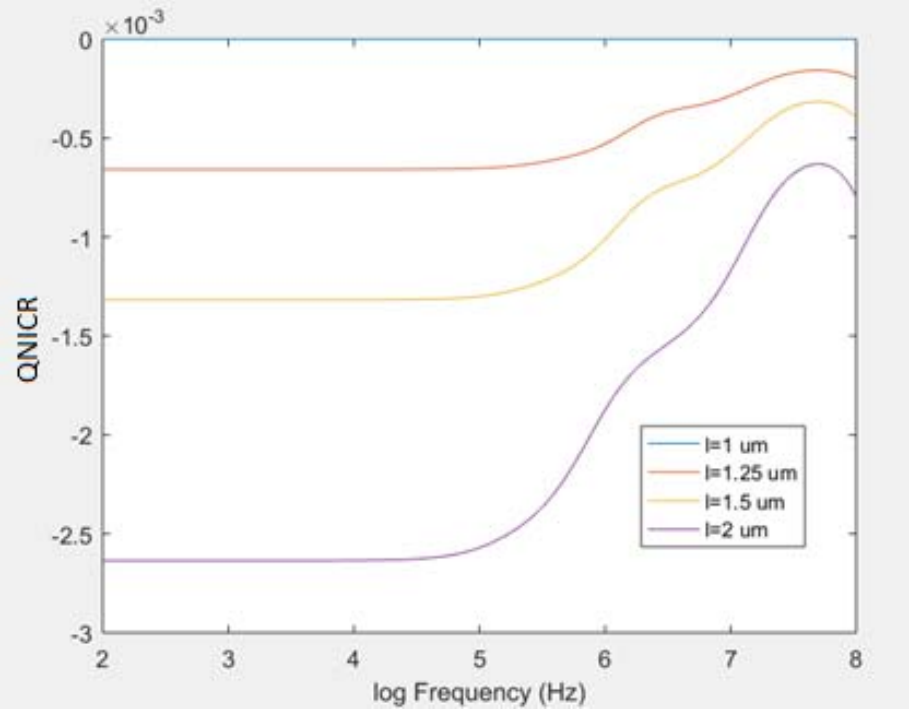

Figure 6-13: The QNICR (%) of two *E. coli* suspensions where the length (l) of a single *E. coli* in the antibiotic chamber changes from 1.048 µm (simplified as l=1 um) to 2.048 µm (simplified as l=2 um) but bacterial concentration and medium conductivity remain stable. The QNICR is reduced to -0.0025% at <100 kHz if the *E. coli* length is 2.048 µm.

Because QNICR is within 0.003% when the bacterial length changes from 1.048 µm to 2.048 µm, it is difficult to detect the altered *E. coli* length by impedance method in 10^7 CFU/mL bacterial concentration.

Colistin can penetrate the outer and inner membranes of a GN bacterium and leak its cytoplasm [242]. If the outer and inner membranes of an *E. coli* are completely permeable, the conductivities of its inner membrane, outer membrane and cytoplasm are all equal to the medium conductivity. Within all phenotypic changes, the outer membrane conductivity alteration is most significant in an impedance spectrum (see Figure 6-6). Figure 6-14 shows the QNICR of two *E. coli* suspensions where the outer membrane conductivity in the antibiotic chamber changes from 0 S/m to 0.35 S/m (medium conductivity) but bacterial concentration and medium conductivity remain stable.

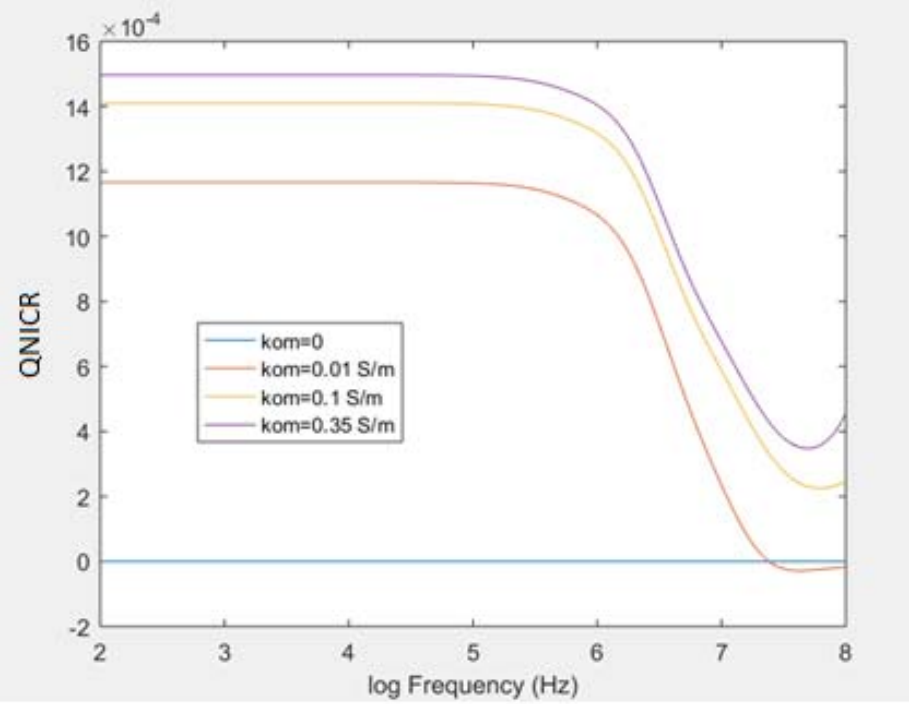

Figure 6-14: The QNICR (%) of two *E. coli* suspension where the *E. coli* outer membrane conductivity (kom) in the antibiotic chamber changes from 0 S/m to 0.35 S/m but bacterial concentration and medium conductivity remain stable. The QNICR increases to around 0.0012% at <1 MHz (10^6 Hz) if the outer membrane conductivity is 0.01 S/m, to 0.0014% at <1 MHz if the outer membrane conductivity is 0.1 S/m, and to 0.0015% at <1 MHz if the outer membrane conductivity is 0.35 S/m, which is the same as that of the medium.

This simulation shows that outer membrane conductivity change can maximally change QNICR by 0.0015%, so impedance detection barely achieves phenotypic detection of the effects of colistin on *E. coli*.

Doxycycline and gentamicin inhibit protein synthesis; ciprofloxacin inhibits DNA replication [39]. Therefore, the cytoplasm conductivity of *E. coli* treated with doxycycline, gentamicin or ciprofloxacin may differ from that of untreated *E. coli*. However, it is an assumption without experimental microbiology results. Figure 6-15 shows the QNICR of two *E. coli* suspensions where the *E. coli* cytoplasm conductivity in the antibiotic chamber changes from 0.1 S/m to 0.5 S/m (normal *E. coli* cytoplasm conductivity is 0.22 S/m) but bacterial concentration and medium conductivity remain stable.

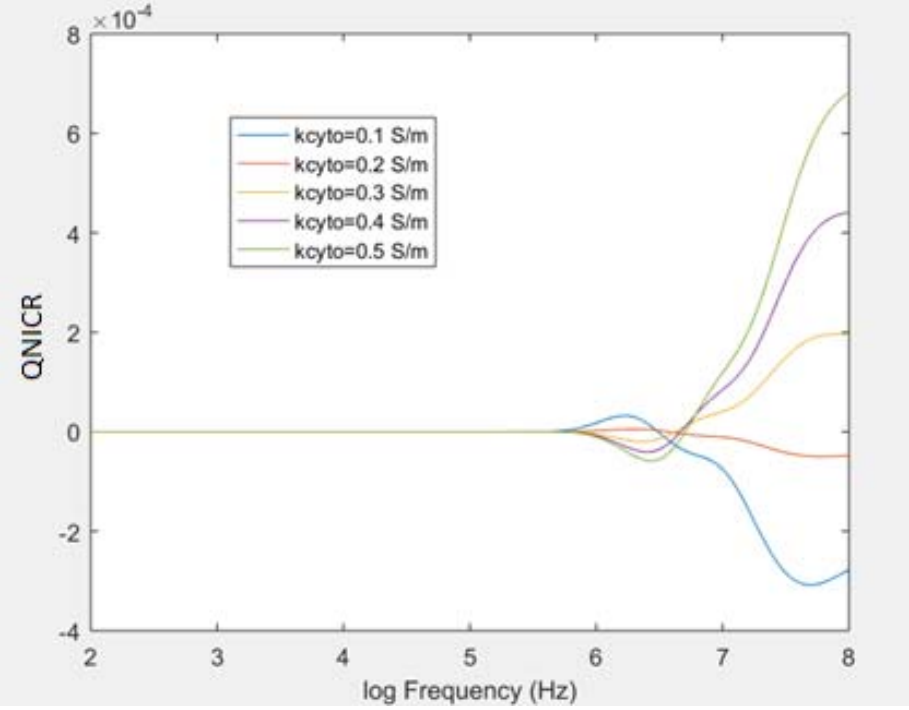

Figure 6-15: the QNICR (%) of two *E. coli* suspensions where the *E. coli* cytoplasm conductivity in the antibiotic chamber changes from 0.1 S/m to 0.5 S/m (normal *E. coli* cytoplasm conductivity is 0.22 S/m) but bacterial concentration and medium conductivity remain stable. The QNICR changes to about -0.0002% at 100 MHz (10^8 Hz) if the cytoplasm conductivity is 0.1 S/m, to about 0.0002% at 100 MHz if the cytoplasm conductivity is 0.3 S/m, to about 0.0004% at 100 MHz if the cytoplasm conductivity is 0.4 S/m, and to about 0.0007% at 100 MHz if the cytoplasm conductivity is 0.5 S/m.

The QNICR is below the sensitivity of the commonly used impedance analysers. Therefore, it is also very difficult to detect the QNICR caused by cytoplasm conductivity change using the impedance method. In conclusion, due to the low volume fraction of *E. coli* at 10^7 CFU/mL, it is difficult for an impedance system to directly detect the mechanism of antibiotics.

Figure 6-16 shows the QNICR of two *E. coli* suspensions where it is assumed that the bacterial concentration in the antibiotic chamber is stable at 10^7 CFU/mL and the medium conductivity varies from 0.35 S/m to 0.42 S/m where antibiotics have partially inhibited the metabolism.

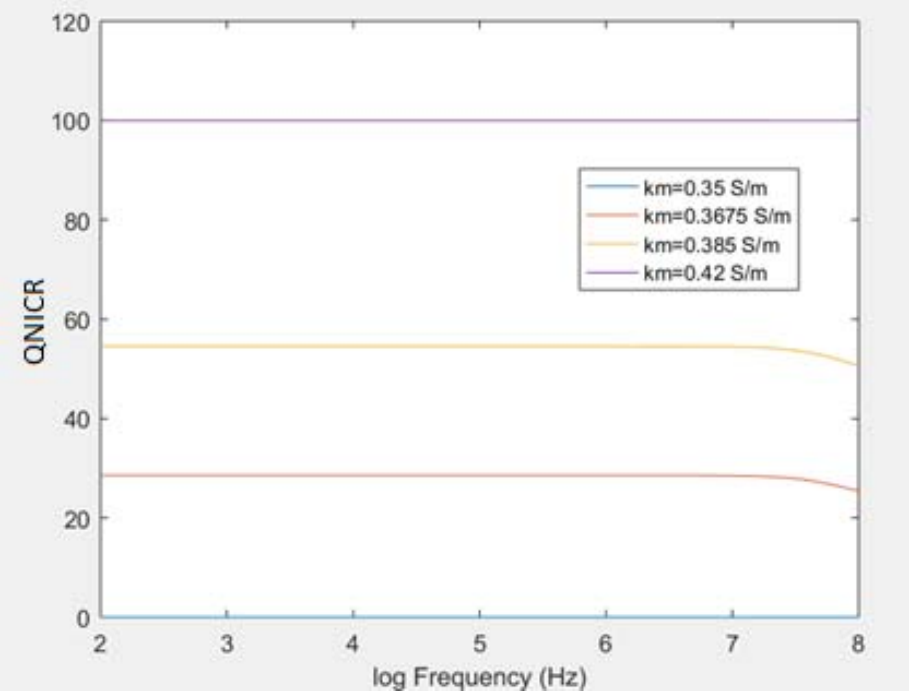

Figure 6-16: The QNICR (%) of two *E. coli* suspensions where antibiotics have partially inhibited the metabolism (km). The QNICR is increased to about 30% at <10 MHz (10^7 Hz) if the medium conductivity is 0.3675 S/m, to about 55% at <10 MHz if the medium conductivity is 0.385 S/m, to 100% at <10 MHz if the medium conductivity is 0.42 S/m, i.e. the same as that of the antibiotic-absent chamber.

In this simulation, significant changes in QNICR can be detected. Therefore, the impedance method can be used to detect metabolism inhibition.

In conclusion, it is difficult for the differential impedance method to directly detect changes in the phenotype or electrical properties of antibiotic-treated *E. coli*. However, the QNICR can be calculated as the growth ratio of the antibiotic-present and antibiotic-absent chambers. If the QNICR is 100%, the metabolism of the antibiotic-present chamber is the same as that of the antibiotic-absent chamber, and at that concentration, the antibiotic has no effect on the bacteria. If the QNICR is 0, the growth speed of antibiotic-present chamber is zero and the antibiotic has inhibited the bacterial metabolism entirely.

6.2.4 Two-terminal impedance spectrum

In the bottom of a 125-µm deep, 400-µm wide channel, two planar electrodes, each covering a 0.08 mm^2 area, are placed 1 mm apart. The channel is filled with an *E. coli* suspension, where 6 µF double layer capacitance is generated on each electrode and 10 pF parasitic capacitance is in parallel with the channel. Figure 6-17 shows the simulated impedance spectrum when the medium conductivity changes from 0.3 S/m to 0.7 S/m because of *E. coli* metabolism.

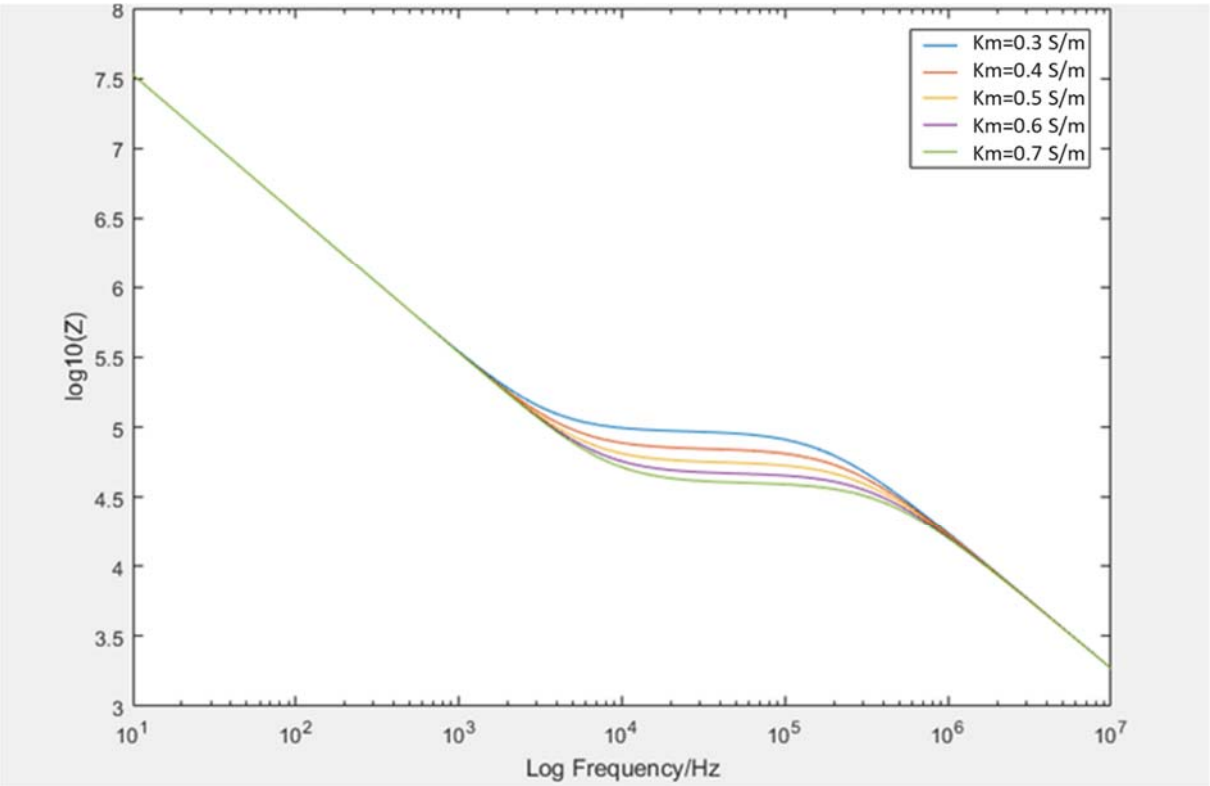

Figure 6-17: The simulated impedance spectrum from 10 Hz to 10 MHz when the solution conductivity (Km) changes from 0.3 S/m to 0.7 S/m because of bacterial metabolism. The simulation result shows that at <5 kHz, double layer capacitance dominates the impedance. At >500 kHz, parasitic capacitance dominates the impedance. An impedance magnitude of 10 kHz to 100 kHz can be used to monitor the medium conductivity.

6.3 DEP force on an *E. coli* bacterium

In this thesis, a DEP enrichment chip was fabricated to capture bacteria. Interdigitated electrodes generate the non-uniform electric field of the DEP chamber. COMSOL software is used to simulate the electric field strength of a hypothetical channel with interdigitated electrodes. Figure 6-18 shows the electric field strength of the channel.

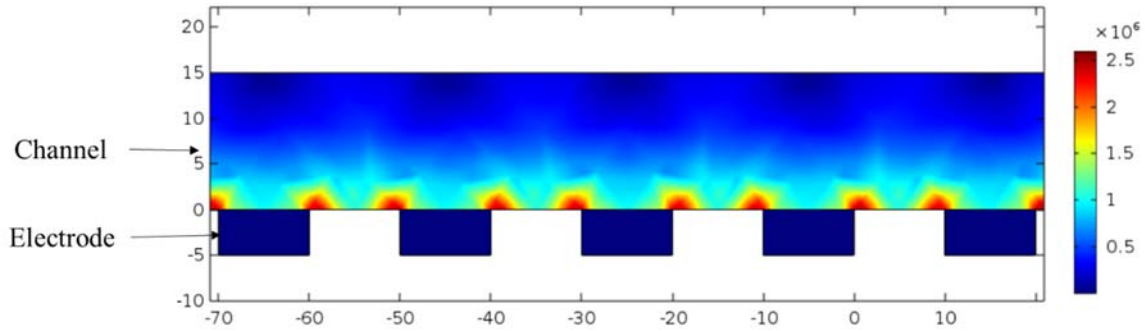

Figure 6-18: The electric field strength of a hypothetical channel via COMSOL software. The channel depth is set as 30 µm. At the bottom of the channel, 20-µm wide with 20-µm gap interdigitated electrodes are placed. A 50 V_{pp} AC signal is applied to the interdigitated electrodes. High electric field zones are at the edges of the electrodes. Low electric field zones are at the top of the channel.

According to equation (5.33), bacteria will catch different directions of forces according to the sign of $Re\{f_{CM}\}$. Figure 6-19 (a) and (b) show the bacteria enrichment positions in pDEP and nDEP settings, respectively.

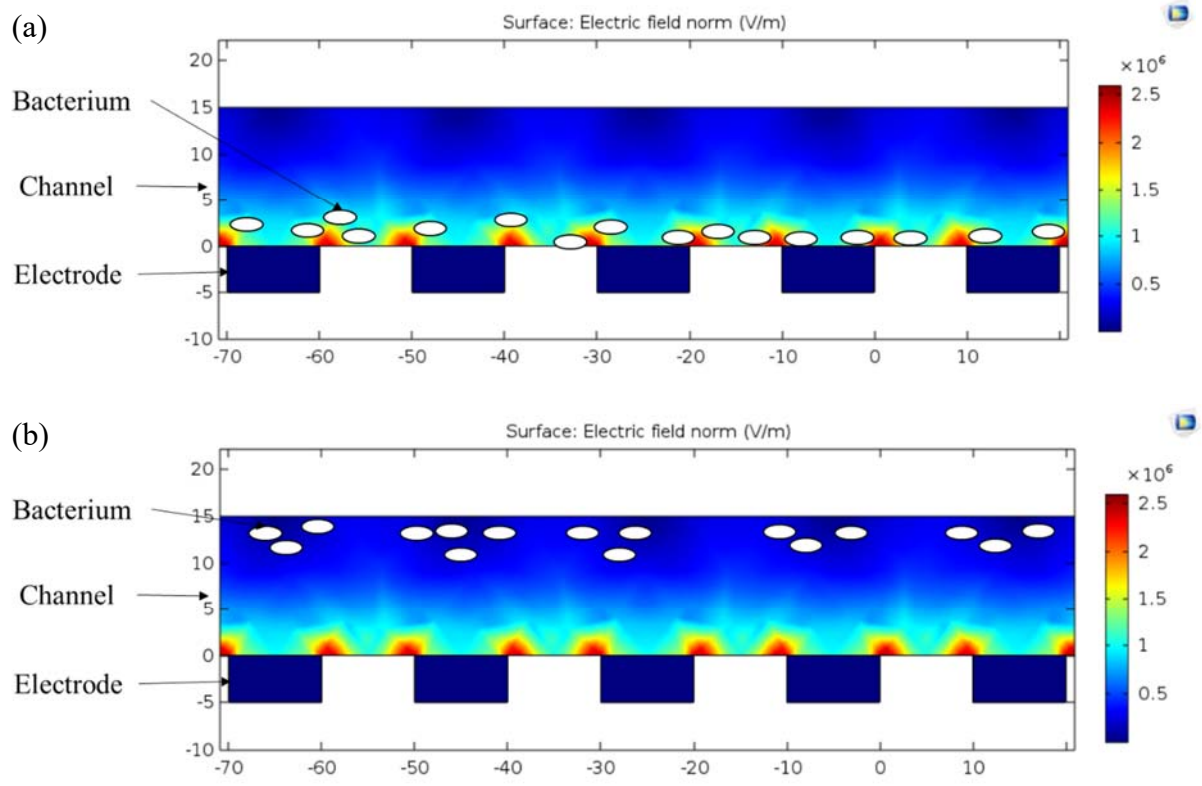

Figure 6-19: (a) In a pDEP setting, bacteria will be enriched at the edge of each electrode. (b) In an nDEP setting, bacteria will be enriched at the top of the channel.

In the DEP enrichment chip, bacteria need to be captured by pDEP force at the bottom of the, so $Re\{f_{CM}\}$ should be positive. For a single ellipsoid *E. coli*, $Re\{f_{CM}\}$ can be calculated from

the average of the frequency-dependent factor Ki for each three axes. Figure 6-20 shows the effective $Re\{f_{CM}\}$ according to medium conductivity.

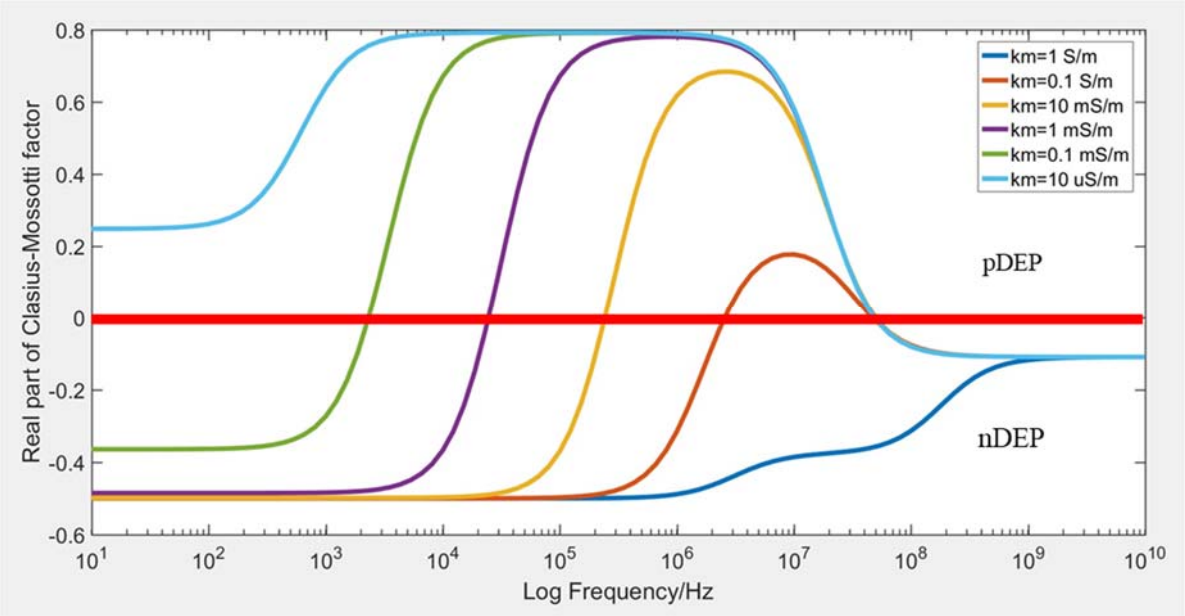

Figure 6-20: The effective $Re(f_{CM})$ according to the medium conductivity (km) of an *E. coli* bacterium. The red line indicates $Re(f_{CM}) = 0$. Only when medium conductivity is <10 mS/m (orange curve) can $Re(f_{CM})$ peak at around 0.7 at 1 MHz, which can provide a practical pDEP force in bacteria capture.

From this simulation, for pDEP at low frequencies (below 1 MHz), the medium conductivity should be <10 mS/m, which is lower than all broths or urine samples. Therefore, in the DEP-enhanced optical system, the bacterial sample conductivity should be reduced before DEP enrichment.

6.4 Discussion and conclusion

This chapter describes simulations of the impedance of an *E. coli* suspension, as well as the DEP force on an *E. coli* bacterium using the three-shell ellipsoid *E. coli* model is introduced. Bai *et al.* (2006) [114] used a similar three-shell simulation model and the permittivity and conductivity reported in Subsection 6.2.1 is similar to Bai *et al*. The simulation results in Subsection 6.2.2 and 6.2.3 demonstrate that when the *E. coli* concentration in the chamber is 10^7 CFU/mL, the low volume fraction means that impedance measurement can barely detect the bacteria.

The simulation results in Subsection 6.2.2 show that when the *E. coli* concentration in the chamber is 10^7 CFU/mL, bacterial metabolism can reduce the medium resistance of the chamber significantly. In Subsection 6.2.3, a differential impedance detection system can directly detect the QNICR based on bacterial metabolism. The only variable in the system is the antibiotic presence. In the differential measurement, the initial bacterial concentration, incubation temperature and other parameters should be exactly same for high-quality detection.

Moreover, when pDEP is used to trap *E. coli*, the medium conductivity of the *E. coli* suspension should be <10 mS/m, therefore, the medium conductivity of the bacterial suspension should be reduced to ensure pDEP capture.

Chapter 7: Methodology

7.1 Bacteria culture and treatment

7.1.1 Bacteria culture

The Technology Development Group (TDG) in Public Health England (PHE) supplied all bacterial strains. The sources of the bacterial strains include the National Collection of Type Cultures (NCTC), the American Type Culture Collection (ATCC), PHE Porton Down, PHE Colindale and University of Leeds. Two bacterial culture methods were used in the experiments: broth culture and plate culture.

In the broth culture, a bacterial isolate was incubated in 3 mL LB broth (Sigma-Aldrich, UK) or MH1 broth (Sigma-Aldrich, UK) on a shaker plate (200 rpm) overnight at 37°C.

In the plate culture, a bacterial isolate was incubated on tryptic soy agar (TSA, Sigma-Aldrich) overnight at 37°C.

Table 7-1 summarises the bacteria species, strains, genotype, name used in this thesis and the source of the bacterial sample tested by the three system.

Table 7-1: The bacteria species, strains, genotype/mutation, name used in this thesis and the source of the bacterial sample.

Bacteria Species	Bacteria Strains	Genotype	Name used in thesis	Source	Culture medium	Tested project
E. coli	TOP10	-	TOP10	PHE Porton Down	LB broth	Optical and pH
	TOP10	*bla*CTX-M-15	CTX-M	PHE Porton Down	LB broth	Optical and pH
	TOP10	*bla*TEM-1	TEM	PHE Porton Down	LB broth	Optical and pH
	NCTC-11341	*bla*CTX-M-15	11341	NCTC	TSA	pH
	NCTC-11560	*bla*TEM-1	11560	NCTC	LB broth and TSA	pH
	NCTC-13351	*bla*TEM-3	13351	NCTC	TSA	pH
	LEC-001	pmrAB	LEC001	University of Leeds	MH1 broth	Impedance
	NCTC- 12923	-	12923	NCTC	MH1 broth	Impedance

Entero-bacter aerogenes	NCTC-14099 (M546)	-	14099	NCTC	TSA	Optical
K. pneumo-niae	NCTC-13438	*bla**KPC*	13438	NCTC	TSA	pH
	M109	*bla**SHV*	M109	PHE Colindale	TSA	pH
	M70	-	M70	PHE Colindale	TSA	pH
	NCTC-13368	*bla**SHV-18*	13368	NCTC	MH1 broth	Impedance
	M6	-	M6	PHE Colindale	MH1 broth	Impedance
Proteus mirabilis	NCTC-13376	-	13376	NCTC	TSA	pH
S. Aureus	EMRSA-15	SCCmer IV	EMRSA 15	PHE Colindale	MH1 broth	Impedance
	ATCC- 9144 (NCTC- 6571)	-	9144	ATCC	MH1 broth	Impedance
A. baumannii	ATCC BAA1710	AYE	AYE	NCTC	MH1 broth	Impedance
	ATCC- 17978	-	17978	ATCC	MH1 broth	Impedance
P. aeruginosa	PAO1	-	PAO1	PHE Colindale	MH1 broth	Impedance
	NCTC- 13437	*bla**VIM-10*, *bla**VEB-1*	13437	NCTC	MH1 broth	Impedance

7.1.2 Sample treatment

In the optical and pH system experiments, after a broth overnight culture, 300 µL bacterial suspension was diluted in 9700 µL fresh LB broth for 1-hour subculture. Next, the OD of samples was set to 0.1 by LB broth, which corresponded 10^8 CFU/mL bacteria and diluted to specific bacterial concentrations in the experiments [244]. Subsequently, the bacterial concentration was counted using the plate count method. When *E. coli* CTX-M and *E. coli* TEM were used to detect the sensitivity of the optical and pH systems, 1mL cell subculture was transferred to an Eppendorf tube and centrifuged at 14000 *g* for 5 minutes. The supernatant was removed and 20 µL B-PER (500 mL, Thermo Fisher Scientific) was added, followed by 20-minute vortexing at 850 rpm at room temperature. Figure 7-1 shows a schematic diagram of the enzyme extraction workflow.

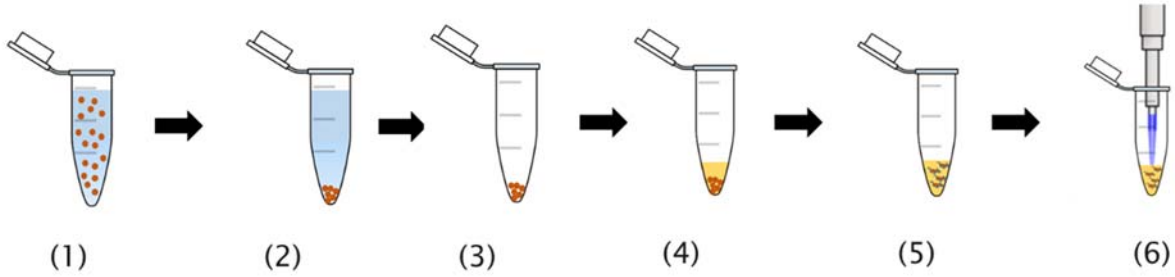

Figure 7-1: A schematic diagram of the enzyme extraction workflow. (1) *E. coli* (1 mL) was injected into a tube. (2) The tube was centrifuged at 14000 *g* for 5 minutes. (3) The supernatant was removed. (4) B-PER (20 µL) was added to the tube. (5) The tube was shaken at 850 rpm for 20 minutes to extract the proteins. (6) The lysates were removed for further experiments.

To verify that it was necessary to use the supernatant in assay, the lysates were further centrifuged at 10000 *g* for 5 minutes and the supernatant was used in assays.

In the optical and pH system experiments, after a plate overnight culture, a 1-loop (1 µL) colony was suspended in 40 µL B-PER for further detection, which corresponded 10^{10} CFU/mL [244].

In the impedance system experiments, the OD of overnight culture was checked by ultraviolet visible (UV-Vis) at 600 nm. In a 96-well plate, 200 µL bacterial suspension in MH1 broth with a final OD at 0.01 (consider 10^6 to 10^7 CFU/mL bacterial concentrations) at 64 µg/mL to 0 µg/mL antibiotics was prepared. The 96-well plate was incubated at 37°C for 21 hours, and the OD of each well was recorded every 15 minutes by a bench-top plate reader. MH1 broth, doxycycline, gentamicin, colistin, ciprofloxacin, imipenem and ceftazidime were purchased from Sigma-Aldrich.

7.2 DEP-enhanced optical system

The DEP-enhanced optical system consists of a filter, a DEP-based concentration chamber and an optical signal detection chip. In the first stage, a 0.22-µm sterile filter was used to increase the bacterial concentration in the sample and to reduce the medium conductivity. The bacteria were then concentrated using pDEP force. The optical detection chip detected a colorimetric change that results from β-lactamase hydrolysis of nitrocefin.

7.2.1 Filter

The filter system consists of a 0.22-µm filter, one waste bottle and three syringes. First, 10 mL sample was pushed into the front of the filter. Bacteria were blocked on the front of the filter, but the LB broth was flowed to the waste bottle. Then DI water (1 mL) was back-flushed into the filter. The re-suspended bacteria in DI water were collected by a 1-mL syringe. The medium conductivity of the bacterial suspension in LB broth and that of the bacterial suspension in DI water was measured by a conductivity meter (RS Pro, 123-8777), and bacterial concentrations were counted using the plate count method.

7.2.2 DEP chip

The DEP chip (15.6 mm × 22.2 mm) comprises interdigitated Pt electrodes (100 pairs, 20 µm × 4.0 mm with a 20-µm gap) on a 0.7-mm thick glass substrate with a PDMS channel (4.0 mm × 4.0 mm electrodes with 50-µm depth) on top. The Pt electrodes were manufactured by standard photolithography (Figure 7-2).

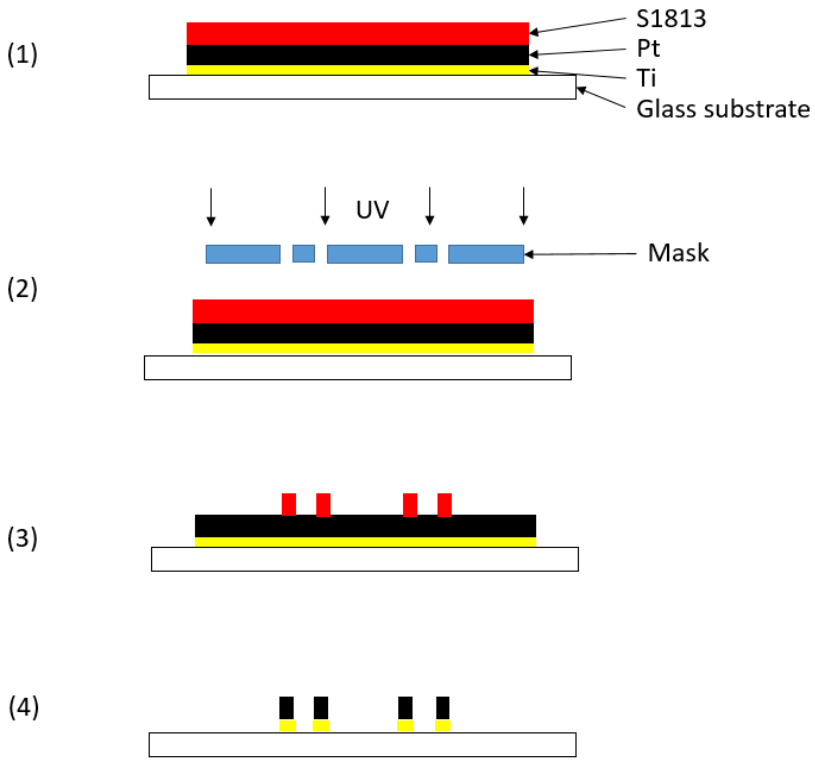

Figure 7-2: A brief description of the interdigitated electrode fabrication. (1) Ti (100 nm) and Pt (300 nm) are sputtered on a 4-inch glass wafer. Then, S1813 photoresist is spun on top. (2) The S1813 photoresist is exposed to UV through a mask. (3) The unexposed S1813 is washed out. The wafer is etched by oxygen plasma. (4) Electrodes are patterned. The photoresist is washed.

The channel was moulded with PDMS (Sylgard 184 Silicone Elastomer, UK) with base and curing agent mixed in a 10:1 ratio. Moulds for the channel were 3D-printed in acylonitrile butadiene styrene (ABS) and cured at 100°C overnight. Liquid PDMS was degassed first, then poured on the mould and baked in a 60°C oven overnight. Input and output were punched in 1-mm diameter. The glass substrate and PDMS channel were bonded by oxygen plasma (Femto, Diener Electronic, USA) for 30 seconds.

An alternating current (AC) signal (1 V_{PP}, 1 MHz) was generated by a signal generator (TTi 100 MHz arbitrary waveform generator, TGA12104), amplified by a 50-time amplifier (Falco System DC-5 MHz high-voltage amplifier, WMA-300) and connected to the interdigitated electrodes as 50 V_{PP}, 1 MHz AC signal. Figure 7-3 (a) shows the schematic diagram for the DEP enrichment, and Figure 7-3 (b) shows the electric field strength of the DEP enrichment chamber as simulated by COMSOL software.

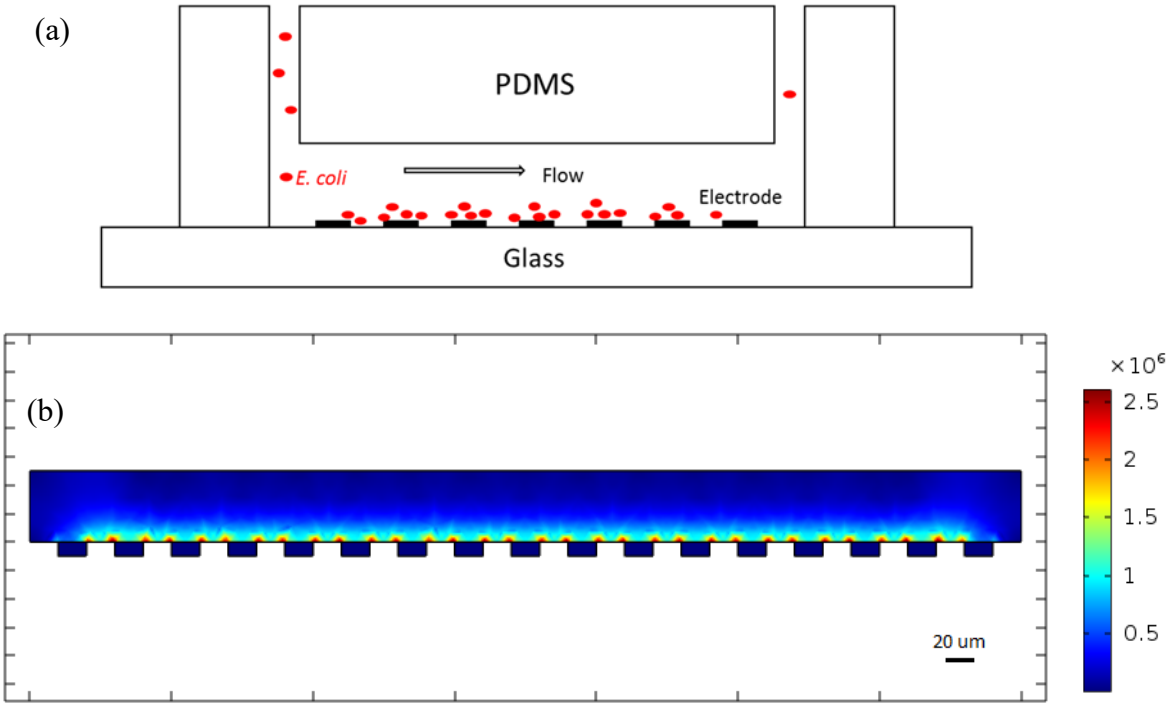

Figure 7-3: (a) A schematic diagram of the bacterial enrichment chamber. The PDMS channel was 50-µm deep. Pt electrodes (100 pairs, 20 µm × 4.0 mm with 20-µm gap) were patterned on a 0.7-mm thick glass substrate. (b) Electric field strength of the DEP chip simulated by COMSOL Multiphysics 5.3a. The high electric field zone is the edge of electrodes.

Diluted *E. coli* TOP10 suspension (1 mL) in DI water was pushed through the DEP enrichment chamber by a syringe pump at different flow rates. The waste was collected in a 1-mL Eppendorf tube. When the 1-mL syringe was empty, the applied AC voltage was cut off. Subsequently, 100 µL DI water was pumped into the chamber at 200 µL/min to collect the captured bacteria in another 1-mL Eppendorf tube. The bacterial concentration of the *E. coli* suspension in the initial syringe, waste Eppendorf and collection Eppendorf were counted using the plate count method.

7.2.3 Optical chip

The channels on the optical chip were milled (LPKF Protomat S100 micromill) from two pieces of 5-mm thick tinted PMMA board [73]. The PMMA boards were exposed to 1 M chloroform ($CHCl_3$, Sigma-Aldrich) for 11 minutes and bonded in a hot press (LPKF laser and electronics AG, Garbsen, Germany). The optical chip had eight absorbance channels (25-mm path length, 4-µL volume) to which a 470-nm LED (HLMP-CB1A-XY0DD: 5MM BLUE) and a light-voltage converter (TLS257, Texas Advanced Optoelectronic Solutions) were adhered on either side by a UV-curable optical adhesive (NOA-68, Norland). The light from the LED was coupled into the absorbance channel and the light-voltage converter collected the transmitted light. Figure 7-4 (a) shows a schematic graph of the optical chip and Figure 7-4 (b) shows the cross-view of a single channel.

(a)

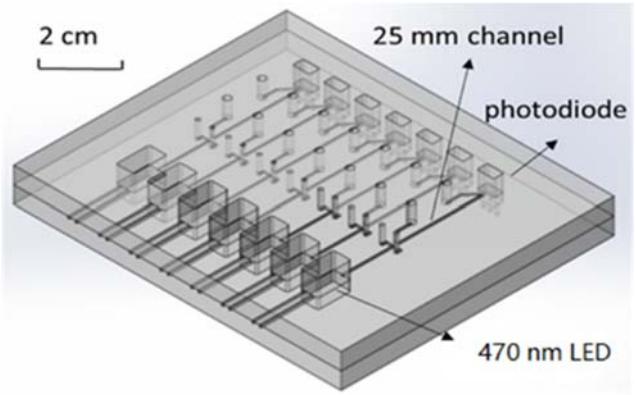

(b)

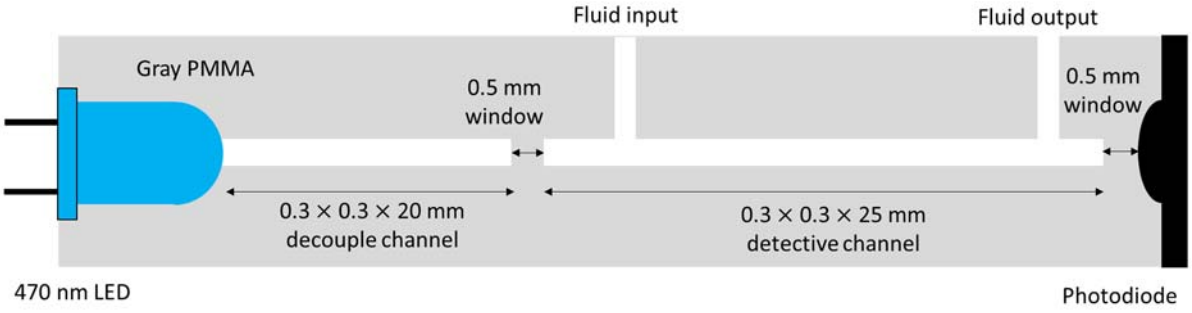

Figure 7-4: (a) A schematic diagram of the PMMA optical chip and (b) the cross-view of the optical chip. The LED generated light at 470±10 nm wavelength. The detection channels were 300-µm wide, 300-µm deep and 25-mm long. The decoupling channels were 300-µm wide, 300-µm deep and 20-mm long. Each chip had eight absorbance detection channels.

The pins of the LEDs and light-voltage converters were soldered to a customized print circuit board (PCB). The LEDs were powered by a DC power supply (Agilent E3631A). To compensate for slight misalignment during fabrication, the voltage applied to each LED was calibrated to give the same photodiode output with a DI water filling channel. A data acquisition (DAQ) card (NI-6008, National Instruments) recorded the output voltage of the light-voltage converters.

The light intensity of a photodiode is proportional to its current output. The TLS257 light-voltage converter integrates a photodiode and a transimpedance amplifier, so the light intensity absorbed by the photodiode is proportional to its voltage output and can be written as:

$$V = R_e I_{DET} \tag{7.1}$$

where V is the output voltage of the light-voltage converter, and R_e is the internal resistance of the light-voltage converter, which is determined by the device manufacturer and remains constant. I_{DET} is the light density passing through the photodiode sensitive area.

The absorbance value of the optical chip was determined from the photodiode output voltage, given by:

$$\frac{I}{I_0} = \frac{I/R_e}{I_0/R_e} = \frac{V}{V_0} \tag{7.2}$$

where V_0 is the initial photodiode voltage.

The absorbance detected by the optical chip can be calculated as:

$$A = -\log_{10}(\frac{V}{V_0}) \tag{7.3}$$

The optical chip was calibrated by Atto 488 dye, which has an absorbance peak at 488 nm. Atto 488 (1–10 μM) was injected into the channels in the optical chip and a UV-Vis spectrometer (NanoDrop 2000, NanoDrop, UK) simultaneously.

7.2.4 Method (optical chip)

The kinetic parameters of a commercial β-lactamase, TEM-1, were detected by the optical chip and plate reader simultaneously. TEM-1 protein (0.49 mg/mL, 17 μM, Life Science, UK) was diluted to 1 μM by 0.1 M TBS and stored in a -85°C freezer. The kinetic parameters were tested with final concentrations of 50 μM nitrocefin solution with 0.4–8 nM (diluted by 0.1 M TSB) TEM-1 protein.

18 μL whole lysates, 50 μL TBS (0.1 M), 32 μL B-PER (to elute the sample through the channel) and 100 μL nitrocefin (100 μM) were mixed in a chamber of a 96-well plate. The absorbance of the 96-well plates was detected using a plate reader.

18 μL whole lysates and 2 μL nitrocefin (500 μM) were mixed. The mixed solution (10 μL) was injected into a channel on the optical chip and the absorbance was detected.

7.2.5 Method (DEP-enhanced optical system)

Different concentrations of *E. coli* CTX-M or wild-type *E. coli* TOP10 were diluted in 10 mL LB broth. Then, the presence of β-lactamases in the bacterial sample was detected using the integrated DEP-enhanced optical system. Figure 7-5 shows a schematic diagram of the integrated DEP-enhanced optical system workflow.

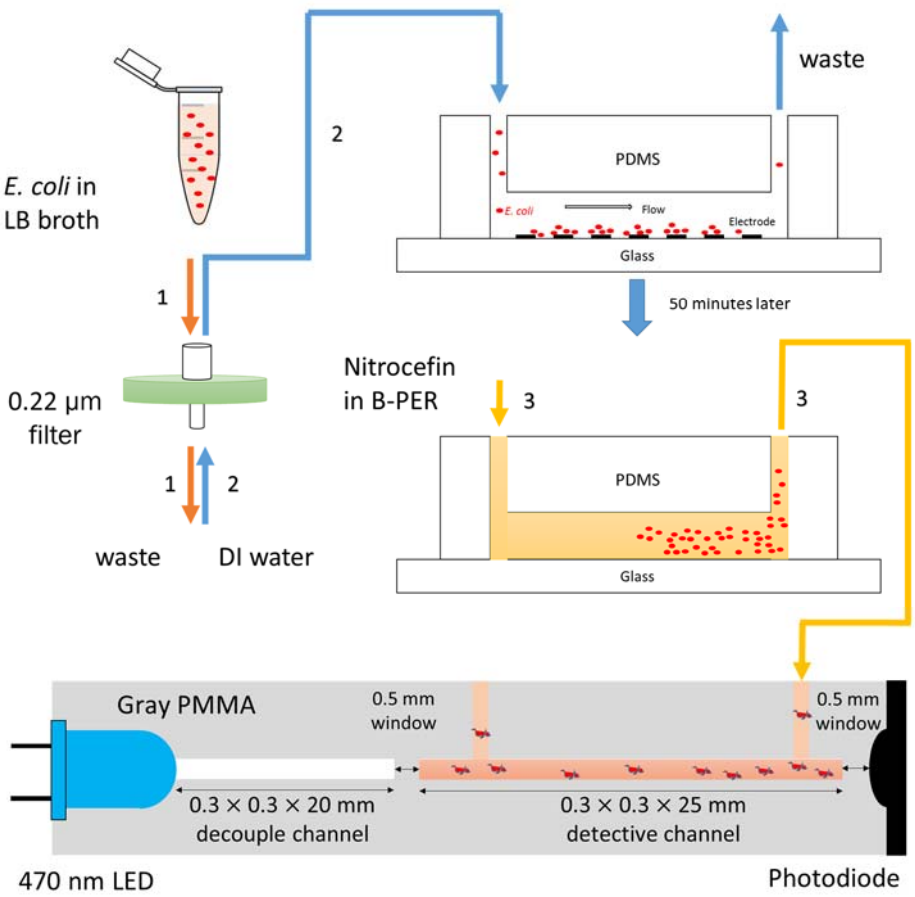

Figure 7-5: A schematic diagram of the integrated DEP-enhanced optical system workflow. Bacterial sample (10 mL) was manually pushed through a sterile filter using a syringe. The filter was back-flushed with 1 mL DI water to produce a concentrated bacterial suspension. The bacterial suspension was pumped into the DEP chip and the bacteria were captured on the electrodes by pDEP force. The concentrated bacteria were then retrieved and lysed for protein extraction in 100 µL solution containing nitrocefin. The lysed bacterial solution and the colorimetric substrate were immediately introduced into the optical module to monitor the absorbance change.

7.3 pH system

7.3.1 pH sensor

Each pH-sensing chamber contains an IrOx electrode, an Ag/AgCl film reference electrode and 2 Pt electrodes (not used). All electrodes were connected to external contacts by metal lines. Figure 7-7 (a) shows a photo of the IrOx pH sensor and Figure 7-7 (b) shows the layout of the electrodes in a pH detection chamber.

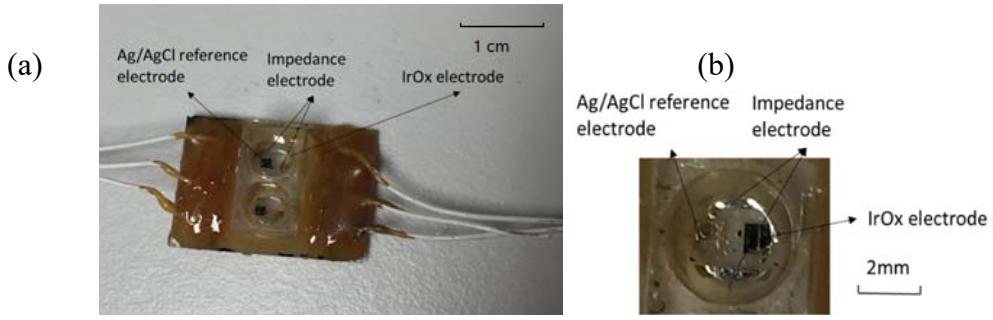

Figure 7-6: (a) A photo of the IrOx pH sensor and (b) the layout of electrodes in a pH detection chamber. Each pH-sensing chamber contains an IrOx electrode, an Ag/AgCl film reference electrode and 2 Pt electrodes (not used). The IrOx film electrodes and the Ag/AgCl reference electrodes are 1 × 1 mm and are spaced 0.8 mm apart. The Pt electrodes are 0.4 mm × 2.8 mm and are spaced 2 mm apart.

The IrOx and Ag/AgCl electrodes were based on Pt electrodes manufactured by standard photolithography, and then covered by IrOx or Ag/AgCl films according to sol-gel and electroplating, respectively. The IrOx and Ag/AgCl electrode filming utilised the protocol reported by Huang *et al.* (2012). Figure 7-8 (a–f) shows the IrOx and Ag/AgCl electrode fabrication process. Figure 7-8 (g) shows a schematic diagram of the IrOx pH sensor.

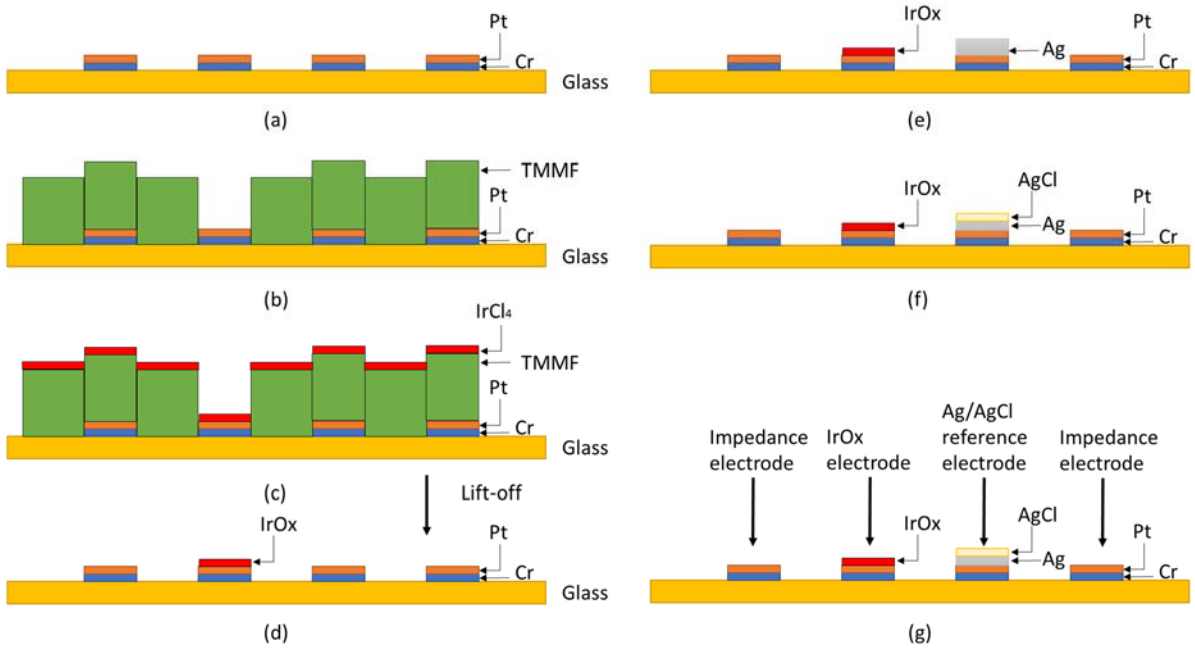

Figure 7-7: The IrOx and Ag/AgCl electrode fabrication process. (a) A 0.7-mm glass substrate wafer is coated with a 100-nm thick Cr layer, followed by a 300-nm thick Pt layer by sputtering. The S1813 positive photoresist is spun on the Pt surface. The wafer is exposed to UV light through an electrode pattern mask. Plasma is used to etch the exposed wafer. Patterned Pt electrodes are formed. (b) TMMF photoresist (S2000, Tokyo Ohka Kogyo Co., Ltd, Japan) is bound to the wafer by a press and the wafer is exposed to UV through an IrOx electrode pattern mask. Thus, a window is patterned on a designed IrOx electrode. (c) Anhydrous iridium chloride ($IrCl_4$, 1 g), 42 mL ethanol (C_2H_5OH) and 10 mL acetic acid (CH_3COOH) are mixed as a coating solution. The coating solution is stirred with a magnetic rod for 1 h, and then the window is dipped in it four times to coat on a thin $IrCl_4$ layer. The wafer is annealed at 300°C for 5 hours in air. (d) The

TMMF scarified layer is removed with tweezers and the wafer is washed with ethanol. (e) Metal cables are soldered to the connection points and protected by epoxy gel (RS Corporation, UK). The wafer is immersed in silver electroplating solution (Spa Company, UK) and 0.5 mA DC current is applied to the reference electrodes for 15 minutes to coat them with an Ag layer. (f) The wafer is immersed in 15% NaClO solution (Sigma-Aldrich) for 4 minutes to coat a brown AgCl layer over the Ag layer. The Ag/AgCl electrode is rinsed with DI water and annealed in a 60°C oven for 12 hours for saturation and stabilization. (g) The schematic diagram of the IrOx pH sensor.

A 15-nm thick IrOx sensing film was coated using sol–gel, and a 50-nm thick Ag layer was coated by electroplating. A portion of the Ag was then converted to AgCl. The detection chamber was patterned by a laser cutter (Epilog Laser Mini, USA) on PMMA board. The detection chamber was 3 mm in diameter and 5-mm thicken, with a total volume of 35.33 µL. The detection chamber was connected to the glass substrate by double-sided tape (3M Company, USA). A potentiostat (PalmSens 3, Palmsens, the Netherlands) was used to record the OCP between the IrOx electrode and the Ag/AgCl electrode via an 8-channel multiplexer (MUX 8, PalmSens). PSTrace 4.8 software was used to control the measurement system and record the OCP. The pH was calculated from the OCP based on calibration results by MATLAB.

7.3.2 pH indicator

The pH indicator was prepared based on the recipe by Raghuraman *et al.* (2006) [245]. Phenol red, chlorophenol red and bromophenol blue were mixed at a 0.46:0.25:0.29 (mole fraction) ratio in DI water. The initial pH indicator concentration was 1 mg/mL (2.16 mM). The pH value was quantified by the absorbance at 560 nm and 450 nm, written as:

$$pH = k \times (Abs_{560nm} - Abs_{450nm}) = k \times \Delta Abs \quad (6.1)$$

Where Abs_{560nm} is the absorbance at 560 nm and Abs_{450nm} is the absorbance at 450 nm in the unit AU. A bench-top plate reader (Promega, UK) was used to record the absorbance at 560 nm and 450 nm in a 96-well plate.

7.3.3 Calibration

Commercial pH buffers at pH 4, pH 6, pH 7, pH 9 and pH 10 (HANNA calibration pH buffer 6004, 6006, 6007, 6009 and 6010, Sigma-Aldrich) were used to calibrate the pH sensor and pH indicator. For the pH indicator, 161.5 µL HANNA pH buffer was mixed with 8.5 µL pH indicator in one well of a 96-well plate. The absorbance of the well at 560 nm and 450 nm was recorded. For the pH sensor, 30 μL HANNA calibration buffer was pipetted into the sensor chamber. The OCP between the IrOx electrode and the Ag/AgCl reference electrode was recorded.

7.3.4 Method

Carbenicillin, a penicillin group β-lactam antibiotic, was used as a model β-lactam substrate to test for the presence of β-lactamases.

The kinetic parameters of a commercial β-lactamase, TEM-1, were detected by a pH sensor and a pH indicator. TEM-1 protein (0.49 mg/mL, 17 μM, Life Science) was diluted by 1 mM HEPES buffer to 1 μM and stored in a -85°C freezer. In the experiment, final concentrations of 10 μM carbenicillin (Sigma-Aldrich), 1 mM HEPES (pH buffer, Sigma-Aldrich), 30 mM NaCl (to stabilize the Ag/AgCl reference electrode, Sigma-Aldrich), 1–4 nM TEM-1 protein and 108 μM pH indicator were mixed in a well plate in a volume of 200 μL. 30 μL of 200 μL mixing solution was injected into the chamber on the pH sensor. The absorbance (450 nm and 560 nm) of 170 μL remaining solution was detected by the plate reader. The pH of the mixing solution was measured by pH sensor and plate reader simultaneously.

When the pH indicator was used to measure the pH of the carbenicillin solution, 20 μL supernatant of bacterial lysates or bacterial lysates extracted from different concentrations of bacterial samples was mixed with 180 μL carbenicillin solution (5 mM) in a chamber of a 96-well plate.

When the pH sensor was used to measure the pH of the carbenicillin solution, 20 μL supernatant of bacterial lysate extracted from different concentrations of bacteria samples was mixed with 10 μL carbenicillin solution (50 mM) in the pH sensing chamber.

7.4 Impedance system

The impedance system detects the impedance change of six bacterial suspensions simultaneously. Five suspensions consisted of bacteria and antibiotics; the remaining suspension had no antibiotics. The two-terminal impedance detection system were used to measure the impedance spectrum of bacterial suspensions from 10 Hz to 10 MHz. The four-terminal impedance detection system were used to measure the impedance of bacterial suspensions at 10 Hz. Figure 7-8 shows a schematic diagram of the two-terminal system.

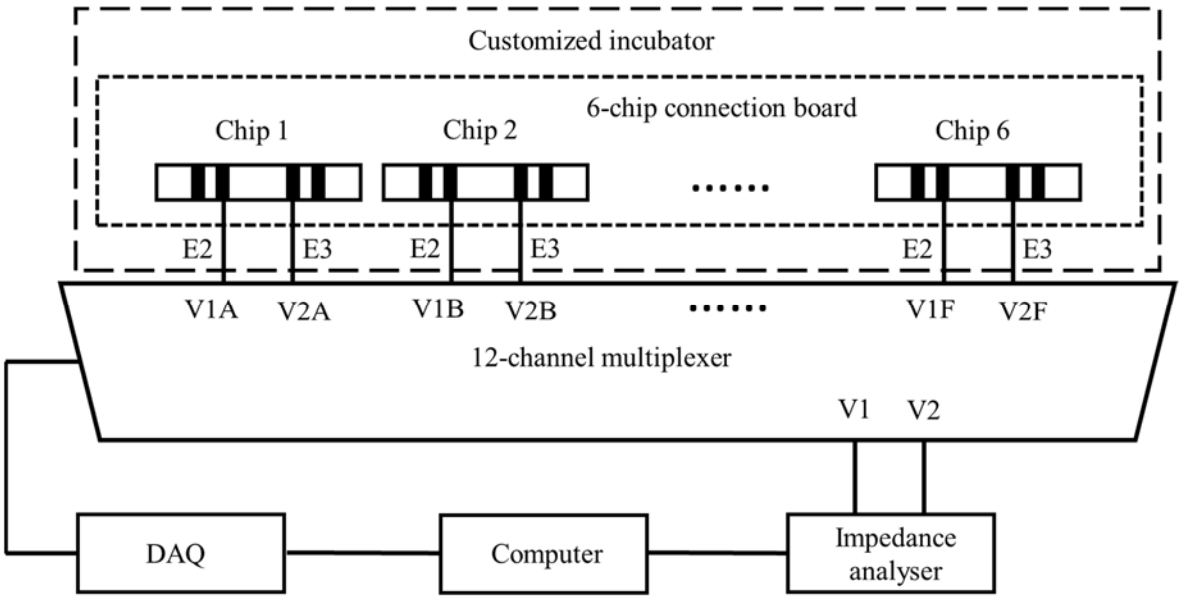

Figure 7-8: A schematic diagram of the two-terminal system. A customized incubator contains a 6-chip connection board, which consists of six impedance detection chips. Each chip has four electrodes in parallel. The middle electrodes (E2 and E3) are connected to a 12-channel multiplexer, which is controlled by a DAQ card. The multiplexer is connected to an impedance analyser. A computer controls the impedance analyser and DAQ card.

Figure 7-9 shows a schematic diagram of the four-terminal system.

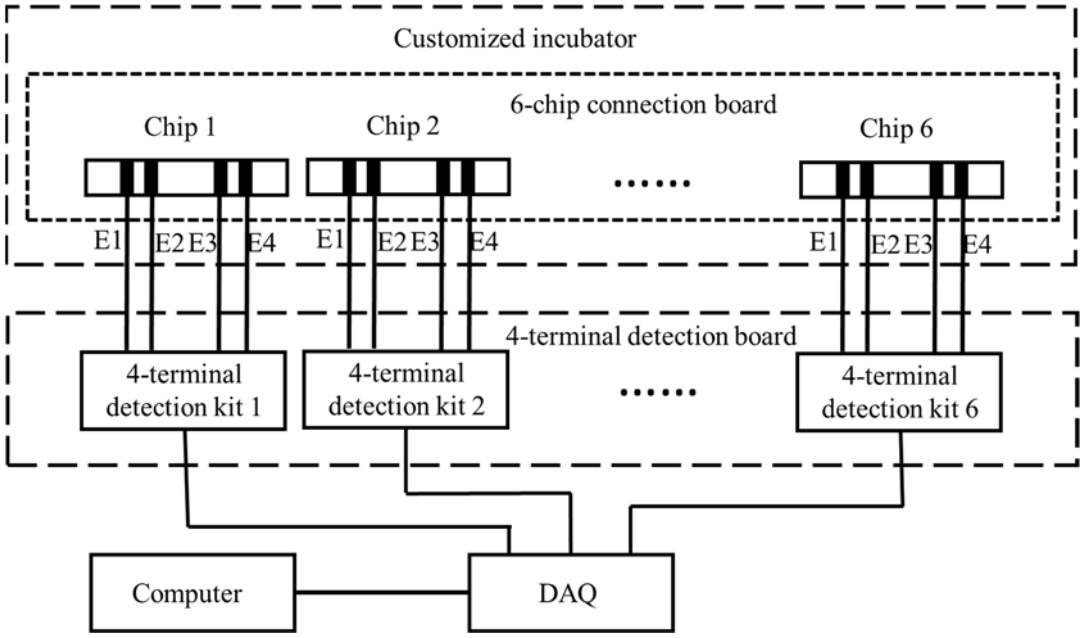

Figure 7-9: A schematic diagram of the four-terminal system. The customized incubator, 6-chip connection board and impedance detection chips are the same as that in the two-terminal system. The four electrodes (E1, E2, E3, E4) are connected to a four-terminal detection kit. The four-terminal detection board consists of six four-terminal detection kits. The detection board is connected to a DAQ card, which is linked with a computer.

7.4.1 Impedance detection

Each impedance detection chip consists of four Pt electrodes on a 0.7-mm thick glass substrate with a PMMA microfluidic channel. The microfluidic channel was made from two PMMA films. The bottom PMMA layer contained a detection channel that was 75-µm thick, 400-µm wide and 2-mm long. The top PMMA layer contained two mineral oil chambers. Each mineral oil chamber was 2-mm thick, 2-mm wide and 400-µm long. The detection channel and the mineral oil chambers were milled by a laser cutter. The two PMMA films were bound together and attached to the glass wafer with double-side tape (3M, 50-µm thick). Figure 7-10 shows the cross-view of one impedance detection chamber.

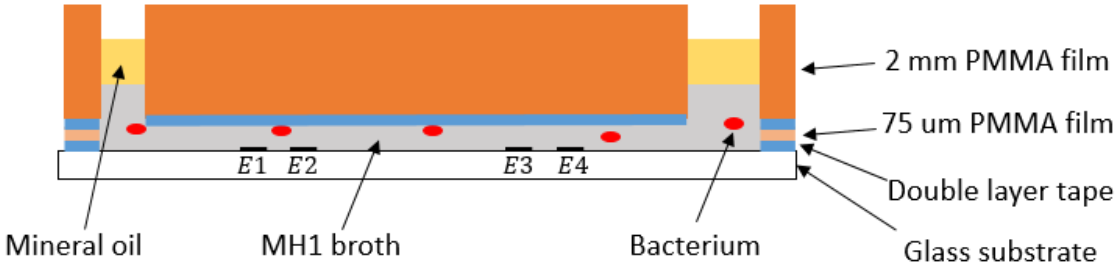

Figure 7-10: Cross view of an impedance detection chip. The inner two electrodes (E2 and E3) were 200-µm wide and spaced 1 mm apart. The outer two electrodes (E1 and E4) were 200-µm wide and spaced 200 µm apart from E2 and E3, respectively. The PMMA channel was 125-µm deep, 2-mm long and 400-µm wide.

Figure 7-12 shows a customized detection board containing six impedance detection chips.

Figure 7-11: A photo of a customized detection board. The detection board contains six impedance detection chips and three customized PCB holders. Each PCB holder was used to transmit signals for two impedance detection chips.

(1) Two-terminal impedance detection

The inner two electrodes (E2 and E3) in an impedance detection chip were connected to a 12-channel multiplexer (ADG726, Analogue Devices, USA) by a 0.2-metre ribbon cable (Farnell, 20 ways). The multiplexer was controlled by a Labview-coded DAQ card (NI 6251, National Instrument). The impedance spectrum of each impedance detection chip was detected by an α-

impedance analyser (Novocontrol Technologies GmbH & Co.) with ZG4 interface. The impedance analyser was controlled using WINDeta software was used to control. The detection voltage was set as 0.5 V_{PP} in the frequency range of 10 Hz to 10 MHz.

(2) Four-terminal impedance detection

Electrodes E1, E2, E3 and E4 on an impedance detection chip were directly connected to a customized four-terminal impedance detection board by a coaxial cable. Figure 7-12 (a) shows a simplified circuit of each four-terminal impedance detection kit. Figure 7-12 (b) shows a photo of the customized four-terminal impedance detection board.

(a)

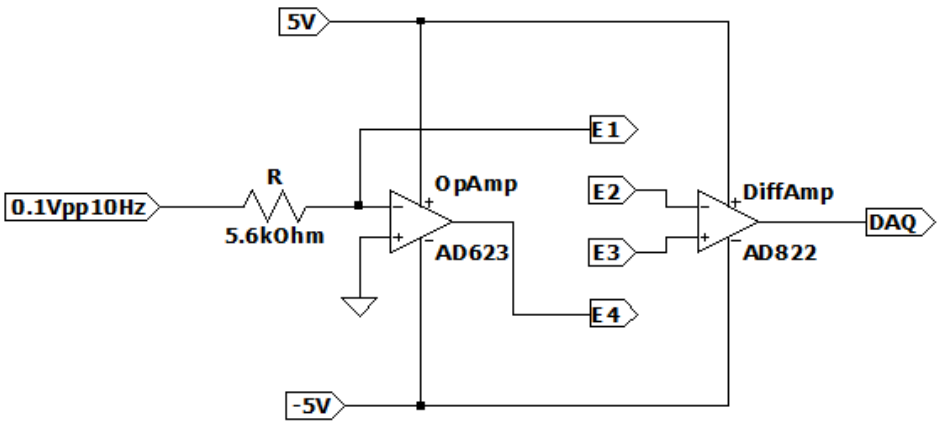

(b)

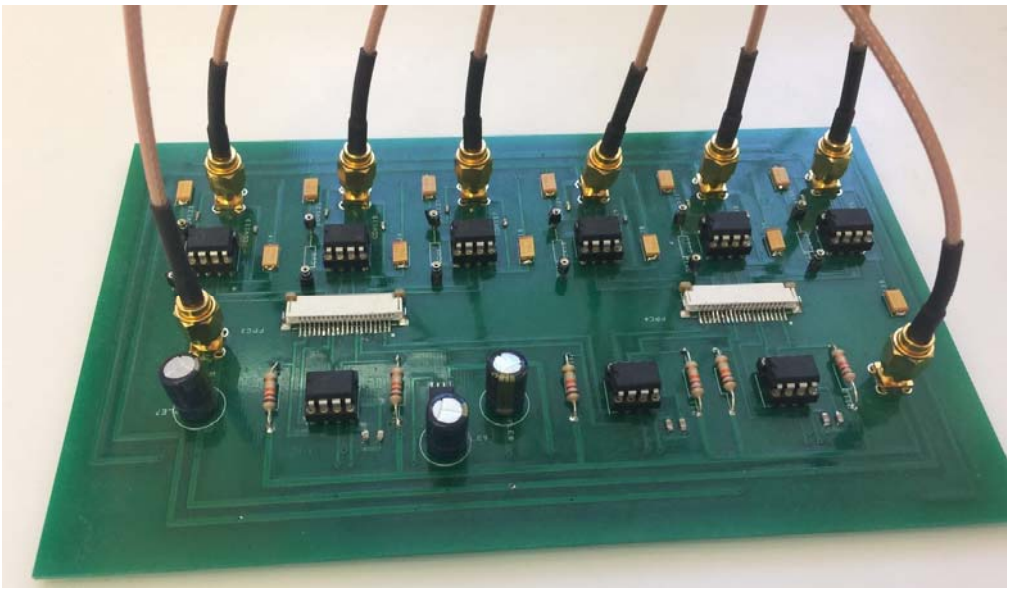

Figure 7-12: (a) Simplified circuit of a four-terminal impedance detection kit. A sine signal (10 Hz, 0.1 V_{pp}) was generated by a LabVIEW-coded DAQ card. An operational amplifier (AD623, OpAmp) and resistor (5.6 kOhm) formed a TCA, which provided 18 µA constant AC between the outer electrodes (E1 and E4). The differential voltage between the inner electrodes (E2 and E3) was detected by a differential amplifier (AD822, DiffAmp). The power supply of the AD623 and AD822 amplifiers was +5 V and -5 V. The output voltage of the differential amplifier was collected by a DAQ card. (b) A photo of the customized four-terminal impedance detection board with six

four-terminal impedance detection kits in parallel. Each AD623 amplifier was used to generate a constant current for two chips.

7.4.2 Customized incubator

In the customized incubator, a PT100 thermocouple was placed beside the detection board for real-time temperature monitoring. Two Kapton heaters (Polyimide Insulated Flexible Heaters, Omega, USA) were attached to the bottom at the customized incubator as the thermal source. A wet tissue was placed on the top of Kapton heaters to stabilize the temperature. A proportional-integral-derivative (PID) controller (Red Lion PXU30020, USA) was used to control the current though Kapton heaters based on the feedback of the thermal couple. The temperature of the customized incubator was set as 37°C.

7.4.3 Calibration

Aqueous solutions at 0.35 S/m, 0.45 S/m, 0.55 S/m, 0.65 S/m and 0.75 S/m conductivity were prepared by pipetting 3 M sodium chloride (NaCl, Sigma-Aldrich) solution into DI water. The conductivity of the calibration solutions was checked using a commercial conductivity meter (RS PRO Precision Conductivity Meter, 123-8777). Aqueous solution (2 μL) was injected into the detection channel. Mineral oil (8 μL) was dripped gently on the mineral oil chambers to prevent evaporation.

7.4.4 Method

In a row of 96-well plates (12 chambers), a 2-fold gradient of antibiotic concentrations were prepared by serial dilution. The antibiotic dilutions were mixed with the test bacteria in MH1 broth. One control chamber contained test bacteria with fresh MH1. One blank chamber contained fresh MH1 broth. The total volume in each chamber was 200 μL and the initial bacterial OD was standardised at 0.01. The test solution (2 μL) was injected into an impedance detection chamber, and 8 μL mineral oil was gently pipetted on the mineral oil chamber to prevent evaporation. The solution resistance of each chamber was detected. Then, the impedance detection chambers were incubated at 37° C for 1 hour. Subsequently, the solution resistance of each chamber was detected again.

In the MIC test, the impedance of the bacterial suspension at 10 Hz was detected by the four-terminal detection system. In the blind test, the impedance magnitude at 10 kHz of the bacterial suspension was recorded by the two-terminal detection system. The ceftazidime, colistin, ciprofloxacin, gentamicin and doxycycline QNICRs for *K. pneumoniae*, *A. baumannii, S. aureus, E. coli, P aeruginosa* strains were calculated.

Chapter 8: Results and discussions

8.1 DEP-enhanced optical system

8.1.1 Optical chip calibration

The absorbance at 470 nm of 1–10 μM Atto 488 was measured by a UV spectrometer and the optical chip simultaneously. The UV-Vis spectrometer had a 1 mm path length and the length of the detection channels in the optical chip was 24.52 ± 0.02 mm. Figure 8-1 shows the absorbance of the Atto 488 detected by the optical chip and the UV-Vis spectrometer at 470 nm.

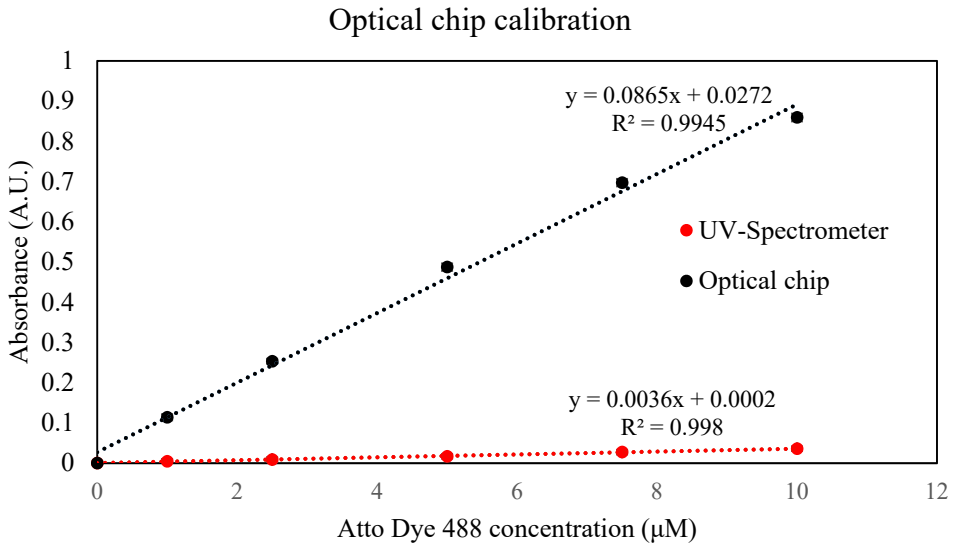

Figure 8-1: Absorbance against Atto 488 concentration. The optical chip showed 24.44 ± 0.17 times higher sensitivity than the UV-Vis spectrometer. The experiment was repeated three times; error bars represent the standard deviations of three measurements.

The optical chip had 24.44 ± 0.17 times higher sensitivity than the UV-Vis spectrometer, which was 99.67% of the path length quotient between the chip and the spectrometer. The difference between may stem from random noise or the manufacture error of the UV-Vis spectrometer, which path length was not exactly 1.00 mm. The lines of best fit had offsets (0.0272 A.U. and 0.0002 A.U., respectively) with zero, this could be the reason for the very slight discrepancy as well. The standard deviations of the optical chip from three repeats was 1.03 mA.U.. Therefore, the LoD (3σ) of the optical chip was 3.1 mA.U..

8.1.2 Kinetic parameters

The enzyme reaction velocity is given by the Michaelis-Menten equation as:

$$v = V_{max}[s]/(K_M + [s]) \quad (8.1)$$

Where V_{max} is the maximum initial velocity of the reaction, K_M is the Michaelis-Menten constant (the substrate concentration needed to achieve a half-maximum enzyme velocity), k_{cat} is the turn over number, $[s]$ is the substrate concentration and v is the reaction speed of the enzyme reaction [39]. The molar absorption coefficient of nitrocefin is 15000 $M^{-1}cm^{-1}$, which is cited from Faheem *et al.* (2013) [246].

The kinetic parameters of an enzyme are determined from a Lineweaver-Burk plot, which is a plot of the reciprocal substrate concentration versus reciprocal maximum reaction speed in different enzyme concentrations [74]. The slope of the Lineweaver-Burk plot is K_M divided by V_{max}, calculated as:

$$slope = \frac{K_M}{V_{max}} \quad (8.2)$$

The value when the fitted line crosses the y-axis equals to $\frac{1}{V_{max}}$, and the k_{cat} can be calculated as $\frac{V_{max}}{[E]}$, where $[E]$ is the enzyme concentration. The value when the fitted line crosses the x axis equals to $-\frac{1}{K_M}$.

The kinetic parameters of the nitrocefin–TEM-1 reaction were measured using a bench-top plate reader at 470 nm and the optical chip at 470 nm simultaneously. Figure 8-2 (a) and Figure 8-2 (b) show the Lineweaver-Burk plots for TEM-1 measured by the plate reader and the chip, respectively. Table 8-1 shows the K_M and k_{cat} calculated from the plots.

(a)

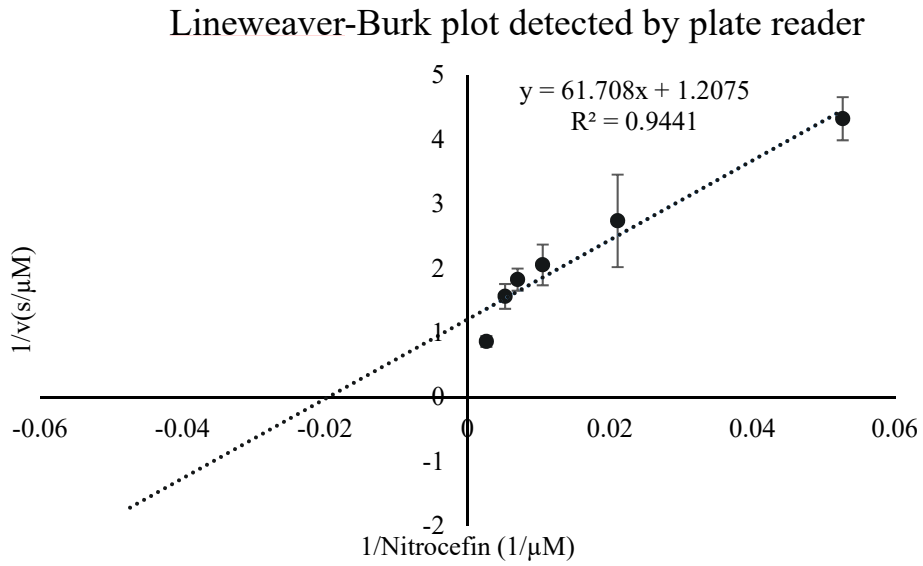

(b)

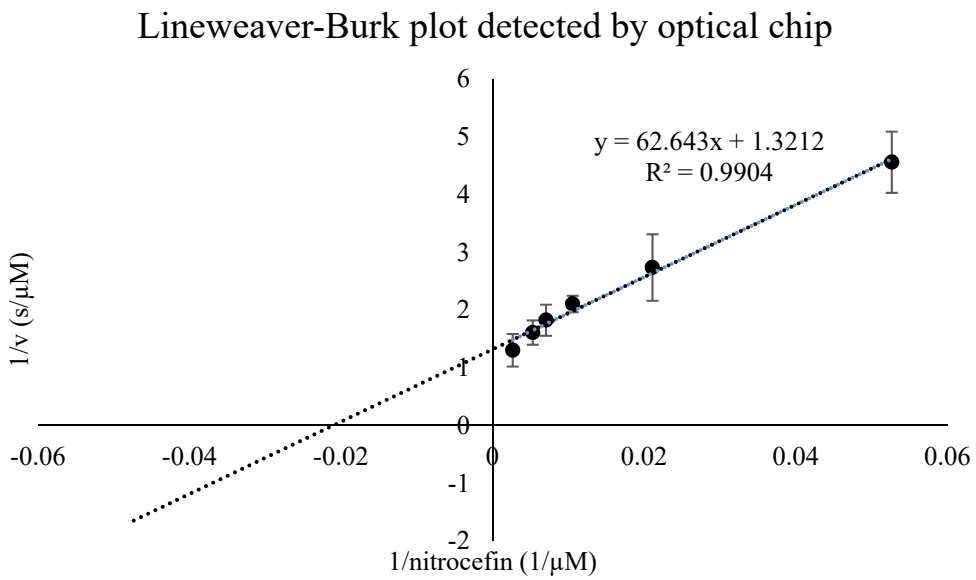

Figure 8-2: The Lineweaver-Burk plots detected by (a) the bench-top plate reader at 470 nm and (b) the optical chip at 470 nm. Error bars represent the standard deviations of three repeats.

Table 8-1: Kinetic parameters of TEM-1 on nitrocefin substrate detected by the plate reader, the optical chip and in the literature. Standard deviations from three repeats are shown.

	Plate reader	Optical chip	Literature [247]
K_M (μM)	51.10 ± 6.89	47.42 ± 2.18	30 ± 10
k_{cat} (s^{-1})	828.16 ± 111.73	757.00 ± 34.85	714 ± 80
K_{cat}/k_M($\mu M^{-1}s^{-1}$)	16.20	15.96	23.80

The plate reader and the optical chip gave similar K_M and k_{cat} values, which suggests that the chip could detect the absorbance change from an enzyme reaction. The standard deviations from the optical chip were less than one-third of that from the plate reader, which suggests that the chip could obtain more reliable results based on its high sensitivity. Compared with Stojanoski *et al.* (2015), K_M detected by the optical chip was 1.58-fold different, but the k_{cat} was the same [247]. The difference may stem from the difference in detecting wavelength because Stojanoski *et al.* detected the absorbance at 482 nm but the optical chip had a 470 nm LED. In conclusion, the optical chip could detect nitrocefin hydrolysis accurately.

8.1.3 Supernatant and bacterial lysates

Commercial TEM-1 is transparent, but the *E. coli* TOP10 lysates are cloudy and may scatter light. The experiment reported here aimed at testing the difference in absorbance change detected from *E. coli* TOP10 TEM lysates (*E. coli* TEM) and *E. coli* TEM supernatant.

The *E. coli* TOP10 TEM lysates were centrifuged for 5 minutes at 10000 *g*, and the supernatant was extracted as *E. coli* TEM supernatant. The lysates and the supernatant were both mixed with nitrocefin. The absorbance changes at 470 nm of the solutions were measured by the optical chip. Figure 8-3 (a) shows the absorbance change of the *E. coli* TEM supernatant. Figure 8-3 (b) shows the absorbance change of the *E. coli* TEM lysates.

(a)

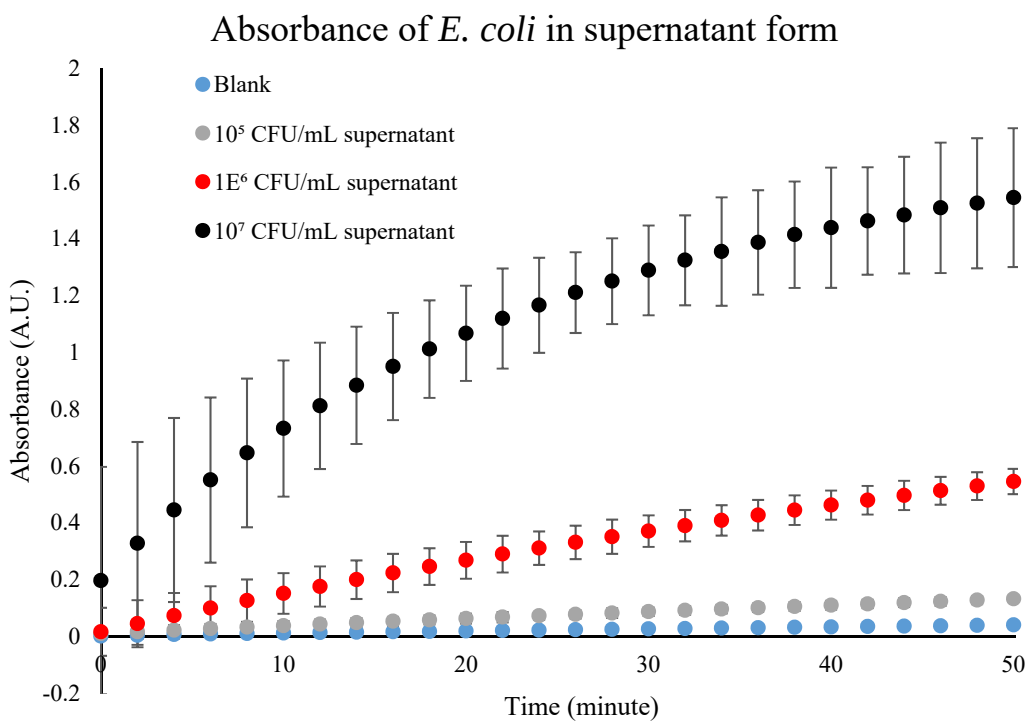

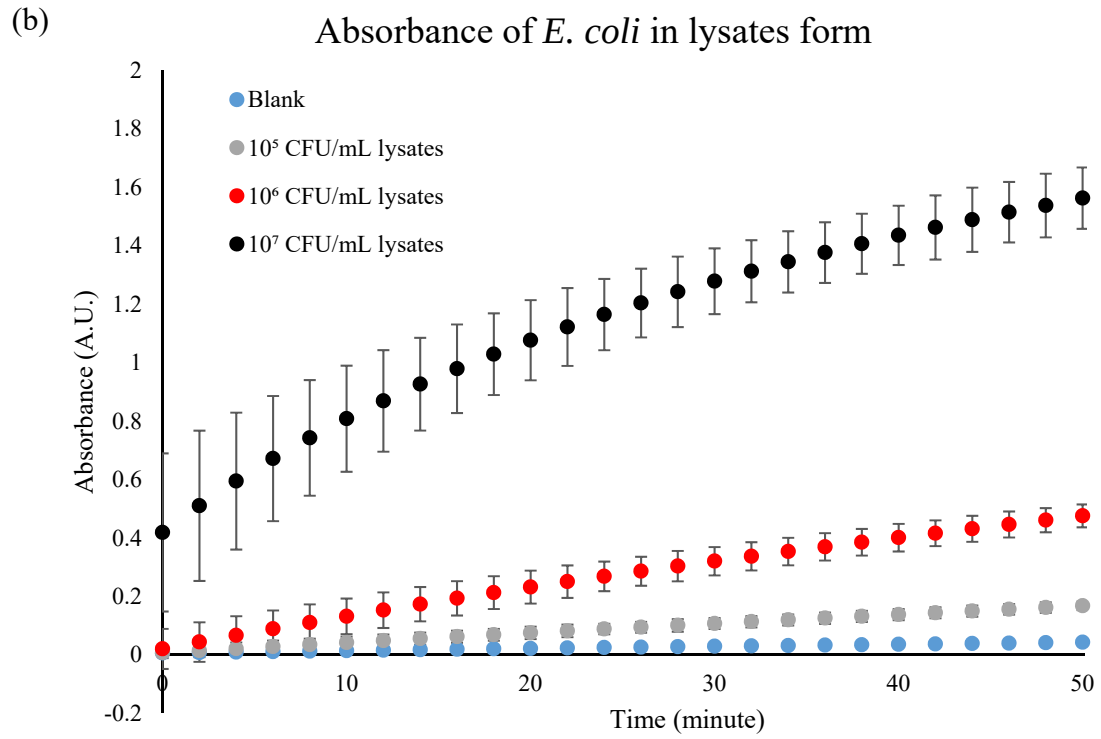

Figure 8-3: Absorbance change against time for *E. coli* TEM in (a) supernatant and (b) lysates form. The absorbance of the two forms was similar. Error bars represent the standard deviations from three repeats. The 10^7 CFU/mL data do not start from 0 due to a delay between solution mixing and injection into the optical chip. Blank represents the absorbance of the nitrocefin solution.

Both the supernatant and whole lysates of *E. coli* TOP10 TEM yielded similar results, which suggests that the cloudy lysates do not affect the absorbance at 470 nm. In further experiments, bacterial lysates were used for β-lactamase detection.

8.1.4 Sensitivity of β-lactamase diagnosis

The sensitivity of β-lactamase diagnosis was evaluated for *E. coli* CTX-M. *E. coli* CTX-M lysates were mixed with nitrocefin solution and injected into a channel on the optical chip or a chamber in a 96-well plate. The absorbance at 470 nm of the solutions was detected by the optical chip and plate reader simultaneously, Figure 8-4 shows the absorbance against time detected by (a) plate reader and (b) optical chip.

(a)

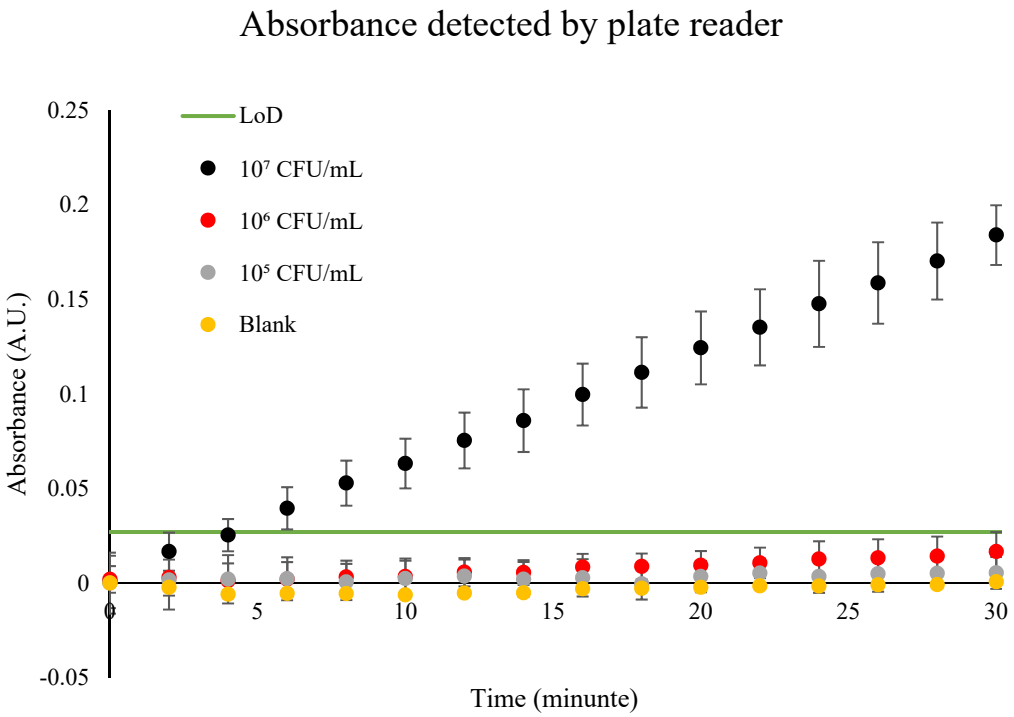

(b)

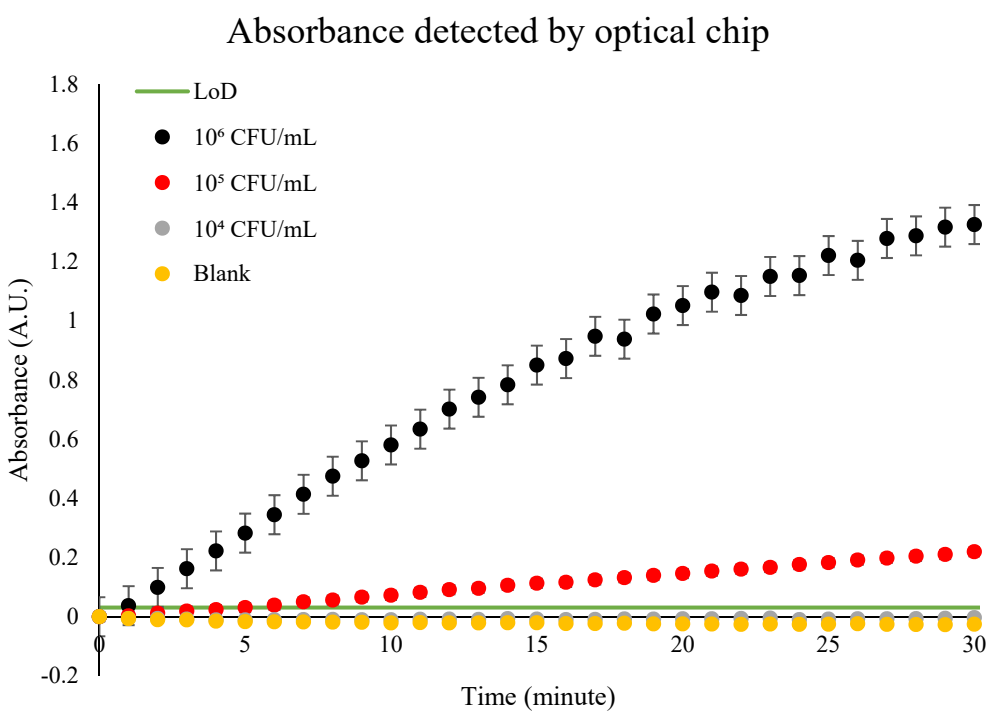

Figure 8-4: Absorbance change against time of *E. coli* CTX-M detected by (a) plate reader and (b) optical chip. The minimum bacterial concentration detected by the plate reader and the optical chip was 10^7 CFU/mL and 10^5 CFU/mL, respectively. The error bars represent the standard deviation of three repeats. Lower bacterial concentration range was used for the optical chip because the longer path length meant the optical chip was more sensitive.

The minimum bacterial concentration for the plate reader for β-lactamase detection was 10^7 CFU/mL; that for the optical chip was 10^5 CFU/mL. The optical chip had two advantages: first, its path length (around 25 mm) was about 6.5 times longer than that of the 96-well plates (about 4.5 mm), so the chip detected significant absorbance change compared to the plate reader. Second, the channel volume of the chip (4 μL) was smaller than that of a chamber in a 96-well plate (200 μL), so the local bacterial concentration of the chip was higher than that of the chamber, although the same amount of enzymes extracted from *E. coli* CTX-M was used. Therefore, the optical chip had 2 order of magnitude greater sensitivity for diagnosing β-lactamases than the plate reader.

8.1.5 Clinical test results

The clinical test of the optical chip was performed by Carrie Turner, PHE. This experiment aimed at verifying the possibility of using the optical chip to detect the presence of β-lactamases from clinical isolates. All test clinical samples were resistant to at least one β-lactam antibiotic as determined by broth dilution. The DNA of all test samples were known; and 55 test samples had β-lactamase–related genes. The enzymes extracted from 66 clinical samples were mixed with nitrocefin, and the absorbance of the mixing solutions was detected by the optical chip. The data has been published [248]. The clinical tests from the optical chip showed 100% selectivity for β-lactamase detection. The species of testing strains and the types of β-lactamases did not influence the diagnosis results. However, the optical chip might produce false negative results on β-lactam resistance diagnosis in clinical settings, as it could not be used to diagnose β-lactam resistance caused by other mechanisms than β-lactamase.

8.1.6 Bacteria enrichment

In the filter system, the bacterial concentrations and medium conductivities of 10 mL bacterial solution in LB broth, 10 mL waste and 1 mL bacterial solution in water were measured. The 0.22-μm filter reduced the medium conductivity from 0.83 S/m in LB broth to 3.3 mS/m in water, also helped increase the bacterial concentration by 10-fold because of the retrieval with elution volume of 1 mL.

In the DEP system, the input, waste and collected *E. coli* concentrations from different flow rates were detected. The bacterial concentrations were determined using the plate count method. The capture efficiency of the DEP chamber was calculated as

$$Capture\ efficiency = \left(1 - \frac{waste\ concentration}{input\ concentration}\right) \times 100\% \qquad (8.3)$$

In the optimized situation, the capture efficacy should be near 100% with the maximum flow rate.

The enrichment factor of the DEP chamber was calculated as

$$Enrichment\ factor = \frac{collected\ concentration}{input\ concentration} \quad (8.4)$$

Because the collected volume (100 µL) was just one tenth of the input volume (1 mL), the enrichment factor should be near 10. Figure 8-5 shows the capture efficiencies and enrichment factors in different flow rates.

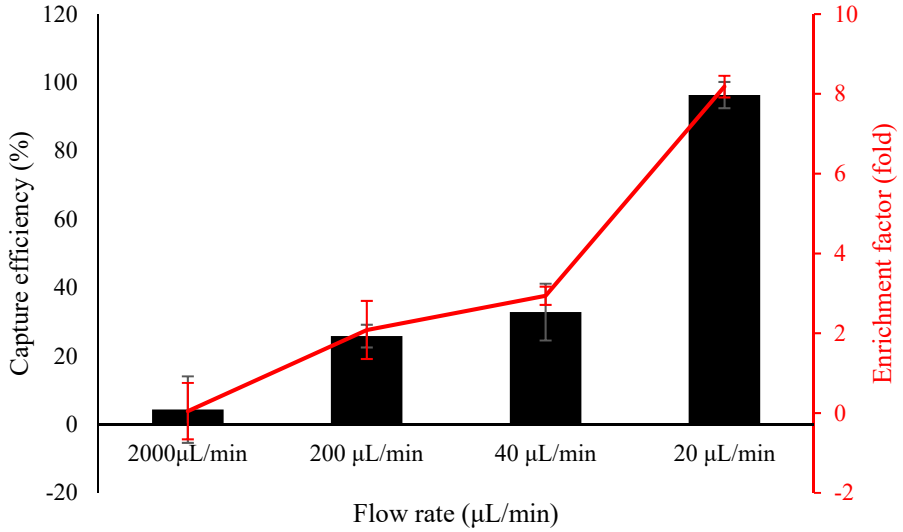

Figure 8-5: The enrichment factors and capture efficiencies in different flow rates. The error bars represent standard deviations from three repeats. For 2000 µL/min flow rate, most of the bacteria were not captured and ended up in the waste. As the flow rate decreased, the capture efficiency increased. At a 20 µL/min flow rate, the DEP chip could capture 95.5% of input *E. coli* and bacterial concentration in the collected solution was eight times higher than that in the input solution.

Combining the filter and the DEP chip, the *E. coli* concentration in 100 µL collected sample was roughly 2 magnitudes higher than that in the 10 mL LB broth. The filter and DEP enrichment could be completed in 55 minutes.

8.1.7 Integrated system

E. coli TEM and wild-type *E. coli* TOP10 were both diluted in 10 mL LB broth, then filtered by a membrane, DEP captured at 20 µL/min flow rate, mixed with nitrocefin and injected into the optical chip. Figure 8-6 shows the absorbance change after start of optical detection.

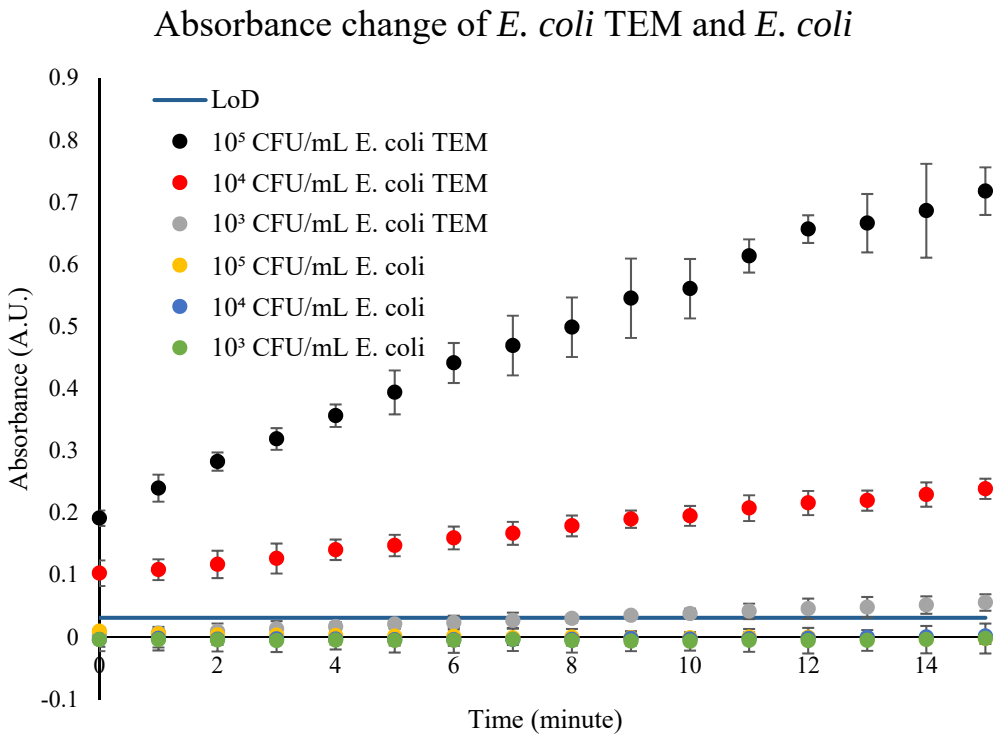

Figure 8-6: The absorbance change after start of optical detection of *E. coli* TEM and wild-type *E. coli* TOP10 (*E. coli*). The LoD is defined as three times the standard deviation of the blank. Error bars represent the standard deviations from three repeats. The 10^5 CFU/mL and 10^4 CFU/mL data do not start from 0 due to a delay between solution mixing and injection into the optical chip.

The minimum bacterial concentration for β-lactamase diagnosis detected by the DEP-enhanced optical system was 10^3 CFU/mL, which cross the LoD at 8-minute. The enrichment chip could enrich the bacterial sample by 2 magnitude in 55 minutes and detection chip could detect the absorbance change within ten minutes. Therefore, the integrated detect β-lactamases at 10^3 CFU/mL in about one hour from 'sample in' to 'results out'.

8.2 pH sensing system

8.2.1 pH sensor calibration and stability test

The pH sensor was calibrated using commercial pH buffers at pH 4, 6, 7, 9 and 10. Figure 8-7 shows the OCP of the IrOx electrode vs Ag/AgCl reference electrode against pH.

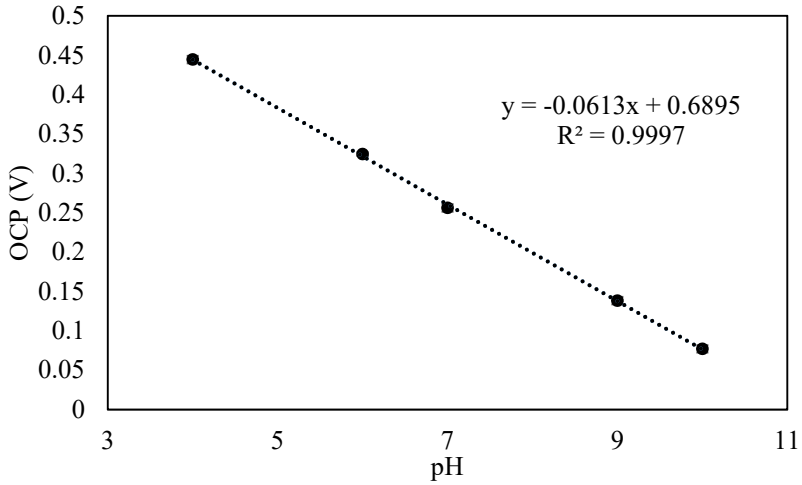

Figure 8-7: The OCP of the IrOx electrode vs Ag/AgCl electrode at different pH. Error bars represent the standard deviations from three repeats. The standard deviation was 5.4 mV.

The IrOx pH sensor showed high linearity and low standard deviation. The sensitivity of the IrOx pH sensor was 61.3 mV/pH and the R^2 was 0.9997. The standard deviation of the OCP was 5.4 mV, so the LoD (3 σ) of this pH sensor was 16.2 mV and corresponding to 0.264 pH based on 61.3 mV/pH sensitivity. The sensitivity and LoD were similar to those reported by Huang *et al.* (2012) [210].

The stability of the IrOx pH sensor was assessed using a solution of 1 mM HEPES and 30 mM NaCl over 50 minutes. Figure 8-8 shows the OCP of the IrOx electrode vs Ag/AgCl electrode against time.

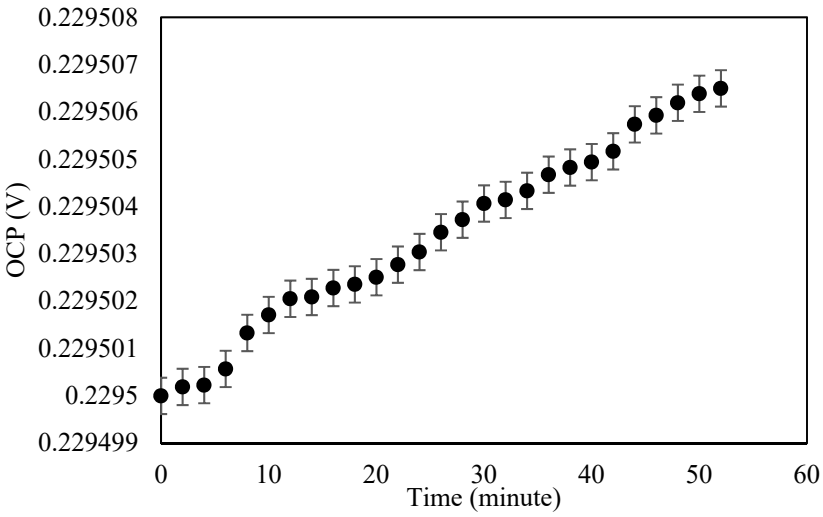

Figure 8-8: The OCP of the IrOx electrode vs Ag/AgCl electrode against time. A solution containing 1 mM HEPES and 30 mM NaCl was used to test the stability of the IrOx pH sensor. Within 50 minutes, the OCP drifted 0.007 mV, which is far blew resolution of the system (0.1 mV). Error bars represent the standard deviations from three repeats..

The IrOx pH sensor yielded a stable reading at 0.2295 V over 50 minutes. The drift of OCP was within the resolution of the system (0.0001 V).

8.2.2 pH indicator calibration and stability test

The pH indicator was calibrated using commercial pH buffers at pH 4, 6, 7, 9 and 10. Figure 8-9 (a) shows the difference in absorbance detected at 560 nm and 450 nm (ΔAbs) against pH. Figure 8-9 (b) shows a photo of the different pH buffers mixed with the pH indicator. The stability of the pH indicator was detected using a solution containing 1 mM HEPES and 30 mM NaCl in 20 hours. Figure 8-9 (c) shows the ΔAbs of the solution against time.

(a)

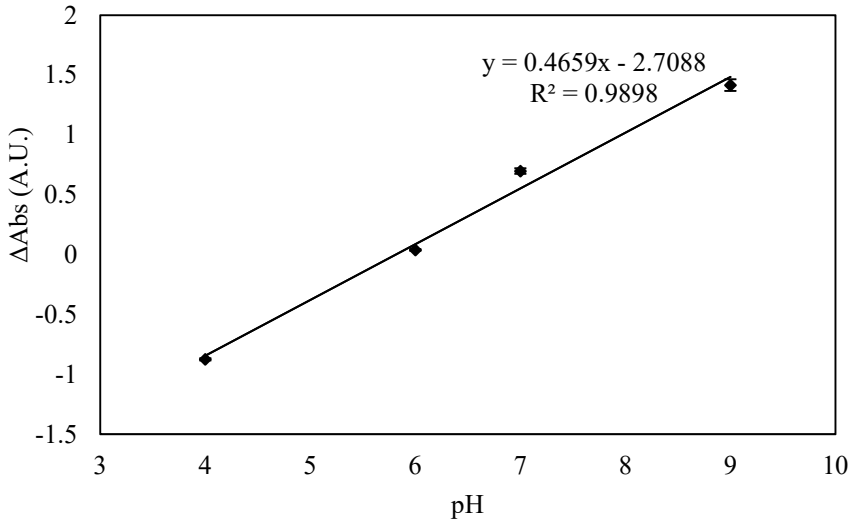

(b)

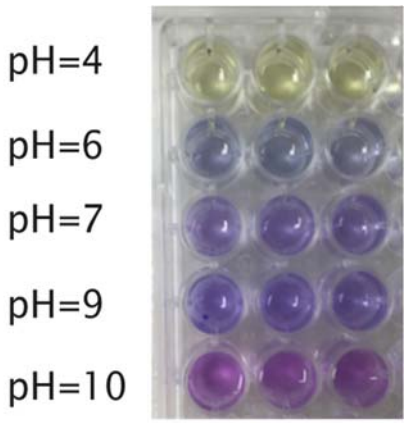

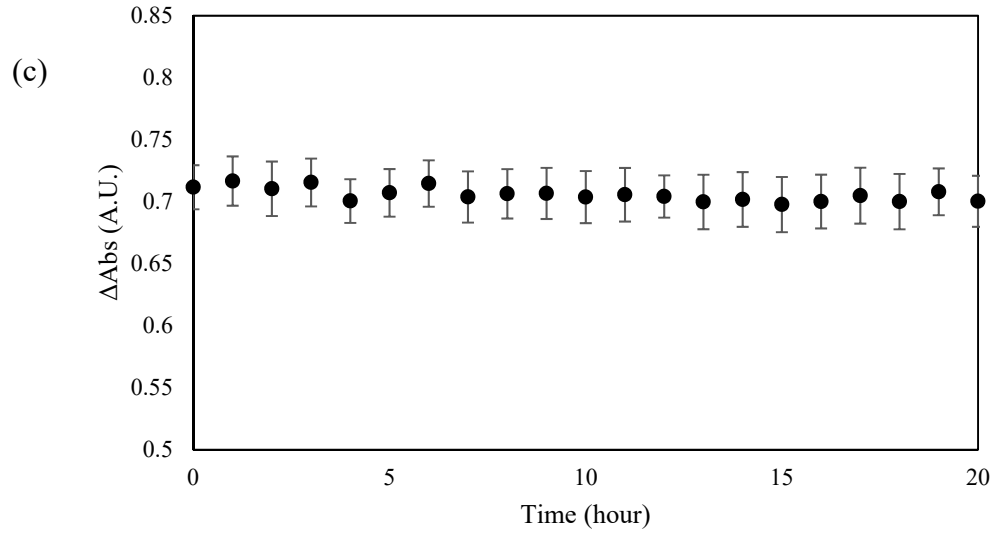

Figure 8-9: (a) The absorbance differences between 560 nm and 450 nm (ΔAbs) against pH. Error bars represent the standard deviations from three repeats. (b) A photo of the pH buffers mixed with the pH indicator. (c) The ΔAbs against time of a solution containing 1 mM HEPES and 30 mM NaCl. Error bars represent the standard deviations from three repeats.

The sensitivity of the pH indicator was 0.466 A.U./pH (1-cm path length). The pH indicator demonstrated a linear relationship between ΔAbs and pH in the range of pH 4–9. The ΔAbs of a solution containing 1 mM HEPES and 30 mM NaCl was stabled at 0.72±0.024 A.U., so the LoD (3σ) of the pH indicator was $\frac{3\times 0.023\ \text{A.U.}}{0.466\ \text{A.U./pH}} = 0.15\ \text{pH}$.

8.2.3 Kinetic parameter

The calculations for K_M and k_{cat} are based on the method described by He *et al.* (2014) [249]. The kinetic parameters of the commercial β-lactamase TEM-1 with carbenicillin substrate were detected by both the pH indicator and pH sensor simultaneously. Figure 8-10 shows the Lineweaver-Burk plots for the pH indicator and pH sensor data. Table 8-2 lists the kinetic parameters calculated from the plots and the kinetic parameters from the literature.

(a)

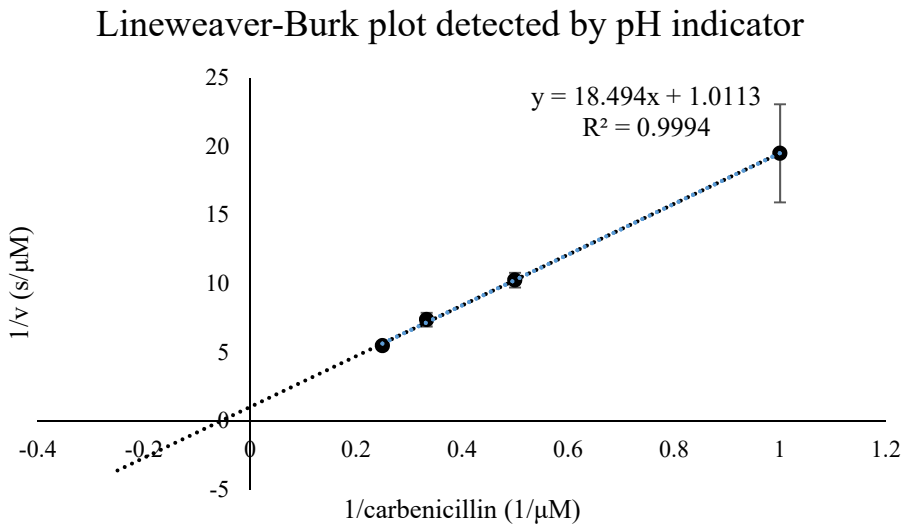

(b)

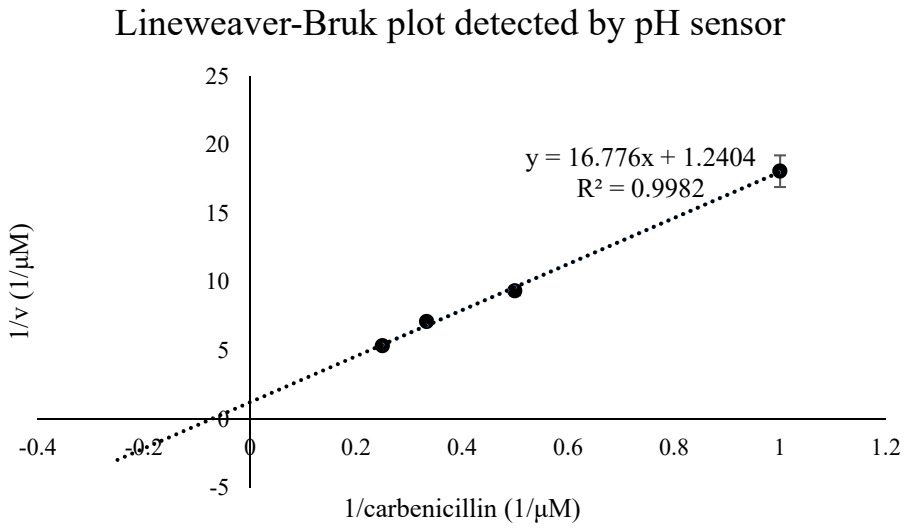

Figure 8-10: Lineweaver-Burk plot of TEM-1 on carbenicillin substrate detected by (a) pH indicator and (b) pH sensor. Error bars represent the standard deviations from three repeats.

Table 8-2: The K_M and k_{cat} of TEM-1 on carbenicillin substrate calculated from the Lineweaver-Burk plots detected by the pH indicator and pH sensor.

	pH indicator	pH sensor	Literature [250]
K_M (μM)	18.5±6.2	13.5±2.0	16±11
k_{cat} (s)	988±329	806±120	750±130

The K_M and k_{cat} measured by the pH indicator and pH sensor were similar to the literature, which proved that the IrOx material and Ag/AgCl material did not influence the reactions between the β-lactamases and β-lactam antibiotics.

8.2.4 Supernatant and bacterial lysates

The Carba NP method uses the supernatant of lysed bacteria rather than the bacterial lysate for rapid carbapenemase diagnosis. The experiment reported in this subsection is aimed at testing the difference in pH change from *E. coli* CTX-M lysates or the supernatant.

The lysates of 10^7 CFU/mL *E. coli* CTX-M were centrifuged for 5 minutes at 10000 *g*, and the supernatant was extracted for further experiments. The lysates and the supernatant were both mixed with carbenicillin. The pH of solutions containing bacterial lysate and carbenicillin (whole lysed cells), bacterial supernatant and carbenicillin (supernatant of lysed cells), carbenicillin only (carbenicillin control) and bacterial lysate only (lysed cell control) were measured by the pH indicator, respectively. The pH reduction slopes over 15 hours were calculated. Figure 8-11 shows the pH against time in 15 hours.

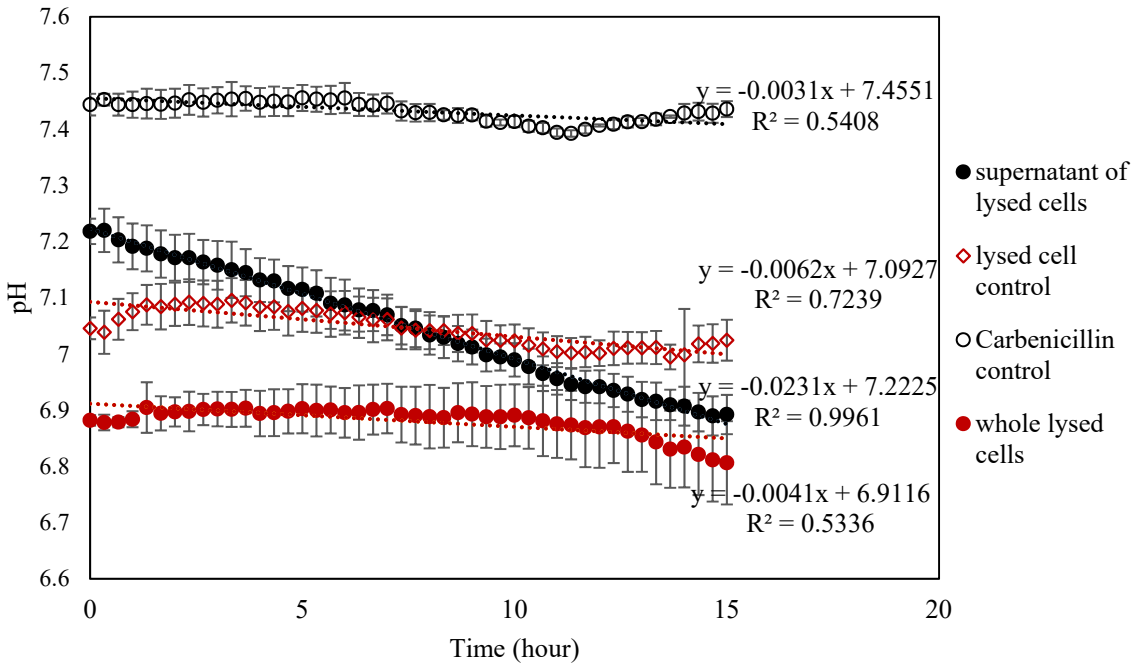

Figure 8-11: The pH of four solutions against time (15 hours). The pH of the solution containing *E. coli* CTX-M lysate supernatant and carbenicillin was reduced but that of the other solutions remained stable. The error bars represent the standard deviations from three repeats.

The slopes of change in pH of the solutions containing supernatant of lysed cells and that containing whole lysed cells were 0.0231 pH/hour and 0.0041 pH/hour, respectively. The pH change in the supernatant was five times quicker than that of the whole lysate solution, so the bacterial lysates could not be used for rapid β-lactamase diagnosis. Some insoluble components in bacteria (lipids, large proteins, DNAs) may absorb protons and maintain a stable pH.

8.2.5 Sensitivity of β-lactamases diagnosis: *E. coli* TEM

The minimum concentration of *E. coli* TEM for β-lactamase diagnosis by the pH method was tested. The supernatant of *E. coli* TEM was mixed with carbenicillin. The pH of the solution was recorded by the pH sensor. Figure 8-12 (a) shows the typical pH of the solution against time. The experiment was repeated three times and Figure 8-12 (b) shows the pH slope from three repeats.

(a)

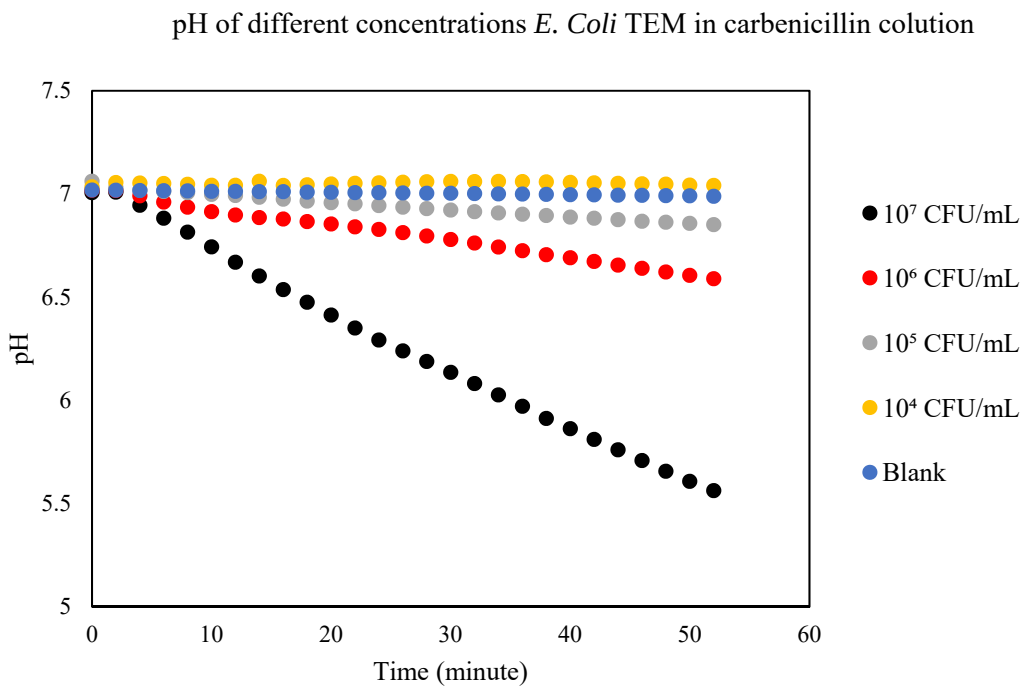

(b)

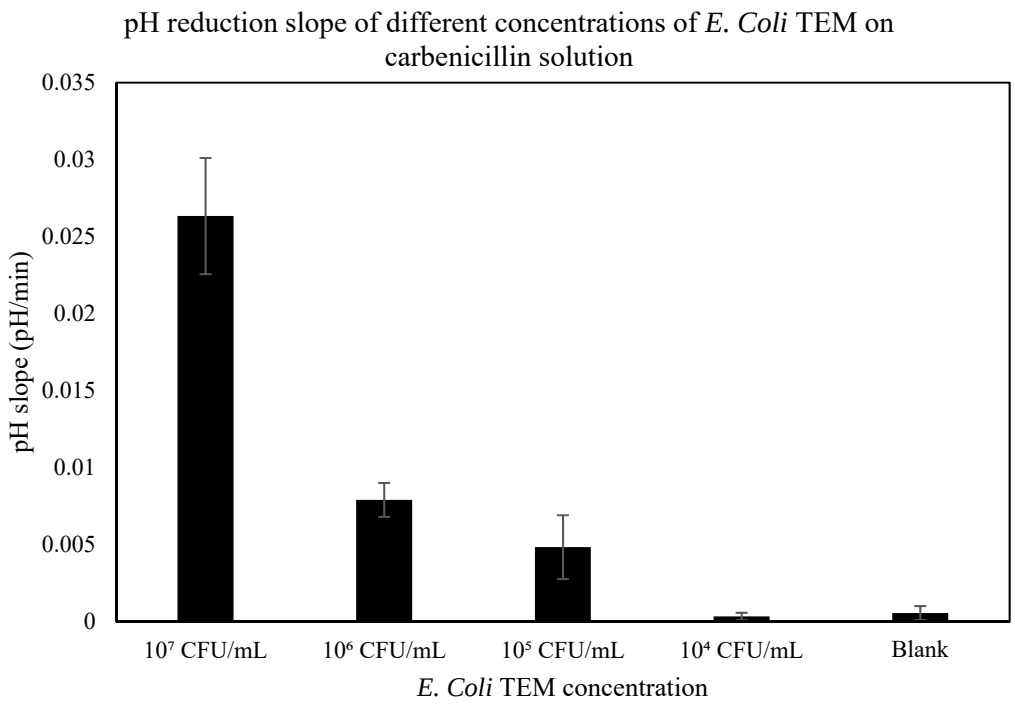

Figure 8-12: (a) Typical pH of a solution containing supernatant *E. coli* TEM and carbenicillin against time. (b) The average pH reduction slope from three repeats. Error bars represent the standard deviation from three repeats. The blank was carbenicillin solution without bacterial supernatant.

The LoD of this pH sensor was 0.264 pH, so the minimum pH reduction detected by the sensor was $\frac{0.264\ \text{pH}}{60\ \text{minute}} = 0.0044\ \text{pH/minute}$ in one hour. Therefore, the minimum concentration of *E. coli* TEM that could produce a pH reduction higher than the detectable pH reduction slope was 10^5 CFU/mL.

8.2.6 Sensitivity of β-lactamases diagnosis: *E. coli* 11560

The minimum concentration of clinical isolate for β-lactamase detection by the pH method was tested. *E. coli* 11560, which produces TEM β-lactamases and is resistant to carbenicillin, was used for testing. The supernatant of *E. coli* 11560 (broth cultured) was mixed with carbenicillin. The pH of the mixing solution was recorded by the pH sensor. Figure 8-13 (a) shows the typical pH of the mixing solution against time. The experiment was repeated three times and Figure 8-13 (b) shows the average pH reduction speed from three repeats.

(a)

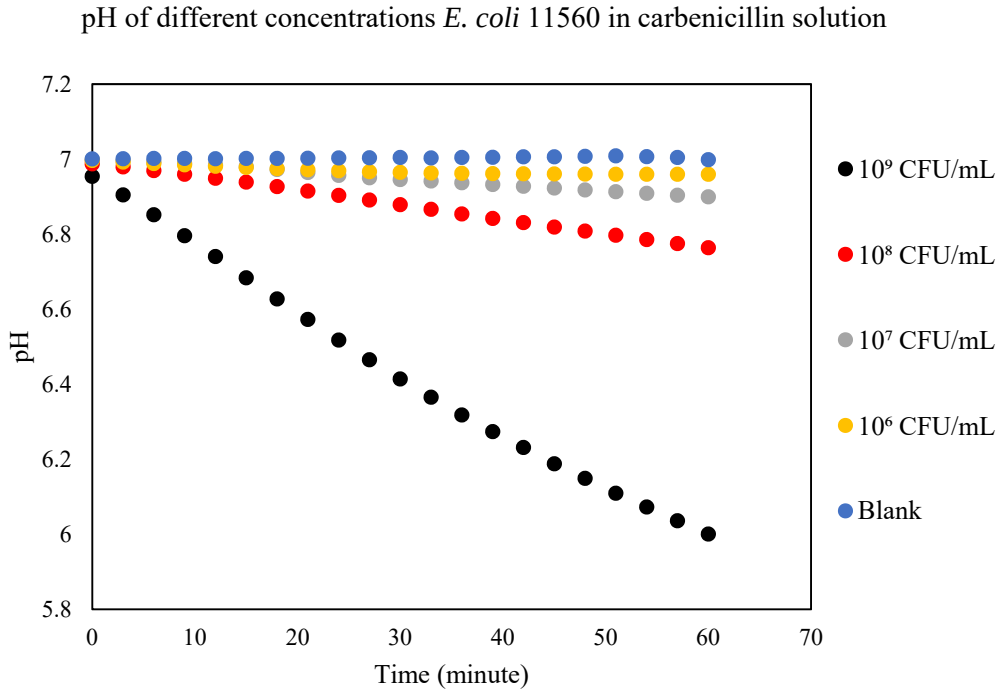

(b)

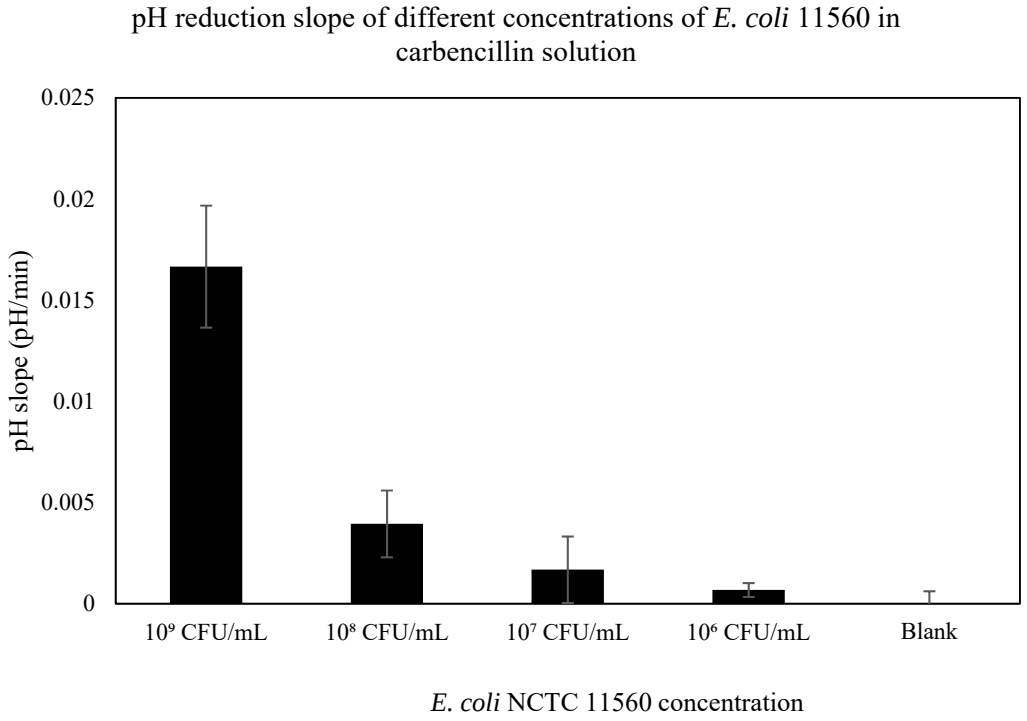

Figure 8-13: (a) Typical pH of solutions containing supernatant from different concentrations of *E. coli* 11560 and carbenicillin against time. (b) The average pH reduction slope from three repeats. The error bars represent the standard deviation from three repeats. The blank was carbenicillin solution without bacterial supernatant.

The minimum *E. coli* 11560 concentration that could produce a pH reduction faster than 0.0044 pH/min (LoD of the pH sensor) was 10^8 CFU/mL. In the clinical setting, the minimum bacterial

concentration detected by the pH method may be higher than that from a lab-safe strain (*E. coli* TEM). Therefore, high bacterial concentration sample (>10^9 CFU/mL) is needed in further clinical test.

8.2.7 Clinical blind test

This experiment aimed at verifying the possibility of using the pH sensor to detect the presence of β-lactamase in clinical isolates. The DNA of all test samples were known; five samples contained β-lactamase–related genes.

The supernatant of eight clinical isolates were mixed with carbenicillin. The pH of the mixing solution was detected by the pH sensor in 1 hour. Table 8-3 summarizes the species and strains of the test clinical isolates, β-lactamase genes contained and the pH reduction slope (pH/min) detected by the pH sensor.

Table 8-3: The species, strains, β-lactamase genes and the pH reduction slope of the pH sensor. A pH reduction slope higher than 0.0044 pH/min (LoD of the pH sensor) was marked as red, which was seen as "resistant"; otherwise, it was diagnosed as 'susceptible'. The blind test was repeated three times. Five of eight blind test strains could produce β-lactamases and the pH sensor could diagnose three correctly.

No.	Species	Strains	β-lactam genes	pH reduction slope (pH/min)
1	*E. coli*	11341	*bla*CTX-M	0.01059 ± 0.00287
2		11560	*bla*TEM-1	0.01565 ± 0.00186
3		13351	*bla*TEM-3	0.00408 ± 0.00014
4	*E. aerogenes*	14099	-	0.00199 ± 0.00076
5	*K. pneumoniae*	13438	*bla*KPC	0.00413 ± 0.00057
6		M109	*bla*SHV	0.00737 ± 0.00081
7		M70	-	-0.00029 ± 0.00121
8	*P. mirabilis*	13376	-	0.00316 ± 0.00056

The isolates enclosed β-lactamase genes showed higher pH reduction slopes than that of β-lactamase gene free isolates. The pH reduction slope of three clinical isolates were higher than 0.0044 pH/min (LoD of the pH sensor) and gave positive results, who enclosed *bla*CTX-M , *bla*TEM-1 and *bla*SHV genes, respectively. The pH reduction slopes of isolates enclosed *bla*TEM-3 and *bla*KPC genes were less than the LoD of the chip. Both *bla*TEM-3 and *bla*KPC enclosed isolates had positive results in the optical chip experiment [248]. Therefore, the blind test

results demonstrate the pH method might yield false negatives in clinical testing for certain strains. Improving the resolution of the pH sensor helps to improve the diagnosis successful rate of the pH system.

8.3 Impedance system

8.3.1 Bacterial concentration at OD=0.01

The minimum period required for bacterial metabolism detection by impedance method is proportional to the bacterial concentration in its suspension. The OD-based method is a convenient bacterial counting method in clinical situation. The bacterial concentrations of typical bacterial strains at OD = 0.01 were checked by the plate count method and are summarized in Table 8-4.

Table 8-4: The bacterial concentrations of typical bacterial strains at OD = 0.01. The bacterial concentrations were counted using the plate count method. Deviations were from three repeats.

Strains	*A. baumannii* AYE	*S. aureus* EMRSA 15	*K. pneumonia* NCTC 13368	*E. coli* NCTC 12923
Bacterial concentration (*10^6 CFU/mL)	13.00 ± 1.95	1.48 ± 0.20	8.50 ± 0.54	1.99 ± 0.26

The concentrations of typical bacterial samples when OD = 0.01 were between 10^6 and 10^7 CFU/mL. The difference may result from the bacterial shape and size [243]. The large discrepancy ($\frac{13.00}{1.48} = 8.73$) between OD and plate count measurements of cell concentration may lead to errors in metabolism detection because the bacterial metabolism is proportional to bacterial concentration rather than OD. Using differential measurement can minimize the impact of different initial bacterial concentrations.

8.3.2 OD-based growth curve

The growth curve of six antibiotics for 10 bacterial isolates were measured using the conventional OD-based broth dilution method. The absorbance at 20-hour of the growth curve were used to determine the MIC of the bacterial stain. The experiment was repeated three times and Table 8-5 lists the MICs detected by OD-based broth dilution method from three measurements.

Table 8-5: MICs detected by OD-based broth dilution method (unit: µg/mL). CIP represents ciprofloxacin, GEN represents gentamicin, DOX represents doxycycline, CEF represents ceftazidime, COL represents colistin, IMI represents imipenem.

No.	Specie	Strain	CIP	GEN	DOX	CEF	COL	IMI
1	*K. pneumonia*	13368	0.5	16	32	16	4	≤0.125
2		M6	≤0.125	8	2	≤0.125	4	≤0.125
3	*E. coli*	LEC-001	>64	1	4	64	4	≤0.125
4		12923	0.5	2	1	≤0.125	<0.125	≤0.125
5	*S. aureus*	EMRSA-15	>64	1	0.5	64	>64	0.25
6		9144	≤0.125	≤0.125	≤0.125	16	64	≤0.125
7	*A. baumannii*	AYE	>64	>64	4	64	1	0.5
8		17978	1	2	0.5	8	≤0.125	≤0.125
9	*P. aeruginosa*	PA01	0.25	2	32	2	0.25	8
10		13437	64	>64	>64	>64	≤0.125	>64

The growth curves summarized from the broth dilution method could be divided into three different types, namely standard growth, delayed growth and fake growth. Mostly, the MICs detected at several-hour were the same as that detected at 20-hour, and were the standard growth type. Figure 8-14 shows the typical standard growth curve of ceftazidime for *K. pneumoniae* 13368.

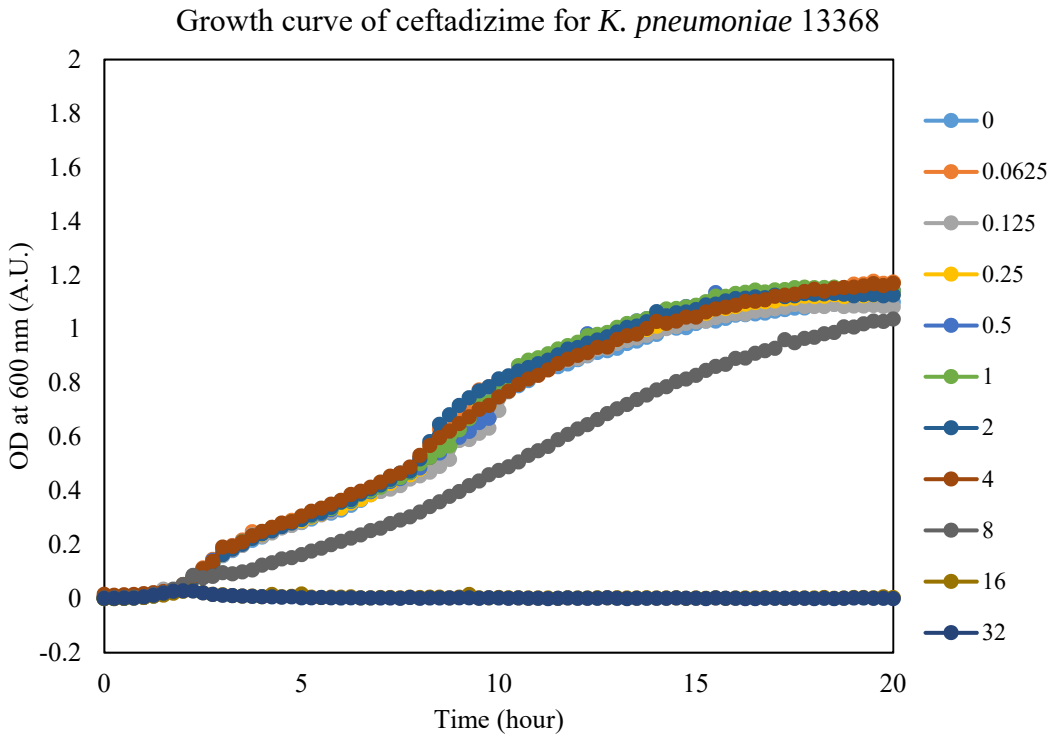

Figure 8-14: The typical standard growth curve of ceftazidime for *K. pneumoniae* 13368. Figure key shows the antibiotic concentrations in µg/mL. The MIC was tested as 16 µg/mL in both 20-hour and 4-hour. The experiment was repeated three times and obtained similar results.

In the delayed growth type, the OD at ½-fold MIC, ¼-fold MIC or even lower concentrations showed several-hour delay compared with the blank. Therefore, MIC detected at the beginning (for example, at 4-hour) was lower than that at 20-hour. The delayed growth of the test strain introduces errors in rapid MIC detection, and is commonly found in the experiments with bacteriostatic antibiotics. Figure 8-15 shows a typical delayed growth curve of doxycycline for *S. aureus* EMRSA-15, whose MIC at 20-hour was observed as 0.5 µg/mL, but that at 4-hour and 7-hour was ≤ 0.125 µg/mL and 0.25 µg/mL, respectively. Eden and Eden (1984) also reported this observation, which is termed shift in detection time [28].

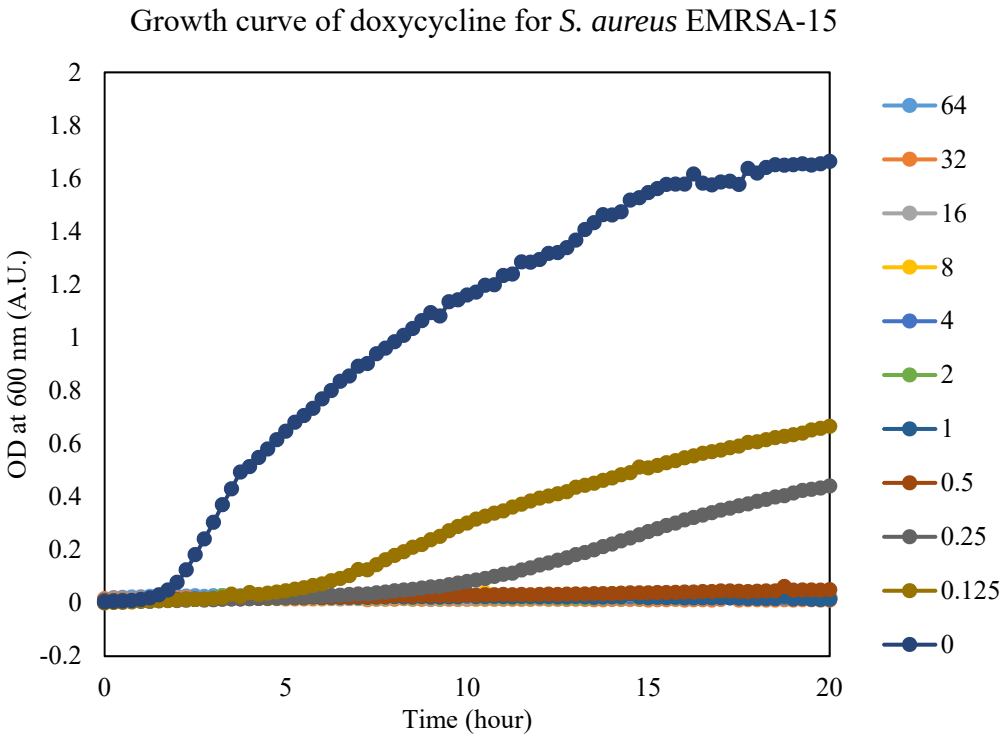

Figure 8-15: The typical delayed growth curve of doxycycline for *S. aureus* EMRSA-15. Figure key shows the antibiotic concentration in µg/mL, where the MIC was 0.5 µg/mL at 20-hour. However, the bacteria began to grow at 0.125 µg/mL and 0.25 µg/mL after 5- and 7-hour, respectively. The MIC at 4-hour was 4-fold lower than that at 20-hour.

In the fake growth, the OD at 2-fold MIC, 4-fold MIC or even higher concentration were similar with the blank at first, but then reduced to their initial level. Therefore, the MIC detected at several-hour was higher than that at 20-hour because some bacteria have the ability to grow normally in a short time after explosion to antibiotics. The fake growth phenomenon is commonly found in *E. coli* and *K. pneumoniae* strains, which Yoursassowsky *et al.* (1986) reported [251]. Figure 8-16 shows a typical fake growth curve of doxycycline for *E. coli* 12923, where the bacterial concentration at 1 µg/mL antibiotic doxycycline increased initially and then reduced after 3-hour antibiotic treatment.

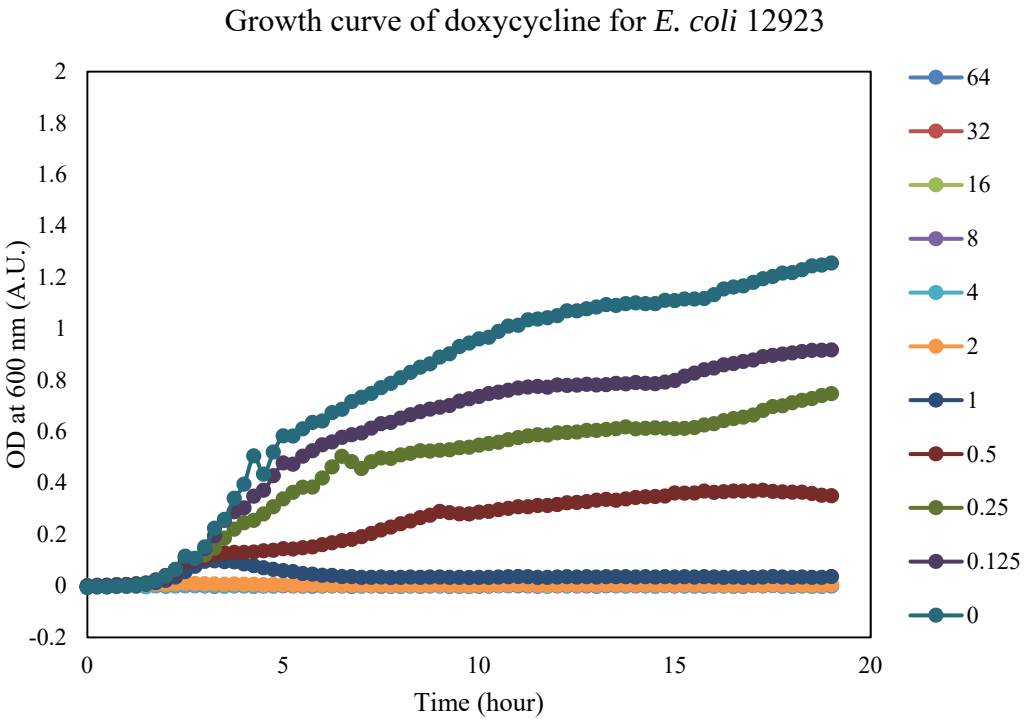

Figure 8-16: A typical fake growth curve of *E. coli* 12923 with doxycycline. Figure key shows the antibiotic concentration in µg/mL. The MIC was 1 µg/mL at 20-hour. The OD increased initially at 1 µg/mL doxycycline, but decreased after 3 hours. Therefore, the MIC at 3-hour is 2-fold higher than that at 20-hour.

The OD-based experiments showed one of the bottlenecks of rapid AST experiments. Bacterial isolates may experience fake growth or delay growth, which are difficult to predict and may introduce errors between the MIC detected at 20-hour and the MIC tested at several-hour.

8.3.3 Two- and four-terminal impedance system calibration and verification

Several two-terminal impedance systems measured the impedance magnitude at 10 kHz to indicate the medium conductivity [37, 91, 92]. However, those two-terminal conductivity meters suffer from the interface of double layer capacitance and require multiplexer for multi-channel detection. To overcome those drawbacks, a customized multi-channel four-terminal impedance system was designed and fabricated, which is low-cost, easy-to-use with high accuracy.

Conductivity error is the difference between the conductivity detected by the impedance system and that detected by a commercial conductivity meter. Aqueous solutions with conductivity of 0.35 S/m, 0.45 S/m, 0.55 S/m, 0.65 S/m and 0.75 S/m were used for impedance system calibration. The calibration was performed at room temperature (21.6–21.9°C) and was repeated three times. Figure 8-17 shows the conductivity error for the two-terminal system at 10 kHz.

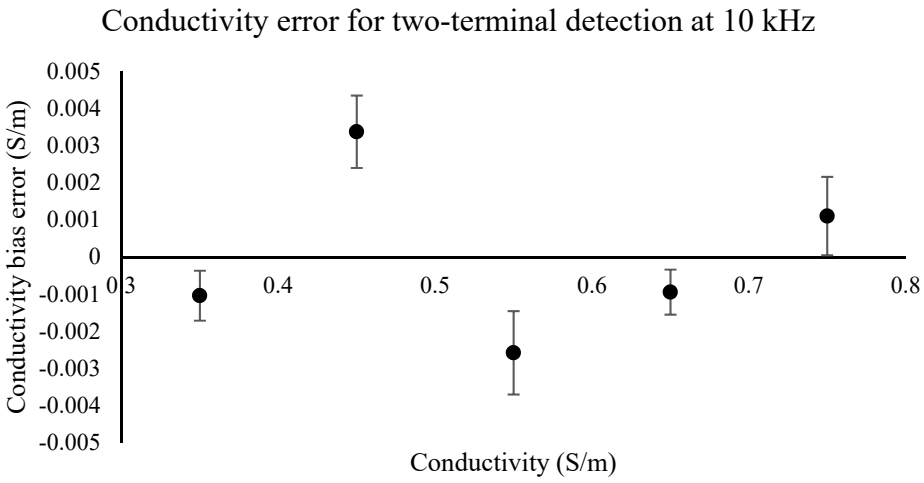

Figure 8-17: Conductivity error for the two-terminal system at 10 kHz. The bias errors were within 0.005 S/m in the range of 0.35–0.75 S/m, and the average conductivity deviation was 0.78% of the original solution. Thus, the LoD (3 × conductivity bias error) of the two-terminal detection system was 2.33% of the detected conductivity. The error bars represent the standard deviation from three repeats.

In the two-terminal method, the LoD of the two-terminal system was 2.33% of the detected conductivity.

Figure 8-18 shows the conductivity error for the four-terminal detection system at 10 Hz.

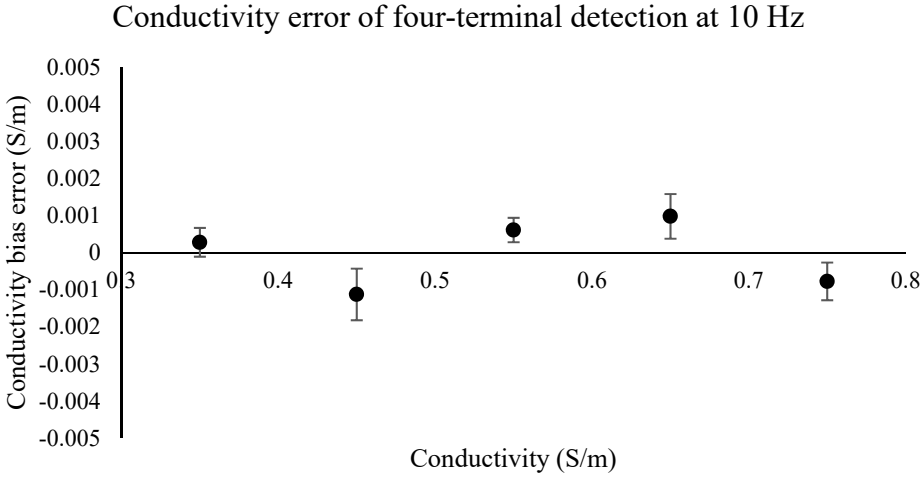

Figure 8-18: Conductivity error for the four-terminal detection system at 10 Hz. The conductivity bias errors were within 0.002 S/m in the range of 0.35–0.75 S/m, and the average conductivity deviation was 0.31% of original solution. Thus, the LoD of this four-terminal detection system was 0.93% of the detected conductivity. The error bars represent the standard deviation from three repeats.

In the four-terminal detection system, the conductivity error might stem from random noise or the proximity effects around the channel, which is the influence from insulating or conducting

object moved into the electric field generated by the electrodes. The LoD in this system was similar to that reported by Huang *et al.* (2012) [252].

Reported by Colvin *et al.* (1977) and Safavieh *et al.* (2017), the normalized impedance change ratio at 1-hour ($NICR_{1h}$) can be used in rapid AST experiments [31, 92], which was calculated as

$$\mathrm{NICR_{1h}} = \frac{|Z_{1h}| - |Z_0|}{|Z_0|} \times 100\% \tag{8.1}$$

where $|Z_{1h}|$ is the impedance magnitude at 10 kHz at 1-hour, $|Z_0|$ is the impedance magnitude at 10 kHz at start.

Figure 8-19 shows a typical impedance spectrum of *E. coli* 12923 detected by the two-terminal system.

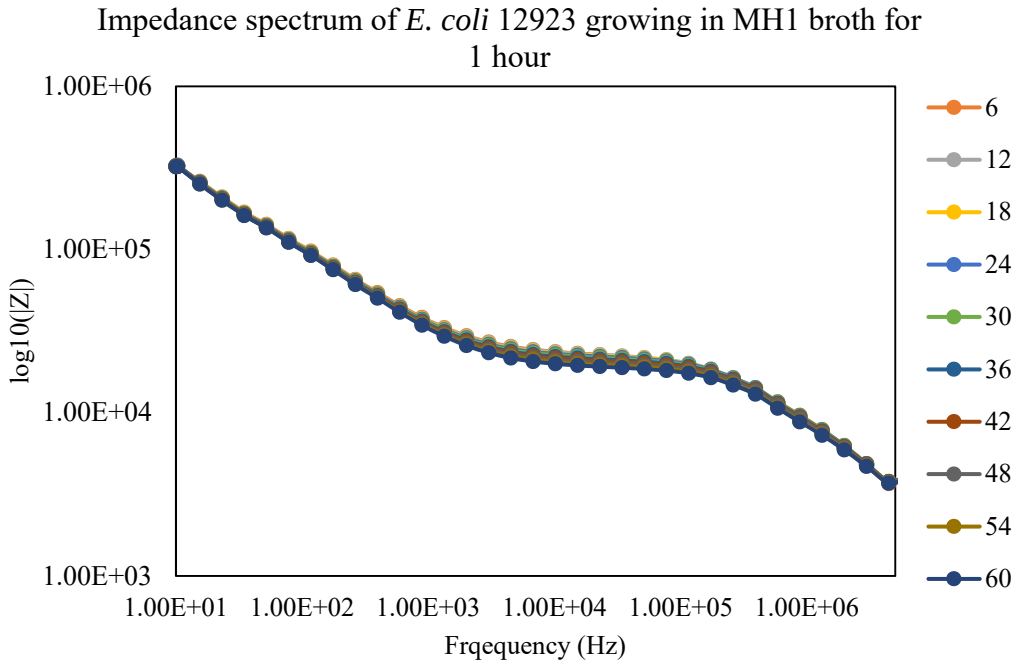

Figure 8-19: Typical impedance spectrum of *E. coli* 12923 grown in MH1 broth for 1 hour. The impedance spectrum was detected by the two-terminal impedance system. Figure key shows the minutes after addition of the sample. The initial OD of the bacterial suspension was set at 0.01. The temperature for detection was set at 37°C. The data for time 0 (minutes after sample adding) was deleted because the temperature at time 0 was not stabilized at 37°C. The experiment was repeated three times.

The impedance spectrum was similar to that of the simulation (Figure 6-17), where a reduction in impedance from bacterial metabolism could be detected at 10–100 kHz. At <5 kHz, the impedance magnitude was dominated by double layer capacitance. At >500 kHz, the impedance magnitude was dominated by parasitic capacitance. Figure 8-20 shows the zoomed-in impedance spectrum of that shown in Figure 8-19.

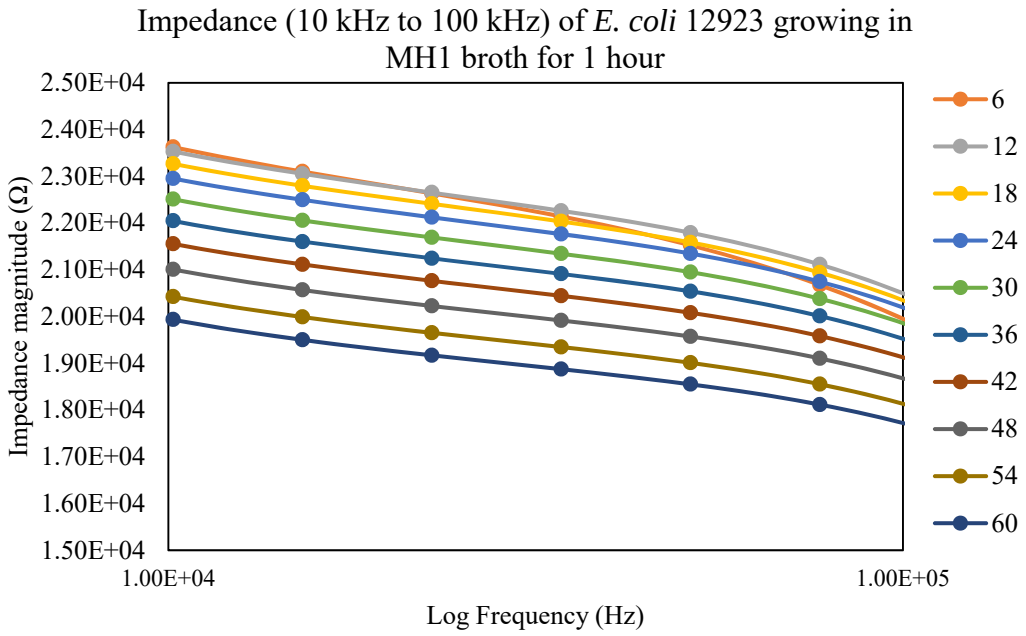

Figure 8-20: The zoom-in of the impedance spectrum for 10–100 kHz shown in Figure 8-19. Figure key shows the minutes after the addition of the sample. Within 1 hour, the impedance magnitude at 10 kHz was reduced from 23.6 kOhm to 19.9 kOhm, which indicated that $NICR_{1h}$=15.67%.

The impedance spectrum of MH1 broth was also recorded by the two-terminal system. Figure 8-21 shows the typical impedance spectrum of MH1 broth.

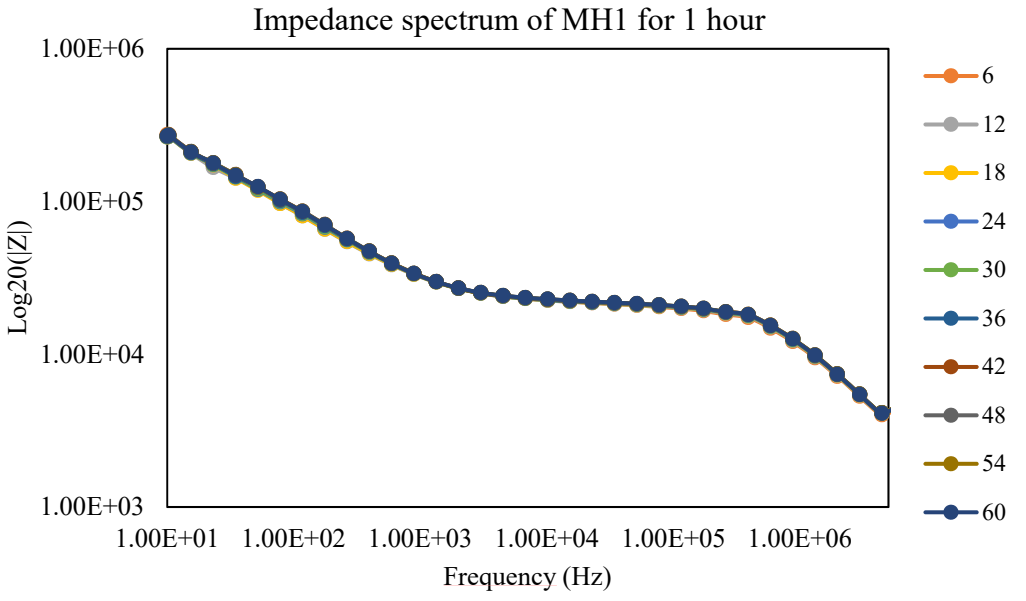

Figure 8-21: The typical impedance spectrum of MH1 broth in 1 hour. The impedance spectrum was detected by the two-terminal impedance system. Figure key shows the minutes after sample injection. The temperature was set at 37°C, and the interval for impedance testing was set as 6 minutes. The data for time 0 were deleted because the temperature at time 0 was not stabilized at 37°C. The experiment was repeated three times.

The impedance spectrum of MH1 broth could be divided into three parts, which are double layer capacitance, solution resistance and parasitic capacitance, respectively. The impedance between 10 kHz and 100 kHz did not change significantly over 1 hour. Figure 8-22 shows the zoomed-in impedance spectrum of that shown in Figure 8-21.

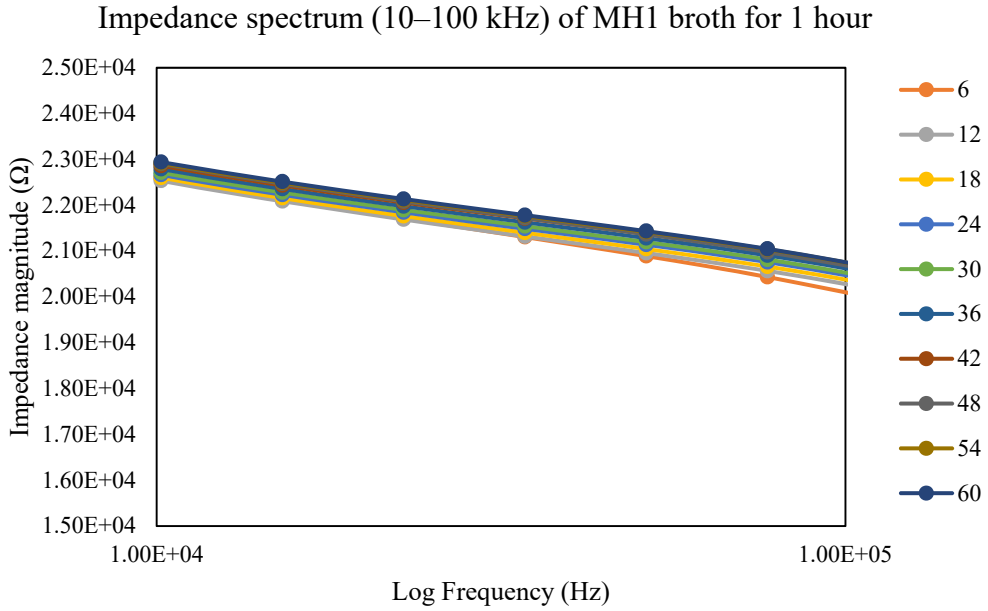

Figure 8-22: The zoomed-in impedance spectrum of that shown in Figure 8-19. Figure key shows the minutes after sample injection. The impedance at 10 kHz drifted from 22.6 kOhm to 22.9 kOhm in 1 hour, which indicated that $NICR_{1h}$= -1.32%.

The $NICR_{1h}$ = -1.32% was recorded in 1 hour, which was below the LoD of the two-terminal impedance detection system. Comparison of Figure 8-20 and Figure 8-22 shows that the impedance detection system could detect bacterial metabolism over 1 hour if the initial bacterial OD reached 0.01. The initial impedance difference between the *E. coli* chamber and MH1 broth chamber at 10 kHz resulted from fabrication errors in channel width and depth, which has been corrected in the calculation of NICR. The LoDs of the two-terminal and four-terminal detection systems were below the estimated conductivity change in the simulation, so the impedance systems could be used to indicate bacterial metabolism after 1-hour.

8.3.4 MIC detect by the impedance method

The impedance magnitude of six antibiotics for ten bacterial isolates were measured using the four-terminal impedance system. Each four-terminal impedance board can monitor the impedance of six chambers simultaneously. Two four-terminal impedance boards were connected to the laptop, so the impedance of up to twelve chambers can be monitored simultaneously. These chambers contained bacterial suspensions with antibiotics at 64 µg/mL, 32 µg/mL, 16 µg/mL, 8 µg/mL, 4 µg/mL, 2 µg/mL, 1 µg/mL, 0.5 µg/mL, 0.25 µg/mL, 0.125 µg/mL concentration and blank. The quotation of NICR at 1 hour ($QNICR_{1h}$) was calculated as

$$QNICR_{1h} = \frac{\frac{|Z_{1h,antibiotics}| - |Z_{0,antibiotics}|}{|Z_{0,antibiotics}|}}{\frac{|Z_{1h,blank}| - |Z_{0,blank}|}{|Z_{0,blank}|}} \times 100\% \quad (8.2)$$

where $|Z_{1h,antibiotics}|$ is the impedance magnitude of the antibiotic chamber at 1 hour; $|Z_{0,antibiotics}|$ is the impedance magnitude of antibiotic chamber at the start; $|Z_{1h,blank}|$ is the impedance magnitude of blank chamber at 1 hour; $|Z_{0,blank}|$ is the impedance magnitude of blank chamber at the start.

Table 8-6 summarizes the means of $QNICR_{1h}$ of six antibiotics for ten bacterial isolates from three repeats.

Table 8-6: The $QNICR_{1h}$ (%) of six antibiotics for ten bacterial isolates in different antibiotic concentrations (N=3). SP represents species, KP represents *K. pneumonia*, EC represents *E. coli*, SA represents *S. aureus*, AB represents *A. baumannii*, PA represents *P. aeruginosa*, CIP represents ciprofloxacin, GEN represents gentamicin, DOX represents doxycycline, CEF represents ceftazidime, COL represents colistin, IMI represents imipenem. The $QNICR_{1h}$ at MIC (OD-based) is marked in red. The strains which MIC >64 μg/mL in OD-based method is labelled by "Y" in the table.

SP	Strain	μg/mL	>64	64	32	16	8	4	2	1	0.5	0.25	≤0.125
KP	13368	CIP		1	0	2	4	1	-1	6	12	57	86
		GEN		2	7	28	63	91	98	97	95	101	99
		DOX		-1	3	-2	9	57	92	99	100	101	101
		CEF		2	2	10	52	98	101	100	103	97	103
		COL		5	0	-1	2	1	27	72	98	101	102
		IMI		1	0	0	2	3	3	1	0	2	5
	M6	CIP		-1	1	2	1	1	4	2	-1	0	3
		GEN		0	3	0	10	25	54	87	97	98	95
		DOX		-2	1	3	-1	-2	1	9	36	87	102
		CEF		1	3	-1	-1	-1	1	2	2	-1	2
		COL		1	0	-1	0	-1	39	89	105	98	100
		IMI		-1	-2	-1	0	4	-1	3	0	-1	-2
EC	LEC-001	CIP	Y	66	93	98	98	100	103	99	98	99	101
		GEN		-4	4	-3	2	1	4	0	21	63	100
		DOX		-5	2	3	4	0	10	21	42	79	108
		CEF		91	97	96	103	97	96	101	99	96	108
		COL		1	1	0	5	-1	20	69	96	95	110
		IMI		2	1	0	-1	1	0	1	0	2	7
	12923	CIP		4	1	-3	-2	3	1	8	31	60	93
		GEN		-1	0	-2	4	1	2	8	36	70	97
		DOX		3	0	2	1	-1	-3	-1	2	19	44
		CEF		3	0	0	1	-2	-4	0	1	-2	2

		COL		-1	8	0	5	2	1	1	1	-1	3
		IMI		3	-2	3	-4	1	-2	-1	1	2	2
SA	EMRSA-15	CIP	Y	91	99	102	100	97	98	102	97	94	100
		GEN	Y	1	-4	3	-5	-2	-1	-1	32	74	97
		DOX		-1	1	2	1	4	4	0	-2	1	3
		CEF		97	99	97	101	100	103	103	106	99	101
		COL	Y	92	97	92	99	100	100	93	101	99	101
		IMI		0	0	-1	-3	4	-3	0	3	-3	-1
	9144	CIP		1	0	-1	1	-1	1	2	1	7	3
		GEN		-1	-3	-2	-2	2	0	3	-4	-3	-1
		DOX		4	-3	-3	6	0	1	-1	-3	1	-1
		CEF		-1	3	8	34	67	92	95	102	98	100
		COL		98	93	95	96	98	95	97	96	93	97
		IMI		-2	0	-3	-3	-3	2	2	2	1	0
AB	AYE	CIP	Y	69	95	98	98	100	98	100	95	99	98
		GEN	Y	99	94	96	102	98	99	101	99	101	100
		DOX		1	-1	1	2	-2	-1	-1	34	83	95
		CEF		104	93	98	96	99	99	99	100	102	97
		COL		0	4	-1	1	1	-4	0	12	43	82
		IMI		1	-2	-2	4	0	-1	-2	-4	24	65
	17978	CIP		4	0	2	2	2	0	22	72	88	87
		GEN		-1	0	2	1	0	4	44	86	97	102
		DOX		-2	-2	-2	1	-2	0	-1	0	4	42
		CEF		3	-1	16	51	81	99	99	101	95	98
		COL		3	4	-1	1	2	2	2	0	-2	1
		IMI		-4	3	0	-1	-2	1	-1	1	1	1
PA	PAO1	CIP		10	-6	4	2	-4	-3	6	7	33	77
		GEN		3	1	3	0	8	54	74	97	105	105
		DOX		3	3	2	27	73	95	93	101	103	102
		CEF		8	-5	6	0	-1	11	60	110	98	103
		COL		-2	-1	-9	1	-1	-2	2	-9	-7	-5
		IMI		-6	4	-5	4	37	79	103	97	107	99
	13437	CIP		100	103	112	95	99	101	91	103	100	105
		GEN	Y	91	104	100	97	89	92	98	97	101	90
		DOX	Y	89	103	97	105	87	95	107	97	98	91
		CEF	Y	106	85	113	112	91	106	108	104	105	96
		COL		9	-1	4	-3	7	0	-1	-7	9	1
		IMI	Y	92	101	99	108	106	87	101	101	116	94

The $QNICR_{1h}$-Threshold is used to decide the MIC detected by the impedance method, which is defined as the minimum antibiotic concentration that the corresponding $QNICR_{1h}$ is less than the $QNICR_{1h}$-Threshold. The $QNICR_{1h}$-Threshold is calculated from the successful rate

that achieving the highest concordance between the OD-based MIC and impedance-based MIC. The successful rate is calculated as

$$successful\ rate = \sum_{i=1}^{n} \begin{matrix} If\left(QNICR_{MIC,i} < QNICR_{Th}\right)\ AND \\ If(QNICR_{\frac{1}{2}-MIC,i} > QNICR_{Th}) \end{matrix} \quad (8.3)$$

where $QNICR_{MIC,i}$ is the $QNICR_{1h}$ at MIC (OD-based method), $QNICR_{1/2-MIC,i}$ is the $QNICR_{1h}$ at 1/2-fold MIC (OD-based method), $QNICR_{Th}$ is the $QNICR_{1h}$-Threshold.

If the $QNICR_{1h}$-Threshold is less than the $QNICR_{1h}$ at 1/2-fold MIC (OD-based method) and larger than the $QNICR_{1h}$ at MIC (OD-based method), the successful rate plus one.

Within 60 impedance-based tests, 10 MICs (OD-based) were > 64 μg/mL. 15 MIC (OD-based) were ≤0.125 μg/mL. They would not contribute to the $QNICR_{1h}$-Threshold calculation. For other tests, the OD-based MIC, $QNICR_{1h}$ at MIC (OD-based) and 1/2-fold MIC (OD-based) are summarized in Table 8-7.

Table 8-7: The OD-based MIC, $QNICR_{1h}$ (%) at MIC (OD-based), 1/2-fold MIC (OD-based) of certain tests. SP represents species, KP represents *K. pneumonia*, EC represents *E. coli*, SA represents *S. aureus*, AB represents *A. baumannii*, PA represents *P. aeruginosa*, CIP represents ciprofloxacin, GEN represents gentamicin, DOX represents doxycycline, CEF represents ceftazidime, COL represents colistin, IMI represents imipenem.

SP	Strain		OD-based MIC (μg/mL)	$QNICR_{1h}$ at MIC	$QNICR_{1h}$ at 1/2-fold MIC
KP	13368	CIP	1	12	57
		GEN	16	28	63
		DOX	32	3	-2
		CEF	16	10	52
		COL	4	1	27
	M6	GEN	8	10	25
		DOX	2	1	9
		COL	4	-1	39
EC	LEC-001	GEN	1	0	21
		DOX	4	0	10
		CEF	64	91	97
		COL	4	-1	20
	12923	CIP	1	31	60
		GEN	2	2	8
		DOX	1	-1	2
SA	EMRSA-15	DOX	1	-2	1
		CEF	64	97	99
		IMI	0.25	-3	-1
	9144	CEF	16	8	34
		COL	64	98	93
AB	AYE	DOX	4	-2	-1

		CEF	64	104	93
		COL	1	0	12
		IMI	1	-4	24
	17978	CIP	1	22	72
		GEN	2	4	44
		DOX	1	0	4
		CEF	8	51	81
PA	PAO1	CIP	0.25	33	77
		GEN	2	54	74
		DOX	32	3	2
		CEF	2	11	60
		COL	0.25	-7	-5
		IMI	8	4	37
	13437	CIP	64	100	103

The $QNICR_{1h}$ of doxycycline antibiotic was abnormal low at MIC (OD-based) and 1/2-fold MIC (OD-based) compared with other kinds of antibiotics. The doxycycline is a bacteriostatic antibiotic, which normally presents a "delay growth" in the OD-based growth curve. Therefore, $QNICR_{1h}$ of doxycycline antibiotic would not contribute to the threshold calculation.

What is more, the $QNICR_{1h}$ of isolates whose MIC = 64 μg/mL were abnormal high at MIC (64 μg/mL) and 1/2-fold MIC (32 μg/mL). A 2-fold tolerance of OD-based MIC is commonly acceptable. The bacterial isolates that MIC = 64 μg/mL may be mixed with isolates whose MIC > 64 μg/mL. Furthermore, 64 μg/mL is above the highest threshold concentration in the EUCAST table. Therefore, the MIC detection at 64 μg/mL shows less importance than MIC detection at the lower concentrations of antibiotics. As a result, the $QNICR_{1h}$ of isolates whose MIC= 64μg/mL would not contribute to the threshold calculation as well. The $QNICR_{1h}$ at MIC (OD-based) and 1/2-fold MIC (OD-based) of other tests are shown in Figure 8-23.

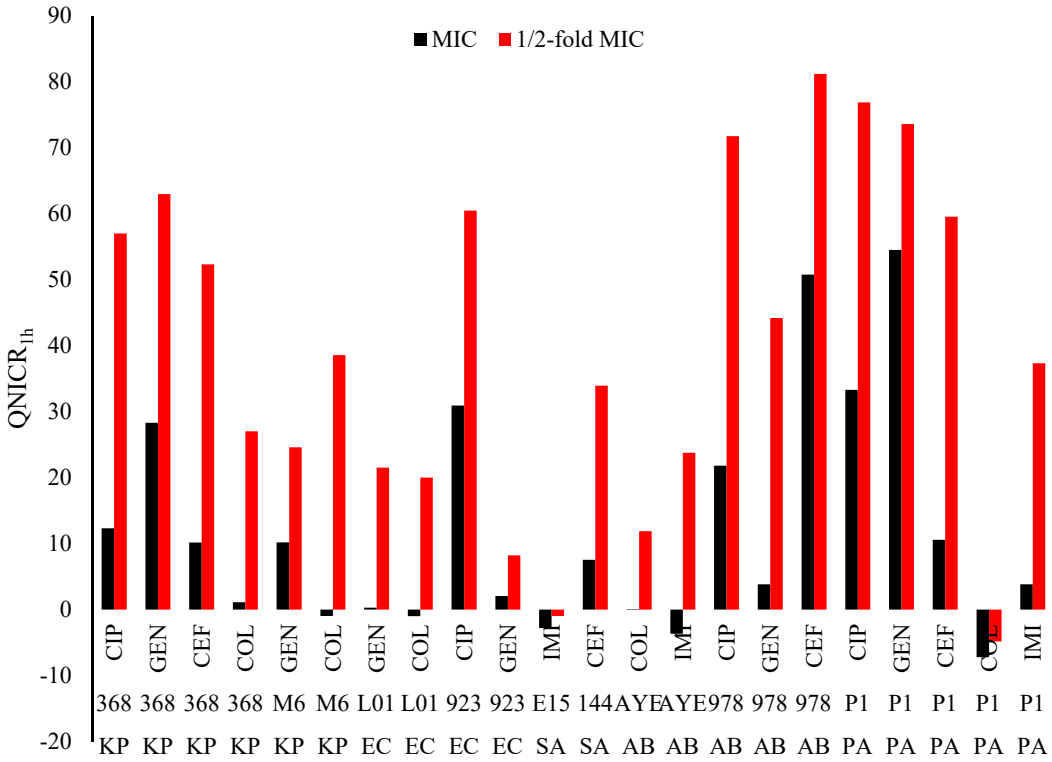

Figure 8-23: The $QNICR_{1h}$ (%) at MIC (OD-based) and 1/2-fold MIC (OD-based) of 22 tests. KP 368 represents *K. pneumonia* 13368, KP M6 represents *K. pneumonia* M6, EC L01 represents *E. coli* LEC-001, EC 923 represents *E. coli* 12923, SA E15 represents *S. aureus* EMRSA-15, SA 144 represents *S. aureus* 9144. AB AYE represents *A. baumannii* AYE, AB 978 represents *A. baumannii* 17978. PA P1 represents *P. aeruginosa* PAO1, CIP represents ciprofloxacin, GEN represents gentamicin, DOX represents doxycycline, CEF represents ceftazidime, COL represents colistin, IMI represents imipenem.

Taking the $QNICR_{1h}$ of 22 tests to Formula 8.3, the $QNICR_{1h}$-Threshold that correspond to the highest successful rate are from 13 % to 19 %. As a result, the $QNICR_{1h}$-Threshold for deciding the MIC detected by the impedance method is set as the mean between 13 % and 19 % as 16 %.

Applying 16% as $QNICR_{1h}$-Threshold to decide bacterial growth, where the lowest antibiotic concentration that $QNICR_{1h}$ less than 16% was defined as the MIC detected by the impedance method, the MIC (impedance-based) and the fold between the MIC (OD-based) are summarized in Table 8-8.

Table 8-8: The MIC (impedance-based) when the $QNICR_{1h}$-Threshold is set as 16% and the fold between the MIC (OD-based). SP represents species, KP represents *K. pneumonia*, EC represents *E. coli*, SA represents *S. aureus*, AB represents *A. baumannii*, PA represents *P. aeruginosa,* CIP represents ciprofloxacin, GEN represents gentamicin, DOX represents doxycycline, CEF represents ceftazidime, COL represents colistin, IMI represents imipenem. 57 out of 60 MICs detected by the impedance method was within 2-fold difference with that of the OD-based broth dilution method.

SP	strain		CIP	GEN	DOX	CEF	COL	IMI
KP	13368	MIC (μg/mL)	0.5	32	8	16	4	≤0.125
		Fold	=	2	4	=	=	=
	M6	MIC (μg/mL)	≤0.125	8	1	≤0.125	4	≤0.125
		Fold	=	=	2	=	=	=
COL	LEC-001	MIC (μg/mL)	>64	1	2	>64	4	≤0.125
		Fold	=	=	2	2	=	=
	12923	MIC (μg/mL)	1	1	0.5	≤0.125	≤0.125	≤0.125
		Fold	2	2	2	=	=	=
EC	EMRSA-15	MIC (μg/mL)	>64	1	≤0.125	>64	>64	≤0.125
		Fold	=	=	4	2	=	2
	9144	MIC (μg/mL)	≤0.125	≤0.125	≤0.125	16	>64	≤0.125
		Fold	=	=	=	=	2	=
SA	AYE	MIC (μg/mL)	>64	>64	1	>64	0.5	0.5
		Fold	=	=	4	2	2	=
	17978	MIC (μg/mL)	2	2	0.25	16	≤0.125	≤0.125
		Fold	2	=	2	2	=	=
PA	PAO1	MIC (μg/mL)	0.5	4	16	2	≤0.125	8
		Fold	2	2	2	=	2	=
	13437	MIC (μg/mL)	>64	>64	>64	>64	≤0.125	>64
		Fold	2	=	=	=	=	=

The table demonstrates that 95% (57 out of 60) of the MICs detected by impedance are within a 2-fold difference with the traditional OD-based broth dilution method. The effects from the mechanisms of bacterial metabolism, incubation temperature or initial bacterial concentrations were removed. However, there was a relatively large difference for doxycycline susceptibility testing. Doxycycline is a bacteriostatic antibiotic whose effect on metabolism inhibition may differ from that of bactericidal antibiotics.

8.3.5 Blind test for *K. pneumoniae*

Ten *K. pneumoniae* isolates were used for Resistance/Not resistance blind test. Final antibiotic concentrations of 4 μg/mL ceftazidime, 2 μg/mL colistin, 0.5 μg/mL ciprofloxacin, 4 μg/mL gentamicin and 2 μg/mL doxycycline were mixed with the testing *K. pneumoniae* isolates in their respective impedance detection chambers. The concentration of each of the 5 antibiotics was set at the resistant/not resistant breakpoint in EUCAST table. In the control chamber, the testing *K. pneumoniae* isolates were mixed with fresh MH1 broth. A two-terminal impedance system was used to detect the impedance magnitude at 10 kHz of six chambers simultaneously. The ceftazidime, colistin, ciprofloxacin, gentamicin and doxycycline MICs against the test isolates were then detected by the OD-based broth dilution method afterwards. Table 8-9 shows the MICs detected by the OD-based broth dilution method, and Table 8-10 summarizes the corresponding OD-based antibiotic susceptibilities depended on the thresholds shown in the table.

Table 8-9: MICs for bacterial isolates detected by the OD-based broth dilution method (N = 3, μg/mL).

Antibiotics	Threshold (μg/mL)	1	2	3	4	5	6	7	8	9	10
Doxycycline	2	8	32	>64	4	4	>64	4	8	32	2
Gentamicin	4	32	>64	>64	>64	>64	>64	16	8	16	8
Ceftazidime	4	>64	>64	>64	>64	>64	>64	>64	0.125	4	0.125
Ciprofloxacin	0.5	16	>64	>64	>64	>64	8	>64	0.125	>64	0.125
Colistin	2	2	0.5	0.25	0.25	>64	2	2	0.25	>64	2

Table 8-10: OD-based antibiotic susceptibility of testing strains depended on thresholds shown in table. The resistant (R) strains detected by the OD method were defined as having higher MIC than the threshold concentrations. In contrast, the not resistant strains (S) were defined as having lower MIC than the threshold concentrations.

Antibiotics	Threshold (μg/mL)	1	2	3	4	5	6	7	8	9	10
Doxycycline	2	R	R	R	R	R	R	R	R	R	R
Gentamicin	4	R	R	R	R	R	R	R	R	R	R
Ceftazidime	4	R	R	R	R	R	R	R	S	R	S

Ciprofloxacin	0.5	R	R	R	R	R	R	R	S	R	S
Colistin	2	R	S	S	S	R	R	R	S	R	R

The $QNICR_{1h}$ detected by the impedance method are shown in Table 8-11 and the Table 8-12 summarizes the corresponding antibiotic susceptibilities based on $QNICR_{1h}$-Threshold=16%.

Table 8-11: $QNICR_{1h}$ for bacterial isolates detected by the impedance method (N = 3, %).

Antibiotics	Concentration (μg/mL)	1	2	3	4	5	6	7	8	9	10
Doxycycline	2	75	100	101	12	12	92	8	5	90	7
Gentamicin	4	99	100	99	99	102	98	89	30	88	91
Ceftazidime	4	97	99	102	100	96	100	84	3	17	2
Ciprofloxacin	0.5	95	103	99	97	100	84	101	0	96	0
Colistin	2	46	2	6	4	101	25	30	14	99	19

Table 8-12: Antibiotic susceptibility based on the impedance method. The resistant (R) strains detected by the impedance method were defined as having higher $QNICR_{1h}$ than 16 %. In contrast, the not resistant strains (S) were defined as $QNICR_{1h}$ lower 16 %. The differences between Table 8-12 and Table 8-10 are marked in red.

Antibiotics	Concentration (μg/mL)	1	2	3	4	5	6	7	8	9	10
Doxycycline	2	R	R	R	S	S	R	S	S	R	S
Gentamicin	4	R	R	R	R	R	R	R	R	R	R
Ceftazidime	4	R	R	R	R	R	R	R	S	R	S
Ciprofloxacin	0.5	R	R	R	R	R	R	R	S	R	S
Colistin	2	R	S	S	S	R	R	R	S	R	R

In the blind test, 45 of 50 (90%) antibiotic susceptibility detected by the impedance method were same of that detected by the broth dilution method. 49 of 50 (98 %) antibiotic susceptibility detected by the impedance method were same with that detected by the OD-based

method if 2-fold tolerance of MIC is acceptable. All errors came from the tests with doxycycline. The blind test results proved that the differential impedance method could be used in antibiotic susceptibility testing of *K. pneumoniae* independently and rapidly.

8.4 Discussion and conclusion

8.4.1 DEP-enhanced optical chip

The DEP-enhanced optical system showed high sensitivity and reliability for β-lactamase detection. For the optical chip, the LoD was 3.1 mA.U., lower than the 4.1 mA.U. reported by Sieben *et al*. (2010) [20], who used the same chip material, path length and electronic components as the present optical chip. The improved LoD resulted from the tinted channel, which absorbed reflected and refracted light. The noise in the photodiode in this optical chip was lower than that reported by Sieben *et al.* (2010).

The optical chip and bench-top plate reader had similar K_M and k_{cat} for TEM-1 with nitrocefin substrate, which proved that the optical chip material did not influence the enzyme reaction catalysed by TEM-1. Moreover, the optical chip detected a smaller deviation of K_M compared to the bench-top plate reader, whose test solution was prepared in a 96-well plate. The meniscus phenomenon in the chambers in the 96-well plate may have caused the larger deviations in the plate reader results, because the path length in each chamber may have been different. The meniscus phenomenon was not present with the optical chip, so it had lower deviations compared to the plate reader.

When *E. coli* TOP10 was used for β-lactamase diagnosis, the cloudy lysates did not affect the absorbance at 470 nm. Furthermore, the optical chip could detect β-lactamases from 10^5 CFU/mL bacteria, while the plate reader could only detect β-lactamases from 10^7 CFU/mL bacteria. The optical chip has two advantages for β-lactamase diagnosis. First, the long path length of the optical chip led to high detection sensitivity. The path length of the optical chip was around 6.5 times longer than that of a chamber in the 96-well plate containing 200 μL solution, so the optical chip had 1-magnitude better detection sensitivity than the plate reader. Second, the volume in the optical chip channel was just 4 μL. When the optical chip channel and the 96-well plate contained the same amount of bacteria, the optical chip had 10-fold higher bacterial concentration than the 96-well plate. Combining the two advantages led to the optical chip having 100-fold greater sensitivity for detecting β-lactamase diagnosis compared to the plate reader.

In clinical tests of 66 clinical isolates, the optical chip showed 100% accuracy for β-lactamase detection. The bacterial species and the β-lactamase type did not influence the diagnosis results. The clinical isolates detected by the optical chip were from a loop dipped on an agar plate, whose bacterial concentration was $>10^9$ CFU/mL [117]. The minimum clinical isolate concentration for β-lactamase detection by the optical method requires further research.

During bacterial enrichment, using a filter to trap bacteria in 10 mL urine sample and retrieve by 1 mL DI water not only increased the bacterial concentration by a factor of 10, but also

reduced the medium conductivity to less than 10 mS/m, which is essential for pDEP to capture bacteria in frequency (≤1 MHz). Avesar *et al.* (2017) reported using a filter to change the medium properties [61]. The filter step worked well for reducing the medium conductivity of LB broth. However, when the urine sample was pumped through the 0.22-μm filter, the filter might be blocked by large particles. A microfluidic H-filter could be used to change the medium conductivity, and relies on different ion and particle diffusion times in laminar flow [253]. The H-filter could be used to solve blockage issues in the future.

The DEP chamber used in this work was improved from the device reported by Páez-Avilés *et al.* (2015), whose DEP chamber could enrich bacteria concentrations by 20-fold in 1 hour [194]. The DEP chip described in this thesis showed 10-fold *E. coli* enrichment ability in 1 hour, which can be improved by reducing the retrieve volume. Embedding interdigitated electrodes in the optical chip channel might further improve the enrichment efficiency of the DEP chip.

This work generated a DEP force using interdigitated electrode (20-μm wide with 20-μm gaps). Kim *et al.* (2015) reported that asymmetrical interdigitated electrodes could also be used to replace the traditional symmetrical interdigitated electrodes for bacteria capture [193]. The DEP force on the edge of the asymmetrical electrodes may be greater than that on the edge of the symmetrical electrodes.

Combining two-step enrichment, the DEP-enhanced optical system could detect β-lactamases from *E. coli* TEM at 10^3 CFU/mL, which was 4-magnitude better than that from the conventional plate-based diagnosis. In the UK, the threshold concentration for UTI is 10^4 CFU/mL [42]. The DEP-enhanced optical chip may be suitable for detecting β-lactamases directly from UTI samples. The DEP-enhanced optical chip requires further clinical testing in the future.

8.4.2 pH system

The IrOx pH sensor is a low-cost, miniaturized and robust pH detection device, which can be used to detect β-lactamases in PoC settings.

The IrOx pH sensor utilised in the present work showed a super-Nernstian response, with 61.3 mV/pH detection sensitivity. Huang *et al.* (2012) reported similar sensitivity [210]. The deviation of three repeats was 5.4 mV and the LoD (3 σ) of the sensor was 0.26 pH. Huang *et al.* (2012) reported similar deviation from three repeats. The present sensor had a lower LoD than a commercial glass pH meter (0.01 pH) [254] or ISFET pH sensor [255], but can be easily miniaturized. The LoD of the metal–metal oxide pH sensor can be improved by using other fabrication protocols or other metal–metal oxide material. For example, Sardarinejad *et al.* (2018) reported that a sputtered ruthenium oxide (RuOx) pH sensor could be used to detect pH with a LoD of 0.015 pH [256]. The improved pH sensor may provide better sensitivity for β-lactamase diagnosis.

The pH indicator had lower linearity and stability than the IrOx pH sensor. The LoD of the prepared pH indicator was 0.15 pH. The pH indicator and pH sensor detected similar K_M and k_{cat} of TEM-1 on carbenicillin substrate.

When carbenicillin solution was mixed with *E. coli* CTX-M lysates, the pH reduction was slow. In contrast, when carbenicillin solution was mixed with lysate supernatant from the same amount of *E. coli* CTX-M, the pH reduction speed was increased five times. A possible reason for the differences in the pH slopes between the solution containing lysates and that containing lysate supernatant is that insoluble components in bacteria (lipids, large proteins, DNAs) can absorb protons and maintain a stable pH value. However, further research is still required to determine the reasons for the variations in the pH reduction slopes caused by the lysates and lysate supernatant.

The pH sensor could measure β-lactamases from 10^5 CFU/mL *E. coli* TEM and 10^8 CFU/mL clinical isolate *E. coli* 11560 in 1 hour. When the same concentration of *E. coli* TEM and *E. coli* 11560 were used for experiments, the *E. coli* TEM sample had a higher pH reduction slope than the *E. coli* 11560 sample. As the same carbenicillin concentration was maintained in the experiment, *E. coli* TOP10 expressed a higher amount of β-lactamase compared to *E. coli* 11560. The reason may be that >1 *bla*TEM gene–encoded plasmids were transferred into *E. coli* TEM, so the *E. coli* TOP10 TEM had a greater amount of *bla*TEM genes than *E. coli* 11560.

In the clinical test, five of eight clinical isolates encoded β-lactamase–related genes. Two β-lactamase–positive samples were diagnosed as β-lactamases–negative by the pH method. The errors in β-lactamase detection may be that the threshold of pH reduction (LoD of the pH sensor) was not suitable for broadband β-lactamase detection.

In conclusion, compared with the conventional Carba NP method, the novel pH method for detecting β-lactamases could simplify the sample preparation step and shorten the experiment time. Furthermore, the pH sensor can be used for detecting kinetic parameters (e.g. K_M and k_{cat}) for reactions catalysed by β-lactamases.

8.4.3 Impedance system

A multi-chamber, temperature-controlled impedance detection system was developed, which could detect the MICs of different antibiotics for clinical isolates in 1 hour. The four-terminal impedance detection system had high accuracy and reliability. The conductivity errors at 10 Hz between the four-terminal system and a commercial conductivity meter were within 0.002 S/m, which was similar to that reported by Huang *et al.* (2011) [252]. The conductivity error detected at 10 kHz between the two-terminal impedance detection system and a commercial conductivity meter was within 0.005 S/m. The conductivity error mainly stemmed from the electrode double layer.

The parasitic capacitance resulting from crosstalk between the signal transmission cables limited impedance detection in the high-frequency range. The electrodes, signal transmission PCB and signal transmission cables require improvement to avoid crosstalk. For example, a ground layer can be added between the top and bottom layers of the signal transmission PCB. Coaxial cable can replace the ribbon cables. Rapid AMR diagnosis by a capacitance monitor was reported by Puttaswamy *et al.* (2013) and could detect antibiotic susceptibility in 4 hours if the bacterial concentration was 10^5 CFU/mL [99]. However, they did not applied a differential design so the results were easily influenced by other factors such as temperature or

initial bacterial concentrations. In the future, an improved impedance system could be used to detect the capacitance of the bacterial suspension.

In this work, the impedance magnitude of an *E. coli* suspension with a bacterial concentration at 10^7 CFU/mL was detected. The NICR was around 15 % in 1 hour, which was similar to that reported in the literature. For example, Yang *et al.* (2005) demonstrated that, at 10^7 CFU/mL *E. coli* concentration, the impedance was reduced by 20% in 1 hour [94]. Safavieh *et al.* (2017) demonstrated that at 10^8 CFU/mL *E. coli* and MRSA, the impedance was reduced by 60% in 1 hour [31]. The NICR depends on the bacterial species, medium conductivity and broth type.

By comparing an antibiotic exposed sample to an unexposed sample as a differential measurement, the effect of an antibiotic on a bacterial strain can be indicated. The $QNICR_{1h}$-Threshold was set as 16 %, based on experiment results from ten bacterial isolates for six different antibiotics. In the comparison between impedance-based method and OD-based method, up to 95 % of the MICs detected by the impedance system in 1 hour were within 2-fold of that detected by the broth dilution method in 20 hours. In blind tests, the antibiotic susceptibility of 10 *K. pneumoniae* strains was detected by impedance and broth dilution method. 90 % of antibiotic susceptibility detected by the impedance system was the same as the gold-standard broth dilution method. 98 % antibiotic susceptibility detected by the impedance method was same with the broth dilution method if 2-fold tolerance of the MIC is acceptable. The clinical tests demonstrate that the impedance system can detect antibiotic susceptibility in a short time, and that the threshold in this system was accurate and promising in most cases.

However, there were relatively large variations in the MIC of doxycycline between the novel impedance method and the conventional broth dilution method. The 1-hour detection period of the impedance method might be insufficient for rapid detection of the susceptibility of a bacteriostatic antibiotic. A bacteriostatic antibiotic might have a longer effective time on metabolism inhibition than a bactericidal antibiotic. What is more, at some concentrations, the absorbance increased initially in first few hours (indicating growth), but then decreased. Therefore, the detection period of the impedance method can be extended for more accurate antibiotic susceptibility diagnosis on bacteriostatic antibiotics. The impedance system can be used for detecting the primary effect (bacteriostatic or bactericidal) of an antibiotic on a bacterial strain. After 1-hour growth in an antibiotic medium, the bacterial sample can be moved to an antibiotic-free environment. The bacterial growth in the antibiotic-free environment is monitored by the impedance system, and the medium resistance change in the antibiotic-free environment can be used to indicate the primary effect of an antibiotic.

Chapter 9: Conclusion, improvement and future work

This chapter summarizes the achievements in this project, lists the improvement of current rapid AMR diagnosis methods and states the future directions to improve the rapid AMR diagnosis systems. Three rapid AMR diagnosis systems are described in this thesis. It was found that the optical system and the pH system are able to diagnose the presence of β-lactamases from bacterial samples even at low concentrations. The third system using impedance demonstrates the ability to diagnose antibiotic susceptibility for clinical isolates in 1 hour.

9.1 Optical system

The optical detection chip monitors the absorbance change due to hydrolysis of a β-lactam analogue (nitrocefin). The minimum concentration needed to detect the presence of β-lactamases from lab safe *E. coli* was 10^5 CFU/mL. The optical chip could distinguish β-lactamase-producing clinical bacteria with 100% accuracy. By combining two bacterial enrichment steps together, the sensitivity of the integrated system to detect the presence of β-lactamases from lab safe *E. coli* can be improved to 10^3 CFU/mL in 1 hour.

The PMMA optical chip showed high sensitivity and robustness for detecting β-lactamases, but the manufacturing cost limits its application in PoC settings. PDMS is an optimal material for moulding because it is cheap, non-fluorescent, non-toxic and non-flammable [257]. The transparent PDMS can be tinted by hydrophobic dye and its absorption coefficient can be changed [258]. Thus, a disposable moulded version of the optical chips has been developed to replace the current PMMA chip.

The tinted PDMS material need to have the same absorption coefficient at 470 nm with the grey PMMA board. Transparent PDMS (Sylgard 184 Silicone Elastomer; base and curing agent mixed in a 10:1 ratio) was mixed with different concentrations of Sudan II (Sigma-Aldrich) and then degassed. Mixing gel (1 mL) was pipetted into a 1-cm path length test tube and baked in a 60°C oven for 3 hours. The UV-Vis spectrum (400 nm to 600 nm) of grey PMMA and the tinted PDMS was detected by a UV-Vis spectrophotometer (Rigol Ultra-3660 UV-Vis Spectrophotometer). Figure 9-1 shows the results.

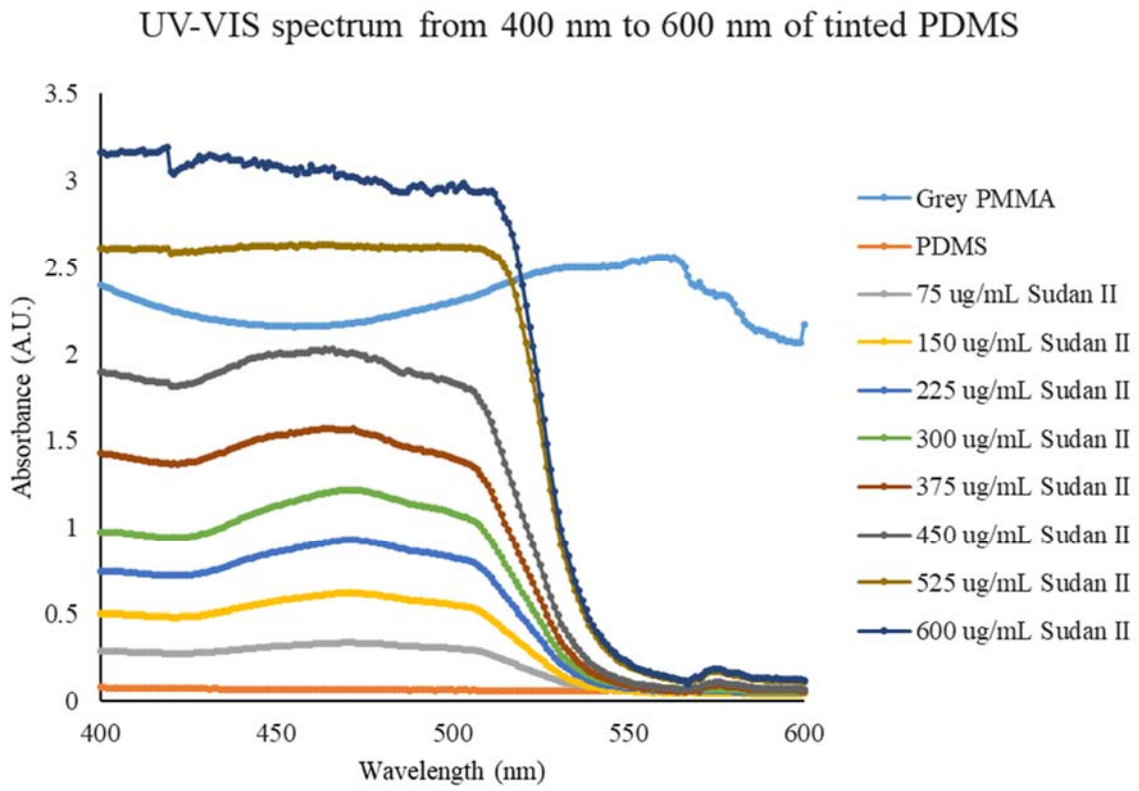

Figure 9-1: The absorbance spectrum of grey PMMA, transparent PDMS and PDMS mixed with Sudan II. At 470 nm, PDMS with 450 µg/mL Sudan II dye had a similar absorption coefficient with the grey PMMA.

PDMS containing 450 µg/mL Sudan II was used to fabricate the moulding optical chip because it has the similar absorption coefficient with the grey PMMA used for optical chip fabrication. The optical chip moulds were 3D-printed in ABS and cured at 100°C overnight. The length of the detection channel was 25 mm, and the width and height was 300 µm. Transparent PDMS (Sylgard 184 Silicone Elastomer; base and curing agent mixed in a 10:1 ratio) was mixed with Sudan II (final concentration, 450 µg/mL; Sigma-Aldrich) and then degassed. Figure 9-2 (a) shows the manufacturing process for moulding the optical chip. The power supply, data recording and data analysis were the same as that for the PMMA chip. Figure 9-2 (b) shows a photo of the customized PCB and one channel of the optical chip.

(a)

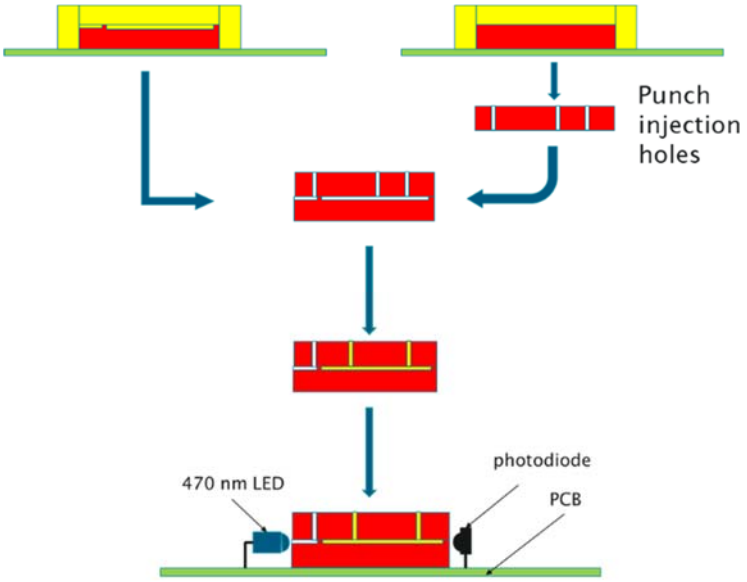

(b)

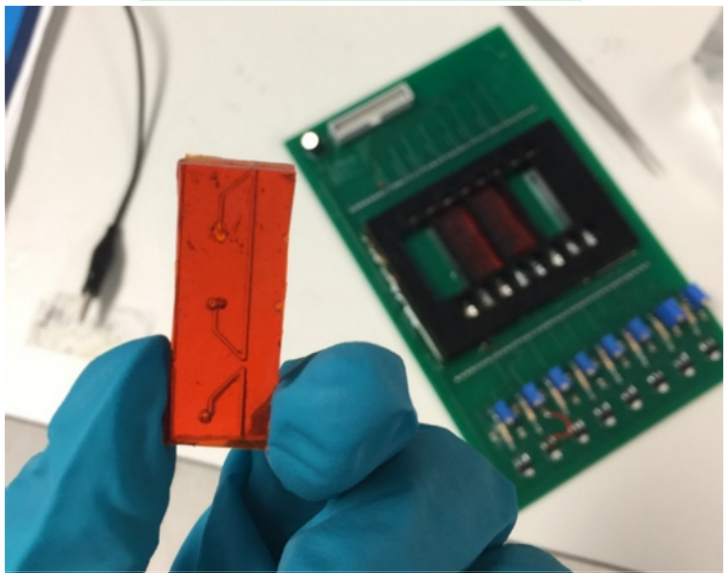

Figure 9-2: (a) The manufacturing process for the moulding optical chip. Tinted PDMS gel was injected into 3D printing moulds, and then baked at 60°C for 3 hours. Fluidic input and output were punched in 1-mm diameter. Two layers of patterned PDMS were bonded by oxygen plasma bonding for 30 seconds. The moulding optical chip was placed in a customized PCB with a 470-nm LEDs and light-voltage converter glued to either side. (b) A photo of the customized PCB and one channel of the moulding optical chip. Each PCB contained four channels.

The chip was calibrated using 0.1–3.2 μM Atto 488. Figure 9-3 shows the absorbance against the Atto 488 concentration.

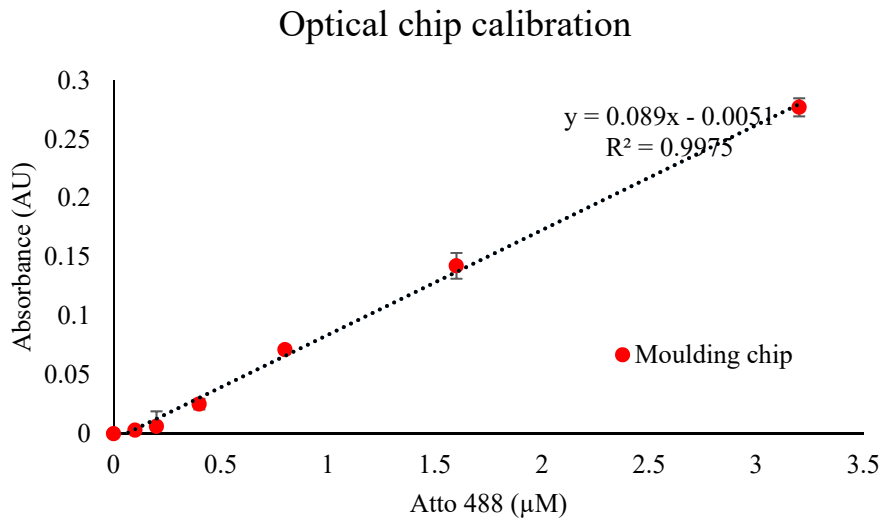

Figure 9-3: The absorbance against Atto 488 detected by the moulding optical chip. Error bars represent the standard deviations from three measurements.

The absorbance/Atto 488 concentration slope detected by the micromilled PMMA optical chip was 0.0865 A.U./μM; and the moulded optical chip was 0.089 A.U./μM, similar sensitivity to the micromilled chip. The difference between the slopes may have been due to the mechanical property of the PDMS, which is soft and easily stretched therefore the path length could be slightly longer. The LoD of the moulded optical chip was 18 mA.U., which was worse than the micromilled optical chip, but remained within a reasonable range for detecting β-lactamases. The lower LoD results from higher standard deviation between three repeats. The channel is removable and the positions might be slightly different during three repeats. The new chip was easy to manufacture and could be disposable in PoC settings. However, Sudan II is toxic, and should be replaced in the future. PDMS has a porous structure, so the solution may evaporate after a long time. Cyclic olefin copolymer (COC) is a glass-like material and can be easily tinted [259], and could be suitable for next generation moulding optical chip

In the future, nitrocefin may be freeze dyed into the channel to simplify operation for β-lactamase diagnosis in PoC situations. Besides this, a low cost FGPA board can replace the DAQ card to control the LED and measure the output voltage from the photodiode.

Other bacterial enrichment technologies can be used to concentrate bacteria as an alternative to the DEP chip, such as spiral cell retention devices or acoustic techniques. The spiral cell retention device is based on inertial focusing [260]. A promising example of this is Kwon *et al.* (2017), who used a spiral cell retention device to separate cells [261]. A schematic diagram of this is shown in Figure 9-4.

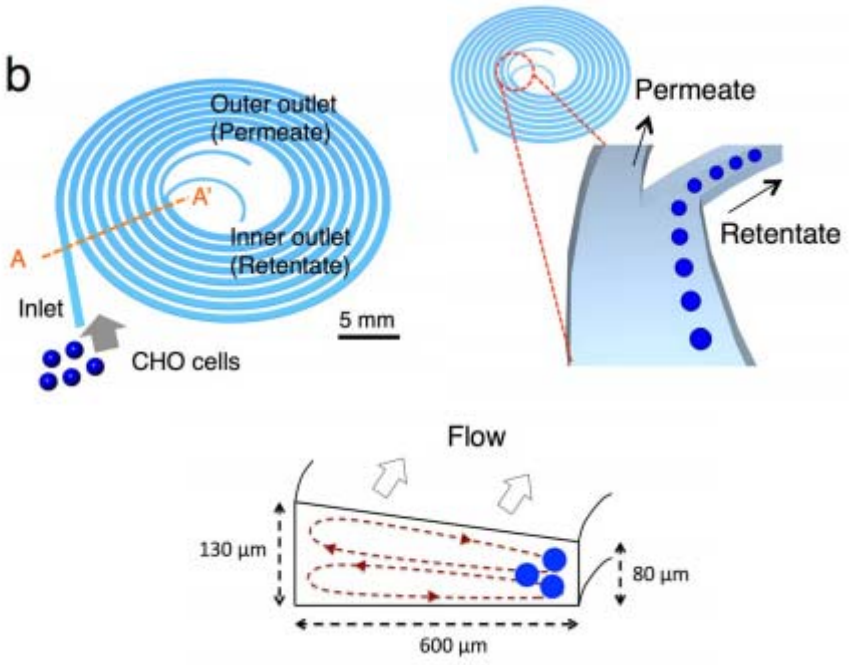

Figure 9-4: The schematic diagram of a spiral retention device reported by Kwon *et al.* (2017). This device separated cells based on the inertial focusing effect.

Acoustic devices were also reported to concentrate bacteria, such as in Ohlsson *et al.* (2018), where the acoustic force was externally applied through an actuator [262]. An ultrasonic transducer was mounted close to the channel and driven to resonance. Therefore, a standing pressure wave was created within the channel and moves particles within the channel to the minima of this standing wave. This technique of using acoustic force can improve the efficiency of bacterial capture.

9.2 pH system

The pH system aims to detect the presence of β-lactamases by monitoring the pH change caused by β-lactam antibiotics hydrolysis. The pH detection system consists of an IrOx electrode and an Ag/AgCl electrode. The IrOx pH sensor showed high sensitivity and linearity. The minimum *E. coli* TOP10 concentration for β-lactamase detection was 10^5 CFU/mL in 1 hour, and the minimum clinical isolate concentration for β-lactamases detection was 10^8 CFU/mL in 1 hour. In the future, the LoD of the pH sensor can be improved by using other fabrication protocols or other metal–metal oxide material.

9.3 Impedance system

The impedance system is a multi-chamber, temperature-controlled impedance detection device, which measures the reduction of the medium's resistance caused by bacterial metabolism. The effect of the antibiotic is indicated by the quotation of impedance change between the chamber with an antibiotic versus the chamber without antibiotics. In a blind test

of five antibiotics with ten *K. pneumoniae* strains, the antibiotics susceptibility was detected at a coincidence of 90% by the impedance system compared with that detected by the broth dilution method, which is the gold standard. For an MIC test of 6 antibiotics with 10 clinical isolates, 95% of the MICs detected by the impedance system were within 2-fold difference with that detected by the broth dilution method.

The growth rate of *E. coli* may be influenced by the gas-permeability and volume-to-surface ratio of the incubation chamber [132]. In the future, a PDMS chip will be used for long-term antibiotic susceptibility detection. PDMS has a porous structure, so oxygen can enter the PDMS channel to maintain bacterial growth for a longer time. Bacteriostatic antibiotics may require longer detection time (>2 hours), so the adaption of a PDMS chip may further increase the accuracy in bacteriostatic AST. The PDMS channel will reduce the cost of manufacture so that the chip can be disposable while increasing the performance. Now, a PDMS impedance detection chip has been fabricated and tested. Figure 9-5 shows a schematic diagram of two PDMS impedance chips bond together for differential measurement.

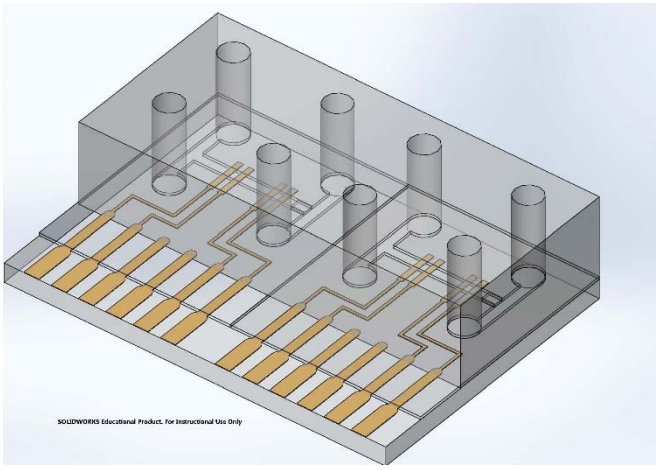

Figure 9-5: A schematic diagram of two PDMS impedance detection chips, which are bonded together to perform differential measurements (with and without antibiotics).

The PDMS impedance chip consists of four electrodes on a glass substrate and a PDMS channel on top. The glass substrate was the same as that used in the current PMMA impedance detection chip. PDMS channel was moulded from a patterned photoresist. A 0.7-mm thick, 4-inch diameter glass wafer was covered with a 50-µm thick TMMF layer. The TMMF layer was exposed to UV light through a mask. Unexposed TMMF was removed. PDMS (Sylgard 184 Silicone Elastomer, base and curing agent mixed in a 10:1 ratio) was degassed and poured on top of the mould at 5 mm thickness, then baked in a 60°C oven for 1 hour. Fluidic holes were punched in 1-mm diameter. The glass substrate and the PDMS channel were bonded by oxygen plasma bonding (Diener Electronic, Femto) for 30 seconds. The droplets that contained bacterial suspensions were generated by fluidic restriction with a 5-µm gap on each side. Aqueous solution was injected into the channel, then flushed out by air flow, leaving an aqueous droplet in the middle channel. FC-40 oil was injected to prevent evaporation. Figure 9-6 shows the droplet formation process.

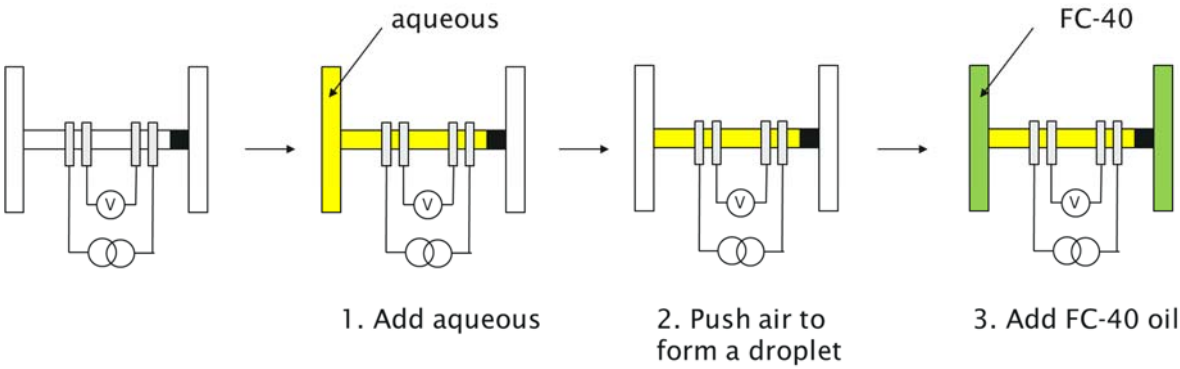

Figure 9-6: Droplet formation process in a moulding impedance chip. Aqueous solution was added first, and a droplet was generated by air pressure. FC-40 oil was used to fill the gap to inhibit aqueous evaporation.

MH1 broth was injected into the chamber to check the possibility of droplet formation. The aqueous–oil interface was checked by microscopy (Nikon N-SIM, Japan). Figure 9-7 shows typical photos of the MH1-FC-40 oil interface.

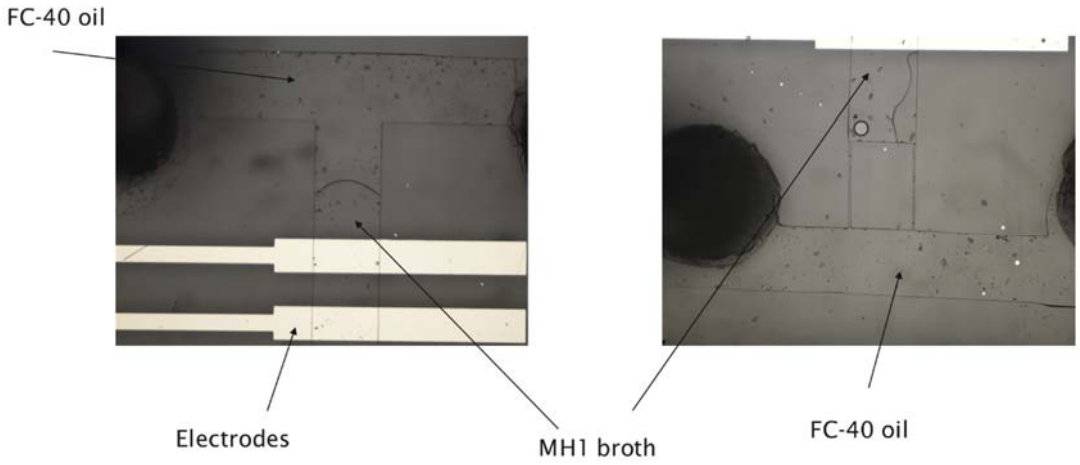

Figure 9-7: Typical photos of aqueous-oil interface on either side of the channel. The channel contained a clear aqueous–oil interface.

A clear aqueous-oil interface was observed in the channel. However, the droplet generation was not 100% successful. In the future, an improved impedance chip will be designed to leave more tolerance for droplet generation.

It is hoped that the advances in this project contribute to the development of a future PoC device that is cheap enough to be disposable, while being easy to use and accurate enough to study AMR. This can help further our understanding of AMR and improve the efficiency of diagnosis so that centralised testing facilities can be made more efficient while improving the quality of care of patients, as well as advance our knowledge of the effects of AMR in patient care.

Appendix: Matlab code for *E. coli* simulation

```
clc;

clear;

%% define original parameters %%

f_1=logspace(2,8,1000);%%frequency magnitude%%
f=2*pi*f_1;%%frequancy%%

%%define cell parameters%%
a=2*10^(-6);%%longer axes
b=0.5*10^(-6);%%shorter axeskwall=7^(-3);%%sm-1

dmem=7*10^(-9);%%m,cell membrane%%
dperiplasmic=10*10^(-9);%%m,periplasmic
dwall=7*10^(-9);%%m,cell wall


%%permittivity
Em=81;%%E0, medium permittivity%%
Ewall=10;%%wall
Eperiplasmic=60;%%periplasmic permittivity
Emem=6;%%E0, membrane permittivity%%
Ecyto=50;%%E0, cytoplasm permittivity%%


%%conductivity
km=0.35;%%Sm-1, medium conductivity%%
kwall=0;%%sm-1
kperiplasmic=3;%%Sm-1
kmem=0;%%Sm-1,
kcyto=0.22;%%Sm-1,cytoplasm conductivity


%%define channel
w=400*10^(-6);%%Width%%
h=125*10^(-6);%%heightm%%
l=1*10^(-3);%%length%%

E0=8.854*10^(-12);%%E0%%

%% complex permittvity %%
Ems=Em-1i*km./(E0.*f);%%complex cytoplasm permittivity%%

Ewalls=Ewall-1i*kwall./(E0.*f);%%complex wall permittivity%%

Eperiplasmics=Eperiplasmic-1i*kperiplasmic./(E0.*f);%%complex periplasm permittivity

Emems=Emem-1i*kmem./(E0.*f);%%complex membrane permittivity%%
```

```
Ecytos=Ecyto-1i*kcyto./(E0.*f);%%complex cytoplasm permittivity%%


%%start calculation
%%define e and p

e1=sqrt(1-(b./a)^2);%%eccentricity between cyto and mem
P1=(a*b*b)./((a+dmem)*(b+dmem)^2);%%volume fractor between cyto and mem

e2=sqrt(1-((b+dmem)/(a+dmem))^2);%%eccentricity between mem and periplasmic
P2=((a+dmem)*(b+dmem)^2)./((a+dmem+dperiplasmic)*(b+dmem+dperiplasmic)^2);%%volume
fractor between mem and periplasmic

e3=sqrt(1-((b+dmem+dperiplasmic)/(a+dmem+dperiplasmic))^2);%%eccentricity between
periplasmic and wall
P3=((a+dmem+dperiplasmic)*(b+dmem+dperiplasmic)^2)./((a+dmem+dperiplasmic+dwall)*(b+dme
m+dperiplasmic+dwall)^2);%%volume fractor between periplasmic and wall

e4=sqrt(1-((b+dmem+dperiplasmic+dwall)./(a+dmem+dperiplasmic+dwall))^2);%%eccentricity
between wall and medium



%%from x axis


%% 1 cyto to mem
A1x=((1-e1^2)/(2*e1^3))*((log((1+e1)/(1-e1)))-2*e1);%%dipolarise factor between cyto and mem

X1x=(1/3).*((Ecytos-Emems)./(Emems+A1x.*(Ecytos-Emems)));%%fcm between cyto and mem

%% 2 mem to periplasmic
A2x=(1-e2^2)/(2*e2^3)*((log((1+e2)/(1-e2)))-2*e2);%%dipolarise factor between mem and
periplasmic

X2x=(1/3).*((Emems-Eperiplasmics)+3.*X1x*P1.*(Emems+A2x.*(Eperiplasmics-
Emems)))./((Eperiplasmics+A2x.*(Emems-Eperiplasmics))+3.*X1x.*P1.*A2x.*(1-A2x).*(Emems-
Eperiplasmics));%%fcm between mem and periplasmic

%% 3 periplasmic to wall
A3x=(1-e3^2)/(2*e3^3)*((log((1+e3)/(1-e3)))-2*e3);

X3x=(1/3).*((Eperiplasmics-Ewalls)+3.*X2x*P2.*(Eperiplasmics+A3x.*(Ewalls-
Eperiplasmics))./((Ewalls+A3x.*(Eperiplasmics-Ewalls))+3.*X2x.*P2.*A3x.*(1-
A3x).*(Eperiplasmics-Ewalls));

%% 4 wall to medium
A4x=(1-e4^2)/(2*e4^3)*((log((1+e4)/(1-e4)))-2*e4);

Kx=1/3.*((Ewalls-Ems)+3.*X3x*P3.*(Ewalls+A4x.*(Ems-Ewalls)))./((Ems+A4x.*(Ewalls-
Ems))+3.*X3x.*P3.*A4x.*(1-A4x).*(Ewalls-Ems));

%%then move to y axis
```

```
A1y=(1-A1x)/2;

X1y=(1/3).*((Ecytos-Emems)./(Emems+A1y.*(Ecytos-Emems)));%%fcm between cyto and mem

%% 2 mem to periplasmic
A2y=(1-A2x)/2;%%dipolarise factor between mem and periplasmic

X2y=(1/3).*((Emems-Eperiplasmics)+3.*X1y*P1.*(Emems+A2y.*(Eperiplasmics-
Emems))./((Eperiplasmics+A2y.*(Emems-Eperiplasmics))+3.*X1y.*P1.*A2y.*(1-A2y).*(Emems-
Eperiplasmics));%%fcm between mem and periplasmic

%% 3 periplasmic to wall
A3y=(1-A3x)/2;

X3y=(1/3).*((Eperiplasmics-Ewalls)+3.*X2y*P2.*(Eperiplasmics+A3y.*(Ewalls-
Eperiplasmics))./((Ewalls+A3y.*(Eperiplasmics-Ewalls))+3.*X2y.*P2.*A3y.*(1-
A3y).*(Eperiplasmics-Ewalls));

%% 4 wall to medium
A4y=(1-A4x)/2;

Ky=1/3.*((Ewalls-Ems)+3.*X3y*P3.*(Ewalls+A4y.*(Ems-Ewalls)))./((Ems+A4y.*(Ewalls-
Ems))+3.*X3y.*P3.*A4y.*(1-A4y).*(Ewalls-Ems));



%%then move to z axis
Kz=Ky;

%%X2z=X2y;

%%Sum all three dimension together
K=1/3.*(Kx+Ky+Kz);
%%K_real=real(Kx)+real(Ky)+real(Kz);


Real_K=real(K);
Imag_K=imag(K);



%%K_cell=real(X2x)+real(X2y)+real(X2z);

Vcell=4/3*pi*a*b*b;


%%will change during growth
CFU=9;%%conting number

CFU_channel=1*10^CFU*(w*h*l)/10^(-6);

Vc_whole=Vcell*CFU_channel/(w*h*l);%%channel volume fraction
```

```
P=0.1;

%%Emixs=Ems.*((1+2*Vc_whole.*K)./(1-Vc_whole.*K));

Emixs=Ems.*((1+2*P.*K)./(1-P.*K));

Permittivity=real(Emixs);
Conductivity=-imag(Emixs)*E0.*f;

%%Zms=l/(w*h)./(1i.*f.*E0.*Emixs);

%%Zcells=l/(w*h)./(1i.*f.*E0.*Ecells);

Zmixs=l/(w*h)./(1i.*f.*E0.*Emixs);


%%double layer

%%Cdl=10^(-8);%%double layer capacitance

%%Zdl=1./(1i.*f*Cdl);


Ztotal=abs(Zmixs);

%%Real_Z=real(Zmixs);
%%Imag_Z=imag(Zmixs);

Z=log10(abs(Ztotal));




%%figure
%%plotyy(log10(f_1),Real_K,log10(f_1),Imag_K);hold on
%%plotyy(log10(f_1),Real_Emixs,log10(f_1),Imag_Emixs);hold on
%%plotyy(log10(f_1),Imag_K);hold on
yyaxis left
plot(log10(f_1),Permittivity);hold on
ylabel('Permittivity');
%%ylim([0,200]);
ylim auto

yyaxis right
plot(log10(f_1),Conductivity);hold on
ylabel('Conductivity (S/m)');
ylim auto

legend('Ecyto=150','Ecyto=100','Ecyto=50');
%%ylim([0,0.5]);
%%legend('10^6 CFU/mL','10^7 CFU/mL','10^8 CFU/mL','10^9 CFU/mL','10^10 CFU/mL');
xlabel('Log Frequency/Hz');
```

```
%%

hold on
```

References

[1] A. Fleming, "On the Antibacterial Action of Cultures of a Penicillium, with Special Reference to Their Use in the Isolation of B. influenzae," *Clinical Infectious Diseases,* vol. 2, no. 1, pp. 129-139, 1980, doi: 10.1093/clinids/2.1.129.

[2] J. Bigger, "Treatment of staphylococcal infections with penicillin by intermittent sterilistation," *The Lancet,* vol. 244, no. 6320, pp. 497-500, 1944, doi: 10.1016/S0140-6736(00)74210-3.

[3] J. O'Neill, "Antimicrobial resistance: Tackling a crisis for the health and wealth of nations," in "Review on Antimicrobial Resistance," 2014. [Online]. Available: https://amr-review.org/home.html

[4] K. Syal *et al.*, "Current and emerging techniques for antibiotic susceptibility tests," (in eng), *Theranostics,* vol. 7, no. 7, pp. 1795-1805, 2017, doi: 10.7150/thno.19217.

[5] F. Davey *et al.*, *Clinical diagnosis and management by laboratory methods*, 20th edn ed. Philadelphia PA.: W. B. Saunders Company, 2001.

[6] P. Dalgaard, T. Ross, L. Kamperman, K. Neumeyer, and T. A. McMeekin, "Estimation of bacterial growth rates from turbidimetric and viable count data," *International Journal of Food Microbiology,* vol. 23, no. 3, pp. 391-404, 1994/11/01/ 1994, doi: https://doi.org/10.1016/0168-1605(94)90165-1.

[7] C. L. Ventola, "The antibiotic resistance crisis: part 1: causes and threats," (in eng), *P T,* vol. 40, no. 4, pp. 277-283, 2015. [Online]. Available: https://www.ncbi.nlm.nih.gov/pmc/articles/PMC4378521/.

[8] R. R. Miller, V. Montoya, J. L. Gardy, D. M. Patrick, and P. Tang, "Metagenomics for pathogen detection in public health," (in eng), *Genome Med,* vol. 5, no. 9, pp. 81-81, 2013, doi: 10.1186/gm485.

[9] S. P. Ravindranath, L. J. Mauer, C. Deb-Roy, and J. Irudayaraj, "Biofunctionalized magnetic nanoparticle integrated mid-infrared pathogen sensor for food matrixes," *Analytical Chemistry,* vol. 81, no. 8, pp. 2840-2846, 2009/04/15 2009, doi: 10.1021/ac802158y.

[10] Y. Zhao, M. Ye, Q. Chao, N. Jia, Y. Ge, and H. Shen, "Simultaneous detection of multifood-borne pathogenic bacteria based on functionalized quantum dots coupled with immunomagnetic separation in food samples," *Journal of Agricultural and Food Chemistry,* vol. 57, no. 2, pp. 517-524, 2009/01/28 2009, doi: 10.1021/jf802817y.

[11] C.-H. Wang, K.-Y. Lien, J.-J. Wu, and G.-B. Lee, "A magnetic bead-based assay for the rapid detection of methicillin-resistant Staphylococcus aureus by using a microfluidic system with integrated loop-mediated isothermal amplification," *Lab on a Chip,* 10.1039/C0LC00430H vol. 11, no. 8, pp. 1521-1531, 2011, doi: 10.1039/C0LC00430H.

[12] NHS England » General practice forward view (GPFV) [Online] Available: https://www.england.nhs.uk/publication/general-practice-forward-view-gpfv/

[13] Point of care testing | Abbott point of care [Online] Available: https://www.pointofcare.abbott/int/en/about-us/benefits-of-point-of-care-testing

[14] Microfluidics? A general overview [Online] Available: https://www.elveflow.com/microfluidic-tutorials/microfluidic-reviews-and-tutorials/microfluidics/

[15] G. Luka *et al.*, "Microfluidics Integrated Biosensors: A Leading Technology towards Lab-on-a-Chip and Sensing Applications," (in eng), *Sensors (Basel),* vol. 15, no. 12, pp. 30011-30031, 2015, doi: 10.3390/s151229783.
[16] Y. Ghallab and W. Badawy, "Sensing methods for dielectrophoresis phenomenon: from bulky instruments to lab-on-a-chip," *IEEE Circuits and Systems Magazine,* vol. 4, no. 3, pp. 5-15, 2004, doi: 10.1109/MCAS.2004.1337805.
[17] M. R. Pulido, M. García-Quintanilla, R. Martín-Peña, J. M. Cisneros, and M. J. McConnell, "Progress on the development of rapid methods for antimicrobial susceptibility testing," *Journal of Antimicrobial Chemotherapy,* vol. 68, no. 12, pp. 2710-2717, 2013, doi: 10.1093/jac/dkt253.
[18] Microfluidics and BioMEMS Applications [Online] Available: 10.1007/978-1-4757-3534-5
[19] C. H. O'Callaghan, A. Morris, S. M. Kirby, and A. H. Shingler, "Novel method for detection of β-Lactamases by using a chromogenic cephalosporin substrate," *Antimicrob Agents Chemother,* vol. 1, no. 4, pp. 283-288, 1972, doi: 10.1128/aac.1.4.283.
[20] V. J. Sieben, C. F. A. Floquet, I. R. G. Ogilvie, M. C. Mowlem, and H. Morgan, "Microfluidic colourimetric chemical analysis system: Application to nitrite detection," *Analytical Methods,* 10.1039/C002672G vol. 2, no. 5, pp. 484-491, 2010, doi: 10.1039/C002672G.
[21] C. F. A. Floquet *et al.*, "Nanomolar detection with high sensitivity microfluidic absorption cells manufactured in tinted PMMA for chemical analysis," (in eng), *Talanta,* vol. 84, no. 1, pp. 235-239, 2011/03// 2011, doi: 10.1016/j.talanta.2010.12.026.
[22] C. M. Rushworth, G. Jones, M. Fischlechner, E. Walton, and H. Morgan, "On-chip cavity-enhanced absorption spectroscopy using a white light-emitting diode and polymer mirrors," *Lab on a Chip,* 10.1039/C4LC01264J vol. 15, no. 3, pp. 711-717, 2015, doi: 10.1039/C4LC01264J.
[23] I. M. Perez de Vargas Sansalvador, C. D. Fay, J. Cleary, A. M. Nightingale, M. C. Mowlem, and D. Diamond, "Autonomous reagent-based microfluidic pH sensor platform," *Sensors and Actuators B: Chemical,* vol. 225, pp. 369-376, 2016/03/31/ 2016, doi: https://doi.org/10.1016/j.snb.2015.11.057.
[24] I. E. T. Nagamune and S. K. T. Yonemoto, *Bioseparation engineering*, 1st Edition ed. Elsevier Science, 2000.
[25] D. Woermann, "R. G. Bates: Determination of pH: Theory and Practice. 2nd Edition, John Wiley & Sons, New York, London, Sydney, Toronto 1973. 479 Seiten. Preis: £ 10.00," *Berichte der Bunsengesellschaft für physikalische Chemie,* vol. 77, no. 9, pp. 737-737, 1973/09/01 1973, doi: 10.1002/bbpc.19730770918.
[26] S. Yao, M. Wang, and M. Madou, "A pH electrode based on melt-oxidized iridium oxide," *Journal of the Electrochemical Society,* vol. 148, pp. 29–36, 2001.
[27] L. Dortet, L. Poirel, and P. Nordmann, "Rapid identification of carbapenemase types in Enterobacteriaceae and Pseudomonas spp. by using a biochemical test," *Antimicrob Agents Chemother,* vol. 56, no. 12, p. 6437, 2012, doi: 10.1128/AAC.01395-12.
[28] G. Eden and R. Eden, *Enumeration of microorganisms by their dynamic AC conductance patterns*. 1984, pp. 193-198.
[29] A. Ur and D. F. J. Brown, "Impedance monitoring of bacterial activity," *Journal of Medical Microbiology,* vol. 8, no. 1, pp. 19-28, 1975, doi: doi:10.1099/00222615-8-1-19.

[30] EUCAST guidelines for detection of resistance mechanisms and specific resistances of clinical and/or epidemiological importance [Online] Available: http://www.eucast.org/fileadmin/src/media/PDFs/EUCAST_files/Resistance_mechanisms/EUCAST_detection_of_resistance_mechanisms_170711.pdf

[31] M. Safavieh *et al.*, "Rapid real-time antimicrobial susceptibility testing with electrical sensing on plastic microchips with printed electrodes," *ACS Applied Materials & Interfaces,* vol. 9, no. 14, pp. 12832-12840, 2017/04/12 2017, doi: 10.1021/acsami.6b16571.

[32] J. Choi *et al.*, "Rapid antibiotic susceptibility testing by tracking single cell growth in a microfluidic agarose channel system," vol. 13, no. 2, pp. 280-287, 2013, doi: 10.1039/c2lc41055a.

[33] J. Choi *et al.*, "A rapid antimicrobial susceptibility test based on single-cell morphological analysis," *Science Translational Medicine,* vol. 6, no. 267, pp. 267ra174-267ra174, 2014, doi: 10.1126/scitranslmed.3009650.

[34] I. Peitz and R. van Leeuwen, "Single-cell bacteria growth monitoring by automated DEP-facilitated image analysis," *Lab on a Chip,* 10.1039/C004691D vol. 10, no. 21, pp. 2944-2951, 2010, doi: 10.1039/C004691D.

[35] N. J. Cira, J. Y. Ho, M. E. Dueck, and D. B. Weibel, "A self-loading microfluidic device for determining the minimum inhibitory concentration of antibiotics," *Lab on a Chip,* 10.1039/C2LC20887C vol. 12, no. 6, pp. 1052-1059, 2012, doi: 10.1039/C2LC20887C.

[36] W.-D. Huang, J. Wang, T. Ativanichayaphong, M. Chiao, and J. C. Chiao, *Development of an IrOx micro pH sensor array on flexible polymer substrate* (SPIE Smart Structures and Materials + Nondestructive Evaluation and Health Monitoring). SPIE, 2008.

[37] P. Cady, "Rapid automated bacterial identification by impedance measurement," *New Approaches to the Identification of Microorganisms,* pp. 73-99, 1975.

[38] S. B. Patil *et al.*, "Decoupling competing surface binding kinetics and reconfiguration of receptor footprint for ultrasensitive stress assays," *Nature Nanotechnology,* Article vol. 10, p. 899, 08/17/online 2015, doi: 10.1038/nnano.2015.174.

[39] J. Willey, L. Sherwood, and C. J. Woolverton, *Prescott's Microbiology*, 10th Edition ed. McGraw Hill, 2017.

[40] T. M. Daniel, "The history of tuberculosis," *Respiratory Medicine,* vol. 100, no. 11, pp. 1862-1870, 2006/11/01/ 2006, doi: https://doi.org/10.1016/j.rmed.2006.08.006.

[41] D. C. Angus, W. T. Linde-Zwirble, J. Lidicker, G. Clermont, J. Carcillo, and M. R. Pinsky, "Epidemiology of severe sepsis in the United States: Analysis of incidence, outcome, and associated costs of care," *Critical Care Medicine,* vol. 29, no. 7, pp. 1303-1310, 2001. [Online]. Available: https://journals.lww.com/ccmjournal/Fulltext/2001/07000/Epidemiology_of_severe_sepsis_in_the_United.2.aspx.

[42] Urinary tract infections information [Online] Available: http://www.uhs.nhs.uk/Media/Controlleddocuments/Patientinformation/Generalmedicine/Urinary-tract-infection-patient-information.pdf

[43] M. Salton and K. K. Structure, *Medical Microbiology*, 4th edition ed. Galveston: University of Texas Medical Branch at Galveston, 1996.

[44] R. J. Fair and Y. Tor, "Antibiotics and bacterial resistance in the 21st century," (in eng), *Perspect Medicin Chem,* vol. 6, pp. 25-64, 2014, doi: 10.4137/PMC.S14459.

[45] The history of antibiotics [Online] Available: https://microbiologysociety.org/education-outreach/antibiotics-unearthed/antibiotics-and-antibiotic-resistance/the-history-of-antibiotics.html
[46] G. S. Chethana, H. Venkatesh K R, F. Mirzaei, and S. M Gopinath, *Review on multidrug resistant bacteria and its implication in medical sciences*. 2013, pp. 32-37.
[47] F. C. Tenover, "Mechanisms of antimicrobial resistance in bacteria," *American Journal of Infection Control,* vol. 34, no. 5, Supplement, pp. S3-S10, 2006/06/01/ 2006, doi: https://doi.org/10.1016/j.ajic.2006.05.219.
[48] R. Cooksey, J. Swenson, N. Clark, E. Gay, and C. Thornsberry, "Patterns and mechanisms of beta-lactam resistance among isolates of Escherichia coli from hospitals in the United States," (in eng), *Antimicrob Agents Chemother,* vol. 34, no. 5, pp. 739-745, 1990, doi: 10.1128/aac.34.5.739.
[49] Antimicrobial resistance [Online] Available: https://www.who.int/antimicrobial-resistance/en/
[50] What causes AMR? | Antimicrobial resistance [Online] Available: https://www.amr.gov.au/about-amr/what-causes-amr
[51] WHO's first global report on antibiotic resistance reveals serious, worldwide threat to public health [Online] Available: https://www.who.int/mediacentre/news/releases/2014/amr-report/en/
[52] J. M. A. Blair, M. A. Webber, A. J. Baylay, D. O. Ogbolu, and L. J. V. Piddock, "Molecular mechanisms of antibiotic resistance," *Nature Reviews Microbiology,* Review Article vol. 13, p. 42, 12/01/online 2014, doi: 10.1038/nrmicro3380.
[53] K. J. Aldred, R. J. Kerns, and N. Osheroff, "Mechanism of quinolone action and resistance," *Biochemistry,* vol. 53, no. 10, pp. 1565-1574, 2014/03/18 2014, doi: 10.1021/bi5000564.
[54] D. G. Wright, *Bacterial resistance to antibiotics: enzymatic degradation and modification.* 2005, pp. 1451-70.
[55] A. H. Delcour, "Outer membrane permeability and antibiotic resistance," *Biochimica et Biophysica Acta (BBA) - Proteins and Proteomics,* vol. 1794, no. 5, pp. 808-816, 2009/05/01/ 2009, doi: https://doi.org/10.1016/j.bbapap.2008.11.005.
[56] J.-P. Lavigne, A. Sotto, M.-H. Nicolas-Chanoine, N. Bouziges, J.-M. Pagès, and A. Davin-Regli, "An adaptive response of Enterobacter aerogenes to imipenem: regulation of porin balance in clinical isolates," *International Journal of Antimicrobial Agents,* vol. 41, no. 2, pp. 130-136, 2013/02/01/ 2013, doi: https://doi.org/10.1016/j.ijantimicag.2012.10.010.
[57] T. Tängdén, M. Adler, O. Cars, L. Sandegren, and E. Löwdin, "Frequent emergence of porin-deficient subpopulations with reduced carbapenem susceptibility in ESBL-producing Escherichia coli during exposure to ertapenem in an in vitro pharmacokinetic model," *Journal of Antimicrobial Chemotherapy,* vol. 68, no. 6, pp. 1319-1326, 2013, doi: 10.1093/jac/dkt044.
[58] L. H. Hansen, E. Johannesen, M. Burmølle, A. H. Sørensen, and S. J. Sørensen, "Plasmid-encoded multidrug efflux pump conferring resistance to olaquindox in Escherichia coli," (in eng), *Antimicrob Agents Chemother,* vol. 48, no. 9, pp. 3332-3337, 2004, doi: 10.1128/AAC.48.9.3332-3337.2004.
[59] O. Lazcka, F. J. D. Campo, and F. X. Muñoz, "Pathogen detection: A perspective of traditional methods and biosensors," *Biosensors and Bioelectronics,* vol. 22, no. 7, pp. 1205-1217, 2007/02/15/ 2007, doi: https://doi.org/10.1016/j.bios.2006.06.036.

[60] CLSI and AST [Online] Available: https://clsi.org/meetings/microbiology/clsi-and-ast/
[61] J. Avesar *et al.*, "Rapid phenotypic antimicrobial susceptibility testing using nanoliter arrays," *Proceedings of the National Academy of Sciences,* vol. 114, no. 29, pp. E5787-E5795, 2017, doi: 10.1073/pnas.1703736114.
[62] J. Turnidge and D. L. Paterson, "Setting and revising antibacterial susceptibility breakpoints," (in eng), *Clin Microbiol Rev,* vol. 20, no. 3, pp. 391-408, 2007, doi: 10.1128/CMR.00047-06.
[63] J. J. Kerremans *et al.*, "Rapid identification and antimicrobial susceptibility testing reduce antibiotic use and accelerate pathogen-directed antibiotic use," *Journal of Antimicrobial Chemotherapy,* vol. 61, no. 2, pp. 428-435, 2007, doi: 10.1093/jac/dkm497.
[64] D. S. Kernodle and A. B. Kaiser, "Efficacy of prophylaxis with beta-lactams and beta-lactam-beta-lactamase inhibitor combinations against wound infection by methicillin-resistant and borderline-susceptible Staphylococcus aureus in a guinea pig model," (in eng), *Antimicrob Agents Chemother,* vol. 37, no. 4, pp. 702-707, 1993, doi: 10.1128/aac.37.4.702.
[65] K. E. Mach *et al.*, "A biosensor platform for rapid antimicrobial susceptibility testing directly from clinical samples," (in eng), *J Urol,* vol. 185, no. 1, pp. 148-153, 2011, doi: 10.1016/j.juro.2010.09.022.
[66] M. Arvanitis, T. Anagnostou, B. B. Fuchs, A. M. Caliendo, and E. Mylonakis, "Molecular and nonmolecular diagnostic methods for invasive fungal infections," (in eng), *Clin Microbiol Rev,* vol. 27, no. 3, pp. 490-526, 2014, doi: 10.1128/CMR.00091-13.
[67] D. A. Mosca, M. A. Hurst, W. So, B. S. Viajar, C. A. Fujii, and T. J. Falla, "IB-367, a protegrin peptide with in vitro and in vivo activities against the microflora associated with oral mucositis," (in eng), *Antimicrob Agents Chemother,* vol. 44, no. 7, pp. 1803-1808, 2000, doi: 10.1128/aac.44.7.1803-1808.2000.
[68] EUCAST [Online] Available: http://www.eucast.org/
[69] Breakpoint tables for interpretation of MICs and zone diameters Version 9.0 [Online] Available: http://www.eucast.org/fileadmin/src/media/PDFs/EUCAST_files/Breakpoint_tables/v_9.0_Breakpoint_Tables.pdf
[70] K. Holten and E. Onusko, "Appropriate prescribing of oral beta-lactam antibiotics," *American Family Physician,* vol. 62, no. 3, pp. 611–20, 2000.
[71] R. Steane. Types of antibiotics [Online] Available: http://www.biotopics.co.uk/g11/antibiotic_types.html.
[72] N. Q. Balaban, J. Merrin, R. Chait, L. Kowalik, and S. Leibler, "Bacterial persistence as a phenotypic switch," *Science,* vol. 305, no. 5690, pp. 1622-1625, 2004, doi: 10.1126/science.1099390.
[73] A. L. Koch, "Bacterial wall as target for attack: past, present, and future research," (in eng), *Clin Microbiol Rev,* vol. 16, no. 4, pp. 673-687, 2003, doi: 10.1128/cmr.16.4.673-687.2003.
[74] A. Pantosti, A. Sanchini, and M. Monaco, "Mechanisms of antibiotic resistance in Staphylococcus aureus," *Future Microbiology,* vol. 2, no. 3, pp. 323-334, 2007/06/01 2007, doi: 10.2217/17460913.2.3.323.

[75] D. F. J. Brown and P. E. Reynolds, "Intrinsic resistance to β-lactam antibiotics in staphylococcus aureus," *FEBS Letters,* vol. 122, no. 2, pp. 275-278, 1980, doi: 10.1016/0014-5793(80)80455-8.
[76] R. P. Elander, "Industrial production of β-lactam antibiotics," *Applied Microbiology and Biotechnology,* vol. 61, no. 5, pp. 385-392, 2003/06/01 2003, doi: 10.1007/s00253-003-1274-y.
[77] Antimicrobial resistance empirical and statistical evidence-base [Online] Available: https://www.gov.uk/government/uploads/system/uploads/attachment_data/file/553267/AMR_EBO_2016.pdf
[78] S.-S. Jean and P.-R. Hsueh, "High burden of antimicrobial resistance in Asia," *International Journal of Antimicrobial Agents,* vol. 37, no. 4, pp. 291-295, 2011/04/01/ 2011, doi: https://doi.org/10.1016/j.ijantimicag.2011.01.009.
[79] B. J. Hartman and A. Tomasz, "Low-affinity penicillin-binding protein associated with beta-lactam resistance in Staphylococcus aureus," (in eng), *Journal of bacteriology,* vol. 158, no. 2, pp. 513-516, 1984. [Online]. Available: https://www.ncbi.nlm.nih.gov/pubmed/6563036.
[80] X. Jiang, Y. Kang, X. Pan, J. Yu, Q. Ouyang, and C. Luo, "Studies of the drug resistance response of sensitive and drug-resistant strains in a microfluidic system," *Integrative Biology,* 10.1039/C3IB40164B vol. 6, no. 2, pp. 143-151, 2014, doi: 10.1039/C3IB40164B.
[81] C. C. Sanders and W. E. Sanders, Jr., "Emergence of resistance to cefamandole: possible role of cefoxitin-inducible beta-lactamases," (in eng), *Antimicrob Agents Chemother,* vol. 15, no. 6, pp. 792-797, 1979, doi: 10.1128/aac.15.6.792.
[82] M. Pietsch *et al.*, "Molecular characterisation of extended-spectrum β-lactamase (ESBL)-producing Escherichia coli isolates from hospital and ambulatory patients in Germany," *Veterinary Microbiology,* vol. 200, pp. 130-137, 2017/02/01/ 2017, doi: https://doi.org/10.1016/j.vetmic.2015.11.028.
[83] B. A. Rasmussen *et al.*, "Characterization of IMI-1 beta-lactamase, a class A carbapenem-hydrolyzing enzyme from Enterobacter cloacae," (in eng), *Antimicrob Agents Chemother,* vol. 40, no. 9, pp. 2080-2086, 1996. [Online]. Available: https://www.ncbi.nlm.nih.gov/pubmed/8878585.
[84] A. M. Queenan and K. Bush, "Carbapenemases: the versatile beta-lactamases," (in eng), *Clin Microbiol Rev,* vol. 20, no. 3, pp. 440-458, 2007, doi: 10.1128/CMR.00001-07.
[85] Nitrocefin test: Principle, procedure, uses and limitations - Microbeonline [Online] Available: https://microbeonline.com/nitrocefin-test-principle-procedure-uses-limitations/
[86] R. J. Worthington and C. Melander, "Overcoming resistance to β-lactam antibiotics," (in eng), *J Org Chem,* vol. 78, no. 9, pp. 4207-4213, 2013, doi: 10.1021/jo400236f.
[87] J. Mairhofer, K. Roppert, and P. Ertl, "Microfluidic systems for pathogen sensing: a review," (in eng), *Sensors (Basel),* vol. 9, no. 6, pp. 4804-4823, 2009, doi: 10.3390/s90604804.
[88] G. N. Stewart, "The charges produced by the growth of bacteria in the molecular concentration and electrical conductivity of culture media," (in eng), *J Exp Med,* vol. 4, no. 2, pp. 235-243, 1899, doi: 10.1084/jem.4.2.235.
[89] L. B. Parsons and W. S. Sturges, "The possibility of the conductivity method as applied to studies of bacterial metabolism," *Journal of Bacteriology,* vol. 11, no. 3, p. 177, 1926. [Online]. Available: http://jb.asm.org/content/11/3/177.abstract.

[90] J. B. Allison, J. A. Anderson, and W. H. Cole, "The method of electrical conductivity in studies on bacterial metabolism," (in eng), *Journal of bacteriology,* vol. 36, no. 6, pp. 571-586, 1938. [Online]. Available: https://www.ncbi.nlm.nih.gov/pubmed/16560176.

[91] J. C. S. Richards, A. C. Jason, G. Hobbs, D. M Gibson, and R. H Christie, *Electronic measurement of bacteria growth*. 1978, pp. 560-8.

[92] H. J. Colvin and J. C. Sherris, "Electrical impedance measurements in the reading and monitoring of broth dilution susceptibility tests," (in eng), *Antimicrob Agents Chemother,* vol. 12, no. 1, pp. 61-66, 1977, doi: 10.1128/aac.12.1.61.

[93] P. Cady, S. W. Dufour, J. Shaw, and S. J. Kraeger, "Electrical impedance measurements: rapid method for detecting and monitoring microorganisms," *Journal of Clinical Microbiology,* vol. 7, no. 3, p. 265, 1978. [Online]. Available: http://jcm.asm.org/content/7/3/265.abstract.

[94] L. Yang, P. P. Banada, Y.-S. Liu, A. K. Bhunia, and R. Bashir, "Conductivity and pH dual detection of growth profile of healthy and stressed Listeria monocytogenes," *Biotechnology and Bioengineering,* vol. 92, no. 6, pp. 685-694, 2005/12/20 2005, doi: 10.1002/bit.20642.

[95] C. M. Harris, R. W. Todd, S. J. Bungard, R. W. Lovitt, J. G. Morris, and D. B. Kell, "Dielectric permittivity of microbial suspensions at radio frequencies: a novel method for the real-time estimation of microbial biomass," *Enzyme and Microbial Technology,* vol. 9, no. 3, pp. 181-186, 1987/03/01/ 1987, doi: https://doi.org/10.1016/0141-0229(87)90075-5.

[96] J. P. Carvell and J. E. Dowd, "On-line measurements and control of viable cell Density in cell culture manufacturing processes using radio-frequency impedance," (in eng), *Cytotechnology,* vol. 50, no. 1-3, pp. 35-48, 2006, doi: 10.1007/s10616-005-3974-x.

[97] S. Sengupta, D. A. Battigelli, and H.-C. Chang, "A micro-scale multi-frequency reactance measurement technique to detect bacterial growth at low bio-particle concentrations," *Lab on a Chip,* 10.1039/B516274B vol. 6, no. 5, pp. 682-692, 2006, doi: 10.1039/B516274B.

[98] S. Puttaswamy and S. Sengupta, "Rapid detection of bacterial proliferation in food samples using microchannel impedance measurements at multiple frequencies," *Sensing and Instrumentation for Food Quality and Safety,* vol. 4, no. 3, pp. 108-118, 2010/12/01 2010, doi: 10.1007/s11694-010-9101-5.

[99] S. Puttaswamy, *Novel electrical method for the rapid determination of minimum inhibitory concentration (MIC) and assay of bactericidal/bacteriostatic Activity*. 2013.

[100] M. Grossi, M. Lanzoni, A. Pompei, R. Lazzarini, D. Matteuzzi, and B. Riccò, "An embedded portable biosensor system for bacterial concentration detection," *Biosensors and Bioelectronics,* vol. 26, no. 3, pp. 983-990, 2010/11/15/ 2010, doi: https://doi.org/10.1016/j.bios.2010.08.039.

[101] B. Luchterhand *et al.*, "Newly designed and validated impedance spectroscopy setup in microtiter plates successfully monitors viable biomass online," (in eng), *Biotechnol J,* vol. 10, no. 8, pp. 1259-1268, 2015/08// 2015, doi: 10.1002/biot.201400534.

[102] C. Ruan, L. Yang, and Y. Li, "Immunobiosensor chips for detection of Escherichia coli O157:H7 using electrochemical impedance spectroscopy," *Analytical Chemistry,* vol. 74, no. 18, pp. 4814-4820, 2002/09/01 2002, doi: 10.1021/ac025647b.

[103] L. Yang, Y. Li, and G. F. Erf, "Interdigitated array microelectrode-based electrochemical impedance immunosensor for detection of Escherichia coli O157:H7," *Analytical Chemistry,* vol. 76, no. 4, pp. 1107-1113, 2004/02/01 2004, doi: 10.1021/ac0352575.
[104] S. M. Radke and E. C. Alocilja, "A high density microelectrode array biosensor for detection of E. coli O157:H7," (in eng), *Biosens Bioelectron,* vol. 20, no. 8, pp. 1662-1667, 2005/02// 2005, doi: 10.1016/j.bios.2004.07.021.
[105] M. Varshney, Y. Li, B. Srinivasan, and S. Tung, "A label-free, microfluidics and interdigitated array microelectrode based impedance biosensor in combination with nanoparticles immunoseparation for detection of Escherichia coli O157:H7 in food samples," vol. 128, pp. 99-107, 2007, doi: 10.1016/j.snb.2007.03.045.
[106] M. Barreiros dos Santos *et al.*, "Label-free ITO-based immunosensor for the detection of very low concentrations of pathogenic bacteria," *Bioelectrochemistry,* vol. 101, pp. 146-152, 2015/02/01/ 2015, doi: https://doi.org/10.1016/j.bioelechem.2014.09.002.
[107] M. S. Mannoor, S. Zhang, A. J. Link, and M. C. McAlpine, "Electrical detection of pathogenic bacteria via immobilized antimicrobial peptides," *Proceedings of the National Academy of Sciences,* vol. 107, no. 45, pp. 19207-19212, 2010, doi: 10.1073/pnas.1008768107.
[108] H. Cui *et al.*, "An AC electrokinetic impedance immunosensor for rapid detection of tuberculosis," *Analyst,* 10.1039/C3AN01112G vol. 138, no. 23, pp. 7188-7196, 2013, doi: 10.1039/C3AN01112G.
[109] H. Etayash, K. Jiang, S. Azmi, T. Thundat, and K. Kaur, "Real-time detection of breast cancer cells using peptide-functionalized microcantilever arrays," (in eng), *Sci Rep,* vol. 5, pp. 13967-13967, 2015, doi: 10.1038/srep13967.
[110] J. Jiang *et al.*, "Smartphone based portable bacteria pre-concentrating microfluidic sensor and impedance sensing system," *Sensors and Actuators B: Chemical,* vol. 193, pp. 653-659, 2014/03/31/ 2014, doi: https://doi.org/10.1016/j.snb.2013.11.103.
[111] N. J. Ronkainen, H. B. Halsall, and W. R. Heineman, "Electrochemical biosensors," *Chemical Society Reviews,* 10.1039/B714449K vol. 39, no. 5, pp. 1747-1763, 2010, doi: 10.1039/B714449K.
[112] J. Paredes, S. Becerro, and S. Arana, "Label-free interdigitated microelectrode based biosensors for bacterial biofilm growth monitoring using Petri dishes," *Journal of Microbiological Methods,* vol. 100, pp. 77-83, 2014/05/01/ 2014, doi: https://doi.org/10.1016/j.mimet.2014.02.022.
[113] K. Settu, C.-J. Chen, J.-T. Liu, C.-L. Chen, and J.-Z. Tsai, "Impedimetric method for measuring ultra-low E. coli concentrations in human urine," *Biosensors and Bioelectronics,* vol. 66, pp. 244-250, 2015/04/15/ 2015, doi: https://doi.org/10.1016/j.bios.2014.11.027.
[114] W. Bai, K. S. Zhao, and K. Asami, "Dielectric properties of E. coli cell as simulated by the three-shell spheroidal model," *Biophysical Chemistry,* vol. 122, no. 2, pp. 136-142, 2006/07/20/ 2006, doi: https://doi.org/10.1016/j.bpc.2006.03.004.
[115] L. Yang, "Electrical impedance spectroscopy for detection of bacterial cells in suspensions using interdigitated microelectrodes," (in eng), *Talanta,* vol. 74, no. 5, pp. 1621-1629, 2008/02// 2008, doi: 10.1016/j.talanta.2007.10.018.
[116] A. Mortari, A. Adami, and L. Lorenzelli, "An unconventional approach to impedance microbiology: Detection of culture media conductivity variations due to bacteriophage generated lyses of host bacteria," *Biosensors and Bioelectronics,* vol. 67, pp. 615-620, 2015/05/15/ 2015, doi: https://doi.org/10.1016/j.bios.2014.09.075.

[117] A. Ebrahimi and M. A. Alam, "Droplet-based non-faradaic impedance sensors for assessment of susceptibility of Escherichia coli to ampicillin in 60 min," *Biomedical Microdevices,* vol. 19, no. 2, p. 27, 2017/04/12 2017, doi: 10.1007/s10544-017-0165-4.
[118] C. S. Price, S. E. Kon, and S. Metzger, "Rapid antibiotic susceptibility phenotypic characterization of Staphylococcus aureus using automated microscopy of small numbers of cells," *Journal of Microbiological Methods,* vol. 98, pp. 50-58, 2014/03/01/ 2014, doi: https://doi.org/10.1016/j.mimet.2013.12.021.
[119] Y. Lu, J. Gao, D. D. Zhang, V. Gau, J. C. Liao, and P. K. Wong, "Single cell antimicrobial susceptibility testing by confined microchannels and electrokinetic loading," *Analytical Chemistry,* vol. 85, no. 8, pp. 3971-3976, 2013/04/16 2013, doi: 10.1021/ac4004248.
[120] Ö. Baltekin, A. Boucharin, E. Tano, D. I. Andersson, and J. Elf, "Antibiotic susceptibility testing in less than 30 min using direct single-cell imaging," *Proceedings of the National Academy of Sciences,* vol. 114, no. 34, pp. 9170-9175, 2017, doi: 10.1073/pnas.1708558114.
[121] P.-H. Tsou *et al.*, "Rapid antibiotic efficacy screening with aluminum oxide nanoporous membrane filter-chip and optical detection system," (in eng), *Biosens Bioelectron,* vol. 26, no. 1, pp. 289-294, 2010/09// 2010, doi: 10.1016/j.bios.2010.06.034.
[122] K. P. Kim *et al.*, "In situ monitoring of antibiotic susceptibility of bacterial biofilms in a microfluidic device," *Lab on a Chip,* 10.1039/C0LC00154F vol. 10, no. 23, pp. 3296-3299, 2010, doi: 10.1039/C0LC00154F.
[123] P. Sun *et al.*, "High-throughput microfluidic system for long-term bacterial colony monitoring and antibiotic testing in zero-flow environments," *Biosensors and Bioelectronics,* vol. 26, no. 5, pp. 1993-1999, 2011/01/15/ 2011, doi: https://doi.org/10.1016/j.bios.2010.08.062.
[124] M. Kalashnikov, J. C. Lee, J. Campbell, A. Sharon, and A. F. Sauer-Budge, "A microfluidic platform for rapid, stress-induced antibiotic susceptibility testing of Staphylococcus aureus," *Lab on a Chip,* 10.1039/C2LC40531H vol. 12, no. 21, pp. 4523-4532, 2012, doi: 10.1039/C2LC40531H.
[125] T. Dong and X. Zhao, "Rapid identification and susceptibility testing of uropathogenic microbes via immunosorbent ATP-bioluminescence assay on a microfluidic simulator for antibiotic therapy," *Analytical Chemistry,* vol. 87, no. 4, pp. 2410-2418, 2015/02/17 2015, doi: 10.1021/ac504428t.
[126] J. Q. Boedicker, L. Li, T. R. Kline, and R. F. Ismagilov, "Detecting bacteria and determining their susceptibility to antibiotics by stochastic confinement in nanoliter droplets using plug-based microfluidics," *Lab on a Chip,* 10.1039/B804911D vol. 8, no. 8, pp. 1265-1272, 2008, doi: 10.1039/B804911D.
[127] Y.-J. Eun, A. S. Utada, M. F. Copeland, S. Takeuchi, and D. B. Weibel, "Encapsulating bacteria in agarose microparticles using microfluidics for high-throughput cell analysis and isolation," *ACS Chemical Biology,* vol. 6, no. 3, pp. 260-266, 2011/03/18 2011, doi: 10.1021/cb100336p.
[128] K. Churski *et al.*, "Rapid screening of antibiotic toxicity in an automated microdroplet system," *Lab on a Chip,* 10.1039/C2LC21284F vol. 12, no. 9, pp. 1629-1637, 2012, doi: 10.1039/C2LC21284F.

[129] Y. Tang, L. Zhen, J. Liu, and J. Wu, "Rapid antibiotic susceptibility testing in a microfluidic pH sensor," *Analytical Chemistry,* vol. 85, no. 5, pp. 2787-2794, 2013/03/05 2013, doi: 10.1021/ac303282j.
[130] P. Nordmann, L. Poirel, and L. Dortet, "Rapid detection of carbapenemase-producing Enterobacteriaceae," (in eng), *Emerg Infect Dis,* vol. 18, no. 9, pp. 1503-1507, 2012, doi: 10.3201/eid1809.120355.
[131] L. Dortet, L. Bréchard, L. Poirel, and P. Nordmann, "Rapid detection of carbapenemase-producing Enterobacteriaceae from blood cultures," *Clinical Microbiology and Infection,* vol. 20, no. 4, pp. 340-344, 2014, doi: 10.1111/1469-0691.12318.
[132] C. H. Chen *et al.*, "Antimicrobial susceptibility testing using high surface-to-volume ratio microchannels," (in eng), *Analytical chemistry,* vol. 82, no. 3, pp. 1012-1019, 2010, doi: 10.1021/ac9022764.
[133] Y.-W. Chen, H. Wang, M. Hupert, and S. A. Soper, "Identification of methicillin-resistant Staphylococcus aureus using an integrated and modular microfluidic system," *Analyst,* 10.1039/C2AN36430A vol. 138, no. 4, pp. 1075-1083, 2013, doi: 10.1039/C2AN36430A.
[134] S. Kalsi, L. S. Sellars, C. Turner, M. J. Sutton, and H. Morgan, "A programmable digital microfluidic assay for the simultaneous detection of multiple anti-microbial resistance genes," *Micromachines,* vol. 8, no. 4, 2017, doi: 10.3390/mi8040111.
[135] D. Kang *et al.*, "Rapid detection of single bacteria in unprocessed blood using Iitegrated comprehensive droplet digital detection," *Nature Communications,* Article vol. 5, p. 5427, 11/13/online 2014, doi: 10.1038/ncomms6427.
[136] C. Toumazou *et al.*, "Simultaneous DNA amplification and detection using a pH-sensing semiconductor system," *Nature Methods,* Article vol. 10, p. 641, 06/09/online 2013, doi: 10.1038/nmeth.2520.
[137] M. Nakano, Z. Ding, H. Kasahara, and J. Suehiro, "Rapid microbead-based DNA detection using dielectrophoresis and impedance measurement," *EPL (Europhysics Letters),* vol. 108, no. 2, p. 28003, 2014/10/01 2014, doi: 10.1209/0295-5075/108/28003.
[138] C.-C. Chung, I.-F. Cheng, W.-H. Yang, and H.-C. Chang, "Antibiotic susceptibility test based on the dielectrophoretic behavior of elongated Escherichia coli with cephalexin treatment," *Biomicrofluidics,* vol. 5, no. 2, p. 021102, 2011, doi: 10.1063/1.3600650.
[139] I. H. Su *et al.*, "Dielectrophoresis system for testing antimicrobial susceptibility of gram-negative bacteria to β-lactam antibiotics," *Analytical Chemistry,* vol. 89, no. 8, pp. 4635-4641, 2017/04/18 2017, doi: 10.1021/acs.analchem.7b00220.
[140] J. D. Besant, E. H. Sargent, and S. O. Kelley, "Rapid electrochemical phenotypic profiling of antibiotic-resistant bacteria," *Lab on a Chip,* 10.1039/C5LC00375J vol. 15, no. 13, pp. 2799-2807, 2015, doi: 10.1039/C5LC00375J.
[141] H. Leonard, R. Colodner, S. Halachmi, and E. Segal, "Recent advances in the race to design a rapid diagnostic test for antimicrobial resistance," *ACS Sens,* vol. 3, no. 11, pp. 2202-2217, Nov 26 2018, doi: 10.1021/acssensors.8b00900.
[142] W. Florio, A. Tavanti, S. Barnini, E. Ghelardi, and A. Lupetti, "Recent advances and ongoing challenges in the diagnosis of microbial infections by MALDI-TOF mass spectrometry," (in English), *Front Microbiol,* Mini Review vol. 9, no. 1097, 2018-May-29 2018, doi: 10.3389/fmicb.2018.01097.

[143] MALDI-TOF/TOF - Bruker's FLEX series for quick and reliable results [Online] Available: https://www.bruker.com/products/mass-spectrometry-and-separations/maldi-toftof.html
[144] VITEK® MS [Online] Available: https://www.biomerieux-diagnostics.com/vitekr-ms-0
[145] MALDI-TOF Mass Spectrometry : SHIMADZU (Shimadzu Corporation) [Online] Available: https://www.shimadzu.com/an/lifescience/maldi/index.html
[146] A.-K. Järvinen *et al.*, "Rapid identification of bacterial pathogens using a PCR- and microarray-based assay," (in eng), *BMC Microbiol,* vol. 9, pp. 161-161, 2009, doi: 10.1186/1471-2180-9-161.
[147] ETEST® [Online] Available: https://www.biomerieux-usa.com/clinical/etest
[148] Accelerate Pheno™ system [Online] Available: http://acceleratediagnostics.com/products/accelerate-pheno-system/
[149] VITEK® 2: Healthcare [Online] Available: https://www.biomerieux-usa.com/clinical/vitek-2-healthcare
[150] Microbiology System MicroScan WalkAway plus [Online] Available: https://www.beckmancoulter.com/en/products/microbiology/microscan-walkaway-plus-system
[151] BD Phoenix™ automated identification and susceptibility testing system [Online] Available: https://www.bd.com/en-us/offerings/capabilities/microbiology-solutions/identification-and-susceptibility-testing/bd-phoenix-automated-identification-and-susceptibility-testing-system
[152] TREK Diagnostic Systems : Case Studies [Online] Available: http://www.trekds.com/casestudies/cs_aris2maine.asp
[153] Class 2 Device Recall Accelerate PhenoTest BC kit [Online] Available: https://www.accessdata.fda.gov/scripts/cdrh/cfdocs/cfres/res.cfm?id=162852
[154] oCelloScope - Automated Microscopy - Live cell imaging - BioSense Solution [Online] Available: https://biosensesolutions.dk/ocelloscope/
[155] dRAST | QuantaMatrix [Online] Available: https://www.quantamatrix.com/qmac-drast
[156] 2019 Attune NxT flow cytometer | Thermo Fisher Scientific - UK [Online] Available: https://www.thermofisher.com/uk/en/home/life-science/cell-analysis/flow-cytometry/flow-cytometers/attune-acoustic-focusing-flow-cytometer.html
[157] 216Dx UTI System - BacterioScan [Online] Available: http://bacterioscan.com/products/216dx-uti-system/
[158] Bacteria live/dead staining kit [Online] Available: https://www.promocell.com/f/2018/01/PK-CA707-30027.pdf
[159] R. T. Hayden *et al.*, "Rapid antimicrobial susceptibility testing ssing forward laser light scatter technology," *Journal of Clinical Microbiology,* vol. 54, no. 11, pp. 2701-2706, 2016, doi: 10.1128/jcm.01475-16.
[160] G. H. Markx and C. L. Davey, "The dielectric properties of biological cells at radiofrequencies: applications in biotechnology," *Enzyme and Microbial Technology,* vol. 25, no. 3, pp. 161-171, 1999/08/01/ 1999, doi: https://doi.org/10.1016/S0141-0229(99)00008-3.
[161] J. C. Maxwell, *A treatise on electricity and magnetism* (Cambridge Library Collection - Physical Sciences). Cambridge: Cambridge University Press, 1873.

[162] K. W. Wagner, "Erklärung der dielektrischen Nachwirkungsvorgänge auf Grund Maxwellscher Vorstellungen," *Archiv für Elektrotechnik,* vol. 2, no. 9, pp. 371-387, 1914/09/01 1914, doi: 10.1007/BF01657322.
[163] R. Pethig and I. Schmueser, "Marking 100 years since Rudolf Höber's discovery of the insulating envelope surrounding cells and of the beta-dispersion exhibited by tissue," Cell membrane; Beta-dispersion; AC impedance measurement vol. 3, pp. 74-79, 2012, doi: 10.5617/jeb.401.
[164] H. Fricke, "The electric capacity of suspensions with special reference to blood," *The Journal of General Physiology,* vol. 9, no. 2, pp. 137-152, 1925, doi: 10.1085/jgp.9.2.137.
[165] H. Fricke, H. P. Schwan, K. A. M. Li, and V. Bryson, "A dielectric study of the low-conductance surface membrane in E. coli," *Nature,* vol. 177, no. 4499, pp. 134-135, 1956/01/01 1956, doi: 10.1038/177134a0.
[166] K. S. Cole, "Electric phase angle of cell membranes," (in eng), *The Journal of general physiology,* vol. 15, no. 6, pp. 641-649, 1932, doi: 10.1085/jgp.15.6.641.
[167] K. S. Cole and R. H. Cole, "Dispersion and absorption in dielectrics I. Alternating current characteristics," *The Journal of Chemical Physics,* vol. 9, no. 4, pp. 341-351, 1941, doi: 10.1063/1.1750906.
[168] E. L. Carstensen, H. A. Cox, W. B. Mercer, and L. A. Natale, "Passive electrical properties of microorganisms: I. Conductivity of Escherichia coli and Micrococcus lysodeikticus," *Biophysical Journal,* vol. 5, no. 3, pp. 289-300, 1965/05/01/ 1965, doi: https://doi.org/10.1016/S0006-3495(65)86717-0.
[169] E. L. Carstensen, "Passive electrical properties of microorganisms: II. Resistance of the bacterial membrane," *Biophysical Journal,* vol. 7, no. 5, pp. 493-503, 1967/09/01/ 1967, doi: https://doi.org/10.1016/S0006-3495(67)86600-1.
[170] E. L. Carstensen and R. E. Marquis, "Passive electrical properties of microorganisms: III. Conductivity of isolated bacterial cell walls," *Biophysical Journal,* vol. 8, no. 5, pp. 536-548, 1968/05/01/ 1968, doi: https://doi.org/10.1016/S0006-3495(68)86506-3.
[171] C. W. Einolf and E. L. Carstensen, "Passive electrical properties of microorganisms: IV. Studies of the protoplasts of Micrococcus lysodeikticus," *Biophysical Journal,* vol. 9, no. 4, pp. 634-643, 1969/04/01/ 1969, doi: https://doi.org/10.1016/S0006-3495(69)86408-8.
[172] C. W. Einolf and E. L. Carstensen, "Passive electrical properties of microorganisms: V. Low-frequency dielectric dispersion of bacteria," *Biophysical Journal,* vol. 13, no. 1, pp. 8-13, 1973/01/01/ 1973, doi: https://doi.org/10.1016/S0006-3495(73)85966-1.
[173] K. Asami, T. Hanai, and N. Koizumi, "Dielectric analysis of Escherichia coli suspensions in the light of the theory of interfacial polarization," *Biophysical Journal,* vol. 31, no. 2, pp. 215-228, 1980/08/01/ 1980, doi: https://doi.org/10.1016/S0006-3495(80)85052-1.
[174] H. Fricke and H. J. Curtis, "The dielectric properties of water–dielectric interphases," *The Journal of Physical Chemistry,* vol. 41, no. 5, pp. 729-745, 1937/05/01 1937, doi: 10.1021/j150383a011.
[175] H. P. Schwan, G. Schwarz, J. Maczuk, and H. Pauly, "On the low-frequency dielectric diespersion of colloidal particles in electrolyte solution 1," *The Journal of Physical Chemistry,* vol. 66, no. 12, pp. 2626-2635, 1962/12/01 1962, doi: 10.1021/j100818a066.

[176] C. T. O'Konski, "Electric properties of macromollecurs. V. Theory of ionic polarization in polyelectrolytes," *The Journal of Physical Chemistry,* vol. 64, no. 5, pp. 605-619, 1960/05/01 1960, doi: 10.1021/j100834a023.
[177] G. Schwarz, "A theory of the low-frequency dielectric dispersion of colloidal particles in electrolyte solution 2," *The Journal of Physical Chemistry,* vol. 66, no. 12, pp. 2636-2642, 1962/12/01 1962, doi: 10.1021/j100818a067.
[178] H. Wendt, "S. S. Dukhin und V. N. Shilov: Dielectric phenomena and the double layer in disperse systems and polyelectrolytes, (Übersetzt aus dem Russischen von D. Ledermann; Herausgeber: P. Greenberg), J. Wiley and Sons, New York, Toronto 1974, (Erscheinungsjahr des Originals: 1972), 192 Seiten, Preis: £ 9.00," *Berichte der Bunsengesellschaft für physikalische Chemie,* vol. 80, no. 2, pp. 177-178, 1976/02/01 1976, doi: 10.1002/bbpc.19760800223.
[179] C. Grosse and V. Zimmerman, "Numerical calculation of the dielectric and electrokinetic properties of vesicle suspensions," *The Journal of Physical Chemistry B,* vol. 109, no. 38, pp. 18088-18095, 2005/09/01 2005, doi: 10.1021/jp053074b.
[180] M. J. Farrow, I. S. Hunter, and P. Connolly, "Developing a real time sensing system to monitor bacteria in wound dressings," *Biosensors,* vol. 2, no. 2, pp. 171-188, 2012. [Online]. Available: https://www.mdpi.com/2079-6374/2/2/171.
[181] K. Asami, "Low-frequency dielectric dispersion of bacterial cell suspensions," *Colloids and Surfaces B: Biointerfaces,* vol. 119, pp. 1-5, 2014/07/01/ 2014, doi: https://doi.org/10.1016/j.colsurfb.2014.04.014.
[182] G. H. Markx, Y. Huang, X.-F. Zhou, and R. Pethig, "Dielectrophoretic characterization and separation of micro-organisms," *Microbiology,* vol. 140, no. 3, pp. 585-591, 1994, doi: doi:10.1099/00221287-140-3-585.
[183] G. H. Markx, P. A. Dyda, and R. Pethig, "Dielectrophoretic separation of bacteria using a conductivity gradient," *Journal of Biotechnology,* vol. 51, no. 2, pp. 175-180, 1996/11/01/ 1996, doi: https://doi.org/10.1016/0168-1656(96)01617-3.
[184] A. P. Brown, W. B. Betts, A. B. Harrison, and J. G. O'Neill, "Evaluation of a dielectrophoretic bacterial counting technique," (in eng), *Biosens Bioelectron,* vol. 14, no. 3, pp. 341-351, 1999/03// 1999, doi: 10.1016/s0956-5663(99)00002-0.
[185] M. Elitas, R. Martinez-Duarte, N. Dhar, J. D. McKinney, and P. Renaud, "Dielectrophoresis-based purification of antibiotic-treated bacterial subpopulations," *Lab on a Chip,* 10.1039/C4LC00109E vol. 14, no. 11, pp. 1850-1857, 2014, doi: 10.1039/C4LC00109E.
[186] J. Suehiro, R. Yatsunami, R. Hamada, and M. Hara, "Quantitative estimation of biological cell concentration suspended in aqueous medium by using dielectrophoretic impedance measurement method," *Journal of Physics D: Applied Physics,* vol. 32, no. 21, pp. 2814-2820, 1999/10/28 1999, doi: 10.1088/0022-3727/32/21/316.
[187] J. Suehiro, R. Hamada, D. Noutomi, M. Shutou, and M. Hara, "Selective detection of viable bacteria using dielectrophoretic impedance measurement method," *Journal of Electrostatics,* vol. 57, no. 2, pp. 157-168, 2003/02/01/ 2003, doi: https://doi.org/10.1016/S0304-3886(02)00124-9.
[188] J. Suehiro, D. Noutomi, M. Shutou, and M. Hara, "Selective detection of specific bacteria using dielectrophoretic impedance measurement method combined with an antigen–antibody reaction," *Journal of Electrostatics,* vol. 58, no. 3, pp. 229-246, 2003/06/01/ 2003, doi: https://doi.org/10.1016/S0304-3886(03)00062-7.
[189] J. Suehiro, T. Hatano, M. Shutou, and M. Hara, "Improvement of electric pulse shape for electropermeabilization-assisted dielectrophoretic impedance measurement for

high sensitive bacteria detection," *Sensors and Actuators B: Chemical,* vol. 109, no. 2, pp. 209-215, 2005/09/14/ 2005, doi: https://doi.org/10.1016/j.snb.2004.12.048.
[190] R. Hamada, J. Suehiro, M. Nakano, T. Kikutani, and K. Konishi, "Development of rapid oral bacteria detection apparatus based on dielectrophoretic impedance measurement method," *IET Nanobiotechnology*, vol. 5, no. 2, pp. 25-31. [Online]. Available: https://digital-library.theiet.org/content/journals/10.1049/iet-nbt.2010.0011
[191] R. Hamada *et al.*, "Improvement of dielectrophoretic impedance measurement method by bacterial concentration utilizing negative dielectrophoresis," *Journal of Physics: Conference Series,* vol. 307, p. 012031, 2011/08/17 2011, doi: 10.1088/1742-6596/307/1/012031.
[192] P. Sabounchi, A. M. Morales, P. Ponce, L. P. Lee, B. A. Simmons, and R. V. Davalos, "Sample concentration and impedance detection on a microfluidic polymer chip," (in eng), *Biomedical microdevices,* vol. 10, no. 5, pp. 661-670, 2008/10// 2008, doi: 10.1007/s10544-008-9177-4.
[193] M. Kim *et al.*, "A microfluidic device for label-free detection of Escherichia coli in drinking water using positive dielectrophoretic focusing, capturing, and impedance measurement," (in eng), *Biosens Bioelectron,* vol. 74, pp. 1011-1015, 2015/12// 2015, doi: 10.1016/j.bios.2015.07.059.
[194] C. Páez-Avilés *et al.*, "Combined dielectrophoresis and impedance systems for bacteria analysis in microfluidic on-chip platforms," (in eng), *Sensors (Basel),* vol. 16, no. 9, p. 1514, 2016, doi: 10.3390/s16091514.
[195] L. Jiang and S. Pau, "Integrated waveguide with a microfluidic channel in spiral geometry for spectroscopic applications," *Applied Physics Letters,* vol. 90, no. 11, p. 111108, 2007, doi: 10.1063/1.2713356.
[196] S. Feng, D. Tseng, D. Di Carlo, O. B. Garner, and A. Ozcan, "High-throughput and automated diagnosis of antimicrobial resistance using a cost-effective cellphone-based micro-plate reader," *Sci Rep,* Article vol. 6, p. 39203, 12/15/online 2016, doi: 10.1038/srep39203.
[197] C. Hu, I. Zeimpekis, K. Sun, S. Anderson, P. Ashburn, and H. Morgan, "Low-cost nanoribbon sensors for protein analysis in human serum using a miniature bead-based enzyme-linked immunosorbent assay," *Analytical Chemistry,* vol. 88, no. 9, pp. 4872-4878, 2016/05/03 2016, doi: 10.1021/acs.analchem.6b00702.
[198] Y. J. Kim, Y. C. Lee, B. K. Sohn, J. H. Lee, and C. S. Kim, "A novel pH microsensor with a built-in reference electrode," *Journal Korean Physical Society,* vol. 43, no. 1, pp. 769-772, 2003.
[199] A. Gao, N. Lu, P. Dai, C. Fan, Y. Wang, and T. Li, "Direct ultrasensitive electrical detection of prostate cancer biomarkers with CMOS-compatible n- and p-type silicon nanowire sensor arrays," *Nanoscale,* 10.1039/C4NR03210A vol. 6, no. 21, pp. 13036-13042, 2014, doi: 10.1039/C4NR03210A.
[200] E. Stern *et al.*, "Label-free biomarker detection from whole blood," *Nature Nanotechnology,* vol. 5, p. 138, 12/13/online 2009, doi: 10.1038/nnano.2009.353.
[201] L. Mu, I. A. Droujinine, N. K. Rajan, S. D. Sawtelle, and M. A. Reed, "Direct, rapid, and label-free detection of enzyme–substrate interactions in physiological buffers using CMOS-compatible nanoribbon sensors," *Nano Letters,* vol. 14, no. 9, pp. 5315-5322, 2014/09/10 2014, doi: 10.1021/nl502366e.
[202] Y. Cui, Q. Wei, H. Park, and C. M. Lieber, "Nanowire nanosensors for highly sensitive and selective detection of biological and chemical species," *Science,* vol. 293, no. 5533, pp. 1289-1292, 2001, doi: 10.1126/science.1062711.

[203] S. E. Naimi, B. Hajji, I. Humenyuk, J. Launay, and P. Temple-Boyer, "Temperature influence on pH-ISFET sensor operating in weak and moderate inversion regime: Model and circuitry," *Sensors and Actuators B: Chemical,* vol. 202, pp. 1019-1027, 2014/10/31/ 2014, doi: https://doi.org/10.1016/j.snb.2014.06.008.
[204] W.-D. Huang, H. Cao, S. Deb, M. Chiao, and J. C. Chiao, "A flexible pH sensor based on the iridium oxide sensing film," *Sensors and Actuators A: Physical,* vol. 169, no. 1, pp. 1-11, 2011/09/10/ 2011, doi: https://doi.org/10.1016/j.sna.2011.05.016.
[205] H. N. McMurray, P. Douglas, and D. Abbot, "Novel thick-film pH sensors based on ruthenium dioxide-glass composites," *Sensors and Actuators B: Chemical,* vol. 28, no. 1, pp. 9-15, 1995/07/01/ 1995, doi: https://doi.org/10.1016/0925-4005(94)01536-Q.
[206] Y.-H. Liao and J.-C. Chou, "Preparation and characteristics of ruthenium dioxide for pH array sensors with real-time measurement system," *Sensors and Actuators B: Chemical,* vol. 128, no. 2, pp. 603-612, 2008/01/15/ 2008, doi: https://doi.org/10.1016/j.snb.2007.07.023.
[207] J. Webster, *The measurement instrumentation and sensors handbook*. Florida: CRC Press and IEEE Press, 1999.
[208] C.-N. Tsai, J.-C. Chou, T.-P. Sun, and S.-K. Hsiung, "Study on the sensing characteristics and hysteresis effect of the tin oxide pH electrode," *Sensors and Actuators B: Chemical,* vol. 108, no. 1, pp. 877-882, 2005/07/22/ 2005, doi: https://doi.org/10.1016/j.snb.2004.11.050.
[209] I. A. Ges, B. L. Ivanov, D. K. Schaffer, E. A. Lima, A. A. Werdich, and F. J. Baudenbacher, "Thin-film IrOx pH microelectrode for microfluidic-based microsystems," *Biosensors and Bioelectronics,* vol. 21, no. 2, pp. 248-256, 2005/08/15/ 2005, doi: https://doi.org/10.1016/j.bios.2004.09.021.
[210] W. Huang, S. Deb, Y. Seo, S. Rao, M. Chiao, and J. C. Chiao, "A passive radio-frequency pH-sensing tag for wireless food-quality monitoring," *IEEE Sensors Journal,* vol. 12, no. 3, pp. 487-495, 2012, doi: 10.1109/JSEN.2011.2107738.
[211] I. Song, K. Fink, and J. H. Payer, "Metal oxide/metal pH sensor: Effect of anions on pH measurements," *CORROSION,* vol. 54, no. 1, pp. 13-19, 1998, doi: 10.5006/1.3284823.
[212] K. Kreider, "Iridium oxide thin-film stability in high-temperature corrosive solutions," *Sensors and Actuators B: Chemical,* vol. 5, no. 1, pp. 165-169, 1991/08/01/ 1991, doi: https://doi.org/10.1016/0925-4005(91)80239-G.
[213] K. Yamanaka, "Anodically electrodeposited iridium oxide films (AEIROF) from alkaline solutions for electrochromic display devices," *Japanese Journal of Applied Physics,* vol. 28, no. Part 1, No. 4, pp. 632-637, 1989/04/20 1989, doi: 10.1143/jjap.28.632.
[214] H. Morgan and N. G. Green, "AC electrokinetics : colloids and nanoparticles," (in English), 2003. [Online]. Available: http://search.ebscohost.com/login.aspx?direct=true&scope=site&db=nlebk&db=nlabk&AN=101789.
[215] A. Arthur Robert Von Hippel, A. v. Hippel, Ed. *Dielectric materials and applications*. 2019.
[216] P. Debye, "Zur theorie der spezifischen Wärmen," *Annalen der Physik,* vol. 344, no. 14, pp. 789-839, 1912/01/01 1912, doi: 10.1002/andp.19123441404.
[217] R. Pethig, "The Clausius–Mossotti factor," in *Dielectrophoresis*, 2017, pp. 119-144.

[218] A. Sihvola and I. V. Lindell, "Polarizability and effective permittivity of layered and continuously inhomogeneous dielectric ellipsoids," *Journal of Electromagnetic Waves and Applications,* vol. 4, no. 1, pp. 1-26, 1990/01/01 1990, doi: 10.1163/156939390X00429.
[219] M. Stubbe and J. Gimsa, "Maxwell's mixing equation revisited: characteristic impedance equations for ellipsoidal cells," *Biophysical Journal,* vol. 109, no. 2, pp. 194-208, 2015/07/21/ 2015, doi: https://doi.org/10.1016/j.bpj.2015.06.021.
[220] A. J. Bard and L. R. Faulkner, *Electrochemical methods: fundamentals and applications*, 2nd edition ed. (no. 12). New York: Wiley, 2001, pp. 1364-1365.
[221] R. Holze, "Book review: Electrochemical methods. Fundamentals and applications (2nd Edition). By Allen J. Bard and Larry R. Faulkner," *Angewandte Chemie International Edition,* vol. 41, no. 4, pp. 655-657, 2002/02/15 2002, doi: 10.1002/1521-3773(20020215)41:4<655::AID-ANIE655>3.0.CO;2-I.
[222] IDC flat ribbon cable [Online] Available: http://www.farnell.com/datasheets/577969.pdf
[223] P. B. Ishai, M. S. Talary, A. Caduff, E. Levy, and Y. Feldman, "Electrode polarization in dielectric measurements: a review," *Measurement Science and Technology,* vol. 24, no. 10, p. 102001, 2013/08/27 2013, doi: 10.1088/0957-0233/24/10/102001.
[224] R. Pereira, L. F. Marchesi, R. G. Freitas, R. Matos, and E. C. Pereira, "A low-cost platinum film deposited direct on glass substrate for electrochemical counter electrodes," *Journal of Power Sources,* vol. 232, pp. 254-257, 2013/06/15/ 2013, doi: https://doi.org/10.1016/j.jpowsour.2013.01.040.
[225] P. Wang and W. L. Olbricht, "Study on electrodeposition of Pt," *Surface Engineering,* vol. 27, no. 9, pp. 662-670, 2011/10/01 2011, doi: 10.1179/1743294410Y.0000000007.
[226] S. E. Stanca *et al.*, "Chemical and electrochemical synthesis of Platinum black," *Sci Rep,* vol. 7, no. 1, p. 1074, 2017/04/21 2017, doi: 10.1038/s41598-017-01040-8.
[227] H. P. Schwan and C. D. Ferris, "Four-electrode null techniques for impedance measurement with high resolution," *Review of Scientific Instruments,* vol. 39, no. 4, pp. 481-485, 1968, doi: 10.1063/1.1683413.
[228] P. E. Gray and C. L. Searle, *Electronic Principles*. John Wiley & Sons Inc. , 1969.
[229] "Standard potential of the silver-silver chloride electrode," in *Pure and Applied Chemistry* vol. 50, ed, 1978, p. 1701.
[230] M. Přibyl and Z. Slouka, "Electrochemical characteristics of ideal polarizable interfaces with limited number of charge carriers," *Physical Review E,* vol. 92, no. 5, p. 052404, 11/20/ 2015, doi: 10.1103/PhysRevE.92.052404.
[231] J. Zhang, Ed. *PEM fuel cell electrocatalysts and catalyst layers: Aundamentals and applications*. 2008.
[232] J. J. Markham, "Reactions of acids and bases in analytical chemistry: By Adam Hulaniciki, Halsted Press, New York, 2nd ed., 1987. 308 pp., $122.95," *Microchemical Journal,* vol. 37, no. 3, pp. 384-385, 1988/06/01/ 1988, doi: https://doi.org/10.1016/0026-265X(88)90154-3.
[233] S. Carroll and R. P. Baldwin, "Self-calibrating microfabricated iridium oxide pH electrode array for remote monitoring," *Analytical Chemistry,* vol. 82, no. 3, pp. 878-885, 2010/02/01 2010, doi: 10.1021/ac9020374.
[234] P. Kurzweil, "Metal oxides and ion-exchanging surfaces as pH sensors in liquids: state-of-the-art and outlook," (in eng), *Sensors (Basel),* vol. 9, no. 6, pp. 4955-4985, 2009, doi: 10.3390/s90604955.

[235] M. L. Hitchman and S. Ramanathan, "Considerations of the pH dependence of hydrous oxide films formed on iridium by voltammetric cycling," *Electroanalysis,* vol. 4, no. 3, pp. 291-297, 1992/03/01 1992, doi: 10.1002/elan.1140040306.
[236] Beer, "Bestimmung der absorption des rothen lichts in farbigen flüssigkeiten," *Annalen der Physik,* vol. 162, no. 5, pp. 78-88, 1852/01/01 1852, doi: 10.1002/andp.18521620505.
[237] M. Castellarnau, A. Errachid, C. Madrid, A. Juárez, and J. Samitier, "Dielectrophoresis as a tool to characterize and differentiate isogenic mutants of Escherichia coli," (in eng), *Biophysical journal,* vol. 91, no. 10, pp. 3937-3945, 2006, doi: 10.1529/biophysj.106.088534.
[238] L. Brown, J. M. Wolf, R. Prados-Rosales, and A. Casadevall, "Through the wall: extracellular vesicles in Gram-positive bacteria, mycobacteria and fungi," *Nature Reviews Microbiology,* Review Article vol. 13, p. 620, 09/01/online 2015, doi: 10.1038/nrmicro3480.
[239] J. Cullum and M. Vicente, "Cell growth and length distribution in Escherichia coli," (in eng), *Journal of bacteriology,* vol. 134, no. 1, pp. 330-337, 1978, doi: 10.1128/JB.134.1.330-337.1978.
[240] G. Sezonov, D. Joseleau-Petit, and R. D'Ari, "Escherichia coli Physiology in Luria-Bertani Broth," *Journal of Bacteriology,* vol. 189, no. 23, pp. 8746-8749, 2007, doi: 10.1128/jb.01368-07.
[241] B. Gibson, D. J. Wilson, E. Feil, and A. Eyre-Walker, "The distribution of bacterial doubling times in the wild," (in eng), *Proc Biol Sci,* vol. 285, no. 1880, p. 20180789, 2018, doi: 10.1098/rspb.2018.0789.
[242] Z. Yu, Y. Cai, W. Qin, J. Lin, and J. Qiu, "Polymyxin E Induces Rapid Paenibacillus polymyxa Death by Damaging Cell Membrane while Ca2+ Can Protect Cells from Damage," *PLoS One,* vol. 10, no. 8, p. e0135198, 2015, doi: 10.1371/journal.pone.0135198.
[243] K. Stevenson, A. F. McVey, I. B. N. Clark, P. S. Swain, and T. Pilizota, "General calibration of microbial growth in microplate readers," *Sci Rep,* Article vol. 6, p. 38828, 12/13/online 2016, doi: 10.1038/srep38828.
[244] Concentration at OD ~0.7 (600nm) - Bacteria Escherichia coli - BNID 106028 [Online] Available: http://www.citethisforme.com/zh/cite/sources/websiteautociteconfirm
[245] B. Raghuraman, G. Gustavson, R. E. G. Van Hal, E. Dressaire, and O. Zhdaneev, "Extended-range spectroscopic pH measurement using optimized mixtures of dyes," *Applied Spectroscopy,* vol. 60, no. 12, pp. 1461-1468, 2006/12/01 2006, doi: 10.1366/000370206779321535.
[246] M. Faheem, M. T. Rehman, M. Danishuddin, and A. U. Khan, "Biochemical characterization of CTX-M-15 from Enterobacter cloacae and designing a novel non-β-lactam-β-lactamase inhibitor," (in eng), *PLoS One,* vol. 8, no. 2, pp. e56926-e56926, 2013, doi: 10.1371/journal.pone.0056926.
[247] V. Stojanoski *et al.*, "A triple mutant in the Ω-loop of TEM-1 β-lactamase changes the substrate profile via a large conformational change and an altered general base for catalysis," (in eng), *J Biol Chem,* vol. 290, no. 16, pp. 10382-10394, 2015, doi: 10.1074/jbc.M114.633438.
[248] W. Jamieson *et al.*, "Development of a rapid phenotypic test on a microfluidic device for carbapenemase detection using the chromogenic compound nitrocefin," *Diagnostic microbiology & infectious disease,* 2019.

[249] X. He, S. Li, and S. G. W. Kaminskyj, "Using Aspergillus nidulans to identify antifungal drug resistance mutations," *Eukaryotic Cell,* vol. 13, no. 2, pp. 288-294, 2014, doi: 10.1128/ec.00334-13.
[250] F. Sanschagrin, E. Thériault, Y. Sabbagh, N. Voyer, and R. C. Levesque, "Combinatorial biochemistry and shuffling of TEM, SHV and Streptomyces albus omega loops in PSE-4 class A β-lactamase," *Journal of Antimicrobial Chemotherapy,* vol. 45, no. 4, pp. 517-519, 2000, doi: 10.1093/jac/45.4.517.
[251] E. Yourassowsky, M. P. Van der Linden, M. J. Lismont, F. Crokaert, and Y. Glupczynski, "Effect on growth curves and killing curves of brief exposure of Escherichia coli to imipenem and piperacillin," *Journal of Antimicrobial Chemotherapy,* vol. 18, no. Supplement_E, pp. 61-65, 1986, doi: 10.1093/jac/18.Supplement_E.61.
[252] X. Huang, R. Pascal, K. Chamberlain, C. Banks, M. Mowlem, and H. Morgan, *A Miniature, High Precision Conductivity and Temperature Sensor System for Ocean Monitoring*. 2011, pp. 3246-3252.
[253] B. Weigl, R. Bardell, N. Kesler, and C. Morris, *Lab-on-a-chip sample preparation using laminar fluid diffusion interfaces - computational fluid dynamics model results and fluidic verification experiments*. 2001, pp. 97-105.
[254] HI98103 | Hanna Instruments pH Meter, 0 → +14 pH HI98103 | RS Components [Online] Available: https://uk.rs-online.com/web/p/ph-meters/0214855/
[255] ISFET pH meter | EDT DirectION [Online] Available: https://www.edt.co.uk/index.php?route=product/product&product_id=231
[256] A. Sardarinejad, D. K. Maurya, and K. Alameh, "The pH sensing properties of RF sputtered RuO2 thin-film prepared using different Ar/O2 flow ratio," *Materials,* vol. 8, no. 6, pp. 3352-3363, 2015. [Online]. Available: https://www.mdpi.com/1996-1944/8/6/3352.
[257] W.-A. C. Bauer, M. Fischlechner, C. Abell, and W. T. S. Huck, "Hydrophilic PDMS microchannels for high-throughput formation of oil-in-water microdroplets and water-in-oil-in-water double emulsions," *Lab on a Chip,* 10.1039/C004046K vol. 10, no. 14, pp. 1814-1819, 2010, doi: 10.1039/C004046K.
[258] O. Hofmann *et al.*, "Monolithically integrated dye-doped PDMS long-pass filters for disposable on-chip fluorescence detection," *Lab on a Chip,* 10.1039/B603678C vol. 6, no. 8, pp. 981-987, 2006, doi: 10.1039/B603678C.
[259] Glass-Like colored COC for pharma packaging, medical devices [Online] Available: https://www.ptonline.com/articles/glass-like-colored-coc-for-pharma-packaging-medical-devices
[260] G. SegrÉ and A. Silberberg, "Radial particle displacements in poiseuille flow of suspensions," *Nature,* vol. 189, no. 4760, pp. 209-210, 1961/01/01 1961, doi: 10.1038/189209a0.
[261] T. Kwon *et al.*, "Microfluidic cell retention device for perfusion of mammalian suspension culture," *Sci Rep,* vol. 7, no. 1, p. 6703, 2017/07/27 2017, doi: 10.1038/s41598-017-06949-8.
[262] P. Ohlsson, K. Petersson, P. Augustsson, and T. Laurell, "Acoustic impedance matched buffers enable separation of bacteria from blood cells at high cell concentrations," (in eng), *Sci Rep,* vol. 8, no. 1, pp. 9156-9156, 2018, doi: 10.1038/s41598-018-25551-0.